Discrete fiber models beyond classical applications

Rigid line inclusions, fiber-based batteries, challenges

Goudarzi, Mohsen

DOI
10.4233/uuid:4741efe6-9a5e-4782-8cef-6d7ed83a3b30

Publication date
2020

Document Version
Final published version

Citation (APA)
Goudarzi, M. (2020). *Discrete fiber models beyond classical applications: Rigid line inclusions, fiber-based batteries, challenges*. [Dissertation (TU Delft), Delft University of Technology].
https://doi.org/10.4233/uuid:4741efe6-9a5e-4782-8cef-6d7ed83a3b30

Important note
To cite this publication, please use the final published version (if applicable).
Please check the document version above.

DISCRETE FIBER MODELS BEYOND CLASSICAL APPLICATIONS

RIGID LINE INCLUSIONS, FIBER-BASED BATTERIES, CHALLENGES

DISCRETE FIBER MODELS BEYOND CLASSICAL APPLICATIONS

RIGID LINE INCLUSIONS, FIBER-BASED BATTERIES, CHALLENGES

Proefschrift

ter verkrijging van de graad van doctor
aan de Technische Universiteit Delft,
op gezag van de Rector Magnificus prof. dr. ir. T.H.J.J. van der Hagen,
voorzitter van het College voor Promoties,
in het openbaar te verdedigen op 28 April 2020 om 12:30 uur

door

Mohsen GOUDARZI

Master in Civil Engineering,
University of Tehran, Iran,
geboren te Tehran, Iran.

Dit proefschrift is goedgekeurd door de promotoren.

Samenstelling promotiecommissie:

Rector Magnificus,	voorzitter
Prof. dr. ir. L. J. Sluys,	TU Delft, promotor
Prof. dr. ir. A. Simone,	University of Padua, Italy, promotor
Onafhankelijke leden:	
Prof. dr. H. J. Böhm	TU Wien, Austria
Prof. dr. L. Asp	Chalmers University of Technology, Sweden
Dr. ir. H. J. M. Geijselaers	University of Twente
Dr. A.M. Aragón	TU Delft
Prof. dr. H.E.J.G. Schlangen	TU Delft

The research presented in this thesis has received funding from the European Research Council under the European Union's Seventh Framework Programme (FP7/2007-2013) / ERC Grant agreement n° 617972.

Keywords: fiber-reinforced composites, embedded reinforcement, rigid line inclusions, fiber neutrality, fiber-based batteries

Printed by: ...

Front & Back: Cover design by Mohsen Goudarzi

ISBN xxx-xx-xxxx-xxx-x

An electronic version of this dissertation is available at
http://repository.tudelft.nl/.

I often think that the night is more alive
and more richly colored than the day.

Vincent van Gogh

CONTENTS

SUMMARY

Reinforced composites are used in many industrial and multi-functional applications. The efficiency of the reinforcements depends mainly on the aspect ratio, material properties, and the adhesion between matrix and reinforcement. Particularly, high aspect ratio fillers and inclusions have gained popularity due to their unique material and geometrical features, where a fundamental understanding of composites hierarchical structure and behavior is crucial for the optimal design and performance. There is however a lack of robust numerical modeling frameworks that are able to accurately represent composites with high aspect ratio reinforcements. Ideally the expensive mesh generation of the standard finite element method or the simplifying assumptions adopted by smeared type or mean-field approaches should be avoided.

A group of numerical techniques here referred to as "embedded methods" eliminate mesh conformity restrictions and significantly reduce the computational cost of the standard finite element method, while still benefiting from the advantages of a direct numerical analysis. In formulating the embedded models, enrichment techniques and different element technologies are considered, and physical assumptions are investigated. Limitations of the classical embedded models are highlighted through numerical examples, on the basis of which possible enhancements are discussed. We specifically highlight the important roles of field gradients continuity/discontinuity and the element size, order, and regularity extensions on the smoothness of the solutions.

A computationally efficient embedded model is then applied to the study of failure and inclusion orientation effects in planar composites. A detailed study is also performed for dense fiber-reinforced composites, where homogenized mechanical properties are extracted and various forms of neutrality of thin fibers are demonstrated. In this context, a part of this thesis is dedicated to one-to-one comparisons between results obtained using the standard finite element method and embedded techniques. This led to a range of model and geometry parameters under which predictions of embedded technique are reliable. Comparisons are reported in terms of homogenized properties and local field variables, namely relative displacement between inclusions and matrix (slips).

Finally as a preliminary step towards multi-functional fiber-based structural batteries, an electro-chemical system characterized by composite cathode in a half cell configuration is considered. The main point of difference with common composite batteries is that active material particles are cast in form of high aspect ratio fibers, which are efficiently discretized by use of the embedded technique. A discrete definition of fibers, unlike the case of mean-field approaches, allows to define local fields and interfacial conditions between fibers and electrolyte and is crucial for the accurate modelling of a battery cell with fiber-based electrodes.

SAMENVATTING

Versterkte composieten worden in veel industriële en multifunctionele toepassingen gebruikt. De efficiëntie van de versterking hangt voornamelijk af van de beeldverhouding, materiaaleigenschappen en de hechting tussen matrix en versterkingen. Vooral fillers/insluitsels met een hoge beeldverhoudingen zijn populair geworden vanwege hun unieke materiaal en geometrische kenmerken,waar een fundamenteel begrip van de hiërarchische structuur en het gedrag van composieten cruciaal is voor een optimaal ontwerp en optimale prestaties. Er is echter een gebrek aan robuuste numerieke modelleer-frameworks die in staat zijn om nauwkeurig composieten met versterkingen van hogebeeldverhoudingen voor te stellen. In het ideale geval moet de dure mesh-generatie van de standaard eindige-elementenmethode of de vereenvoudigende aannames die in mean-field methodes worden gedaan, worden vermeden.

Een groep van numerieke technieken, hier aangeduid als "ingebedde methoden", elimineert beperkingen in mesh conformiteit en verminderen aanzienlijk de computationele kosten van de standaard eindige-elementenmethode, terwijl ze nog steeds profiteert van de voordelen van een directe numerieke analyse. Bij het formuleren van de ingebedde modellen worden verschillende verrijkings- en elemententechnologieën overwogen en worden fysieke aannames onderzocht. Beperkingen van de klassieke ingebedde modellen worden benadrukt door middel van numerieke voorbeelden, op basis waarvan mogelijke verbeteringen worden besproken. We benadrukken met name de belangrijke rol van continuïteit/discontinuïteit van veldgradiënten en de element grootte, orde en verlengingen van regelmaat op de soepelheid van de oplossingen.

Een computationeel goedkoop ingebed model wordt vervolgens toegepast op de studie van het falen en insluiten van oriëntatie effecten in vlakke composieten. Een gedetailleerd onderzoek wordt ook uitgevoerd voor vezel-versterkte composieten met een hoge beeldverhouding, waar gehomogeniseerde mechanische eigenschappen worden geëxtraheerd en verschillende vormen van neutraliteit van dunne vezels worden aangetoond. In deze context is een deel van deze thesis gewijd aan een één-op-één vergelijkingen tussen resultaten verkregen met behulp van de standaard eindige-elementenmethode en ingebedde technieken. Dit leidde tot een reeks model en geometrie parameters waarmee betrouwbare voorspellingen van de ingebedde technieken kunnen worden gedaan. Vergelijkingen worden gerapporteerd in termen van gehomogeniseerde eigenschappen en lokale veldvariabelen, namelijk relatieve verplaatsing tussen insluitsels en matrix (slips).

Als laatste stap in de richting van multifunctionele vezel-gebaseerde structurele batterijen, wordt een elektrochemisch systeem beschouwd dat wordt gekenmerkt door een composietkathode in een configuratie met halve cellen. Het belangrijkste verschil met gewone composietbatterijen is dat actieve materiaaldeeltjes worden gegoten in de vorm van vezels met een hoge beeldverhouding, die efficiënt worden gediscretiseerd met behulp van de ingebedde techniek. Een afzonderlijke definitie van vezels, in tegenstelling tot bij mean-field methoden, maakt het mogelijk lokale velden en interfaciale omstandigheden tussen de

vezels en elektrolyt te definiëren en is cruciaal voor de nauwkeurige modellering van een batterijcel met op vezels gebaseerde elektroden.

1

INTRODUCTION

1.1. MOTIVATION

Reinforced composite materials are ubiquitous with their response (mechanical, thermal, electro-chemical, etc) tailored for a variety of applications. Although reinforcements come in many different shapes, high aspect ratio discrete inclusions or platelets are commonly adopted due to their ideal performance, flexibility in use, and ease of production. Discrete inclusions generally vary in geometrical details (e.g., level of waviness), and are found in non-uniform or arbitrary distributions (e.g., agglomerated or intercalated) making an accurate representation of the composite micro-structure difficult. A computational approach is however crucial due to the dependence of the composite response on these micro details. In this regard, applying a direct finite element method (FEM) is among the most accurate options.

A well known limitation when treating high aspect ratio inclusion arrangements is to generate a finite element discretization of the micro-structure. In fact, a quality mesh can only be generated for rather simple inclusion arrangements. Averaging theorems and multi-scale approaches are therefore normally favored over direct numerical models, but usually introduce modeling complexities or substantial physical simplifications.

This thesis presents efficient numerical techniques that facilitate the reproduction of the effect of the geometry of high aspect ratio (thin) inclusions on the basis of the FEM. Although the presented methods can also be used as a sub-model in a multi-scale framework, we specifically avoid averaging techniques to preserve the advantages gained by a direct numerical method. At the same time we try to eliminate the expensive steps by the use of advanced numerical discretization techniques such as embedded mesh and extended/generalized finite element methods.

In the reminder of this chapter, general considerations on the examples of composites with high aspect ratio (thin) inclusions are given. This is followed by a general overview of the available computational strategies along with their limitations when used for micro-mechanical analyses. The thesis outline is given at the end.

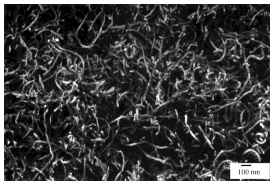

(a)

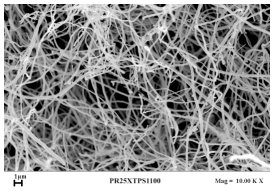

(b)

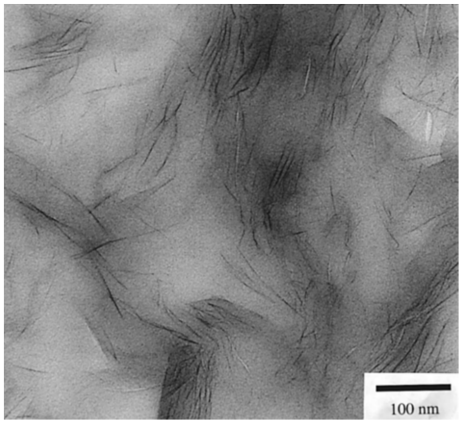

(c)

Figure 1.1: Examples of high aspect ratio fiber-reinforced composites: (a) SEM image of a 50 wt.% PVOH/nanotube composite [7], (b) SEM image of CNFs (PR25XTPS1100) [8], (c) TEM image of 10 wt.% Cloisite 30A in a diamine-cured epoxy [9].

1.2. BACKGROUND

1.2.1. APPLICATIONS

In many composite materials the reinforcements are in the shape of short fibers, whiskers or platelets with their axial dimension much larger that the lateral ones (Figure 1.1). Such high aspect ratio geometry enables favorable mechanical properties for a wide range of materials with low stiffnesses, including cement based materials, thermosets, and thermoplastics. There also exist many instances in naturally occurring composites, such as nacre, enamel, and silk where stiff inclusions of high aspect ratio are regarded as their smallest building block [1]. Inclusion type vary depending on the context with common synthetic examples being glass fiber, aramid fiber (such as Kevlar^{TM}), carbon nanofibers (CNFs)/carbon nanotubes (CNTs) [2, 3] and clay plates in noncomposites [4]. Biological tissues of cytoskeleton filament networks [5, 6] and minerals in tooth are some of the biological or natural examples.

In conventional applications, inclusions are expected to provide desirable stiffness (e.g. Young's modulus), strength or toughness for composites working mainly under mechanical loadings. A recent trend is however towards multi-functional composite materials, where composites are tailored for a combination of mechanical and non-mechanical tasks. For example, nanofibers used as reinforcement of the interface of advanced carbon-fiber laminated composites can increase heat dissipation functionality leading to a multifunctional composite with ideal structural and thermal behavior [10]. Moreover, the addition of nanofibers improves the mechanical properties of polymers, as a percolated network of CNTs or CNFs ensures great thermal conductivity of the resultant composite. Another recent area of research are high-performance and structural batteries [11], in which short fiber composites are receiving increasing attention for their possible applications as active materials. In the

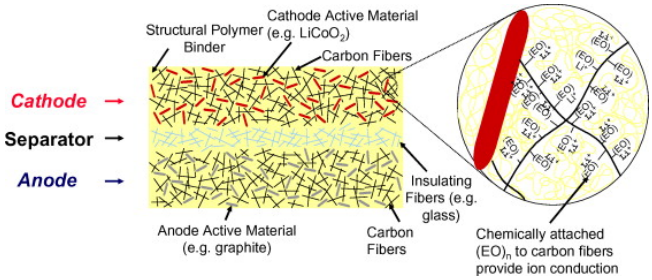

Figure 1.2: Design of a structural battery from Reference [11]. As compared to traditional batteries, all particulate fillers are replaced by fibers. A high molecular weight polymer serves as the structural polymer binder. On the surface of carbon fibers are polyethylene (PEO) oligomers that facilitate lithium ion transport. Insulating fibers further reinforce the separator region.

design of these battery cells, the electrolyte (either liquid or solid) accommodates fiber-type functional components. The main advantage of nanofibers with high aspect ratio is that they are characterized by a larger surface area to volume ratio compared to their particle-shaped counterpart [12], resulting in an enhanced lithium exchange with the electrolyte that eventually improves the battery performance (Figure 1.2).

1.2.2. MICRO-MECHANICAL ANALYSIS

The elastic or nonlinear response of composite or heterogeneous materials is the outcome of a dedicated micromechanical analysis. Analytical models like Eshelby-based [13] mean-field homogenization techniques have gained popularity due to their efficiency, simplicity in use, and accuracy in the elastic range [14], with two step homogenization schemes available for fillers of different shapes, densities and spatial orientations [15–17]. Similar to some multi-scale approaches, mean-field methods assume that inclusions are isolated and constitutive relations hold on an average sense without providing a local representation of field variables such as strains and stresses, which are essential in many cases (e.g., for a failure analysis).

A dedicated finite element analysis provides a way to deal with practical situations by incorporating the reinforcements shape, different forms of interface, material and geometrical nonlinearities and interactions between reinforcements [18] (Figure 1.3), but obviously at a significantly higher computational cost compared to mean-field approaches. To alleviate the computational effort, mesh-independent numerical discretization techniques like the generalized/extended finite element method [19, 20], interface generalized finite element method [21, 22], domain fitting algorithms [23, 24], finite cell method [25], and the embedded mesh technique [26] have been proposed over the years. The main advantages gained by these methods is that the conformity restriction between lines of discontinuity (such as inclusion edges) and matrix elements is removed, and various forms of weak/strong discontinuities can be effortlessly incorporated.

The case of high aspect ratio inclusions however still requires fine meshes even when used along with such advanced numerical techniques. For this especial case, embedded reinforcement techniques [27, 28] have been designed on the basis of complementary and

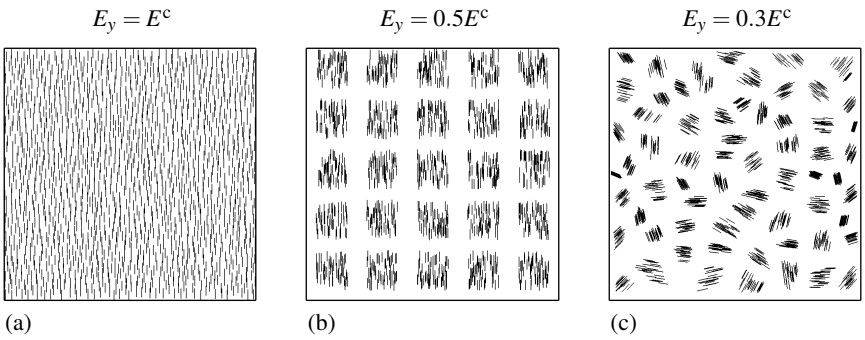

Figure 1.3: Three composite micro-structures with the same number of inclusions and different intercalation levels. A numerical discretization of the problem shows that inclusion intercalation strongly influences the effective mechanical properties in the vertical direction. An analytical micro-mechanical model however is not sensitive to the distribution patterns and interactions between inclusions are not captured.

simplifying assumptions on the kinematics of field variables, namely displacements and their gradients in mechanics or electric potential and concentration and their gradients in electro-chemistry. Another common physical simplification is the dimensional reduction of cylindrical shaped fibers (or inclusion with certain thickness in two dimensions) into line elements, which further simplifies a mesh-independent distribution of inclusions embedded into a coarse background matrix.

1.3. SCOPE AND OUTLINE OF THE THESIS

This thesis presents a numerical micro-mechanical analysis of high aspect ratio (thin) inclusion composites. Special focus is given to the assumptions involved in the numerical aspects of embedded reinforcement methods, and detailed verifications against fully-resolved FEM are provided. We consider a wide range of applications including the linear elastic analysis of nanocomposites, damage and shear-band formation due to rigid inclusion, micro-mechanical analysis of dense fiber composites, and fiber-based electrodes in batteries.

As such we start in Chapter 2 with a comprehensive evaluation of various aspects of traditional embedded techniques along with novel methods with enhanced features. The investigated aspects include accuracy of local fields (e.g., displacement and strains in mechanics), previously unknown inherent drawbacks of embedded methods, and convergence analyses where more accurate models with a weak discontinuity or models with higher regularity or approximation order are proposed. Chapter 3 is a computational step towards the limit case of rigid inclusions (known as rigid line inclusions or RLIs) using the embedded technique where the role of inclusions as shear band promoting agents in a visco-plastic damage model are discussed. A detailed micro-mechanical analysis and a one-to-one comparison between a fully resolved finite element method and the embedded technique are given in Chapter 4. In this regard we evaluate the role of fiber orientation on the mechanical properties, where features like fiber neutrality in terms of various homogenized properties and under certain mechanical loadings are discussed in detail. Finally the fiber model is

extended to a coupled formulation of electro-chemistry for the study of multi-field batteries with composite electrodes. A general tool is proposed by taking into account local interface electro-chemical reactions. The discussed framework has been validated against available numerical methods and can also be used for thermal analysis of fiber-reinforced composites with interface imperfections.

REFERENCES

[1] P. Pingle, J. Sherwood, and L. Gorbatikh, *Properties of rigid-line inclusions as building blocks of naturally occurring composites,* Composites Science and Technology **68**, 2267 (2008).

[2] E. Hammel, X. Tang, M. Trampert, T. Schmitt, K. Mauthner, A. Eder, and P. Pötschke, *Carbon nanofibers for composite applications,* Carbon **42**, 1153 (2004).

[3] Y. Chen, F. Pan, Z. Guo, B. Liu, and J. Zhang, *Stiffness threshold of randomly distributed carbon nanotube networks,* Journal of the Mechanics and Physics of Solids **84**, 395 (2015).

[4] N. Sheng, M. C. Boyce, D. M. Parks, G. C. Rutledge, J. I. Abes, and R. E. Cohen, *Multiscale micromechanical modeling of polymer/clay nanocomposites and the effective clay particle,* Polymer **45**, 487 (2004).

[5] M. Das and F. C. MacKintosh, *Poisson's ratio in composite elastic media with rigid rods,* Physical Review Letters **105**, 138102 (2010).

[6] V. Pelletier, N. Gal, P. Fournier, and M. L. Kilfoil, *Microrheology of microtubule solutions and actin-microtubule composite networks,* Physical Review Letters **102**, 188303 (2009).

[7] M. S. Shaffer and A. H. Windle, *Fabrication and characterization of carbon nanotube/poly (vinyl alcohol) composites,* Advanced Materials **11**, 937 (1999).

[8] L. Guadagno, M. Raimondo, V. Vittoria, L. Vertuccio, K. Lafdi, B. De Vivo, P. Lamberti, G. Spinelli, and V. Tucci, *The role of carbon nanofiber defects on the electrical and mechanical properties of cnf-based resins,* Nanotechnology **24**, 305704 (2013).

[9] J. M. Brown, D. Curliss, and R. A. Vaia, *Thermoset-layered silicate nanocomposites. quaternary ammonium montmorillonite with primary diamine cured epoxies,* Chemistry of Materials **12**, 3376 (2000).

[10] F. Gardea, M. Naraghi, and D. Lagoudas, *Effect of thermal interface on heat flow in carbon nanofiber composites,* ACS Applied Materials & Interfaces **6**, 1061 (2013).

[11] P. Liu, E. Sherman, and A. Jacobsen, *Design and fabrication of multifunctional structural batteries,* Journal of Power Sources **189**, 646 (2009).

[12] R. E. Garcia, Y.-M. Chiang, W. C. Carter, P. Limthongkul, and C. M. Bishop, *Microstructural modeling and design of rechargeable lithium-ion batteries,* Journal of The Electrochemical Society **152**, A255 (2005).

[13] J. D. Eshelby, *The determination of the elastic field of an ellipsoidal inclusion, and related problems,* Proceedings of the Royal Society of London A **241**, 376 (1957).

[14] D. Hull and T. W. Clyne, *An Introduction to Composite Materials* (Cambridge University Press, 1996).

[15] O. Pierard, C. Friebel, and I. Doghri, *Mean-field homogenization of multi-phase thermo-elastic composites: A general framework and its validation,* Composites Science and Technology **64**, 1587 (2004).

[16] I. Doghri and L. Tinel, *Micromechanical modeling and computation of elasto-plastic materials reinforced with distributed-orientation fibers,* International Journal of Plasticity **21**, 1919 (2005).

[17] W. Tian, L. Qi, C. Su, J. Zhou, and Z. Jing, *Numerical simulation on elastic properties of short-fiber-reinforced metal matrix composites: Effect of fiber orientation,* Composite Structures **152**, 408 (2016).

[18] J. M. Guedes and N. Kikuchi, *Preprocessing and postprocessing for materials based on the homogenization method with adaptive finite element methods,* Computer methods in applied mechanics and engineering **83**, 143 (1990).

[19] J. M. Melenk and I. Babuška, *The partition of unity finite element method: Basic theory and applications,* Computer Methods in Applied Mechanics and Engineering **139**, 289 (1996).

[20] N. Moës, M. Cloirec, P. Cartraud, and J. F. Remacle, *A computational approach to handle complex microstructure geometries,* Computer Methods in Applied Mechanics and Engineering **192**, 3163 (2003).

[21] S. Soghrati, A. M. Aragón, A. C. Duarte, and P. H. Geubelle, *An interface-enriched generalized FEM for problems with discontinuous gradient fields,* International Journal for Numerical Methods in Engineering **89**, 991 (2012).

[22] S. Soghrati and P. H. Geubelle, *A 3D interface-enriched generalized finite element method for weakly discontinuous problems with complex internal geometries,* Computer Methods in Applied Mechanics and Engineering **217–220**, 46 (2012).

[23] S. Omerović and T.-P. Fries, *Conformal higher-order remeshing schemes for implicitly defined interface problems,* International Journal for Numerical Methods in Engineering **109**, 763 (2017).

[24] S. Soghrati, A. Nagarajan, and B. Liang, *Conforming to interface structured adaptive mesh refinement: new technique for the automated modeling of materials with complex microstructures,* Finite Elements in Analysis and Design **125**, 24 (2017).

[25] J. Parvizian, A. Düster, and E. Rank, *Finite cell method,* Computational Mechanics **41**, 121 (2007).

[26] J. D. Sanders, T. A. Laursen, and M. A. Puso, *A Nitsche embedded mesh method,* Computational Mechanics **49**, 243 (2012).

[27] S. Balakrishnan and D. W. Murray, *Finite element prediction of reinforced concrete behavior*, Structural Engineering Report No. 138 (1986).

[28] A. E. Elwi and T. M. Hrudey, *Finite element model for curved embedded reinforcement,* Journal of Engineering Mechanics **115**, 740 (1989).

2

DISCRETE INCLUSION MODELS FOR REINFORCED COMPOSITES

We report the results of a comparative analysis of mesh independent discrete inclusion models and point out some shortcomings of classical approaches in the approximation of the strain field across an inclusion (artificial continuity) and the slip profile along an inclusion (oscillatory behavior). We also present novel embedded reinforcement models based on partition of unity enrichment strategies, adaptive *h*-refinement, and order/regularity extensions. These novel models are assessed by means of mesh convergence studies and it is shown that they improve the quality of the solution by significantly decreasing local spurious oscillations in the slip profile along an inclusion.

2.1. INTRODUCTION

A reliable prediction of the mechanical behavior of a reinforced composite can only be obtained with the aid of modeling approaches that describe geometry and deformations of reinforcing agents with adequate precision and are equipped with appropriate constitutive models. With reference to high aspect ratio inclusions such as platelets or fibers (or, equivalently, rebars), the most accurate modeling approach for this task is the finite element method (FEM) with conformal meshing of individual inclusions, an approach that might be (prohibitively) expensive if done at an adequate resolution level [1, Figure 2]. Embedded reinforcement models, lifting the meshing constraints typical of classical FEM approaches, are a viable alternative to conformal FEM discretizations. In this contribution we compare the performance of existing and novel embedded reinforcement models while highlighting some of their limitations and suggesting strategies to improve their performance. Although in the examples we make reference to thin (high aspect ratio) platelet inclusions in a two-dimensional setting for convenience, the results of this study hold also for high aspect ratio

Reprinted from: M. Goudarzi and A. Simone, Discrete inclusion models for reinforced composites: Comparative performance analysis and modeling challenges, *Computer Methods in Applied Mechanics and Engineering*, 355:535–557, 2019.

fibers as both inclusions can be approximated as one dimensional objects under planar conditions. Fibers and platelets are referred to as inclusions throughout the chapter when discussing general concepts.

Fibers or platelet inclusions as reinforcing agents can be modeled in several manners by borrowing approaches originally developed for rebars in reinforced concrete structures or by means of dedicated approaches [2–13]. A simplistic classification can be into two broad categories: implicit and explicit approaches. In the first approach, also called continuous approach, the collective effect of the inclusions on the response of the composite is taken into account in an indirect manner by means of suitable modifications to the constitutive model and material properties of the composite, which is seen as a continuum with homogeneous properties; in the second approach, also known as the discrete approach, each inclusion is directly taken into account either using solid finite elements or simplified dimensionally reduced discretizations. In this study we focus on the latter.

In explicit inclusion models we distinguish between conformal and non-conformal approaches, depending on the way the inclusion is discretized with respect to the discretization of the matrix material. Explicit approaches can then be classified according to the fidelity of the discretization with respect to the actual geometry. In the most accurate approaches, geometrical details of the inclusions are discretized using the standard conformal finite element method with solid elements [1, 3, 14, 15]. Similar studies have been conducted for high aspect ratio platelet clay inclusions, represented by means of two-dimensional [16] and three-dimensional [17] finite element models. Although very accurate, explicit inclusion models suffer from costly mesh generation procedures, hence making the study of composites with a large number of inclusions difficult. An exception is the conformal method proposed by Soghrati *et al.* [15] in which background elements cut by an interface are morphed to generate a conformal discretization, thus simplifying the meshing procedure and reducing its cost. Based on advances in the use of enriched basis functions in the finite element method [18], it is possible to describe intra-element discontinuous fields, thus relaxing the mesh conformity restrictions of classical FEM approaches. Such an approach has been pursued by Moës *et al.* [19] who adopted a material discontinuity enrichment function to represent the intra-element perfectly bonded interface between matrix and inclusion. Related approaches include the work of Omerović and Fries [20] and the interface-enriched generalized finite element method (IGFEM) [21, 22].

Such methods however are not easily applicable to dense inclusion distributions and may require extremely fine discretizations, especially for high aspect ratio fiber inclusions such as rebars, thin fibers, or carbon nanotubes. In these cases, the geometrical configuration of the inclusion allows considerable modeling simplifications as it can be represented as a one-dimensional object in a finite element discretization, similar to the approach employed in early finite element analyses of reinforced concrete structures. A further simplifications originates from the common understanding that in composites with high aspect ratio fibers the axial deformation contribution to the strain energy is significantly larger compared to that of other deformation mechanisms, thus allowing to represent a fiber by means of kinematic quantities related to the axial deformation only. Phillips and Zienkiewicz [23] were the first to consider these simplifications in a computational study of reinforced concrete by employing axially-deformable bar elements to represent rebars. In their approach, rebars are perfectly bonded and discretized in a non-conformal manner with respect to the

matrix material mesh. Such non-conformal approaches are known as embedded reinforcement models.

The idea of adopting explicit degrees of freedom (DOFs) to represent the relative tangential displacement between inclusion and matrix (slip) was first employed by Balakrishnan and Murray [2]. This approach, which will be referred to as embedded reinforcement model with slip (ERS model) in this chapter, can be understood as a generalization of the embedded reinforcement model proposed by Phillips and Zienkiewicz [23] to imperfect interfaces and has been successfully applied to numerous engineering problems [24–28].

One-dimensional fiber inclusions in a two-dimensional setting can also be represented by means of a partition of unity enrichment strategy. The approach proposed by Radtke *et al.* [29] enriches the nodes of the elements crossed by a fiber inclusion with DOFs representing the relative displacement between inclusion and matrix (including normal and tangential components). Although the approach allows to incorporate a priori known enrichment functions to improve the convergence rate of the numerical solution, the corresponding enrichment scheme is relatively expensive, especially its extension to three-dimensions, as it effectively doubles the number of elemental DOFs when an element is crossed by a fiber. This is in contrast with the ERS model, which only requires slip DOFs to be placed at matrix-fiber intersection points. A related XFEM based approach was proposed by Pike and Oskay [30] who were the first to consider both weak and strong discontinuity enrichments (referred to as fiber and debonding enrichments) to represent the effect of a debonding fiber in the matrix displacement field. As shown in Section 2.2.2, these two enrichments are necessary as a fiber inclusion introduces weak and strong discontinuities in the displacement field of the matrix material. Both approaches [29, 30] use the partition of unity enrichment strategy and therefore require a distributed enrichment scheme (all nodes of elements crossed by a fiber are enriched, with one extra set of DOFs for enrichment). In contrast, ERS models (Section 2.3) require dedicated DOFs along the fiber itself but cannot properly represent the weak discontinuity (Section 2.4.1) because of the assumptions in the displacement field (*i.e.*, artificial continuity of the strain field in the matrix across an inclusion). Incorporating such discontinuities adds to the complexity in terms of implementation as it requires a dedicated independent conformal integration mesh similar to that used by Pike and Oskay [30]. Also, a direct three-dimensional extension is not straightforward (Pike and Oskay [31] have incorporated short fibers as deformable rectangular planar inclusions).

Among the discrete approaches described above, the techniques with an exact geometrical representation of the inclusions are, obviously, the most accurate. Accuracy, however, comes with high computational costs even for limited number of inclusions. Dimensionally reduced approaches of the ERS type combine adequate accuracy with numerical efficiency. Their classical version and several novel formulations designed to improve specific characteristics are assessed in Sections 2.4 and 2.5. It is shown that some formulations are more effective than others in addressing the occurrence of oscillations in the slip profile but none can remove them.

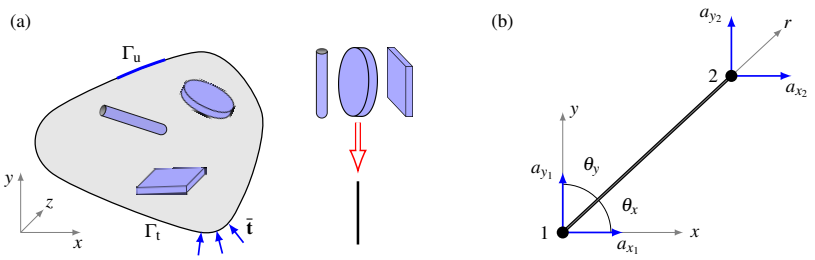

Figure 2.1: (a) Schematic of a composite with several types of high aspect ratio inclusions (these inclusions can be described as line inclusions). (b) Local coordinate system for an arbitrary two-dimensional inclusion segment.

2.2. GOVERNING EQUATIONS

Under the assumption of small deformations, the principle of virtual work for the two-phase reinforced composite occupying the volume Ω in Figure 2.1a reads

$$\int_\Omega \boldsymbol{\sigma} : \nabla^s \delta\mathbf{u} \, d\Omega + \int_{\Gamma_{int}} \mathbf{t}_{int} \cdot \delta\mathbf{w} \, d\Gamma_{int} - \int_{\Gamma_t} \bar{\mathbf{t}} \cdot \delta\mathbf{u} \, d\Gamma_t = 0 \tag{2.1}$$

for every virtual displacement field $\delta\mathbf{u}$, and with the displacement gap vector $\mathbf{w}$ a function of the displacement vector $\mathbf{u}$. In (2.1), we have neglected body forces, $\boldsymbol{\sigma}$ is the stress tensor, and ∇^s is the symmetric gradient operator. The first integral has not been divided yet into matrix and inclusion components as they obey the same governing equations. Since the inclusion is not perfectly bonded, the second term in (2.1) represents the virtual mechanical work across the matrix-inclusion interface Γ_{int} due to the interface tractions $\mathbf{t}_{int}$ and the corresponding matrix-inclusion displacement gap vector $\mathbf{w}$. The last term represents the work done by the external tractions $\bar{\mathbf{t}}$ on the external surface Γ_t.

2.2.1. DISCRETIZATION USING CONFORMAL FEM

We now describe a reference model in the context of the standard finite element method and solve a benchmark problem that will also be used later with the discretization techniques discussed in Section 2.3. The domain Ω is subdivided into matrix and inclusion subdomains ($\bar{\Omega} = \bar{\Omega}_m \cup \bar{\Omega}_i$, with subscripts i and m indicating inclusion and matrix contributions, respectively). This reference model is based on the model by Ngo and Scordelis [32]. Here, the discretized one-dimensional inclusion Ω_i is linked to the underlying discretized matrix material Ω_m by an interface element that allows a relative displacement between inclusion and matrix. The inclusion has to be understood as being superimposed on the matrix rather than being surrounded by it. A conformal discretization for matrix and inclusion is assumed where standard four-node quadrilateral (Q4) or three-node triangular (T3) finite elements are used for the matrix, and a one-dimensional discretization, described in the next section, is employed for inclusion and corresponding matrix-inclusion interface contributions (the second term in (2.1)). The last term is discretized following standard procedures.

Inclusion The conformal discretization approach can be used for fiber based composites in two and three dimensions and for platelet inclusions in a two-dimensional setup (under

the plane strain assumption). All the examples discussed in this chapter make reference to platelets; we thus assume that inclusions are in the shape of high aspect ratio platelets and are discretized by means of conventional two node truss elements (assuming therefore plane strain conditions in all the examples). Consequently, each inclusion element is characterized by a one-dimensional displacement field along its axis. The stiffness matrix in the global xy coordinate system for an inclusion element of length L is then given by

$$\mathbf{K}_{\mathrm{i}} = \frac{\bar{E}_{\mathrm{i}}\, A_{\mathrm{i}}}{L} \begin{pmatrix} l^2 & lm & -l^2 & -lm \\ lm & m^2 & -lm & -m^2 \\ -l^2 & -lm & l^2 & lm \\ -lm & -m^2 & lm & m^2 \end{pmatrix}, \quad \text{with } l = \frac{x_2 - x_1}{L} \;,\; m = \frac{y_2 - y_1}{L}, \tag{2.2}$$

where $\bar{E}_{\mathrm{i}} = E_{\mathrm{i}} - E_{\mathrm{m}}$ is the effective stiffness of the inclusion with E_{m} and E_{i} the Young's moduli of matrix and inclusion, respectively. The inclusion effective stiffness has been introduced to remove the contribution of the matrix material related to the inclusion region. The coordinates of an inclusion segment endpoints (points 1 and 2 in Figures 2.1a and 2.2) are (x_1, y_1) and (x_2, y_2), and its cross sectional area is $A_{\mathrm{i}} = d_{\mathrm{i}}\, t_{\mathrm{i}}$, with d_{i} and $t_{\mathrm{i}} = 1\ \mu m$ the in-plane and out-of-plane widths of the inclusion segment, respectively.

Inclusion-matrix interface The relative displacement between an inclusion and the underlying matrix can be represented with the aid of conventional zero-thickness conformal interface elements (Figure 2.2a) that are equivalent to the linkage elements proposed by Ngo and Scordelis [32]. Since the discretization of the matrix material is not modified when an inclusion is superimposed on it, the continuity of the underlying matrix displacement field is not influenced. The interface gap vector (this is the relative displacement between interface and matrix) in the coordinate system local to the inclusion is discretized by

$$\mathbf{w} = \mathbf{R}\,\mathbf{N}_{\mathrm{int}}\,\mathbf{d}_{\mathrm{int}}, \tag{2.3}$$

where $\mathbf{R}$ is the conventional global-to-local rotation matrix, and the interface shape function matrix and interface nodal displacement vector are defined as

$$\mathbf{N}_{\mathrm{int}} = \begin{bmatrix} N_{\mathrm{i}1} & 0 & N_{\mathrm{i}2} & 0 & -N_{\mathrm{m}1} & 0 & -N_{\mathrm{m}2} & 0 \\ 0 & N_{\mathrm{i}1} & 0 & N_{\mathrm{i}2} & 0 & -N_{\mathrm{m}1} & 0 & -N_{\mathrm{m}2} \end{bmatrix} \tag{2.4}$$

and

$$\mathbf{d}_{\mathrm{int}} = \begin{bmatrix} \mathbf{u}_{\mathrm{i}1} & \mathbf{u}_{\mathrm{i}2} & \mathbf{u}_{\mathrm{m}1} & \mathbf{u}_{\mathrm{m}2} \end{bmatrix}^{\mathrm{T}}, \tag{2.5}$$

respectively, where subscripts 1 and 2 indicate corresponding inclusion endpoints, N indicates one-dimensional shape functions (along the inclusion segment and along the edge of the matrix element next to it), and $\mathbf{u}$ are displacement vectors in the global coordinate system.

Substituting (2.3) into the second term in (2.1) and following standard procedures yield the interface stiffness contribution

$$\mathbf{K}_{\mathrm{int}} = C_{\mathrm{i}} \int_L {\mathbf{N}_{\mathrm{int}}}^{\mathrm{T}}\, \mathbf{R}^{\mathrm{T}}\, \mathbf{D}_{\mathrm{b}}\, \mathbf{R}\, \mathbf{N}_{\mathrm{int}}\, \mathrm{d}r \tag{2.6}$$

in which L is the length of the inclusion-matrix interface element (known also as bond element and with length equal to that of the inclusion element), $C_\mathrm{i} = 2\,t_\mathrm{i}$ is a factor, together with L, taking into account the actual surface of the inclusion-matrix interface region, and r is the local coordinate along the bond element. A linear traction separation law is considered ($\mathbf{t}_\mathrm{int} = \mathbf{D}_\mathrm{b}\mathbf{w}$), with the elastic interface constitutive matrix $\mathbf{D}_\mathrm{b} = \mathrm{diag}\,(K_\mathrm{bt}, K_\mathrm{bn})$, where the constants K_bt and K_bn represent the stiffness of the interface in the directions tangential and normal to the inclusion axis, respectively. In this conformal model, we only allow the relative displacement in the tangential direction (slip) by constraining the normal relative displacement by using large values of the interface normal stiffness K_bn. Preliminary analyses of the global stiffness matrix for the case of one inclusion indicate that its condition number does not significantly change by changing the interface constants. The condition number is in any case higher than the original system without inclusion, and this can be attributed to the augmented structure of the stiffness matrix when inclusions are considered. In these situations, a direct numerical solver is to be preferred; iterative solvers could also be used, but require appropriate preconditioners.

2.2.2. BENCHMARK PROBLEM

The benchmark problem discussed in this section is used to evaluate the performance of the numerical models presented throughout the chapter. Figure 2.3 shows geometry and boundary conditions of a $4\ \mu\mathrm{m} \times 4\ \mu\mathrm{m}$ polymer-clay nano-composite sample [16]. Young's moduli of matrix and inclusion are taken as $E_\mathrm{m} = 3$ GPa and $E_\mathrm{i} = 300$ GPa, respectively. In this benchmark problem, one horizontal ($\theta = 0$) 2 μm long inclusion with $d_\mathrm{i} = 5$ nm and aspect ratio equal to 400 is placed in the middle of the specimen. The matrix Poisson's ratio ν_m is equal to 0.35.

For the reference numerical calculations, a 600×600 uniform grid of bilinear quadrilateral elements is employed. The right-hand side edge is uniformly displaced by $\bar{\delta} = 0.05\ \mu\mathrm{m}$ (Figure 2.3). Unlike in similar studies [16, 17], the inclusion is not perfectly bonded to the matrix and elastic sliding is therefore allowed (the interface tangential stiffness K_bt is set equal to $0.025\ \mathrm{N}/\mu\mathrm{m}^3$).

Analysis of the strain field in the matrix material While the displacement field in the matrix across the inclusion is continuous, some of the components of the strain field can be discontinuous.

The strain tensor components along the vertical lines shown in Figure 2.4a are plotted in Figures 2.4b-d. The vertical lines are aligned with the location of the integration points in the finite elements used to discretize the matrix material, thus allowing the direct sampling of the strain field. As shown in Figure 2.4c, the shear component ε_{xy} of the matrix strain tensor is not continuous across the inclusion unlike the other two components ε_{xx} and ε_{yy} (Figure 2.4b,d). These results have been confirmed with the double interface model presented in Reference [33] which describes a fiber surrounded by the interface in a two-dimensional setting—this model is to be understood as the dimensional reduction of a solid fiber embedded in a three-dimensional body. As shown later, the classical ERS model [2] (Section 2.3.1) cannot reproduce this discontinuity in the gradient of the matrix displacement field.

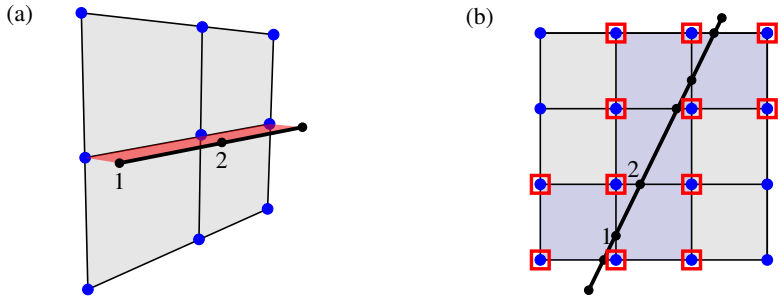

Figure 2.2: (a) Schematic of the reference composite model with conformal discretization of the inclusion. Blue and black dots represent matrix and inclusion nodes, respectively. Zero-thickness interface elements (red shaded region) are placed between inclusion (solid black line) and matrix elements. Strain discontinuity is naturally achieved because of the standard FEM displacement field approximation. (b) An arbitrarily-located inclusion discretized with the ERS model (Section 2.3.1); strain discontinuity is achieved by enriching the nodes of the elements crossed by the inclusion (marked with a red squares) with a weak discontinuity enrichment function as discussed in Section 2.3.2.

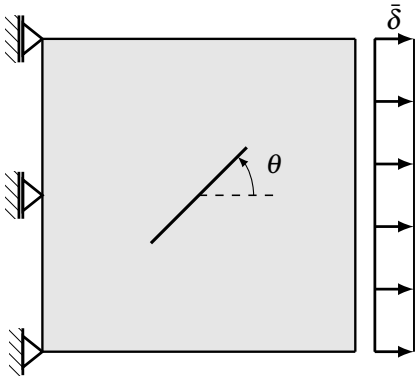

Figure 2.3: Schematic of the benchmark problem with one inclusion.

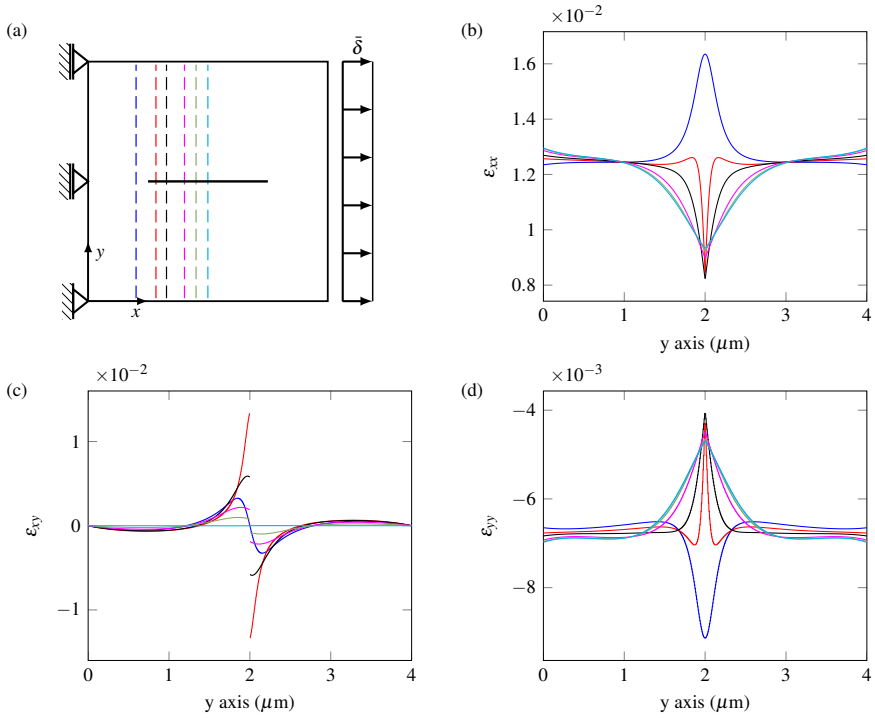

Figure 2.4: (a) Schematic of the single inclusion problem with sampling lines for the strain tensor components reported in the other panels: ε_{xx} (b), ε_{xy} (c), and ε_{yy} (d). The problem is solved using the conformal FEM model with a uniform 600×600 Q4 discretization.

2.3. MESH-INDEPENDENT MODELS

In the reference model introduced in the previous section the inclusion was modeled using a conformal discretization. In principle, this is restrictive when handling a large number of inclusions. In this section, various numerical models that allow the inclusion to be positioned anywhere in the composite domain with respect to the underlying matrix discretization are discussed. At variance with the reference model, inclusion endpoints can be placed within an element, and there is no theoretical limit on the number of inclusions that can be included in an element.

2.3.1. EMBEDDED REINFORCEMENT MODELS

Embedded reinforcement models cannot reproduce the discontinuity in the strain field discussed in the previous section. In these models, the displacement of an inclusion is usually determined indirectly, by means of the relative displacement $\mathbf{u}_{\mathrm{rel}}$ between inclusion and matrix which is taken as an additional field. This implies that the displacement field $\mathbf{u}$ is decomposed into matrix component $\mathbf{u}_{\mathrm{m}}$, valid in the matrix domain Ω_{m}, and inclusion displacement component $\mathbf{u}_{\mathrm{d}} + \mathbf{u}_{\mathrm{rel}}$, valid in the inclusion domain Ω_{i}, where the component $\mathbf{u}_{\mathrm{d}}$ is called concrete displacement [2] or duct displacement [27]; this quantity is later expressed as a function of the matrix displacement field $\mathbf{u}_{\mathrm{m}}$ of the elements crossed by the fiber. The matrix and inclusion stress tensors are defined as $\boldsymbol{\sigma}_{\mathrm{m}}$ and $\boldsymbol{\sigma}_{\mathrm{i}}$, respectively. With this decomposition, the principle of virtual work, valid for many embedded reinforcement models [2, 24, 26, 29], reads

$$\begin{cases} \displaystyle\int_{\Omega_{\mathrm{m}}} \nabla^{\mathrm{s}} \delta\mathbf{u}_{\mathrm{m}} : \boldsymbol{\sigma}_{\mathrm{m}} \,\mathrm{d}\Omega_{\mathrm{m}} + \int_{\Omega_{\mathrm{i}}} \nabla^{\mathrm{s}} \delta\mathbf{u}_{\mathrm{d}} : \boldsymbol{\sigma}_{\mathrm{i}} \,\mathrm{d}\Omega_{\mathrm{i}} = \int_{\Gamma_{\mathrm{t}}} \delta\mathbf{u}_{\mathrm{m}} \cdot \bar{\mathbf{t}} \,\mathrm{d}\Gamma_{\mathrm{t}}, \\ \displaystyle\int_{\Omega_{\mathrm{i}}} \nabla^{\mathrm{s}} \delta\mathbf{u}_{\mathrm{rel}} : \boldsymbol{\sigma}_{\mathrm{i}} \,\mathrm{d}\Omega_{\mathrm{i}} + \int_{\Gamma_{\mathrm{int}}} \delta\mathbf{u}_{\mathrm{rel}} \cdot \mathbf{t}_{\mathrm{int}} \,\mathrm{d}\Gamma_{\mathrm{int}} = 0. \end{cases} \tag{2.7}$$

Note that there are only two independent fields in the above relations: $\mathbf{u}_{\mathrm{m}}$ and $\mathbf{u}_{\mathrm{rel}}$.

As already mentioned in the introduction, with reference to high aspect ratio inclusions (Figure 2.1a), the integrals over inclusion volume Ω_{i} and inclusion-matrix interface Γ_{int} can be simplified to line integrals along the inclusion length l_{i}. With these modifications, and introducing Hooke's law for matrix and inclusion constituents, the principle of virtual work (2.7) reads

$$\begin{cases} \displaystyle\int_{\Omega} \nabla^{\mathrm{s}} \delta\mathbf{u}_{\mathrm{m}} : \mathbf{D}_{\mathrm{m}} : \nabla^{\mathrm{s}} \mathbf{u}_{\mathrm{m}} \,\mathrm{d}\Omega + A_{\mathrm{i}} \int_{l_{\mathrm{i}}} \nabla^{\mathrm{s}} \delta\mathbf{u}_{\mathrm{d}} : (\mathbf{D}_{\mathrm{i}} - \mathbf{D}_{\mathrm{m}}) : \nabla^{\mathrm{s}} \mathbf{u}_{\mathrm{d}} \,\mathrm{d}l_{\mathrm{i}} + A_{\mathrm{i}} \int_{l_{\mathrm{i}}} \nabla^{\mathrm{s}} \delta\mathbf{u}_{\mathrm{d}} : \mathbf{D}_{\mathrm{i}} : \nabla^{\mathrm{s}} \mathbf{u}_{\mathrm{rel}} \,\mathrm{d}l_{\mathrm{i}} = \int_{\Gamma_{\mathrm{t}}} \delta\mathbf{u}_{\mathrm{m}} \cdot \bar{\mathbf{t}} \,\mathrm{d}\Gamma_{\mathrm{t}}, \\ A_{\mathrm{i}} \displaystyle\int_{l_{\mathrm{i}}} \nabla^{\mathrm{s}} \delta\mathbf{u}_{\mathrm{rel}} : \mathbf{D}_{\mathrm{i}} : \nabla^{\mathrm{s}} \mathbf{u}_{\mathrm{d}} \,\mathrm{d}l_{\mathrm{i}} + A_{\mathrm{i}} \int_{l_{\mathrm{i}}} \nabla^{\mathrm{s}} \delta\mathbf{u}_{\mathrm{rel}} : \mathbf{D}_{\mathrm{i}} : \nabla^{\mathrm{s}} \mathbf{u}_{\mathrm{rel}} \,\mathrm{d}l_{\mathrm{i}} + C_{\mathrm{i}} \int_{l_{\mathrm{i}}} \delta\mathbf{u}_{\mathrm{rel}} \cdot (\bar{\mathbf{D}}_{\mathrm{b}} \mathbf{u}_{\mathrm{rel}}) \,\mathrm{d}l_{\mathrm{i}} = 0, \end{cases} \tag{2.8}$$

where $\bar{\mathbf{D}}_{\mathrm{b}} = \mathbf{R}^{\mathrm{T}} \mathbf{D}_{\mathrm{b}} \mathbf{R}$ is the rotated elastic interface tensor. The first integral is evaluated over the whole domain Ω and, as a consequence, the effective stiffness $\mathbf{D}_{\mathrm{i}} - \mathbf{D}_{\mathrm{m}}$ is introduced in the inclusion contribution (second integral) with $\mathbf{D}_{\mathrm{m}}$ and $\mathbf{D}_{\mathrm{i}}$ the matrix and inclusion isotropic elasticity tensors, respectively. This formulation is analogous to that by Radtke *et al.* [29] discussed in Section 2.3.1. The components $\mathbf{u}_{\mathrm{d}}$ and $\mathbf{u}_{\mathrm{rel}}$ of the inclusion displacement can be approximated in different manners as discussed next.

EMBEDDED REINFORCEMENT MODEL WITH SLIP (ERS MODEL)

In classical embedded reinforcement models with slip [2, 24, 26], slip DOFs are located along an inclusion axis (they are therefore defined in a coordinate system local to the inclu-

sion) and at their intersections with matrix element edges. As it is assumed that an inclusion works mainly under axial deformation, the component of the displacement normal to the inclusion are neglected. Thus the inclusion displacement components $\mathbf{u}_\mathrm{d}$ and $\mathbf{u}_\mathrm{rel}$ in (2.8) are replaced by corresponding scalar quantities u_d and u_s in the direction of the inclusion axis leading to

$$\begin{cases} \displaystyle\int_\Omega \nabla^\mathrm{s}\delta\mathbf{u}_\mathrm{m} : \mathbf{D}_\mathrm{m} : \nabla^\mathrm{s}\mathbf{u}_\mathrm{m}\,\mathrm{d}\Omega + A_\mathrm{i}(E_\mathrm{i}-E_\mathrm{m})\int_{l_\mathrm{i}} \delta u_{\mathrm{d},r} u_{\mathrm{d},r}\,\mathrm{d}l_\mathrm{i} + A_\mathrm{i}E_\mathrm{i}\int_{l_\mathrm{i}} \delta u_{\mathrm{d},r} u_{\mathrm{s},r}\,\mathrm{d}l_\mathrm{i} = \int_{\Gamma_\mathrm{t}} \delta\mathbf{u}_\mathrm{m}\cdot\bar{\mathbf{t}}\,\mathrm{d}\Gamma_\mathrm{t}, \\ A_\mathrm{i}E_\mathrm{i}\displaystyle\int_{l_\mathrm{i}} \delta u_{\mathrm{s},r} u_{\mathrm{d},r}\,\mathrm{d}l_\mathrm{i} + A_\mathrm{i}E_\mathrm{i}\int_{l_\mathrm{i}} \delta u_{\mathrm{s},r} u_{\mathrm{s},r}\,\mathrm{d}l_\mathrm{i} + C_\mathrm{i}\int_{l_\mathrm{i}} \delta u_\mathrm{s} K_\mathrm{bt} u_\mathrm{s}\,\mathrm{d}l_\mathrm{i} = 0, \end{cases} \tag{2.9}$$

where u_s is the slip of the inclusion, and the subscript r indicates a derivative with respect to the inclusion local axis.

p-ENRICHED MATRIX EMBEDDED REINFORCEMENT MODEL WITH SLIP (*p*ERS MODEL)
In an attempt to improve the performance of the ERS model, an enriched finite element discretization is employed to approximate the matrix displacement field close to an inclusion. To this end, the high-order generalized finite element method (GFEM) approximation

$$\mathbf{u}_\mathrm{m}(\mathbf{x}) = \sum_{\alpha=1}^{n} N_{\mathrm{m}\alpha}(\mathbf{x})\mathbf{u}^\mathrm{std}_{\mathrm{m}\alpha} + \sum_{\alpha=1}^{n} N_{\mathrm{m}\alpha}(\mathbf{x}) \sum_{\beta=1}^{n_\mathrm{enr}} \mathbf{u}^\mathrm{enr}_{\mathrm{m}\alpha\beta} P_{\beta\alpha}(\mathbf{x}) = \mathbf{N}_\mathrm{m}\mathbf{d} \tag{2.10}$$

is adopted, where $N_{\mathrm{m}\alpha}$ are standard element nodal shape functions, n is the number of element nodes, n_enr is the number of enrichment terms, $\mathbf{u}^\mathrm{std}_{\mathrm{m}\alpha}$ and $\mathbf{u}^\mathrm{enr}_{\mathrm{m}\alpha\beta}$ are the standard and enrichment components of the matrix displacement vector, respectively, and $\mathbf{N}_\mathrm{m}$ and $\mathbf{d}$ are the total (*i.e.*, including standard and enrichment terms) shape function matrix and displacement vector at the element level, respectively. The enrichment terms of the matrix displacement vector are defined following a hierarchical enrichment approach [34, 35] using the generalized basis function vector

$$\left\{P_{\beta\alpha}\right\}_{\beta=1}^{n_\mathrm{enr}} = \left\{ \frac{(x-x_\alpha)}{h_\alpha}, \frac{(y-y_\alpha)}{h_\alpha}, \frac{(x-x_\alpha)^2}{h_\alpha^2}, \frac{(x-x_\alpha)(y-y_\alpha)}{h_\alpha^2}, \frac{(y-y_\alpha)^2}{h_\alpha^2}, \cdots \right\}. \tag{2.11}$$

In this study, and in the equation above, we have used up to 5 enrichment terms ($n_\mathrm{enr} = 5$) thus enriching the solution space with polynomials up to the second order. This enrichment leads to a quadratic approximation of the matrix displacement field with the first two terms ($n_\mathrm{enr} = 2$) and to a cubic approximation when all the terms ($n_\mathrm{enr} = 5$) are used. The scaling factor h_α [35], usually taken as the diameter of the largest finite element sharing node α, is here taken equal to unity for convenience. Since the hierarchical enrichment scheme is not stable for quadrilateral elements [36], a versatile technique based on the *p*-version of the finite element method [37] is employed to locally increase their approximation order in a similar manner as discussed in Section 2.5.2.

DISCRETIZATION OF THE INCLUSION AND DISPLACEMENT APPROXIMATIONS
Inclusions are discretized into segments using the non-uniform sequence of points obtained from their intersection points with matrix element edges (if an inclusion ends within an element, the inclusion tip is taken as one of the inclusion segment endpoints). As defined earlier, the inclusion displacement is defined by $u_\mathrm{d} + u_\mathrm{s}$. We now discuss the approaches we follow to approximate both components.

Inclusion displacement: Nonslip component With reference to an arbitrary inclusion segment with endpoints 1 and 2 (Figure 2.1b), the nonslip component u_{d} of the inclusion displacement is written as

$$u_{\mathrm{d}} = N_{\mathrm{i}1}a_1 + N_{\mathrm{i}2}a_2, \tag{2.12}$$

where a_1 and a_2 are the inclusion axial displacements at the two endpoints and $N_{\mathrm{i}1}(r)$ and $N_{\mathrm{i}2}(r)$ are linear Lagrange shape functions related to the segment endpoints and defined along the inclusion segment local axis.

Equation (2.12) is expressed in terms of displacements in the global coordinate system as

$$u_{\mathrm{d}} = \begin{bmatrix} N_{\mathrm{i}1}\cos\theta_x & N_{\mathrm{i}1}\cos\theta_y & N_{\mathrm{i}2}\cos\theta_x & N_{\mathrm{i}2}\cos\theta_y \end{bmatrix} \mathbf{a}_{\mathrm{d}}, \tag{2.13}$$

where θ_x and θ_y are the directional angles defined in the global xy coordinate system (Figure 2.1b), and the displacement vector

$$\mathbf{a}_{\mathrm{d}} = \begin{bmatrix} a_{x_1} & a_{y_1} & a_{x_2} & a_{y_2} \end{bmatrix}^{\mathrm{T}} \tag{2.14}$$

is obtained from the interpolation of the nodal displacement vector at the elemental level (matrix element) to endpoints (x_1, y_1) and (x_2, y_2) of the inclusion element related to that matrix element (*i.e.*, using the approximation (2.10) evaluated at the inclusion endpoints).

The displacement u_{d} and its derivative are therefore

$$u_{\mathrm{d}} = \mathbf{N}_{\mathrm{d}}\mathbf{H}\mathbf{d} \qquad \text{and} \qquad u_{\mathrm{d},r} = \mathbf{B}_{\mathrm{d}}\mathbf{H}\mathbf{d}, \tag{2.15}$$

with

$$\mathbf{N}_{\mathrm{d}} = \begin{bmatrix} N_{\mathrm{i}1}\cos\theta_x & N_{\mathrm{i}1}\cos\theta_y & N_{\mathrm{i}2}\cos\theta_x & N_{\mathrm{i}2}\cos\theta_y \end{bmatrix} \tag{2.16}$$

and

$$\mathbf{B}_{\mathrm{d}} = \begin{bmatrix} N_{\mathrm{i}1,r}\cos\theta_x & N_{\mathrm{i}1,r}\cos\theta_y & N_{\mathrm{i}2,r}\cos\theta_x & N_{\mathrm{i}2,r}\cos\theta_y \end{bmatrix}, \tag{2.17}$$

where the transformation matrix

$$\mathbf{H} = \begin{bmatrix} \mathbf{H}^{\mathrm{std}} & \mathbf{H}^{\mathrm{enr}}_{\beta=1} & \cdots & \mathbf{H}^{\mathrm{enr}}_{\beta=n_{\mathrm{enr}}} \end{bmatrix}, \tag{2.18}$$

with standard component

$$\mathbf{H}^{\mathrm{std}} = \begin{bmatrix} N_{\mathrm{m}1}\big|_1 & 0 & \cdots & N_{\mathrm{m}n}\big|_1 & 0 \\ 0 & N_{\mathrm{m}1}\big|_1 & \cdots & 0 & N_{\mathrm{m}n}\big|_1 \\ N_{\mathrm{m}1}\big|_2 & 0 & \cdots & N_{\mathrm{m}n}\big|_2 & 0 \\ 0 & N_{\mathrm{m}1}\big|_2 & \cdots & 0 & N_{\mathrm{m}n}\big|_2 \end{bmatrix} \tag{2.19}$$

and enrichment component

$$\mathbf{H}^{\mathrm{enr}}_{\beta} = \begin{bmatrix} P_{\beta,1}N_{\mathrm{m}1}\big|_1 & 0 & \cdots & P_{\beta,n}N_{\mathrm{m}n}\big|_1 & 0 \\ 0 & P_{\beta,1}N_{\mathrm{m}1}\big|_1 & \cdots & 0 & P_{\beta,n}N_{\mathrm{m}n}\big|_1 \\ P_{\beta,1}N_{\mathrm{m}1}\big|_2 & 0 & \cdots & P_{\beta,n}N_{\mathrm{m}n}\big|_2 & 0 \\ 0 & P_{\beta,1}N_{\mathrm{m}1}\big|_2 & \cdots & 0 & P_{\beta,n}N_{\mathrm{m}n}\big|_2 \end{bmatrix}, \tag{2.20}$$

links $\mathbf{a}_{\mathrm{d}}$ to the matrix nodal displacements vector $\mathbf{d}$ at the element level. In these expressions, the matrix shape functions are evaluated at the discontinuity segment endpoints. The above derivations therefore show that the u_{d} component of the inclusion displacement is computed using information from the matrix displacement field.

Inclusion displacement: Slip component The displacement slip component u_s and its derivative can be approximated as

$$u_\mathrm{s} = \mathbf{N}_\mathrm{s}\mathbf{b}_\mathrm{s} \qquad \text{and} \qquad u_{\mathrm{s},r} = \mathbf{B}_\mathrm{s}\mathbf{b}_\mathrm{s}, \tag{2.21}$$

where $\mathbf{b}_\mathrm{s} = [b_1,\, b_2]^\mathrm{T}$ is the vector of endpoint slip DOFs, and

$$\mathbf{N}_\mathrm{s} = \begin{bmatrix} N_{\mathrm{i}1} & N_{\mathrm{i}2} \end{bmatrix} \qquad \text{and} \qquad \mathbf{B}_\mathrm{s} = \begin{bmatrix} N_{\mathrm{i}1,r} & N_{\mathrm{i}2,r} \end{bmatrix}. \tag{2.22}$$

DISCRETIZED SYSTEM OF EQUATIONS

Introducing the discretized expressions (2.10), (2.15) and (2.21) into the principle of virtual work (2.9) yields the system of equations

$$\begin{bmatrix} \mathbf{K}_\mathrm{mm} & \mathbf{K}_\mathrm{mi} \\ \mathbf{K}_\mathrm{im} & \mathbf{K}_\mathrm{ii} \end{bmatrix} \begin{bmatrix} \mathbf{d} \\ \mathbf{b} \end{bmatrix} = \begin{bmatrix} \mathbf{f}_\mathrm{m} \\ \mathbf{0} \end{bmatrix} \tag{2.23}$$

valid at the element level for the case of a single inclusion. The vectors $\mathbf{d}$ and $\mathbf{b}$ contain matrix and slip DOFs, respectively, $\mathbf{f}_\mathrm{m}$ is the external force vector, and the stiffness matrix submatrices are

$$\begin{aligned}
\mathbf{K}_\mathrm{mm} &= \int_{\Omega_\mathrm{e}} \mathbf{B}_\mathrm{m}{}^\mathrm{T}\mathbf{D}_\mathrm{m}\mathbf{B}_\mathrm{m}\,\mathrm{d}\Omega_\mathrm{e} + A_\mathrm{i}\int_L \mathbf{H}^\mathrm{T}\mathbf{B}_\mathrm{d}{}^\mathrm{T}\bar{E}\mathbf{B}_\mathrm{d}\mathbf{H}\,\mathrm{d}r, \\
\mathbf{K}_\mathrm{mi} &= A_\mathrm{i}\int_L \mathbf{H}^\mathrm{T}\mathbf{B}_\mathrm{d}{}^\mathrm{T}E_\mathrm{i}\mathbf{B}_\mathrm{s}\,\mathrm{d}r, \\
\mathbf{K}_\mathrm{im} &= A_\mathrm{i}\int_L \mathbf{B}_\mathrm{s}{}^\mathrm{T}E_\mathrm{i}\mathbf{B}_\mathrm{d}\mathbf{H}\,\mathrm{d}r, \\
\mathbf{K}_\mathrm{ii} &= A_\mathrm{i}\int_L \mathbf{B}_\mathrm{s}{}^\mathrm{T}E_\mathrm{i}\mathbf{B}_\mathrm{s}\,\mathrm{d}r + C_\mathrm{i}\int_L \mathbf{N}_\mathrm{s}{}^\mathrm{T}K_\mathrm{bt}\mathbf{N}_\mathrm{s}\,\mathrm{d}r,
\end{aligned} \tag{2.24}$$

where Ω_e is the domain of the element and L is the length of the inclusion segments within it. This discretized system of equation is valid for the ERS and pERS models. For cases with more than one inclusion, the system of equations is modified as shown in Hartl [27] or Radtke *et al.* [29].

SLIP ENRICHED PARTITION OF UNITY MODEL (SLIPPOU)

Radtke *et al.* [29] proposed an approach alternative to the ERS model. In their formulation, in which the displacement field is decomposed as in Section 2.3.1, the partition of unity property of finite element shape functions is employed to enrich the matrix displacement field with information about the inclusion kinematics. Matrix-inclusion relative displacement DOFs expressed in the global coordinate system are assigned to all the nodes of elements intersected by an inclusion. Following the procedure described in Radtke *et al.* [29] yields a global system of equations that can be written as (2.23) with submatrices

$$\begin{aligned}
\mathbf{K}_\mathrm{mm} &= \int_{\Omega_\mathrm{e}} \mathbf{B}_\mathrm{m}{}^\mathrm{T}\mathbf{D}_\mathrm{m}\mathbf{B}_\mathrm{m}\,\mathrm{d}\Omega_\mathrm{e} + A_\mathrm{i}\int_L \mathbf{B}_\mathrm{m}{}^\mathrm{T}\left(\mathbf{D}_\mathrm{i} - \mathbf{D}_\mathrm{m}\right)\mathbf{B}_\mathrm{b}\,\mathrm{d}r, \\
\mathbf{K}_\mathrm{mi} &= A_\mathrm{i}\int_L \mathbf{B}_\mathrm{m}{}^\mathrm{T}\mathbf{D}_\mathrm{i}\mathbf{B}_\mathrm{b}\,\mathrm{d}r, \\
\mathbf{K}_\mathrm{im} &= A_\mathrm{i}\int_L \mathbf{B}_\mathrm{m}{}^\mathrm{T}\mathbf{D}_\mathrm{i}\mathbf{B}_\mathrm{b}\mathbf{H}\,\mathrm{d}r, \\
\mathbf{K}_\mathrm{ii} &= A_\mathrm{i}\int_L \mathbf{B}_\mathrm{m}{}^\mathrm{T}\mathbf{D}_\mathrm{i}\mathbf{B}_\mathrm{b}\,\mathrm{d}r + C_\mathrm{i}\int_L \mathbf{N}_\mathrm{b}{}^\mathrm{T}\bar{\mathbf{D}}_\mathrm{b}\mathbf{N}_\mathrm{b}\,\mathrm{d}r,
\end{aligned} \tag{2.25}$$

where $\mathbf{N}_\mathrm{m}$ and $\mathbf{B}_\mathrm{b} = \mathbf{B}_\mathrm{m}$ are the standard FEM shape function and derivative matrices, respectively. In this model, the number of DOFs in an element intersected by an inclusion doubles to take into account the additional relative displacement DOFs defined at each node, thus yielding a larger system of equations compared to that obtained with the ERS model described in the previous section. The relative displacement is approximated by making reference to the shape functions of the parent element. In the applications discussed later in this chapter, the results of this model are provided only for the sake of comparison with the more efficient ERS model. As discussed in Section 2.2.1, we do not allow the relative displacement in the normal direction by choosing large values of the interface normal stiffness K_bn.

2.3.2. STRAIN DISCONTINUITY ENRICHED EMBEDDED REINFORCEMENT MODEL WITH SLIP (SDERS MODEL)

A simple approach to allow a strain discontinuity in an embedded formulation is to enrich the displacement approximation of the matrix material with a weak discontinuity enrichment function using the partition of unity enrichment method [18, 34, 38, 39]. This approach is applied to the embedded reinforcement model proposed by Goudarzi and Simone [33]. The governing equations for the inclusion depicted in Figure 2.2b can be obtained by a modification of the equations derived for the conformal model in Figure 2.2a. The goal of this modification is to design a kinematic field in which the displacement is continuous and its gradient can be discontinuous, similar to the strain fields obtained with the conformal model described in Section 2.2.1. This can be achieved by adopting the enriched approximation

$$\mathbf{u}_\mathrm{m}(\mathbf{x}) = \sum_{\alpha=1}^{n} N_{\mathrm{m}\alpha}(\mathbf{x})\mathbf{u}_{\mathrm{m}\alpha}^{\mathrm{std}} + \sum_{\alpha=1}^{n} N_{\mathrm{m}\alpha}(\mathbf{x})\Upsilon(\mathbf{x})\mathbf{u}_{\mathrm{m}\alpha}^{\mathrm{enr}} \tag{2.26}$$

for the matrix displacement field expressed at the elemental level in the global coordinate system, where $\mathbf{u}_{\mathrm{m}\alpha}^{\mathrm{std}}$ and $\mathbf{u}_{\mathrm{m}\alpha}^{\mathrm{enr}}$ are the standard and enrichment matrix displacement vectors, respectively. To ensure continuous displacements with discontinuous gradients, the enrichment function [19]

$$\Upsilon(\mathbf{x}) = \sum_{\alpha=1}^{n} N_{\mathrm{m}\alpha}(\mathbf{x})\,|\zeta_\alpha| - \left|\sum_{\alpha=1}^{n} N_{\mathrm{m}\alpha}(\mathbf{x})\zeta_\alpha\right| \tag{2.27}$$

is employed, where ζ_α is the level-set function that measures the shortest distance between an element node and the inclusion. This enrichment function ensures that the displacement approximation can reproduce the strain fields in Figure 2.4. The displacement vector $\mathbf{d}_\mathrm{int}$ in (2.3) and the interface shape function matrix $\mathbf{N}_\mathrm{int}$ in (2.4) are modified accordingly as

$$\mathbf{d}_\mathrm{int} = \left[\begin{array}{cc|ccc|ccc} \mathbf{u}_{\mathrm{i}1} & \mathbf{u}_{\mathrm{i}2} & \mathbf{u}_{\mathrm{m}1}^{\mathrm{std}} & \cdots & \mathbf{u}_{\mathrm{m}n}^{\mathrm{std}} & \mathbf{u}_{\mathrm{m}1}^{\mathrm{enr}} & \cdots & \mathbf{u}_{\mathrm{m}n}^{\mathrm{enr}} \end{array}\right]^\mathrm{T} \tag{2.28}$$

and

$$\mathbf{N}_\mathrm{int} = \left[\begin{array}{cc|ccc|ccc} N_{\mathrm{i}1}\,\mathbf{I} & N_{\mathrm{i}2}\,\mathbf{I} & -N_{\mathrm{m}1}\,\mathbf{I} & \cdots & -N_{\mathrm{m}n}\,\mathbf{I} & -\Upsilon N_{\mathrm{m}1}\,\mathbf{I} & \cdots & -\Upsilon N_{\mathrm{m}n}\,\mathbf{I} \end{array}\right], \tag{2.29}$$

respectively, where $\boldsymbol{I}$ is the 2×2 identity matrix and the other quantities have been defined earlier. For the discretization of the inclusion we make reference to Section 2.2.1.

2.4. COMPARATIVE ANALYSIS OF THE PERFORMANCE OF EMBEDDED REINFORCEMENT MODELS

As mentioned in Section 2.2.2, a discontinuity in the matrix strain field is expected across embedded inclusions. The discrete models described in Section 2.3.1 do not capture intra-element discontinuities. Those simplified models are however significantly cheaper when dealing with large inclusion volumes compared with the conformal or discontinuous approaches described in Sections 2.2.1 and 2.3.2, respectively. The approximation features of these discrete models is assessed by repeating the analysis of the strain field in Section 2.2.2; a further assessment is performed by means of convergence studies on one or multiple inclusion composites. Reference is made to the material parameters and geometrical properties of the polymer/clay nanocomposite discussed in Section 2.2.2.

2.4.1. SINGLE INCLUSION

The case of a single inclusion is considered first. A detailed study of the strain components and a mesh convergence study are provided.

STRAIN DISTRIBUTION ACROSS THE INCLUSION

The study presented in Section 2.2.2 is repeated here by comparing strain fields obtained with conformal FEM model (Section 2.2.1), ERS model (Section 2.3.1), and strain discontinuity enriched ERS (sdERS) model (Section 2.3.2). The FEM reference solution (thin cyan line) is obtained with a uniform 600×600 Q4 conformal discretization, while a uniform 100×100 (Q4) mesh is used for both ERS models. Strains are sampled at integration point locations along a vertical line located near the tip of the inclusion (Figure 2.5a). The most evident difference in the results obtained with the two ERS models lies in the continuity of the mixed component of the strain tensor (ε_{xy}), with the ERS model (red line) being clearly unable to represent the discontinuity reported by the reference conformal FEM model (Figure 2.5c). Other notable difference is the overall resemblance of the solutions obtained with the enriched model (blue line) and the reference FEM solution around the inclusion (see insets in Figures 2.5b,d), where the ERS model shows a piecewise constant strain profile. Differences are however minute far from the inclusion.

CONVERGENCE STUDY

To assess the quality of the strain discontinuity enriched ERS model (Section 2.3.2), a mesh convergence study is performed. The role of the bond stiffness is evaluated by adopting three different tangential stiffness values K_{bt} (0.025, 0.05, and 0.25 N/μm^3). Figure 2.6 shows the resulting slip profiles obtained with a conformal FEM analysis using a 600×600 uniform grid of bilinear quadrilateral elements.

As a closed-form analytical solution is not available for this problem, the reference strain energy values used in the convergence study are estimated. Following [40], an estimate of the exact strain energy is extracted using hierarchical sequences of finite element spaces by means of the expression

$$\frac{\pi_3 - \pi}{\pi_2 - \pi} = \left(\frac{\pi_2 - \pi}{\pi_1 - \pi} \right)^{Q} \qquad \text{with} \qquad Q = \log \frac{N_2}{N_3} \left(\log \frac{N1}{N2} \right)^{-1}, \tag{2.30}$$

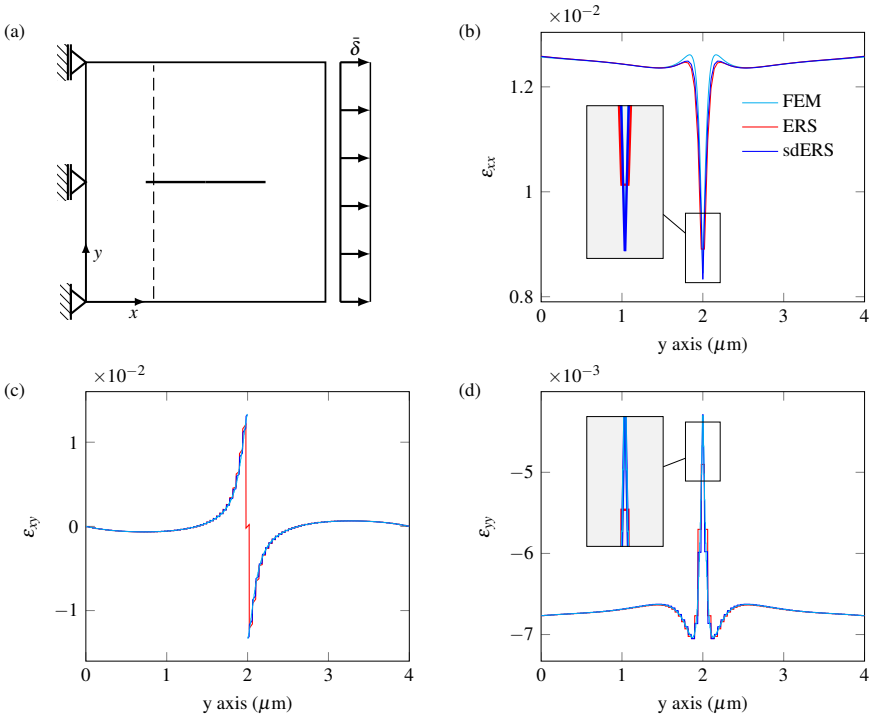

Figure 2.5: (a) Schematic of the single inclusion problem with sampling line for the strain tensor components reported in the other panels: ε_{xx} (b), ε_{xy} (c), and ε_{yy} (d). The problem is solved using the conformal FEM, ERS, and strain discontinuity enriched ERS (sdERS) models with a uniform 100×100 Q4 discretization.

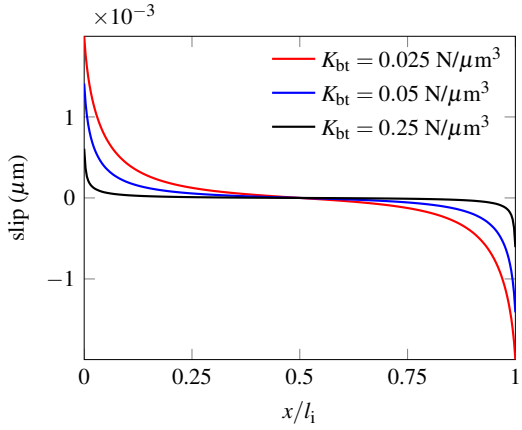

Figure 2.6: Slip profiles corresponding to various interface tangential stiffness values adopted in the mesh convergence study (Section 2.4.1).

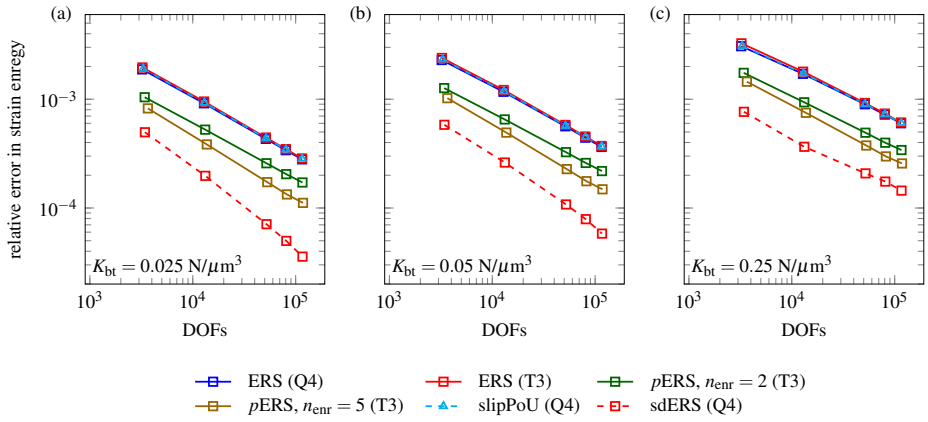

Figure 2.7: Relative errors in strain energy for the single inclusion problem under uniform mesh refinements. Results are shown for the ERS model with T3 and Q4 discretizations, the p-enriched matrix ERS (pERS) model with local quadratic ($n_{enr} = 2$, $p = 2$) and cubic ($n_{enr} = 5$, $p = 3$) approximations, the slip enriched partition of unity (slipPoU) model, and the strain discontinuity enriched ERS (sdERS) model for three values of the bond stiffness.

with $N_1 < N_2 < N_3$ the numbers of degrees of freedom and π_1, π_2, and π_3 the corresponding strain energy values. For the numerical solutions, uniformly refined unstructured T3 meshes with 9,013, 34,901 and 138,571 nodes are employed. Equation (2.30) is then solved for the estimated exact strain energy π that is used as the reference value in the mesh convergence study.

Figure 2.7 compares the results obtained with the strain discontinuity enriched ERS (sdERS) model against those obtained with the ERS model (Section 2.3.1) with T3 and Q4 discretizations, the p-enriched matrix ERS (pERS) model (Section 2.3.1) with local quadratic ($n_{enr} = 2$) and cubic ($n_{enr} = 5$) approximations, and the slip enriched partition of unity (slipPoU) model (Section 2.3.1) for three values of the bond stiffness.

The performance of the ERS model with both discretizations and that of the slipPoU model are indistinguishable. Expectedly, the strain discontinuity enriched ERS model performs better compared to the ERS model. This is attributed to the appropriate representation of the strain field in elements crossed by the inclusion. As discussed earlier, the ERS model cannot represent discontinuities in the strain field across an inclusion. To improve the quality of the solution, the displacement field in the elements crossed by an inclusion is therefore enhanced by elevating its approximation order. The results show the improved performance of the pERS model compared to that of the ERS. Although the strain discontinuity enriched ERS model provides the most accurate solution, it can considerably increase the complexity of the numerical implementation. Indeed, this model requires the integration of the weak enrichment function (2.27) using integration subdomains, and this task can be prohibitively expensive when dealing with dense inclusion distributions. A simpler strategy, although less effective, is to use high order displacement approximations (pERS).

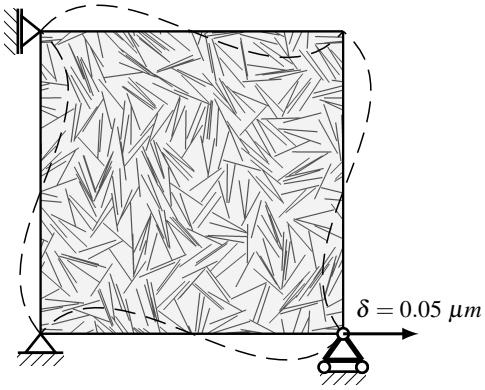

Figure 2.8: Periodic random distribution of 367 non-intersecting inclusions used in the multiple inclusion problem.

2.4.2. RANDOMLY DISPERSED INCLUSIONS

The goal of this section is to show the effectiveness of the models described in the previous section in the analysis of a composite with a relative large number of interacting inclusions. This is a situation in which ERS models are key to this type of numerical exercise as conformal FEM and strain discontinuity enriched ERS models are very expensive options.

Figure 2.8 shows a typical periodic square unit cell setup used in this mesh convergence study with 367 randomly dispersed and non-intersecting clay platelets with a spatial arrangement similar to that reported in Reference [17]. The periodic boundary conditions described in Reference [41] are imposed on the unit cell, with the horizontal displacement δ set equal to 0.05 μm at the lower right-hand side node (Figure 2.8). As in the previous case, the inclusions are not perfectly bonded and the elastic interface tangent K_{bt} is set equal to 0.05 N/μm^3. The inclusions have all the same length $l_{\text{i}} = 0.52$ μm. The approximated reference strain energy is extracted with the procedure described earlier for the single inclusion case using the ERS model (Section 2.3.1) with the matrix discretized using uniform grids of 250×250, 500×500 and 1,000×1,000 bilinear quadrilateral elements.

Figure 2.9 shows the results obtained with the finest ERS discretization for the distribution in Figure 2.8 in terms of the von Mises stress field together with axial stress and slip fields for three inclusions. These results indicate that solution fields local to an inclusion vary depending on its position in the composite, an information that mean-field approaches cannot predict.

MESH CONVERGENCE STUDY WITH UNIFORM MESH REFINEMENT

Figure 2.10a shows the relative error plots for the strain energy obtained with the ERS model (Section 2.3.1) and the slip enriched partition of unity (slipPoU) model (Section 2.3.1). The domain is discretized using bilinear quadrilateral elements uniformly refined. Both models rely on similar assumptions, the major difference being the allocation of slip DOFs—slip DOFs are assigned to all the nodes of a crossed element in the slipPoU model, while

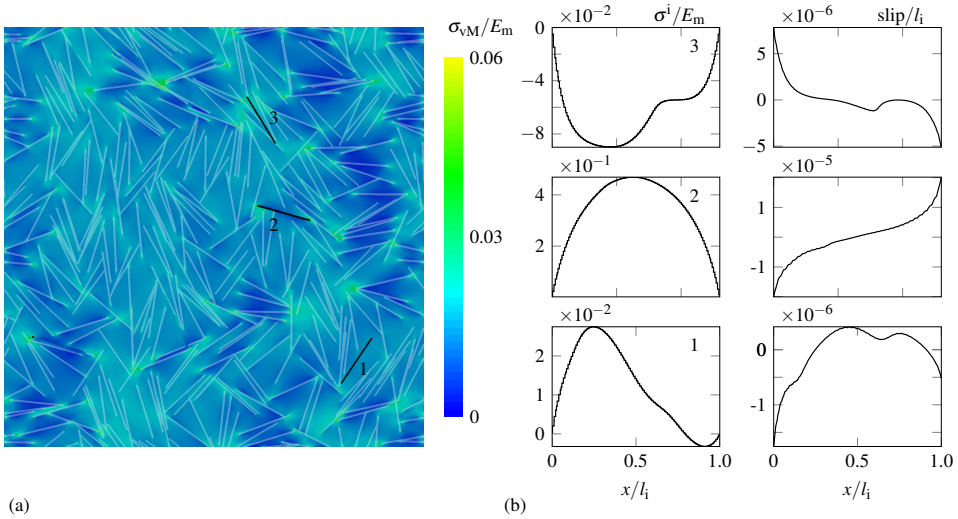

Figure 2.9: (a) von Mises stress distribution for the problem with 367 randomly-distributed inclusions. (b) Axial stress and slip fields for the three labeled inclusions in panel (a).

in the ERS model they are only assigned to the intersection points between inclusion and element edges and are aligned along the inclusion axis. Unlike the case of the single inclusion problem discussed in the previous section (Figure 2.7), the curves for a given number of inclusions do not overlap and the error produced by the slipPoU model is larger.

The same study is now repeated using the p-enriched matrix ERS (pERS) model proposed in Section 2.3.1 with a T3 discretization generated by splitting each quadrangular element in a regular structured grid into two triangles. Linear ($n_{enr} = 0$, equivalent to ERS) and cubic ($n_{enr} = 5$) approximations are considered. This enrichment strategy is advantageous over traditional Lagrange cubic elements because it can be applied locally to certain element groups (those crossed by the inclusions), while keeping the order of the approximation unchanged in the rest of domain (we refer to this enrichment scheme as local). For a fair comparison, the same approximation is also employed throughout the whole domain (global enrichment scheme). Figure 2.10b shows the error plots for different cases. Using a cubic approximation leads in any case to lower errors compared to the results obtained with the ERS model. The use of a global enrichment strategy does not seem to be advantageous as the error is close to that obtained with the local enrichment. Although the rate of convergence is improved for pERS compared to ERS, the improvements are not significant due to artificial continuity of the strain fields.

MESH CONVERGENCE STUDY WITH ADAPTIVE REFINEMENT

The uniform refinement case just discussed is not efficient as it leads to the refinement of regions where steep gradients are absent. Also, close to the elements crossed by an inclusion, inaccurate intra-element strains are present and a finer discretization would be preferred. To address these problems, we employ an adaptive refinement procedure based on a strain

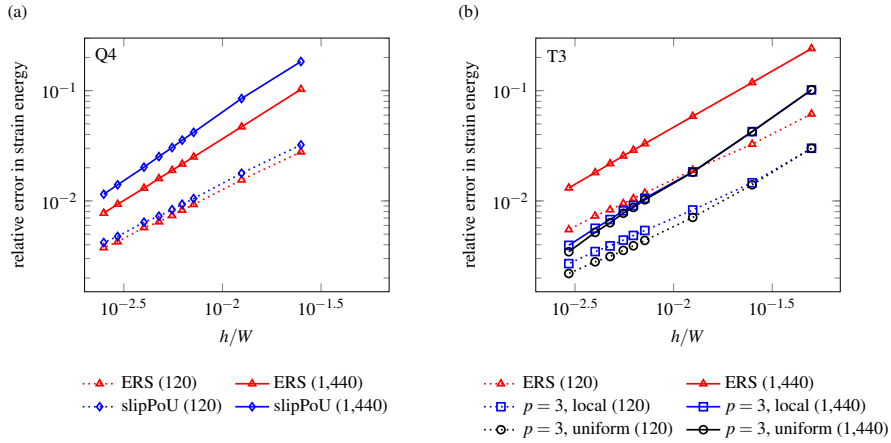

Figure 2.10: Plots of the relative error in strain energy for the problem with the randomly-distributed inclusions for two inclusion distributions (number of inclusions shown between parentheses). Results are shown for (a) the ERS model and the slip enriched partition of unity (slipPoU) model using uniform Q4 discretizations, (b) the ERS model and the p-enriched matrix ERS (pERS) model with cubic ($n_{\text{enr}} = 5$, $p = 3$) approximation for all elements (uniform) or for elements intersected by the inclusions (local) using uniform T3 discretizations. Element and domain size are h and $W = 4$ μm, respectively.

energy error estimator. For the local mesh refinement in regions with high stress concentration, the technique of Zienkiewicz and Zhu [42] is used. Reference (enhanced) strain fields are predicted using the super-convergent patch recovery technique [43]. For the local refinement of triangular element meshes we use the longest edge bisection algorithm by Rivara [44], while for quadrilateral meshes we use a non-conformal adaptive mesh refinement technique with hanging nodes. A hanging node is treated by constraining it to surrounding matrix element nodes, with the multifreedom constraint relations satisfied by the use of the master-slave elimination technique.

Strain energy convergence plots are shown in Figure 2.11 for quadrilateral and triangular element discretizations and for different numbers of inclusions. Compared with the uniform refinement, h-adaptivity reduces the computational costs in all cases by eliminating unnecessary mesh refinement. Additionally, as shown in Figure 2.11b, if h-adaptivity is combined with a local high order enrichment scheme (pERS) applied only in elements crossed by an inclusion, the numerical performance is enhanced and errors are considerably reduced.

Figure 2.12 shows typical discretizations obtained with the adaptive refinement scheme for the case with 367 inclusions. Note how the adaptive refinement algorithm identified the regions around the inclusion where mesh refinement is most needed—compare the different discretizations around inclusions 1 and 2 (labeled in Figure 2.9) with the corresponding stress field.

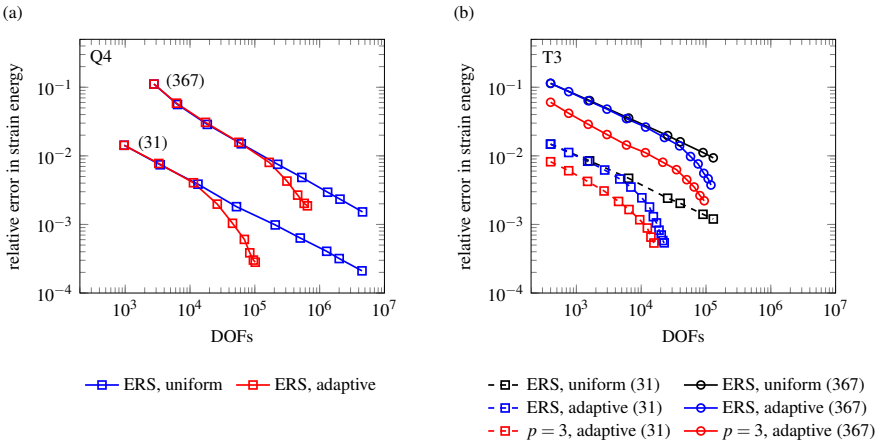

Figure 2.11: Relative error in strain energy for the problem with the randomly-distributed inclusions for two inclusion distributions (number of inclusions shown between parentheses). Results are shown for (a) the ERS model with uniform and adaptive Q4 discretizations, and (b) the ERS model and the p-enriched matrix ERS (pERS) model with cubic ($n_{\text{enr}} = 5$, $p = 3$) approximation for elements intersected by the inclusions using uniform and adaptive T3 discretizations.

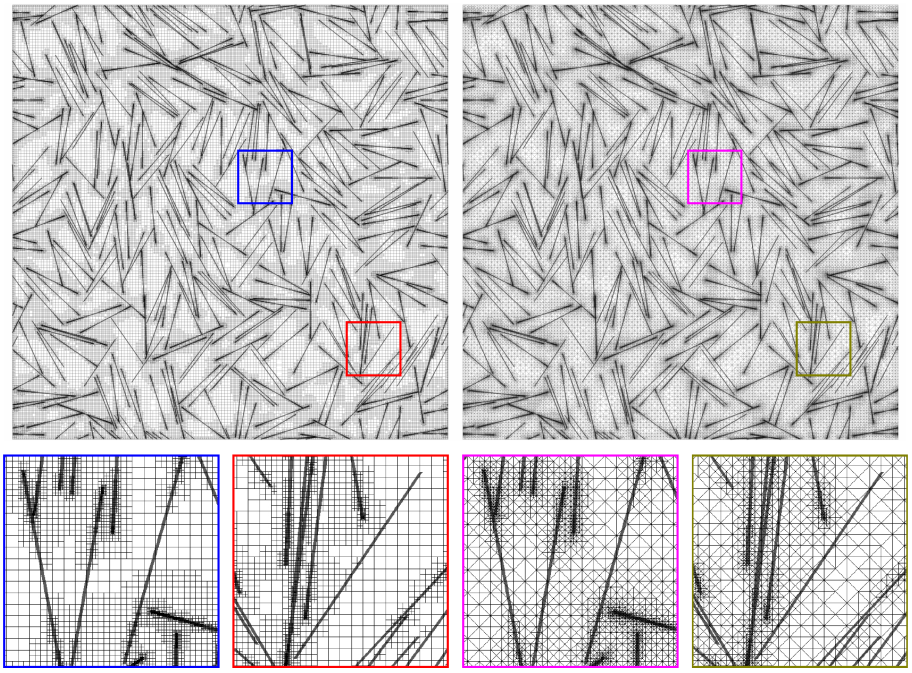

Figure 2.12: Adaptively refined meshes using Q4 and T3 discretizations for the case with 367 randomly distributed inclusions.

2.5. SLIP PROFILES

So far the embedded techniques were assessed in terms of their global response. In this section we demonstrate that the slip is, under certain conditions, not smooth due to the presence of unphysical oscillations and provide some remedies to reduce them. In all the simulations performed with an embedded reinforcement approach, each inclusion segment contained in a matrix element has been uniformly refined in eight segments. A Newton-Cotes integration scheme is used, and the reported slip values are sampled at the integration point locations (and these coincide with the inclusion elements nodes in each matrix element). As the inclusion segments are sufficiently refined, the slip profiles do not noticeably change by including more sampling points along each inclusion segment.

2.5.1. SLIP OSCILLATIONS

The problem of the oscillations in the slip profile is illustrated with reference to the two-dimensional one-inclusion composite depicted in Figure 2.3 with $\theta = 0.7$ rad with input parameters and boundary conditions described in Section 2.2.2.

Before performing slip tests on the single inclusion problem, the effect of the interface stiffness K_{bt} on the homogenized Young's modulus $E_{\text{c}x}$ of the composite is studied in Figure 2.13; for a sensible increases of $E_{\text{c}x}$, 21 aligned inclusions are considered. The profile of the homogenized Young's modulus plateaus for $K_{\text{bt}} > 10$ N/μm^3. This means that for those values of the bond stiffness, the inclusion can be regarded as perfectly bonded to the matrix with negligible slip; for all other values of the bond stiffness, the slip is physically meaningful.

With reference to the single inclusion problem, Figure 2.14 shows the slip profiles obtained for the bond stiffness values marked by the red squares in Figure 2.13. The profiles are extracted from solutions obtained with relatively coarse and fine discretizations with bilinear quadrilateral elements and are accompanied by predictions obtained with a conformal 600×600 uniform grid of bilinear quadrilateral elements. The results indicate that oscillations in the slip profile emerge for relatively large values of the bond stiffness, while the reference conformal FEM predictions remain smooth for the whole range of interface stiffness values.

The results in this subsection are obtained with the embedded reinforcement model proposed in Reference [33], which is endowed with inclusion displacement DOFs. Results not reported here indicate that the inclusion displacement is a smooth function, irrespective of material parameters and underlying mesh quality, therefore implying that the non-smoothness of the slip profile is due to the non-smoothness of the interpolated matrix displacement field at the inclusion nodes. Identical oscillatory results, not reported here, are also obtained with all the embedded reinforcement models discussed in Section 2.3.1, which are endowed with slip DOFs—some mild oscillations are indeed present in the results discussed earlier in the chapter (slip profile of the second inclusion in Figure 2.9b). Both models share the inability to reproduce a discontinuity in the matrix strain field across an inclusion, thus suggesting that slip oscillations are related to the matrix strain field. As discussed earlier in Section 2.3.2 enriching the matrix displacement field with a weak discontinuity function endows the model with a discontinuous strain field across an inclusion (its effectiveness in addressing this problem is discussed next). The strain discontinuity enriched ERS model is however expensive, and in the next section we explore the effective-

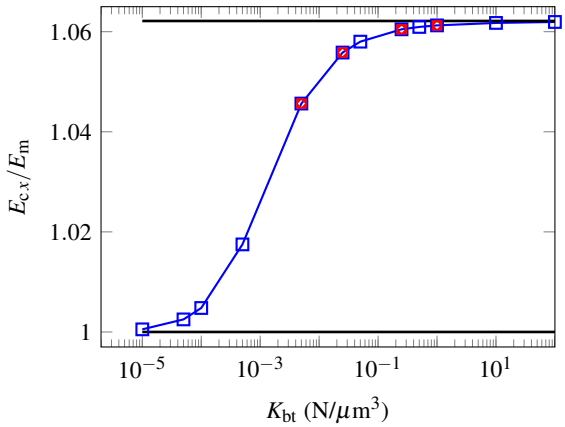

Figure 2.13: A situation of near perfect bonding between matrix and inclusion can be achieved by increasing the interface tangential bond stiffness value. The normalized effective elastic Young's modulus of the composite with 21 aligned inclusions is plotted as a function of the interface tangential stiffness.

ness of alternative solutions using the models described in Section 2.3.1. As a side note, oscillations in the slip profile were observed using either Gauss or Newton-Cotes quadrature schemes and therefore are not of the type discussed in Reference [45].

Although the results in this section are specific to an example and a set of material parameters, results not reported here indicate that similar oscillatory results are obtained with very different material properties. Our numerical evidence seems to imply that oscillations are an intrinsic feature of these models, rather than a feature triggered by a special combination of material parameters. As of now, we can only suggest to produce a study similar to that in Figure 2.13 and verify the existence of oscillatory slip profiles if the chosen value of the bond stiffness is close to that considered as the perfect bond threshold. Needless to say an erroneous prediction of the slip profile might have adverse consequences in the interpretation of the results or in nonlinear analyses as nonlinearity might be artificially triggered.

2.5.2. APPROACHES TO IMPROVE THE SLIP PROFILES

As the quality of the matrix displacement field in elements crossed by an inclusion seems to dictate the quality of the slip profile along that inclusion, the strategies discussed next rely on improvements of the approximation of the matrix displacement field when needed. An optimal solution requires the development of intra-element discontinuous displacement gradients in elements crossed by inclusions. Such weak displacement discontinuity can be reproduced with the strain discontinuity enriched ERS model proposed in Section 2.3.2. An alternative approach consists in the approximation of the discontinuity in the strain field by means of more sophisticated displacement approximations that do not introduce a weak discontinuity enrichment in the displacement field but have the necessary flexibility to represent it in an appropriate manner. To obtain a model with such capabilities, we have

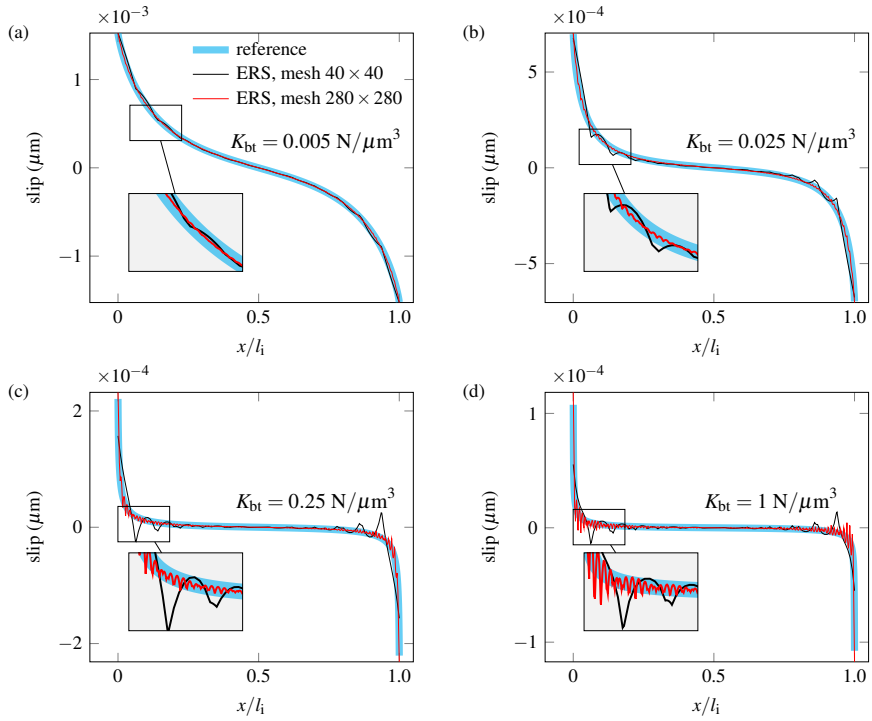

Figure 2.14: Slip profiles for the single inclusion problem obtained with the ERS model corresponding to the bond stiffness values marked by the red squares in Figure 2.13. The results are shown for relatively coarse and fine Q4 discretizations and are accompanied by the reference slip profiles obtained with a conformal FEM approach (uniform 600×600 Q4 discretization).

considered the embedded reinforcement model proposed in Reference [33] and replaced its shape functions with moving least squares (MLS) [46, 47] functions over the entire domain (this is an element free discretization for the matrix domain similar to that proposed by Nayroles *et al.* [48]). With reference to the sdERS model in Section 2.3.2, the enrichment component in (2.26) is removed and the matrix shape functions are replaced with MLS shape functions constructed using a linear basis. A regular cubic spline weight function is used [49], while the size of support domain is set equal to three times the nodal spacing to ensure a smooth stress profile.

We also tested our hypothesis on the quality of the displacement field in the matrix by employing a model based on the p-version of the finite element method (p-FEM) [37, 50]. This model, conceptually similar to the p-enriched matrix ERS model presented in Section 2.3.1, employs hierarchical Legendre polynomials and arbitrary selective order elevation (up to order 7 in this study) in elements crossed by an inclusion. Its implementation is similar to that described for the MLS shape functions.

As a measure of the quality of the improved approximations, we perform a convergence study on the slip profile by measuring the absolute error through its L_2 norm defined as

$$\|e_{\mathrm{s}}\| = \frac{\sqrt{\int_{l_{\mathrm{i}}} \|s_{\mathrm{ref}} - s_{\mathrm{h}}\|^2 \,\mathrm{d}r}}{\sqrt{\int_{l_{\mathrm{i}}} \|s_{\mathrm{ref}}\|^2 \,\mathrm{d}r}}, \tag{2.31}$$

where s_{h} and s_{ref} are the approximated and reference slip values, respectively. The integrals are evaluated along the inclusion axis, l_{i}, and the reference slip solution s_{ref} is extracted from a reference FEM solution (Section 2.2.2) obtained with a 600×600 uniform grid of bilinear quadrilateral elements.

The results of this study are reported in Figure 2.15 in terms of the error convergence plots for three different K_{bt} values, and in Figures 2.16 and 2.17 in terms of the slip profiles for the two largest K_{bt} values. An improved approximation of the displacement field in the matrix material has a positive impact on the solution. In terms of local quantities, a visual inspection of the slip profiles clearly shows that compared to a basic ERS formulation all proposed approaches reduce the oscillations in the slip profiles, with the p-FEM based approximation performing better. The least improvement seems to be related to the strain discontinuity enriched ERS model. The results in terms of a global measure however (Figure 2.15) indicate that the MLS based model performs the worse. Noteworthy, the p-FEM based approximation performs better than the strain discontinuity enriched ERS model only for $p \geq 4$.

Although slip oscillations are attributed to the poor quality of intra-element displacements related to the artificial continuity of the strain field in the ERS model, oscillations are still present in the sdERS model where the strain discontinuity is explicitly described. At present we cannot give a definite answer about the origin of these oscillations.

2.6. CONCLUSIONS

When modeling high aspect ratio inclusions, ERS models are considered to be efficient replacements for conformal discretization approaches. The main shortcomings of these

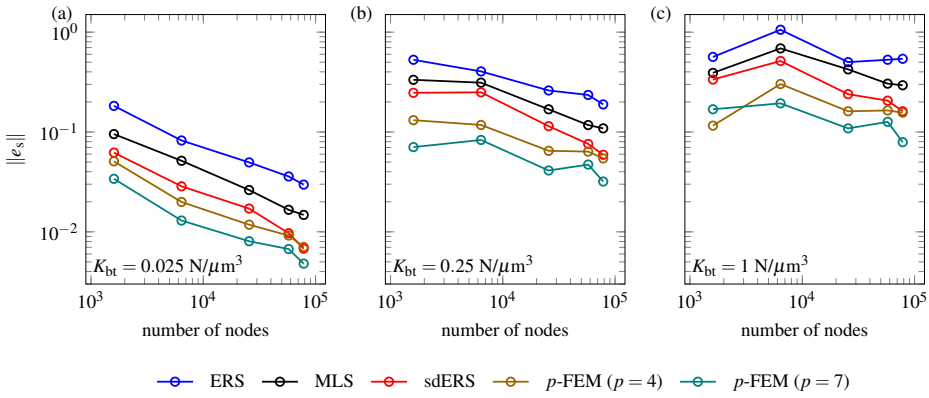

Figure 2.15: Relative error in slip profiles for the single inclusion problem for different mesh densities and using various interface tangential stiffness values. The results are shown for the ERS model, the strain discontinuity enriched ERS (sdERS) model, the moving least squares (MLS) based model, and the p-version of the finite element based model (p-FEM with p equal to 4 and 7) using uniform Q4 discretizations.

non-conformal approaches were demonstrated in this study and impair their general applicability. Although not reported here, the limitations reported in this study holds also under plane stress conditions and have been observed in three-dimensional simulations. These limitations are attributed to the continuity of field derivatives (*i.e.*, the matrix displacement gradients) across an inclusion.

Inaccuracies in the slip profile can become a limiting factor depending on the adopted material parameters. Inclusion stiffness, interface tangent stiffness, and inclusion cross sectional area are the model parameters which were found to have the most adverse effect when relatively large values are used. To minimize these inaccuracies, one expensive treatment would be to use the proposed strain discontinuity enriched embedded reinforcement model with slip (sdERS). This model however requires the generation of a background integration mesh, an expensive task that is not advised in situations when an element is crossed by more than an inclusion. Besides, the complexity of a three-dimensional implementation does not make this model competitive. A relatively simpler strategy is the local elevation of the approximation order using either polynomial enrichments or the p-version of the finite element method. This strategy is preferred to the sdERS approach due to its simplicity. A more effective strategy might consists in improving the sdERS model with high order matrix displacement approximations but its generalization to higher dimensions is not straightforward.

REFERENCES

[1] H. R. Lusti and A. A. Gusev, *Finite element predictions for the thermoelastic properties of nanotube reinforced polymers,* Modelling and Simulation in Materials Science and Engineering **12**, S107 (2004).

[2] S. Balakrishnan and D. W. Murray, *Finite element prediction of reinforced concrete*

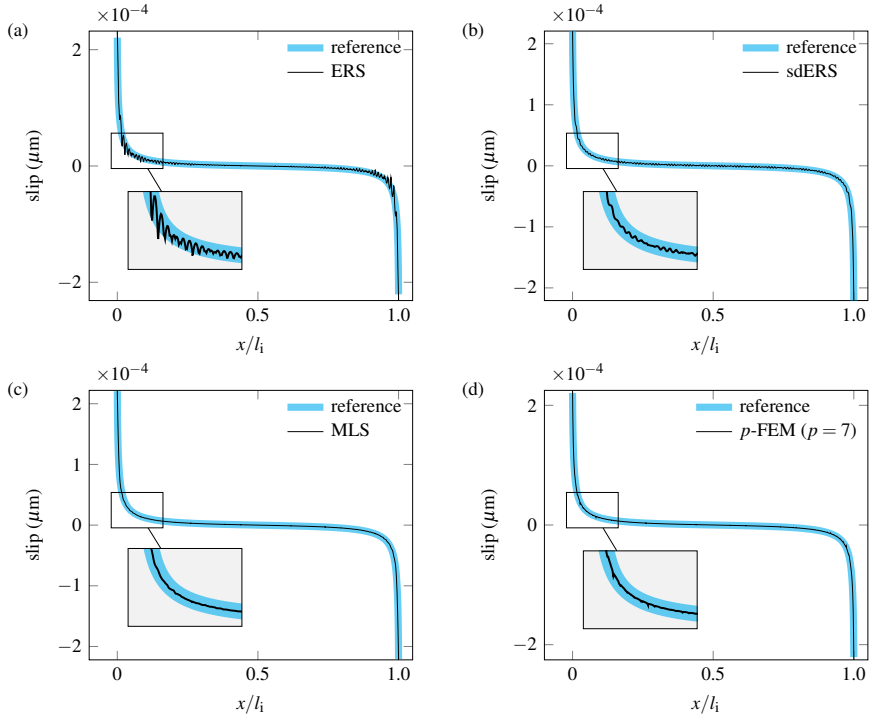

Figure 2.16: Slip profiles for the single inclusion problem corresponding to the bond stiffness $K_{\mathrm{bt}} = 0.25$ N/μm^3 obtained with the ERS model, the strain discontinuity enriched ERS (sdERS) model, moving least squares (MLS) based model, and p-version of the finite element based model (p-FEM with $p = 7$). The results are shown using a uniform 280×280 Q4 discretization and are accompanied by the reference slip profile obtained with a conformal FEM approach (uniform 600×600 Q4 discretization).

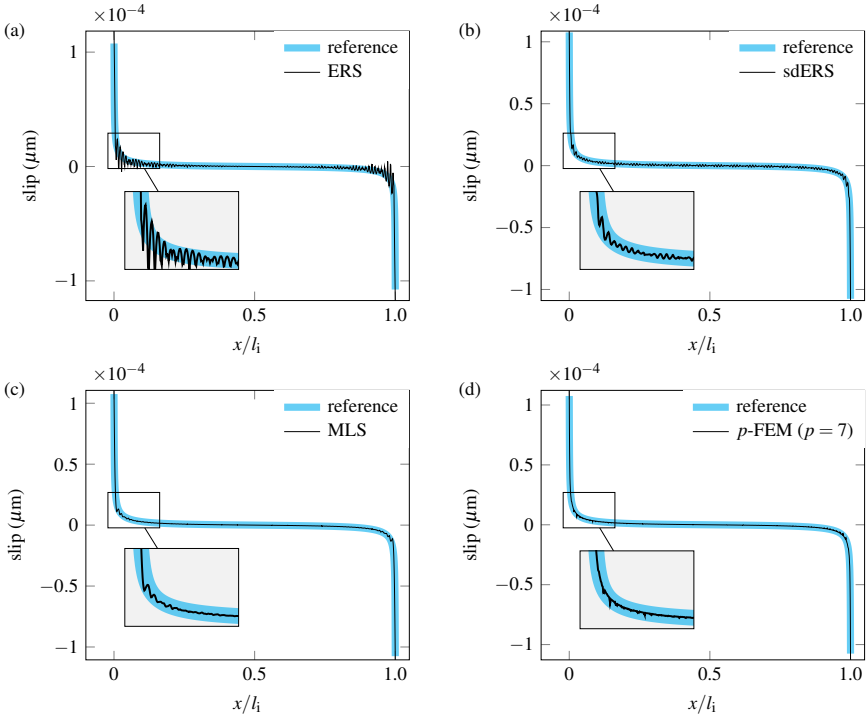

Figure 2.17: Slip profiles for the single inclusion problem corresponding to the bond stiffness $K_{bt} = 1$ N/μm^3 obtained with the ERS model, the strain discontinuity enriched ERS (sdERS) model, moving least squares (MLS) based model, and p-version of the finite element based model (p-FEM with $p = 7$). The results are shown using a uniform 280×280 Q4 discretization and are accompanied by the reference slip profile obtained with a conformal FEM approach (uniform 600×600 Q4 discretization).

behavior, Tech. Rep. Structural Engineering Report No. 138 (Department of Civil Engineering, The University of Alberta, 1986).

[3] J. M. Guedes and N. Kikuchi, *Preprocessing and postprocessing for materials based on the homogenization method with adaptive finite element methods,* Computer Methods in Applied Mechanics and Engineering **83**, 143 (1990).

[4] E. A. Schauffert and G. Cusatis, *Lattice discrete particle model for fiber-reinforced concrete. I: Theory,* Journal of Engineering Mechanics. **138**, 826 (2012).

[5] J. E. Bolander, S. Choi, and S. R. Duddukuri, *Fracture of fiber-reinforced cement composites: effects of fiber dispersion,* International Journal of Fracture **154**, 73 (2008).

[6] J. E. Bolander and S. Saito, *Discrete modeling of short-fiber reinforcement in cementitious composites,* Advanced Cement Based Materials **6**, 76 (1997).

[7] Y. Liu, N. Nishimura, and Y. Otani, *Large-scale modeling of carbon-nanotube composites by a fast multipole boundary element method,* Computational Materials Science **34**, 173 (2005).

[8] A. Ibrahimbegovic, A. Boulkertous, L. Davenne, and D. Brancherie, *Modelling of reinforced-concrete structures providing crack-spacing based on X-FEM, ED-FEM and novel operator split solution procedure,* International Journal for Numerical Methods in Engineering **83**, 452 (2010).

[9] F. K. F. Radtke, A. Simone, and L. J. Sluys, *A computational model for failure analysis of fibre reinforced concrete with discrete treatment of fibres,* Engineering Fracture Mechanics **77**, 597 (2010).

[10] A. Pros, P. Diez, and C. Molins, *Modeling steel fiber reinforced concrete: numerical immersed boundary approach and a phenomenological mesomodel for concrete-fiber interaction,* International Journal for Numerical Methods in Engineering **90**, 65 (2012).

[11] G. Markou and M. Papadrakakis, *An efficient generation method of embedded reinforcement in hexahedral elements for reinforced concrete simulations,* Advances in Engineering Software **45**, 175 (2012).

[12] V. M. C. F. Cunha, J. A. O. Barros, and J. M. Sena-Cruz, *A finite element model with discrete embedded elements for fibre reinforced composites,* Computers & Structures **94**, 22 (2012).

[13] C. Octávio, D. D. da Costa, J. Alfaiate, and E. Júlio, *Modelling the behaviour of steel fibre reinforced concrete using a discrete strong discontinuity approach,* Engineering Fracture Mechanics **154**, 12 (2016).

[14] B. Mortazavi, M. Baniassadi, J. Bardon, and S. Ahzi, *Modeling of two-phase random composite materials by finite element, Mori–Tanaka and strong contrast methods,* Composites Part B: Engineering **45**, 1117 (2013).

[15] S. Soghrati, A. Nagarajan, and B. Liang, *Conforming to interface structured adaptive mesh refinement: new technique for the automated modeling of materials with complex microstructures,* Finite Elements in Analysis and Design **125**, 24 (2017).

[16] N. Sheng, M. C. Boyce, D. M. Parks, G. C. Rutledge, J. I. Abes, and R. E. Cohen, *Multiscale micromechanical modeling of polymer/clay nanocomposites and the effective clay particle,* Polymer **45**, 487 (2004).

[17] K. Hbaieb, Q. X. Wang, Y. H. J. Chia, and B. Cotterell, *Modelling stiffness of polymer/clay nanocomposites,* Polymer **48**, 901 (2007).

[18] J. M. Melenk and I. Babuška, *The partition of unity finite element method: Basic theory and applications,* Computer Methods in Applied Mechanics and Engineering **139**, 289 (1996).

[19] N. Moës, M. Cloirec, P. Cartraud, and J. F. Remacle, *A computational approach to handle complex microstructure geometries,* Computer Methods in Applied Mechanics and Engineering **192**, 3163 (2003).

[20] S. Omerović and T.-P. Fries, *Conformal higher-order remeshing schemes for implicitly defined interface problems,* International Journal for Numerical Methods in Engineering **109**, 763 (2017).

[21] S. Soghrati, A. M. Aragón, A. C. Duarte, and P. H. Geubelle, *An interface-enriched generalized FEM for problems with discontinuous gradient fields,* International Journal for Numerical Methods in Engineering **89**, 991 (2012).

[22] S. Soghrati and P. H. Geubelle, *A 3D interface-enriched generalized finite element method for weakly discontinuous problems with complex internal geometries,* Computer Methods in Applied Mechanics and Engineering **217–220**, 46 (2012).

[23] D. V. Phillips and O. C. Zienkiewicz, *Finite element non-linear analysis of concrete structures,* Proceedings of the Institution of Civil Engineers **61**, 59 (1976).

[24] A. E. Elwi and T. M. Hrudey, *Finite element model for curved embedded reinforcement,* Journal of Engineering Mechanics **115**, 740 (1989).

[25] M. S. M. Sampaio, R. R. Paccola, and H. B. Coda, *Fully adherent fiber–matrix FEM formulation for geometrically nonlinear 2D solid analysis,* Finite Elements in Analysis and Design **66**, 12 (2013).

[26] F. Barzegar and S. Maddipudi, *Three-dimensional modeling of concrete structures. II: Reinforced concrete,* Journal of Structural Engineering **123**, 1347 (1997).

[27] H. Hartl, *Development of a Continuum-Mechanics-Based Tool for 3D Finite Element Analysis of Reinforced Concrete Structures and Application to Problems of Soil-Structure Interaction*, Doctoral thesis, Graz University of Technology, Austria (2002).

[28] J. Ninić, J. Stascheit, and G. Meschke, *Beam–solid contact formulation for finite element analysis of pile–soil interaction with arbitrary discretization,* International Journal for Numerical and Analytical Methods in Geomechanics **38**, 1453 (2014).

[29] F. K. F. Radtke, A. Simone, and L. J. Sluys, *A partition of unity finite element method for obtaining elastic properties of continua with embedded thin fibres,* International Journal for Numerical Methods in Engineering **84**, 708 (2010).

[30] M. G. Pike and C. Oskay, *XFEM modeling of short microfiber reinforced composites with cohesive interfaces,* Finite Elements in Analysis and Design **106**, 16 (2015).

[31] M. G. Pike and C. Oskay, *Three-dimensional modeling of short fiber-reinforced composites with extended finite-element method,* Journal of Engineering Mechanics **142**, 04016087 (2016).

[32] D. Ngo and A. C. Scordelis, *Finite element analysis of reinforced-concrete beams,* ACI Journal, Proocedings **64**, 152 (1967).

[33] M. Goudarzi and A. Simone, *Fiber neutrality in fiber-reinforced composites: Evidence from a computational study,* International Journal of Solids and Structures **156–157**, 14 (2019).

[34] C. A. M. Duarte and J. T. Oden, *An* hp *adaptive method using clouds,* Computer Methods in Applied Mechanics and Engineering **139**, 237 (1996).

[35] C. A. Duarte, I. Babuška, and J. T. Oden, *Generalized finite element methods for three-dimensional structural mechanics problems,* Computers & Structures **77**, 215 (2000).

[36] R. L. Taylor, O. C. Zienkiewicz, and E. Oñate, *A hierarchical finite element method based on the partition of unity,* Computer Methods in Applied Mechanics and Engineering **152**, 73 (1998).

[37] P. Solin, K. Segeth, and I. Dolezel, *Higher-Order Finite Element Methods* (CRC Press, 2003).

[38] C. A. M. Duarte and J. T. Oden, Hp *clouds – An* hp *meshless method,* Numerical Methods for Partial Differential Equations **12**, 673 (1996).

[39] A. M. Aragón, C. A. Duarte, and P. H. Geubelle, *Generalized finite element enrichment functions for discontinuous gradient fields,* International Journal for Numerical Methods in Engineering **82**, 242 (2010).

[40] B. Szabó and I. Babuška, *Introduction to Finite Element Analysis: Formulation, Verification and Validation* (John Wiley & Sons, 2011).

[41] O. Van der Sluis, P. J. G. Schreurs, W. A. M. Brekelmans, and H. E. H. Meijer, *Overall behaviour of heterogeneous elastoviscoplastic materials: effect of microstructural modelling,* Mechanics of Materials **32**, 449 (2000).

[42] O. C. Zienkiewicz and J. Z. Zhu, *A simple error estimator and adaptive procedure for practical engineerng analysis,* International Journal for Numerical Methods in Engineering **24**, 337 (1987).

[43] O. C. Zienkiewicz and J. Z. Zhu, *The superconvergent patch recovery and a posteriori error estimates. Part 1: The recovery technique,* International Journal for Numerical Methods in Engineering **33**, 1331 (1992).

[44] M. C. Rivara, *Algorithms for refining triangular grids suitable for adaptive and multigrid techniques,* International Journal for Numerical Methods in Engineering **20**, 745 (1984).

[45] J. C. J. Schellekens and R. De Borst, *On the numerical integration of interface elements,* International Journal for Numerical Methods in Engineering **36**, 43 (1993).

[46] P. Lancaster and K. Salkauskas, *Surfaces generated by moving least squares methods,* Mathematics of Computation **37**, 141 (1981).

[47] D. H. McLain, *Drawing contours from arbitrary data points,* The Computer Journal **17**, 318 (1974).

[48] B. Nayroles, G. Touzot, and P. Villon, *Generalizing the finite element method: Diffuse approximation and diffuse elements,* Computational mechanics **10**, 307 (1992).

[49] J. Dolbow and T. Belytschko, *An introduction to programming the meshless Element Free Galerkin method,* Archives of Computational Methods in Engineering **5**, 207 (1998).

[50] B. Szabó and I. Babuška, *Finite Element Analysis* (John Wiley & Sons, 1991).

3

RIGID LINE INCLUSIONS AS ELASTIC STIFFENERS AND SHEAR BAND INSTABILITY TRIGGERS

The embedded-reinforcement method is employed to reveal the mechanical role of rigid line inclusions (RLIs) as elastic stiffeners in linear elastic materials and as instability triggers in viscoplastic-damage materials. Validated against available analytical predictions, this numerical method is employed to assess the effect of various geometrical RLI properties, including spatial orientation and mutual interactions. Beside the stiffening of the effective elastic response of the resulting composite material, RLIs are shown to become sources of local material instability by promoting the nucleation of shear bands when embedded in an inelastic solid. More precisely, the RLIs interaction within a matrix is characterized at collapse, by varying their spatial distribution, and ranges from an almost null effect to a dramatic alteration of the dominant failure mechanism. These results offer new insights into the energy dissipation mechanisms of reinforced materials emerging from the interaction of highly stiff inclusions.

3.1. INTRODUCTION

Biological nanocomposites with stiff minerals embedded in a relatively soft protein-based matrix [1], polymer nanocomposites with platelet-like clay particles [2], and graphene-based composite materials [3, 4] are some instances of composites where the reinforcing agents are so much stiffer than the matrix that they can be effectively modeled as rigid elements. This type of composites, and the role of the highly stiff phase on their mechan-

Reprinted from: M. Goudarzi, F. Dal Corso, D. Bigoni and A. Simone, Rigid line inclusions as elastic stiffeners and shear band instability triggers, *to be submitted*.

ical responses, could in principle be studied with available numerical approaches. The major drawback in such analyses is the computational complexity stemming from the possibly large number of arbitrarily-oriented inclusions, a requirement necessary to understand the mechanics of composite specimens with sophisticated geometries for optimizing their practical design. A computationally affordable method is employed here to overcome this limitation and to reveal the complex interactions between rigid inclusions in elastic and inelastic solids.

The numerical characterization of composites with realistic volume fractions of high aspect ratio inclusions has been mainly hindered by the requirement of conformal discretizations, a requirement inherent to classical finite element methods. A further complication arises in those cases where the matrix-inclusion interface is imperfect, and thus the relative matrix-inclusion displacement is represented by means of interface elements that require ad-hoc meshing procedures. In general, these aspects are not conceptually challenging and classical finite element method (FEM) approaches are more than adequate when the inclusion volume is moderate. Nevertheless, when the number of inclusions increases, classical FEM approaches become inadequate as the simulation cost might become very high (an example of such a situation with perfectly bonded fibers discretized as cylinders in a three-dimensional space can be found in Lusti and Gusev [5]). With reference to platelet-like inclusions, simplifying modeling assumptions rely on various dimensional reduction procedures, the most common being the two-dimensional projection of the problem geometry, followed, when possible, by a further dimensional reduction due to the high aspect ratio of the projection. The former is an accepted simplification in the numerical analysis of polymer-clay nanocomposites, where the elongated rectangular cross section of a three-dimensional clay platelet is discretized by means of a conformal two-dimensional mesh [6]. The latter simplification consists in the reduction of the narrow two-dimensional rectangular projection into a one-dimensional line inclusion as conveniently done by [7]. Moreover, such approach is also pursued in the rigid line inclusion (RLI) model, which essentially is a two-dimensional analytical model of a rigid inclusion in a deformable matrix.

Although line inclusions could be adequately discretized in a two-dimensional setting by means of finite elements traditionally employed for the analysis of (fiber-)reinforced concrete or composites (i.e., a bar or a beam element surrounded by continuum elements), the crux of the problem lies with the conformal discretization of matrix and inclusion. The mesh-conformity problem has been addressed by means of embedded reinforcement methods [8–14], lattice models [15–17], boundary element methods [18, 19], partition of unity enrichment techniques [20–22], interface-constraint methods [23, 24] and other mesh-free approaches [25, 26]. A characterizing feature of these methods is that line inclusions can be placed in the computational domain independently of the matrix domain discretization, and thus overriding the need for conformal discretizations. Among these approaches, embedded reinforcement methods are the closest to a classical FEM approach in terms of implementation and offer a good compromise between accuracy and computational burden, making them ideal tools for the characterization of dense inclusion distributions.

In this chapter, we show that the mechanics of composites with numerous RLIs can be adequately modeled by means of an embedded reinforcement method. Although the approach described in Section 3.2.2 is meant for elastic inclusions with imperfect interfaces, the study in Section 3.2.4 demonstrates that RLIs can be properly represented by tuning

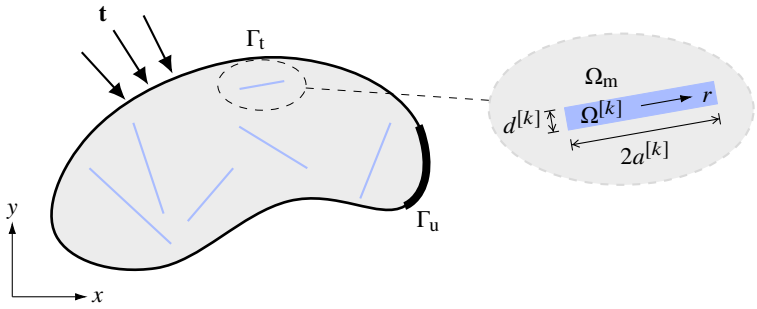

Figure 3.1: Schematic of the inclusion problem.

the parameters defining the matrix-inclusion bond and inclusion stiffnesses. Sections 3.2.4 and 3.3.1 show that the method can adequately approximate the linear elastic fields predicted by analytical solutions [27–30], which show analogies with the corresponding fields in crack problems but are also characterized by distinctive features [31–34], and reproduce the peculiar cases of stress annihilation/inclusion neutrality [27, 28, 35, 36]. These validation examples are complemented in Section 3.4 by a detailed micromechanical analysis on the role of inclusion orientation and interaction. The latter part of the study addresses shear band formation and interaction in an elastic-viscoplastic-damage material matrix, motivated by the intriguing nature of the highly localized stress zones nucleated at the inclusion tips. Indeed, experimental and analytical evidence indicate that the role of an inclusion changes from reinforcing agent into source of material instability [33, 37–39], with consequences in terms of energy dissipation mechanism in the non-linear regime.

3.2. PROBLEM STATEMENT AND METHOD OF ANALYSIS

The mechanical response of solids reinforced by stiff platelets of the type described in Section 3.2.1 is investigated by means of a dimensionally-reduced method of the type traditionally employed to model discrete fiber reinforcements embedded in a continuum matrix. The method, summarized in Section 3.2.2, is validated in Section 3.2.4 through comparison with available analytical solutions for RLIs embedded in an elastic medium and applied to the analysis of the elastic stiffening in Section 3.3; its application to shear banding problems in Section 3.4 makes use of the isotropic elastic-viscoplastic-damage model summarized in Section 3.2.3. In the reminder of the chapter, a stiff (line) inclusion refers to the numerical approximation of a RLI.

3.2.1. PROBLEM DESCRIPTION

The spatial arrangement of M platelets in the configuration considered in this study (Fig. 3.1) corresponds to a non-uniform distribution of material properties in the $x-y$ plane and a uniform distribution of material properties along the z axis. With reference to very thick specimens with thickness h measured along the z axis, the analysis is conducted in the $x-y$ plane under the plane strain assumption; thus, the out-of-plane coordinate z is disregarded in the following. The volume of the k-th inclusion ($k = 1,...,M$) equals the specimen thick-

ness h multiplied by the cross sectional area $S^{[k]} = 2a^{[k]}\,d^{[k]}$ of the rectangular region that the inclusion forms with the $x-y$ plane ($2a^{[k]}$ and $d^{[k]}$ are the rectangle sides as shown in the inset of Fig. 3.1). The inclusions are assumed to be very thin ($a^{[k]} \gg d^{[k]}$) so that the k-th platelet inclusion can be approximated by a (zero-thickness) straight line of half-length $a^{[k]}$, inclined at an angle $\overline{\theta}^{[k]}$ with respect to the x axis and centered at $x^{[k]}$ and $y^{[k]}$. The domain $\Omega^{[k]}$ of the k-th inclusion is therefore defined by

$$\Omega^{[k]} = \left\{ x,y \,\middle|\, x = x^{[k]} + r\cos\overline{\theta}^{[k]},\, y = y^{[k]} + r\sin\overline{\theta}^{[k]},\, r \in \left[-a^{[k]}, a^{[k]}\right] \right\}, \tag{3.1}$$

with r the inclusion local coordinate with origin at the inclusion midpoint. Each inclusion interacts with the matrix material through its interface defined by its two lateral surfaces, each with area $2a^{[k]}\,h$.

3.2.2. EMBEDDED REINFORCEMENT METHOD

The embedded reinforcement method used in this study is based on the formulation proposed by Balakrishnan and Murray [9]. In embedded formulations, the inclusion is represented by means of an independent discretization superimposed to the matrix discretization and equipped with a dedicated kinematic field.

KINEMATIC FIELD

The method is based on the introduction of the sliding displacement $u_{\mathrm{s}}^{[k]}$, also known as slip, between the k-th inclusion and the matrix, so that the (discontinuous) displacement field $\mathbf{u}$ within the composite material is defined as

$$\mathbf{u} = \begin{cases} \mathbf{u}_{\mathrm{b}} & \text{in } \Omega, \\ \mathbf{u}_{\mathrm{b}} + u_{\mathrm{s}}^{[k]}\mathbf{e}^{[k]} & \text{for } \{x,y\} \in \Omega^{[k]}, \end{cases} \tag{3.2}$$

where $\mathbf{u}_{\mathrm{b}}$ is a continuous field representing the matrix (i.e., bulk) displacement field in $\Omega \setminus \Omega^{[k]}$, and $\mathbf{e}^{[k]} = \{\cos\overline{\theta}^{[k]}, \sin\overline{\theta}^{[k]}\}$ is the unit vector aligned with the k-th inclusion line. Expression (3.2) implies that the tangential component of the displacement field of an inclusion is given by the sum of a non-slip contribution, $\mathbf{u}_{\mathrm{b}} \cdot \mathbf{e}^{[k]}$, and a slip contribution, $u_{\mathrm{s}}^{[k]}$. The non-slip component is also known as concrete displacement [9] or duct displacement [12]. The slip component can be eliminated from the formulation for the analysis of a RLI; this component is however kept for didactic purposes to demonstrate that a classical embedded reinforcement formulation with slip, available in some commercial FEM packages, can also be used to describe the behavior of RLIs by means of appropriate values of bond stiffness and inclusion Young's modulus as shown in Section 3.2.4. This choice has a minor impact on the simulation burden and no impact on the results.

GOVERNING EQUATIONS

Next, the governing equations are given for a single ($M = 1$) inclusion; their extension to multiple ($M > 1$) inclusions can be readily obtained following Hartl [12]. With reference to the displacement field $\mathbf{u}$ defined in (3.2) and considering infinitesimal deformations, the principle of virtual work for a body Ω with unit out-of-plane thickness and containing a

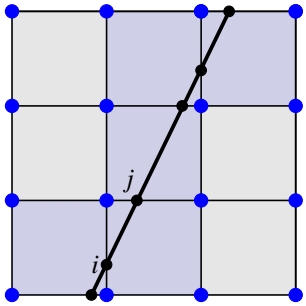

Figure 3.2: An arbitrarily-located inclusion discretized with en embedded formulation. The discretization of the inclusion is superimposed to the matrix discretization.

single inclusion can be expressed as

$$\begin{aligned} &\int_{\Omega\setminus\Omega^{[1]}} \nabla^{\mathrm{s}}\delta\mathbf{u}_{\mathrm{b}} : \boldsymbol{\sigma}_{\mathrm{b}}\, \mathrm{d}\Omega + d^{[1]} \int_{-a^{[1]}}^{a^{[1]}} \left(\delta\mathbf{u}_{\mathrm{b}}\cdot\mathbf{e}^{[1]}\right)_{,r} \sigma^{[1]}\, \mathrm{d}r = \int_{\Gamma_{\mathrm{t}}} \delta\mathbf{u}_{\mathrm{b}}\cdot\bar{\mathbf{t}}\, \mathrm{d}\Gamma_{\mathrm{t}}, \\ &d^{[1]} \int_{-a^{[1]}}^{a^{[1]}} \delta u_{\mathrm{s},r}^{[1]} \sigma^{[1]}\, \mathrm{d}r + 2\int_{-a^{[1]}}^{a^{[1]}} \delta u_{\mathrm{s}}^{[1]} t^{[1]}\, \mathrm{d}r = 0, \end{aligned} \tag{3.3}$$

where the subscript "$,r$" denotes the derivative with respect to r, ∇^{s} and δ are the symmetric gradient and the first variation operators, respectively, the matrix stress tensor is indicated by $\boldsymbol{\sigma}_{\mathrm{b}}$, the inclusion axial stress, a scalar, is denoted as $\sigma^{[1]}$, $\bar{\mathbf{t}}$ is the external traction vector acting along the solid boundary $\Gamma_{\mathrm{t}} \subseteq \partial\Omega$, and $t^{[1]}$ is the interface tangential traction acting along the matrix-inclusion interface.

The first equation in (3.3) defines the virtual work done by the displacement field $\mathbf{u}_{\mathrm{b}}$ in the whole body, comprising matrix and inclusion domains with the exception of the matrix-inclusion interface. The second equation represents the virtual work done by the slip component of the inclusion displacement and includes inclusion and matrix-inclusion interface contributions.

DISCRETIZATION AND LINEARIZATIONS

The discretized version of (3.3) at the matrix element level is obtained by expressing matrix displacement and strain fields as

$$\mathbf{u}_{\mathrm{b}} = \mathbf{N}_{\mathrm{b}}\mathbf{b} \qquad \text{and} \qquad \nabla^{\mathrm{s}}\mathbf{u}_{\mathrm{b}} = \mathbf{B}_{\mathrm{b}}\mathbf{b}, \tag{3.4}$$

respectively, where $\mathbf{N}_{\mathrm{b}}$ collects finite element nodal shape functions, $\mathbf{B}_{\mathrm{b}}$ collects the corresponding derivatives according to the displacement-strain relation, and vector $\mathbf{b}$ contains nodal matrix displacement.

Matrix and inclusions are discretized independently. For convenience, an inclusion is discretized by means of inclusion segments defined between two consecutive intersection points between matrix and inclusion as shown in Fig. 3.2. The quantities below are expressed with reference to an inclusion segment with endpoints i and j. The inclusion non-slip component $\mathbf{u}_{\mathrm{b}}$ and its derivative $\mathbf{u}_{\mathrm{b,r}}$ are computed from the displacement field of

the matrix elements crossed by the inclusion as

$$\mathbf{u}_{\mathrm{b}} \cdot \mathbf{e}^{[1]} = \mathbf{N}_{\mathrm{d}}^{[1]} \mathbf{H}^{[1]} \mathbf{b} \qquad \text{and} \qquad \mathbf{u}_{\mathrm{b,r}} \cdot \mathbf{e}^{[1]} = \mathbf{B}_{\mathrm{d}}^{[1]} \mathbf{H}^{[1]} \mathbf{b}, \tag{3.5}$$

where the expressions of the matrices $\mathbf{N}_{\mathrm{d}}^{[1]}$, $\mathbf{B}_{\mathrm{d}}^{[1]}$, and $\mathbf{H}^{[1]}$ are given in [40]. The slip component $u_{\mathrm{s}}^{[1]}$ and its derivative $u_{\mathrm{s},r}^{[1]}$ can be approximated as

$$u_{\mathrm{s}}^{[1]} = \mathbf{N}_{\mathrm{s}}^{[1]} \mathbf{s}^{[1]} \qquad \text{and} \qquad u_{\mathrm{s},r}^{[1]} = \mathbf{B}_{\mathrm{s}}^{[1]} \mathbf{s}^{[1]}, \tag{3.6}$$

where $\mathbf{s}^{[1]} = [s_i,\ s_j]^{\mathrm{T}}$ is the vector of endpoint slips, and

$$\mathbf{N}_{\mathrm{s}}^{[1]} = [N_i \quad N_j] \qquad \text{and} \qquad \mathbf{B}_{\mathrm{s}}^{[1]} = [N_{i,r} \quad N_{j,r}] \tag{3.7}$$

are inclusion shape function matrix and inclusion shape function derivative matrix, respectively.

Next, the discretized displacements (3.4), (3.6), and (3.5) are introduced in the weak form (3.3). The resulting discretized weak form, obtained following standard procedures, can be interpreted as the equilibrium conditions

$$\mathbf{f}_{\mathrm{int,b}} = \bar{\mathbf{f}}_{\mathrm{ext,b}} \qquad \text{and} \qquad \mathbf{f}_{\mathrm{int,s}}^{[1]} = \bar{\mathbf{f}}_{\mathrm{ext,s}}^{[1]} \tag{3.8}$$

between internal and external forces related to bulk and inclusion contributions with

$$\begin{aligned}
\mathbf{f}_{\mathrm{int,b}} &= \int_{\Omega \setminus \Omega^{[1]}} \mathbf{B}_{\mathrm{b}}^{\mathrm{T}} \boldsymbol{\sigma}_{\mathrm{b}} \, \mathrm{d}\Omega + d^{[1]} \int_{-a^{[1]}}^{a^{[1]}} \mathbf{H}^{[1]\mathrm{T}} \mathbf{B}_{\mathrm{d}}^{[1]\mathrm{T}} \sigma^{[1]} \, \mathrm{d}r, \\
\bar{\mathbf{f}}_{\mathrm{ext,b}} &= \int_{\Gamma_{\mathrm{t}}} \mathbf{N}_{\mathrm{b}}^{\mathrm{T}} \bar{\mathbf{t}} \, \mathrm{d}\Gamma_{\mathrm{t}}, \\
\mathbf{f}_{\mathrm{int,s}}^{[1]} &= d^{[1]} \int_{-a^{[1]}}^{a^{[1]}} \mathbf{B}_{\mathrm{s}}^{[1]\mathrm{T}} \sigma^{[1]} \, \mathrm{d}r + 2 \int_{-a^{[1]}}^{a^{[1]}} \mathbf{N}_{\mathrm{s}}^{[1]\mathrm{T}} t^{[1]} \, \mathrm{d}r, \\
\bar{\mathbf{f}}_{\mathrm{ext,s}}^{[1]} &= \mathbf{0},
\end{aligned} \tag{3.9}$$

where it is assumed that the inclusion only interacts with the surrounding matrix (i.e., no external forces $\bar{\mathbf{f}}_{\mathrm{ext,s}}^{[1]}$ act on it).

To obtain the linearized version of the discretized weak form, we pose the constitutive relations in a rate form, where rate quantities are identified by a superimposed dot, $\dot{(\cdot)}$. The stress rate for the continuum is expressed in terms of nodal displacement velocities as

$$\dot{\boldsymbol{\sigma}}_{\mathrm{b}} = \mathbf{D}_{\mathrm{b}} \, \mathbf{B}_{\mathrm{b}} \, \dot{\mathbf{b}}, \tag{3.10}$$

where $\mathbf{D}_{\mathrm{b}}$ relates the stress and strain rates in the bulk. The rates of the inclusion axial stress $\dot{\sigma}^{[1]}$ and the interface tangential traction $\dot{t}^{[1]}$ are defined as

$$\dot{\sigma}^{[1]} = E_{\mathrm{i}}^{[1]} \left(\mathbf{B}_{\mathrm{d}}^{[1]} \mathbf{H}^{[1]} \dot{\mathbf{b}} + \mathbf{B}_{\mathrm{s}}^{[1]} \dot{\mathbf{s}}^{[1]} \right), \qquad \dot{t}^{[1]} = K_{\mathrm{bt}}^{[1]} \mathbf{N}_{\mathrm{s}}^{[1]} \dot{\mathbf{s}}^{[1]}, \tag{3.11}$$

where linear elastic behavior is assumed for both inclusion and matrix-interface, with $E_i^{[1]}$ the Young's modulus of the inclusion and $K_{\mathrm{bt}}^{[1]}$ the elastic constant defining its interfacial stiffness.

Following standard procedures leads to the relation

$$\begin{bmatrix} \mathbf{K}_{\mathrm{bb}}^{j-1} & \mathbf{K}_{\mathrm{bs}}^{[1]\,j-1} \\ \mathbf{K}_{\mathrm{sb}}^{[1]\,j-1} & \mathbf{K}_{\mathrm{ss}}^{[1]\,j-1} \end{bmatrix} \begin{bmatrix} \delta\mathbf{b}^{j} \\ \delta\mathbf{s}^{[1]\,j} \end{bmatrix} = \begin{bmatrix} \bar{\mathbf{f}}_{\mathrm{ext,b}}^{j-1} \\ \mathbf{0} \end{bmatrix} - \begin{bmatrix} \mathbf{f}_{\mathrm{int,b}}^{j-1} \\ \mathbf{f}_{\mathrm{int,s}}^{[1]\,j-1} \end{bmatrix}, \tag{3.12}$$

expressed in terms of the iterative displacements $\delta\mathbf{b}$ and $\delta\mathbf{s}^{[1]}$ at the j-th iteration of a generic incremental step in a Newton-Raphson solution scheme; the sub-matrices at the j-th iteration read (dropping the superscript j for clarity):

$$\begin{aligned}
\mathbf{K}_{\mathrm{bb}} &= \int_{\Omega\setminus\Omega^{[1]}} \mathbf{B}_{\mathrm{b}}^{\mathrm{T}}\mathbf{D}_{\mathrm{b}}\mathbf{B}_{\mathrm{b}}\,\mathrm{d}\Omega + E_{\mathrm{i}}^{[1]}d^{[1]}\int_{-a^{[1]}}^{a^{[1]}} \mathbf{H}^{[1]\,\mathrm{T}}\mathbf{B}_{\mathrm{d}}^{[1]\,\mathrm{T}}\mathbf{B}_{\mathrm{d}}^{[1]}\mathbf{H}^{[1]}\,\mathrm{d}r, \\
\mathbf{K}_{\mathrm{bs}}^{[1]} &= E_{\mathrm{i}}^{[1]}d^{[1]}\int_{-a^{[1]}}^{a^{[1]}} \mathbf{H}^{[1]\,\mathrm{T}}\mathbf{B}_{\mathrm{d}}^{[1]\,\mathrm{T}}\mathbf{B}_{\mathrm{s}}^{[1]}\,\mathrm{d}r, \\
\mathbf{K}_{\mathrm{sb}}^{[1]} &= E_{\mathrm{i}}^{[1]}d^{[1]}\int_{-a^{[1]}}^{a^{[1]}} \mathbf{B}_{\mathrm{s}}^{[1]\,\mathrm{T}}\mathbf{B}_{\mathrm{d}}^{[1]}\mathbf{H}^{[1]}\mathrm{d}r, \\
\mathbf{K}_{\mathrm{ss}}^{[1]} &= E_{\mathrm{i}}^{[1]}d^{[1]}\int_{-a^{[1]}}^{a^{[1]}} \mathbf{B}_{\mathrm{s}}^{[1]\,\mathrm{T}}\mathbf{B}_{\mathrm{s}}^{[1]}\,\mathrm{d}r + 2K_{\mathrm{bt}}^{[1]}\int_{-a^{[1]}}^{a^{[1]}} \mathbf{N}_{\mathrm{s}}^{[1]\,\mathrm{T}}\mathbf{N}_{\mathrm{s}}^{[1]}\,\mathrm{d}r.
\end{aligned} \tag{3.13}$$

In practice, the integrals over $\Omega\setminus\Omega^{[1]}$ in $\mathbf{f}_{\mathrm{int,b}}$ and $\mathbf{K}_{\mathrm{bb}}$ are computed with reference to the domain Ω; this implies that the contribution along the inclusion line is counted twice because of the second integrals in $\mathbf{f}_{\mathrm{int,b}}$ and $\mathbf{K}_{\mathrm{bb}}$. However, since we are dealing with stiff inclusions, these extra contributions to the inclusion stiffness have a negligible influence on the results.

3.2.3. CONSTITUTIVE MODELS FOR THE MATRIX MATERIAL

For the linear elastic analyses reported in Section 3.2.4, the incremental stiffness for the matrix is taken as the standard linear isotropic elasticity matrix ($\mathbf{D}_{\mathrm{b}} = \mathbf{D}_{\mathrm{b}}^{\mathrm{el}}$). In the numerical simulations discussed in Section 3.4, bulk degradation is described by means of the coupled elastic-viscoplastic-damage model proposed by Simone and Sluys [41, Section 2]. Assuming small strain viscoplasticity, the total strain rate $\dot{\boldsymbol{\varepsilon}}_{\mathrm{b}}$ is decomposed into elastic ($\dot{\boldsymbol{\varepsilon}}_{\mathrm{b}}^{\mathrm{el}}$) and viscoplastic ($\dot{\boldsymbol{\varepsilon}}_{\mathrm{b}}^{\mathrm{vp}}$) contributions according to

$$\dot{\boldsymbol{\varepsilon}}_{\mathrm{b}} = \dot{\boldsymbol{\varepsilon}}_{\mathrm{b}}^{\mathrm{el}} + \dot{\boldsymbol{\varepsilon}}_{\mathrm{b}}^{\mathrm{vp}}. \tag{3.14}$$

Under plastic flow ($\tilde{f} \geq 0$, where $\tilde{f}$ is the yield function), the viscoplastic strain rate for Perzyna viscoplasticity is expressed in the associative form according to

$$\dot{\boldsymbol{\varepsilon}}_{\mathrm{b}}^{\mathrm{vp}} = \frac{1}{\tau}\,\tilde{\phi}\left(\tilde{f}\right)\,\tilde{f}_{\boldsymbol{\sigma}}, \tag{3.15}$$

where τ is the relaxation time and $\tilde{f}_{\boldsymbol{\sigma}} = \partial\tilde{f}/\partial\tilde{\boldsymbol{\sigma}}_{\mathrm{b}}$. The overstress function $\tilde{\phi}\left(\tilde{f}\right)$ is expressed in the power-law form

$$\tilde{\phi}\left(\tilde{f}\right) = \left(\frac{\tilde{f}}{\bar{\sigma}_0}\right)^{N}, \tag{3.16}$$

where N ($N \geq 1$) is a real number and $\bar{\sigma}_0$ is the initial yield stress. The softening rule governing the yield stress is described by means of the relation

$$\bar{\sigma}(\tilde{\kappa}) = \bar{\sigma}_0 \left((1+a)\, \mathrm{e}^{-b\tilde{\kappa}} - a\mathrm{e}^{-2b\tilde{\kappa}} \right), \tag{3.17}$$

where a and b are model parameters, and $\tilde{\kappa}$ is the equivalent plastic strain.

Quantities with a tilde superscript are defined in the effective stress space to allow a simple algorithmic treatment of the coupled elastic-viscoplastic-damage model as proposed by Ju [42] for an analogous class of models. Accordingly, the rate-dependent effective stress tensor is expressed as

$$\tilde{\boldsymbol{\sigma}}_\mathrm{b} = \frac{\boldsymbol{\sigma}_\mathrm{b}}{1-\omega} = \mathbf{D}_\mathrm{b}^\mathrm{el} : \boldsymbol{\varepsilon}^\mathrm{el} = \mathbf{D}_\mathrm{b}^\mathrm{el} : \left(\boldsymbol{\varepsilon}_\mathrm{b} - \boldsymbol{\varepsilon}_\mathrm{b}^\mathrm{vp} \right), \tag{3.18}$$

where ω is a scalar damage parameter ($0 \leq \omega \leq 1$) defined as

$$\omega = \alpha \left(1 - \mathrm{e}^{-\beta\tilde{\kappa}} \right), \tag{3.19}$$

with α and β damage model parameters.

Following standard procedures, detailed in Simone and Sluys [41, Section 2], the consistent tangent operator $\mathbf{D}_\mathrm{b}$ for the elastic-viscoplastic-damage model is expressed as

$$\mathbf{D}_\mathrm{b} = (1-\omega)\tilde{\mathbf{D}}^\mathrm{p} - \frac{\partial}{\partial\omega}\tilde{\kappa}\,\tilde{\boldsymbol{\sigma}}_\mathrm{b} \otimes \tilde{\mathbf{r}}, \tag{3.20}$$

where the consistent tangent for the viscoplastic contribution takes the form

$$\tilde{\mathbf{D}}^\mathrm{p} = \tilde{\mathbf{R}} - \frac{\tilde{\mathbf{R}} : \tilde{f}_{\boldsymbol{\sigma}} \otimes \tilde{f}_{\boldsymbol{\sigma}} : \tilde{\mathbf{R}}}{\tilde{f}_{\boldsymbol{\sigma}} : \tilde{\mathbf{R}} : \tilde{f}_{\boldsymbol{\sigma}} - \tilde{f}_\kappa \tilde{\kappa}_\lambda + \tau / \left(\Delta t \tilde{\phi}_{\tilde{f}} \right)} \tag{3.21}$$

with

$$\tilde{\mathbf{R}} = \left(\mathbf{I} + \Delta\tilde{\lambda}\mathbf{D}^\mathrm{el}\tilde{f}_{\boldsymbol{\sigma}\boldsymbol{\sigma}} \right)^{-1} \mathbf{D}^\mathrm{el}, \tag{3.22}$$

$\tilde{f}_{\boldsymbol{\sigma}\boldsymbol{\sigma}} = \partial\tilde{f}_{\boldsymbol{\sigma}}/\partial\tilde{\boldsymbol{\sigma}}_\mathrm{b}$, $\tilde{f}_\kappa = \partial\tilde{f}/\partial\tilde{\kappa}$, $\tilde{\kappa}_\lambda = \partial\tilde{\kappa}/\partial\tilde{\lambda}$, the plastic multiplier $\tilde{\lambda}$, the time increment Δt, the fourth-order identity tensor $\mathbf{I}$, and the second-order tensor

$$\tilde{\mathbf{r}} = \frac{\tilde{\mathbf{R}} : \tilde{f}_{\boldsymbol{\sigma}}}{\tilde{f}_{\boldsymbol{\sigma}} : \tilde{\mathbf{R}} : \tilde{f}_{\boldsymbol{\sigma}} - \tilde{f}_\kappa \tilde{\kappa}_\lambda + \tau / \left(\Delta t \tilde{\phi}_{\tilde{f}} \right)}. \tag{3.23}$$

3.2.4. VALIDATION

The elastic constitutive parameters of the inclusion are calibrated to reproduce analytical solutions for a single RLI embedded in an unbounded linear elastic matrix. Henceforth, the superscript indicating the inclusion number is omitted for clarity.

A SUMMARY OF LINEAR ELASTIC ANALYTICAL RESULTS

Next, basic fracture mechanics concepts and analytical solutions in planar elasticity are recalled for RLIs. For convenience, a local reference system $\hat{x} - \hat{y}$ centered at the midpoint of the RLI and with $\hat{x}$ defined by the versor $\mathbf{e}$ is introduced (Fig. 3.3a).

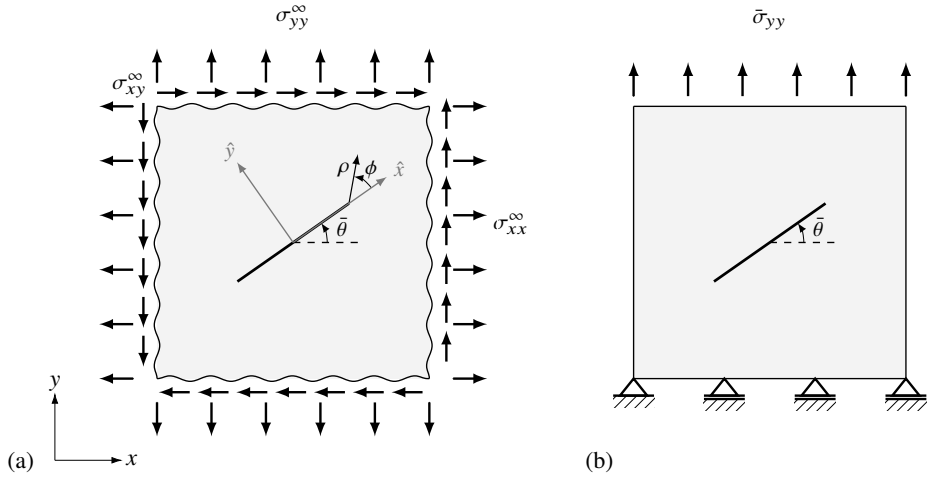

Figure 3.3: (a) A RLI in an infinite domain subjected to a remote stress field; (b) A stiff inclusion in a square domain of size L under uniform vertical tractions. The versor $\mathbf{e} = \{\cos\bar{\theta}, \sin\bar{\theta}\}$ identifies the direction of the inclusion.

Asymptotic stress field and stress intensity factors Figure 3.3a shows a RLI embedded in an infinite elastic isotropic domain. The asymptotic stress field near the tip of the inclusion is expressed as [43]

$$\begin{aligned}
\sigma_{\hat{x}\hat{x}}(\rho,\phi) &= \frac{\mathscr{K}_{\mathrm{I}}^{(\varepsilon)}}{\kappa\sqrt{2\pi\rho}}\cos\frac{\phi}{2}\left(\frac{3+\kappa}{2}-\sin\frac{\phi}{2}\sin\frac{3\phi}{2}\right)+\frac{\mathscr{K}_{\mathrm{II}}^{(\varepsilon)}}{\kappa\sqrt{2\pi\rho}}\sin\frac{\phi}{2}\left(\frac{3-\kappa}{2}+\cos\frac{\phi}{2}\cos\frac{3\phi}{2}\right),\\
\sigma_{\hat{y}\hat{y}}(\rho,\phi) &= -\frac{\mathscr{K}_{\mathrm{I}}^{(\varepsilon)}}{\kappa\sqrt{2\pi\rho}}\cos\frac{\phi}{2}\left(\frac{\kappa-1}{2}-\sin\frac{\phi}{2}\sin\frac{3\phi}{2}\right)+\frac{\mathscr{K}_{\mathrm{II}}^{(\varepsilon)}}{\kappa\sqrt{2\pi\rho}}\sin\frac{\phi}{2}\left(\frac{1+\kappa}{2}-\cos\frac{\phi}{2}\cos\frac{3\phi}{2}\right),\\
\sigma_{\hat{x}\hat{y}}(\rho,\phi) &= \frac{\mathscr{K}_{\mathrm{I}}^{(\varepsilon)}}{\kappa\sqrt{2\pi\rho}}\sin\frac{\phi}{2}\left(\frac{1+\kappa}{2}+\cos\frac{\phi}{2}\cos\frac{3\phi}{2}\right)+\frac{\mathscr{K}_{\mathrm{II}}^{(\varepsilon)}}{\kappa\sqrt{2\pi\rho}}\cos\frac{\phi}{2}\left(\frac{\kappa-1}{2}-\sin\frac{\phi}{2}\sin\frac{3\phi}{2}\right),
\end{aligned} \tag{3.24}$$

where ρ is the distance from the inclusion tip, ϕ is the counterclockwise polar angle measured from the inclusion axis $\hat{x}$ (Fig. 3.3a), κ is the Kolosov constant ($\kappa = 3-4\nu$ in plane strain and $\kappa = (3-\nu)/(1+\nu)$ in plane stress, being ν the Poisson's ratio), and $\mathscr{K}_{\mathrm{I}}^{(\varepsilon)}$ and $\mathscr{K}_{\mathrm{II}}^{(\varepsilon)}$ are, respectively, the mode I and mode II RLI Stress Intensity Factors (SIFs) defined as [32]

$$\mathscr{K}_{\mathrm{I}}^{(\varepsilon)} = 2\mu\lim_{\rho\to 0}\sqrt{2\pi\rho}\,\varepsilon_{\hat{x}\hat{x}}(\rho,\phi=0) \qquad \text{and} \qquad \mathscr{K}_{\mathrm{II}}^{(\varepsilon)} = \frac{4\kappa\mu}{\kappa-1}\lim_{\rho\to 0}\sqrt{2\pi\rho}\,\varepsilon_{\hat{x}\hat{y}}(\rho,\phi=0), \tag{3.25}$$

where μ is the shear modulus (Lamé's second parameter). The asymptotic expansion (3.24) shows a square-root singularity in the radial direction from the inclusion tip. These expressions are only valid for a linear elastic matrix.

***J*-integral** Introduced by [44] and [45] for problems involving fractures, the J-integral

$$J = \int_{\Gamma} \left(U \, \mathrm{d}\hat{y} - \boldsymbol{T} \cdot \frac{\partial \boldsymbol{u}}{\partial \hat{x}} \, \mathrm{d}s \right) \tag{3.26}$$

is a path-independent quantity also when computed for RLI problems. In this expression, U is the strain energy density, $\boldsymbol{T}$ is the surface traction vector, $\boldsymbol{u}$ is the displacement vector, and Γ is any closed counterclockwise contour enclosing the inclusion tip. With the asymptotic expansions (3.24), the J-integral expression reduces to

$$J = -\frac{1+\kappa}{8\kappa\mu} \left[\left(\mathscr{K}_{\mathrm{I}}^{(\varepsilon)} \right)^2 + \left(\mathscr{K}_{\mathrm{II}}^{(\varepsilon)} \right)^2 \right], \tag{3.27}$$

which, unlike the J-integral for fracture problems, is always non positive (with the physical meaning that a reduction in length of the RLI would lead to a decrease of the total potential energy). It is therefore interesting to investigate the annihilation condition of the J-integral as it defines neutral RLI orientations that correspond to a homogeneous stress state (i.e., those situations in which the RLI has no influence on the stress field). Such condition is defined as

$$\text{neutrality condition:} \qquad \mathscr{K}_{\mathrm{I}}^{(\varepsilon)} = \mathscr{K}_{\mathrm{II}}^{(\varepsilon)} = 0 \qquad \Leftrightarrow \qquad J = 0. \tag{3.28}$$

A single inclusion embedded in an infinite elastic matrix subject to uniform remote stress condition Consider a single RLI of half-length a inclined at an angle $\bar{\theta}$ with respect to the x axis and embedded in an infinite elastic matrix subject to a uniform remote stress field with components σ_{xx}^{∞}, σ_{yy}^{∞} and σ_{xy}^{∞} (Fig. 3.3a). The stress field ahead the RLI has been obtained by Atkinson [28] using a complex potentials technique and reads

$$\begin{aligned}
\sigma_{\hat{x}\hat{x}}(\hat{x}, \hat{y} = 0) &= -(\kappa+3) \, \frac{\mu \, \varepsilon_{\hat{x}\hat{x}}^{\infty}}{\kappa} \left(1 - \frac{|\hat{x}|}{\sqrt{\hat{x}^2 - a^2}} \right) \\
\sigma_{\hat{y}\hat{y}}(\hat{x}, \hat{y} = 0) &= (\kappa-1) \, \frac{\mu \, \varepsilon_{\hat{x}\hat{x}}^{\infty}}{\kappa} \left(1 - \frac{|\hat{x}|}{\sqrt{\hat{x}^2 - a^2}} \right) \qquad \text{for } |\hat{x}| > a \\
\sigma_{\hat{x}\hat{y}}(\hat{x}, \hat{y} = 0) &= \sigma_{\hat{x}\hat{y}}^{\infty}
\end{aligned} \tag{3.29}$$

with

$$\begin{aligned}
\varepsilon_{\hat{x}\hat{x}}^{\infty} &= \frac{(\kappa+1)\sigma_{\hat{x}\hat{x}}^{\infty} + (\kappa-3)\sigma_{\hat{y}\hat{y}}^{\infty}}{8\mu}, & \sigma_{\hat{x}\hat{x}}^{\infty} &= \sigma_{xx}^{\infty} \cos^2\bar{\theta} + \sigma_{yy}^{\infty} \sin^2\bar{\theta} + \sigma_{xy}^{\infty} \sin 2\bar{\theta}, \\
\sigma_{\hat{y}\hat{y}}^{\infty} &= \sigma_{xx}^{\infty} \sin^2\bar{\theta} + \sigma_{yy}^{\infty} \cos^2\bar{\theta} - \sigma_{xy}^{\infty} \sin 2\bar{\theta}, & \sigma_{\hat{x}\hat{y}}^{\infty} &= -(\sigma_{xx}^{\infty} - \sigma_{yy}^{\infty}) \sin\bar{\theta} \cos\bar{\theta} + \sigma_{xy}^{\infty} \cos 2\bar{\theta}.
\end{aligned} \tag{3.30}$$

Using these expressions, the SIFs (3.25) at the RLI tips are [32]

$$\mathscr{K}_{\mathrm{I}}^{(\varepsilon)\infty} = 2\mu\varepsilon_{\hat{x}\hat{x}}^{\infty}\sqrt{\pi a}, \qquad \mathscr{K}_{\mathrm{II}}^{(\varepsilon)\infty} = 0, \tag{3.31}$$

where the superscript ∞ has been added to $\mathscr{K}_{\mathrm{I}}^{(\varepsilon)}$ and $\mathscr{K}_{\mathrm{II}}^{(\varepsilon)}$ to highlight the unbounded elastic domain.

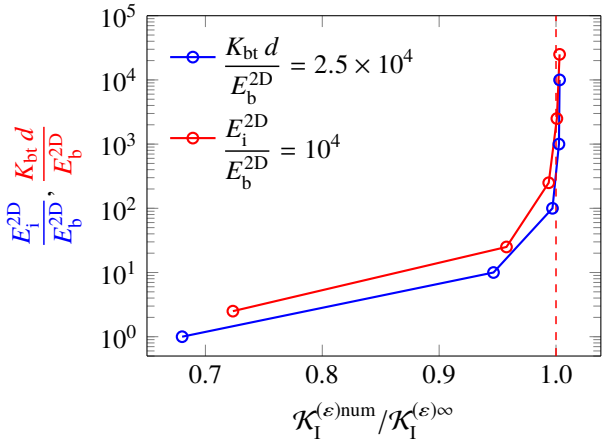

Figure 3.4: Convergence to the mode I analytical stress intensity factor $(3.31)_1$ of a rigid inclusion for a stiff inclusion in the finite size specimen depicted in Fig. 3.3b as a function of the stiffness ratios E_i^{2D}/E_b^{2D} (blue line) or $K_{bt}\,d/E_b^{2D}$ (red line). With reference to the prescribed limit values, convergence is assumed to be attained for $E_i^{2D}/E_b^{2D} > 100$ (blue line) or $K_{bt}\,d/E_b^{2D} > 250$ (red line).

Neutral inclusion configurations It is evident that the inclusion does not perturb a mechanical field whenever it lies along a zero-elongation line in an unperturbed field. In the case of an unbounded matrix subject to a remote uniaxial stress state obtained by imposing $\sigma_{yy}^\infty = \bar\sigma$ as the only non-null stress component (namely, $\sigma_{xx}^\infty = \sigma_{xy}^\infty = 0$), the J-integral (3.27) reduces to

$$J = -\frac{\kappa(1+\kappa)\pi a\bar\sigma^2}{128\mu}\left[1-\frac{1+2\cos 2\bar\theta}{\kappa}\right]^2, \tag{3.32}$$

and therefore the neutral inclinations $\bar\theta = \bar\theta_n$ of the RLI with respect to the x-axis for which the J-integral vanishes are given by

$$\bar\theta_n = \pm\frac{1}{2}\arccos\left(\frac{\kappa-1}{2}\right), \tag{3.33}$$

a condition implying $\sigma_{\hat y\hat y}^\infty = -(\kappa+1)/(\kappa-3)\sigma_{\hat x\hat x}^\infty$ and $\varepsilon_{\hat x\hat x}^\infty = 0$.

CALIBRATION OF INCLUSION AND INTERFACE STIFFNESSES

A RLI can be represented by the embedded inclusion model through appropriate values of model parameters characterizing inclusion stiffness (E_i^{2D}) and matrix-inclusion tangential bond stiffness (K_{bt}). These values are calibrated through a comparison of analytical predictions and numerical results. The calibration is actually based on the comparison of the numerical stress intensity factor $\mathcal{K}_I^{(\varepsilon)num}$, derived from the numerically-evaluated J-integral evaluated along a circular path of radius $0.1a$ centered at the inclusion tip, with the corresponding theoretical value $\mathcal{K}_I^{(\varepsilon)\infty}$. A uniform stress loading condition with only one non-null stress component as described in Section 3.2.4 has been considered in both cases. Here and in the following the planar Young's modulus E_l^{2D} (l=m for the matrix while l=i

for the inclusion) corresponds to E_l under plane stress and $E_l/(1-\nu_l^2)$ under plane strain conditions, where E_l is the three-dimensional elasticity modulus.

Figure 3.4 shows the stress intensity factor $\mathscr{K}_{\mathrm{I}}^{(\varepsilon)\mathrm{num}}$ normalized by its analytical value $\mathscr{K}_{\mathrm{I}}^{(\varepsilon)\infty}$ as a function of normalized inclusion stiffness $E_{\mathrm{i}}^{2\mathrm{D}}/E_{\mathrm{b}}^{2\mathrm{D}}$ and matrix-inclusion bond stiffness $K_{\mathrm{bt}}\,d/E_{\mathrm{b}}^{2\mathrm{D}}$. The analytical predictions, summarized in Section 3.2.4, refers to a RLI embedded in an unbounded domain; the numerical results are obtained from numerical simulations of a horizontal line inclusion of half-length a (Fig. 3.3b, $\bar{\theta}=0$) centered in a linear elastic square domain of size $L=10a$. The square domain of size L is discretized by a 542×542 uniform mesh of bilinear elements. Plane strain conditions with Poisson's ratio $\nu_{\mathrm{b}}=0.2$ are assumed together with $d=0.1L$ (note that this value is immaterial in the sense that it acts as an amplification factor to E_{i} in the discrete set of equations). The numerical results in Figure 3.4 have been obtained by keeping fixed one stiffness ratio (either $E_{\mathrm{i}}^{2\mathrm{D}}/E_{\mathrm{b}}^{2\mathrm{D}}$ or $K_{\mathrm{bt}}\,d/E_{\mathrm{b}}^{2\mathrm{D}}$ to the corresponding limit value) and varying the other (either $K_{\mathrm{bt}}\,d/E_{\mathrm{b}}^{2\mathrm{D}}$ or $E_{\mathrm{i}}^{2\mathrm{D}}/E_{\mathrm{b}}^{2\mathrm{D}}$ up to the corresponding limit value). The employed limit values are $E_{\mathrm{i}}^{2\mathrm{D}}/E_{\mathrm{b}}^{2\mathrm{D}}=10^4$ and $K_{\mathrm{bt}}\,d/E_{\mathrm{b}}^{2\mathrm{D}}=2.5\times 10^4$.

Since the inclusion is not rigid, the numerical J-integral (3.26) is not path-independent. Because the inclusion and its adhesion with the matrix are elastic and not rigid, the comparison with analytical results becomes meaningful only in the case of very high values of inclusion and bond stiffnesses. For practical purposes however, the comparison is acceptable for high values of these quantities. Indeed, the comparison in Fig. 3.4 suggests to adopt $E_{\mathrm{i}}^{2\mathrm{D}}/E_{\mathrm{b}}^{2\mathrm{D}}>100$ and $K_{\mathrm{bt}}\,d/E_{\mathrm{b}}^{2\mathrm{D}}>250$, being these values related to a relative error lower than 5% in the numerical evaluation of the SIFs compared to the analytical predictions.

RELIABILITY ASSESSMENT

Next, the numerical approach is validated for the problem of a single inclusion in a finite elastic domain and a pair of collinear inclusions in an infinite elastic domain. The inclusions, embedded in a square domain matrix of size L, have material parameters $E_{\mathrm{i}}^{2\mathrm{D}}/E_{\mathrm{b}}^{2\mathrm{D}}=10^4$ and $K_{\mathrm{bt}}\,d/E_{\mathrm{b}}^{2\mathrm{D}}=2.5\times 10^4$. Unspecified parameters and boundary conditions are identical to those employed in the calibration of inclusion and interface stiffnesses.

Effect of finite domain size on SIF The stress intensification at the tips of a stiff inclusion of half-length a centered in a square elastic domain of size L has been numerically evaluated by varying the ratio a/L. The numerical results have been obtained with a structured mesh of 453944 bilinear elements, locally refined around the inclusion. Figure 3.5 shows the excellent agreement of the numerical results with the predictions by Chen [30] who used an eigenfunction expansion variational method. It is noted that the interaction with the free edges is responsible for the reduction in the stress intensification with increasing ratio a/L. The figure also indicates that the analytical SIF for the infinite plane $\mathscr{K}_{\mathrm{I}}^{(\varepsilon)\infty}$ is well captured when $a\leq 0.1L$; in agreement with this results, we have considered this limit value in the remainder of this study.

Pair of collinear inclusions The proposed embedded method is validated towards its exploitation in the micromechanical study of large inclusion volumes where the ability to capture interaction effects between inclusions, neglected in available analytical estimates

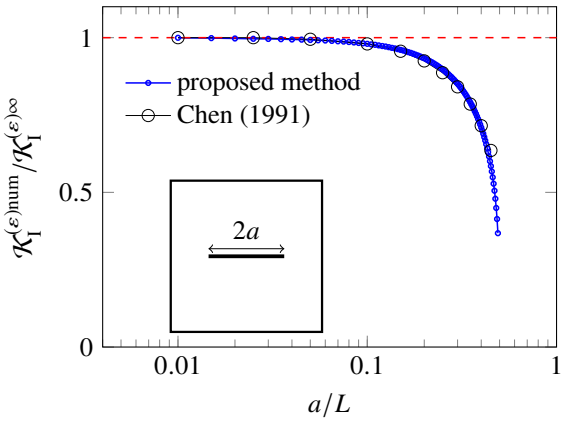

Figure 3.5: Effect of the finite boundary size on the stress state at the inclusion tip. The numerical SIF deviates from that related to a single inclusion $(3.31)_1$ for increasing inclusion length relative to the domain size.

of elastic properties (e.g. [46]), is crucial. Although RLIs have smaller stress amplification regions compared to cracks [47], their interaction can be quite severe when placed sufficiently close to each other. Based on the duality between solutions of cracks and rigid-line inclusions [48], Pingle *et al.* [49] derived a relation to express the amplification of the stress intensity factors for the case of multiple RLIs embedded in an elastic matrix subject to a uniform remote stress field with components σ^{∞}_{xx}, σ^{∞}_{yy} and σ^{∞}_{xy}. In the case of two collinear (non-intersecting) inclusions, each of half-length a, aligned along the x axis (parallel to the $\hat{x}$ axis because $\bar{\theta}=0$), and with their centers at a distance $\Delta+2a$ from each other, the SIFs (3.25) at the RLI tips are given by

$$\begin{aligned}
&\mathscr{K}_{\mathrm{I}}^{(\varepsilon)}(\pm a,\Delta)=\mu\varepsilon^{\infty}_{xx}\sqrt{\frac{a}{\pi}}\int_{-1}^{1}\left[1+\frac{1}{1-\frac{1}{2}\left(\sqrt{8+\frac{6\Delta}{a}+\frac{\Delta^2}{a^2}}-\sqrt{\frac{2\Delta}{a}+\frac{\Delta^2}{a^2}}-2\right)}\frac{\xi+2+\frac{\Delta}{a}}{\sqrt{\left(\xi+2+\frac{\Delta}{a}\right)^2-1}}\right]\sqrt{\frac{1\pm\xi}{1\mp\xi}}\,\mathrm{d}\xi,\\
&\mathscr{K}_{\mathrm{II}}^{(\varepsilon)}(\pm a,\Delta)=0,
\end{aligned}\tag{3.34}$$

where $x=-a$ refers to the inner tips, i.e., those closest to each other, while $x=+a$ relates to the outer ones.

The analytical predictions of the two mode I SIFs (made dimensionless through division by the mode I SIF $\mathscr{K}_{\mathrm{I}}^{(\varepsilon)\infty}$ $(3.31)_1$ for the single inclusion within an unbounded matrix) are reported in Fig. 3.6a with varying ratio Δ/a. An identical setup for the inclusions has been considered in the numerical evaluation of the SIF, with the inclusions placed in the middle of a square domain of size L (refer to Fig. 3.6b). Two inclusion-domain size ratios ($a/L=\{0.05,0.1\}$) were studied. The domain has been discretized with a very fine mesh of bilinear elements locally refined along the inclusion axial direction. To improve the accuracy of the computed J-integral for the inner tips, the integration domain size related to an inclusion tip (i.e., the region surrounding an inclusion tip used for the computation of the corresponding J-integral) was initially adjusted based on the offset distance Δ. This region was further modified to limit the influence of the other tip on the stress field.

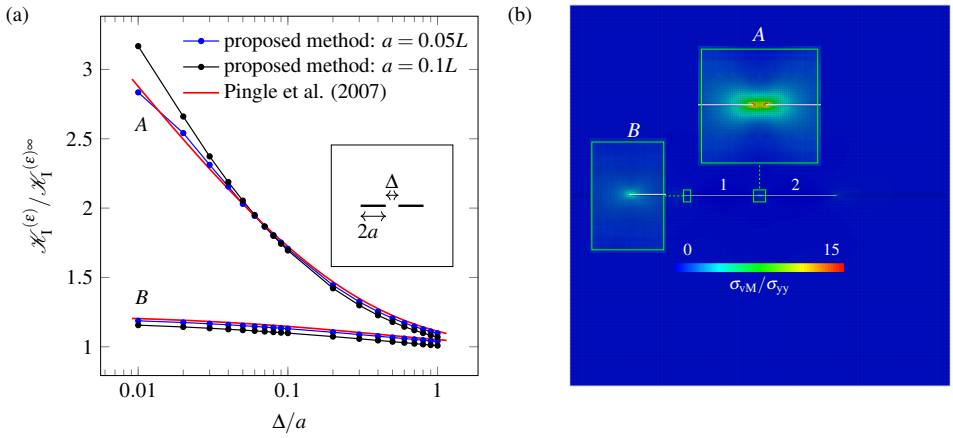

Figure 3.6: Two collinear horizontal rigid inclusions interact under transverse (vertical) loading: (a) numerical and analytical stress intensity factor amplification near inclusion tips for varying offset distance between inclusions; (b) von Mises stress field around the inclusion tips for $\Delta/a = 0.01$ obtained with the proposed method.

Figure 3.6a shows a good agreement between the numerical results and the analytical prediction by Pingle *et al.* [49]. Due to influence of the finite boundaries in the numerical simulations, small inclusions ($a = 0.05L$) yield a better agreement between numerical and analytical results. Figure. 3.6b shows the amplification of the stress field in terms of the von Mises stress field for an offset ratio $\Delta/a = 0.01$ (this ratio corresponds to a threefold amplification of the stress intensity factor).

3.3. STIFF LINE INCLUSIONS AS REINFORCING ELEMENTS: ELASTIC STIFFENING

Next, the effective elastic response of a medium with different distributions of embedded stiff inclusions is studied. The examples can be considered representative of buckypaper (i.e., carbon nanotube sheets) planar inclusion [50] or clay platelet [6] nanocomposites. Stiff inclusions are modeled with $E_{\mathrm{i}}^{2\mathrm{D}}/E_{\mathrm{b}}^{2\mathrm{D}} = 2.5 \times 10^3$ and $K_{\mathrm{bt}}\, d/E_{\mathrm{b}}^{2\mathrm{D}} = 1.25 \times 10^4$. The inclusions, up to a 4.6% volume fraction corresponding to 1500 inclusions, have the same size (half-length $a = 0.02L$ and $d = 0.00077L$) and are embedded in a periodic square cell of size L with unit out-of-plane thickness.

3.3.1. INCLUSION ORIENTATION ROLE

Orientation effects on the effective elastic response are studied for the case of 1000 inclusions inclined at an angle $\bar{\theta}$ and with their midpoints randomly distributed in the simulation box (Fig. 3.7a). The mechanical properties of the orthotropic composite (with orthotropy axes $\hat{x} - \hat{y}$) are extracted using an averaging procedure [51] where periodic boundary conditions are imposed in terms of individual strain components.

Figure 3.7b shows the effective planar Young's modulus along the y-axis $E_{\mathrm{eff},y}^{2\mathrm{D}}$, normal-

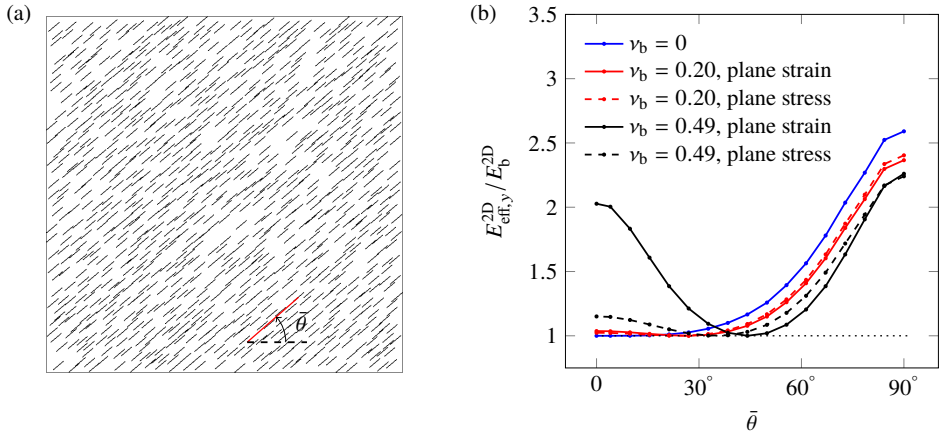

Figure 3.7: The effective planar Young's modulus $E^{2D}_{eff,y}$, normalized by the planar Young's modulus E^{2D}_{b} of the matrix, is plotted in panel b for a distribution of 1000 randomly-positioned aligned inclusions (shown in panel a) as a function of the inclusion inclination $\bar{\theta}$ at different values of the matrix Poisson's ratio ν_b. Neutrality of multiple inclusions emerges at the orientation (3.33) of a single rigid inclusion problem. The domain in panel a is discretized by a 542×542 uniform mesh of bilinear elements.

ized by the planar Young's modulus E^{2D}_{b} of the matrix, as a function of inclusion orientation $\bar{\theta}$ for different values of the Poisson's ratio ν_b of the elastic matrix under plane stress or plane strain conditions.

As expected, the stiffest response along the y-axis is attained when the inclusions are parallel to that direction. In addition, the effective response of the composite is stiffer than that of the matrix material for all but one specific inclination, which depends on the matrix Poisson's ratio ν_b. For this inclination, corresponding to the neutrality angle $\bar{\theta} = \bar{\theta}_n(\nu_b)$ of a single inclusion in (3.33), the effective planar Young's modulus of the composite $E^{2D}_{eff,y}$ coincides with that (E^{2D}_{b}) of the matrix material. Such property is trivially consistent with that related to one inclusion, as neutrality of one inclusion at angle $\bar{\theta}_n$ automatically implies, in virtue of the neutrality property, neutrality of any number of inclusions, all inclined at $\bar{\theta}_n$.

For the special case of a nearly incompressible bulk (with $\nu_b = 0.49$) under a plane strain condition, the neutral orientation is $\bar{\theta}_n \approx 45°$. This implies that the orthotropic reinforced system approaches cubic symmetry becoming biaxially neutral, so that comparable longitudinal and transverse Young's moduli are attained (i.e., $E^{2D}_{eff,x} \approx E^{2D}_{eff,y} \approx E^{2D}_{b}$). This observation is in line with the results reported in Liu *et al.* [52], where significantly stiffened staggered biocomposites in both longitudinal and transverse directions were generated by increasing the Poisson's ratio of the soft matrix towards its incompressibility limit value. It is finally remarked that the stiffening in the effective response for small inclinations is significant only under plane strain conditions.

3.3.2. INCLUSION ARRANGEMENT AND MULTIPLICITY ROLE

The influence of the inclusion arrangement and their multiplicity on the effective planar Young's modulus $E^{2D}_{eff,y}$ of a composite is determined by means of uniformly distributed

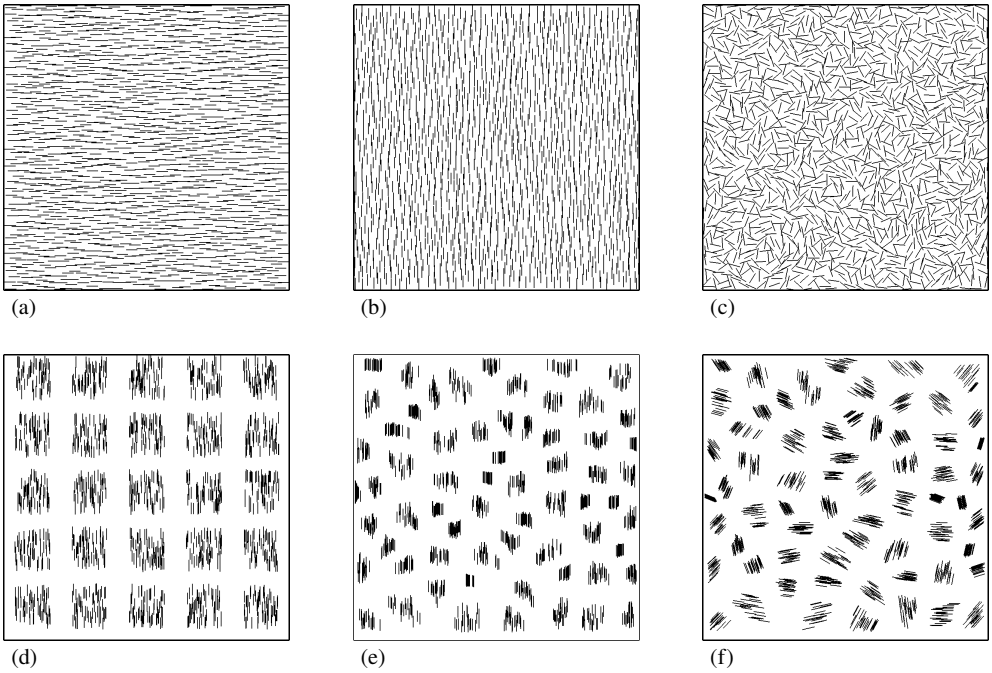

Figure 3.8: Inclusion distributions employed to determine inclusion arrangement and multiplicity role on the composite mechanical properties: 1500 (a) horizontal, (b) vertical, and (c) random uniformly distributed stiff inclusions; 1500 (d, e) vertically intercalated and (f) randomly intercalated stiff inclusions.

parallel (Fig. 3.8a-b), and random (Fig. 3.8c) stiff inclusions, and intercalated (Fig. 3.8d-f) stiff inclusions. The intercalated arrangements are typical of polymer-clay nanocomposites [53]. The numerical results discussed next are obtained with simulations performed under plane stress conditions with Poisson's ratio $\nu_b = 0.2$. The domain is discretized by a 804×804 uniform mesh of bilinear elements.

Among the distributions shown in Fig. 3.8 and with reference to the results related to 1500 inclusions reported in Fig. 3.9a, the uniform distribution of vertical inclusions (Fig. 3.8 b) displays the stiffest response, with a stiffening factor of 3.8. The stiffening is reduced for intercalated distributions, with an increase factor of 2 and 1.5 for the vertically intercalated distributions in panels d and e, respectively. As a side remark, analytical micromechanical approaches [46] and two-step homogenization schemes [54] are not sensitive to the inclusion distribution pattern and yield identical estimates, not reported for brevity, for exfoliated and intercalated distributions such as those in panels b and d. Random inclusion orientations yields much softer composites, with an increase factor of 1.6 observed for the fully exfoliated distribution in panel c and 1.16 for the randomly intercalated distribution in panel f. Obviously, inclusions in a horizontal arrangement (panel a) yield a negligible increase factor. Inclusions inclined at the neutral angle $\bar{\theta} \approx 24.09^\circ$, in arrangements similar to those in panels a or b, yield no increase of the effective planar Young's modulus. The marked nonlinear increase in the response of the composite with the vertical distribution in Fig. 3.8b (blue line) is an indication that the interaction between inclusions is maximized for that particular distribution and boundary conditions.

Panel b in Fig. 3.9 compares numerical predictions with analytical micromechanical estimates (Voigt, Halpin-Tsai (H-T), and Mori-Tanaka (M-T)) for the uniform distribution of 1500 vertical inclusions in Fig. 3.8b for different inclusion Young's modulus ratios E_i^{2D}/E_b^{2D}. The agreement between numerical and analytical estimates is generally better for soft inclusions. For stiff inclusions, Voigt estimate is the most unreliable and overestimates numerical predictions and estimates from other micromechanical models. Among all estimates, numerical predictions are found in a relatively better match with Halpin-Tsai estimates, although all analytical micromechanical models are found unreliable for stiff inclusions.

3.4. STIFF LINE INCLUSIONS AS INSTABILITY TRIGGERS: NUCLEATION OF SHEAR BANDS

Homogeneous mechanical fields become unstable when material failure is approached. This type of instability manifests itself through the formation of shear bands, i.e., localized regions of intense shearing deformation in materials undergoing plastic deformation. In quasi-static failure problems, this phenomenon is theoretically explained by means of the loss of ellipticity of the incremental constitutive tensor or, equivalently, the loss of positive definiteness of the acoustic tensor. Hence, shear bands may emerge in a solid when the stress tensor reaches a critical condition. Shear bands are triggered by inhomogeneities and their emergence therefore redefines the failure mechanism and consequently the load-bearing capacity of any specimen when compared to the same specimen with homogeneous material properties.

In addition to the stiffening of the effective behavior, the introduction of a hard phase in

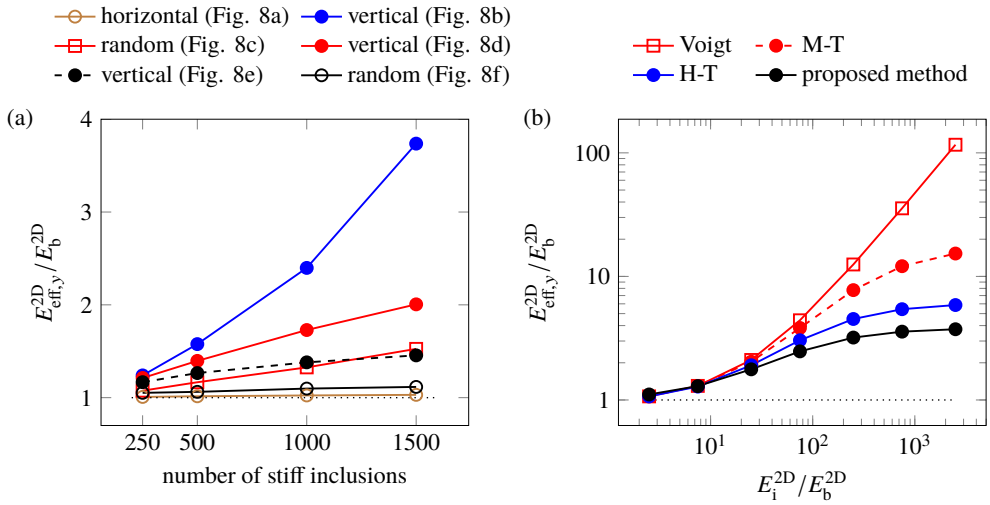

Figure 3.9: Predicted effective Young's modulus $E^{2D}_{eff,y}$ of a composite (a) with an increasing number of stiff inclusions for distributions similar to those shown in Fig. 3.8 and (b) for 1500 uniformly distributed vertical inclusions (i.e., oriented along the y axis) as a function of the inclusion Young's modulus E^{2D}_i – the predicted values are compared with analytical micromechanical estimates (Voigt, Halpin-Tsai (H-T), and Mori-Tanaka (M-T)).

a soft material promotes the emergence of shear bands at the inclusions tips due to the high stress concentrations in a region around them. Indeed, experiments performed on specimens with a ductile bulk material reinforced by stiff platelets show that shear bands emergence at the inclusion tips is the preferential failure mode [33, 37, 38].

Shear bands are numerically investigated in this section by means of an elastic-viscoplastic-damage model summarized in Section 3.2.3 that enables an objective, mesh independent analysis in case of strain localization. Quasi-static damage evolution and failure mechanisms are thoroughly investigated for different inclusion distributions embedded in a square domain of size L under plane stress conditions with Poisson's ratio $\nu_b = 0.2$. Keeping unstressed two of its sides, the domain is stretched along the y axis at a constant displacement rate $\dot{\bar{u}}_y$ until the final displacement $\bar{U} = 0.0015385L$ is reached in 200 equal time-steps. The mixed boundary conditions are represented in Figure 3.3b considering the imposed uniform tractions $\bar{\sigma}_{yy}$ replaced by the uniform displacement boundary condition $\bar{u}_y$. Stiff inclusions are modeled with $E^{2D}_i/E^{2D}_b = 2.5\times10^3$ and $K_{bt}\,d/E^{2D}_b = 1.25\times10^4$, using therefore the same set of parameters employed in Section 3.3. Material degradation is described by means of a J_2 material response with von Mises yield stress $\bar{\sigma}_0 = 0.0001E^{2D}_b$, the exponential softening rule (3.17) governing the cohesion capacity of the material with $a = -1$ and $b = 200$, and damage parameters $\alpha = 0.99$ and $\beta = 300$ in (3.19). As for the Perzyna parameters, $N = 1$ in the overstress function (3.16) and the ratio $\tau/\Delta t = 8000$ in (3.21). For the considered constitutive parameters, the shear bands (identified by highly damaged narrow regions) are inclined at the conjugate angles of $\theta^{(\pm)}_{sb} \approx \pm 37^\circ$ with respect to the x-axis when elongation is imposed along the y-axis (refer to Fig. 3.14).

The shear bands patterns are examined and compared for different inclusion distribu-

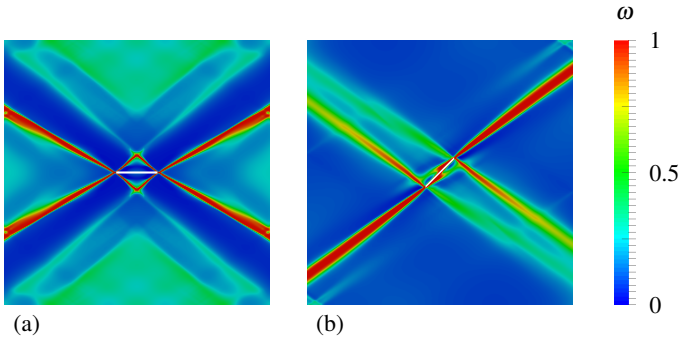

Figure 3.10: Damage fields at imposed displacement $\bar{u}_y = \bar{U}$ in a specimen with a single inclusion inclined at an angle $\bar{\theta} = 0$ (a) and $\bar{\theta} = 45^\circ$ (b) with respect to the horizontal axis.

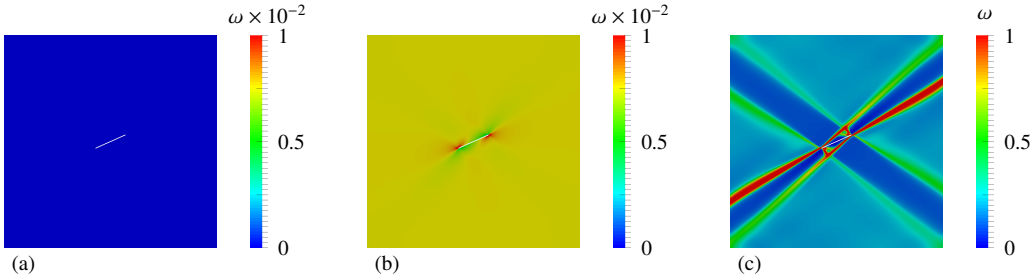

Figure 3.11: Damage field evolution in a specimen with a single inclusion at the neutral inclination $\bar{\theta} = \bar{\theta}_n \approx 24.09^\circ$ with respect to the horizontal: (a) elastic regime just before damage initiation ($\bar{u}_y = 0.065\bar{U}$); (b) inelastic regime right after damage initiation ($\bar{u}_y = 0.085\bar{U}$); and (c) inelastic regime at the final imposed displacement $\bar{u}_y = \bar{U}$.

tions for an imposed displacement $\bar{u}_y = \bar{U}$, for which the load-carrying capacity of the different specimens is almost exhausted and therefore failure can be considered attained.

3.4.1. A SINGLE STIFF LINE INCLUSION

A stiff line inclusion of half-length $a \approx 0.077L$ is centered in a square domain and considered with various inclinations.

Figure 3.10 shows the damage fields ω at an imposed displacement $\bar{u} = \bar{U}$ for two different inclusion inclinations, $\bar{\theta} = 0^\circ$ (left) and $\bar{\theta} = 45^\circ$ (right). The numerical predictions are in agreement with results obtained from experiments performed on epoxy matrices containing Cu-W laminates [38] or aluminum platelets [33], and PMMA matrices containing steel inclusions [37], showing that deformation localizes along narrow regions, i.e., shear bands, nucleating from the inclusion tips. More specifically, localization of deformation is symmetric, with two equivalent failure directions, under a symmetric setting (Fig. 3.10a), while failure shows a main direction when symmetry is lost (Fig. 3.10b). In the latter case, the shear band with the inclination most aligned with the inclusion axis is the most intense if compared to that along the conjugate direction.

Shear bands formation for a stiff inclusion inclined at the (elastic) neutral inclination $\bar{\theta} = \bar{\theta}_{\rm n} \approx 24.09^\circ$ (for the considered Poisson's ratio $\nu_{\rm b} = 0.2$) is analyzed in Figure 3.11, where the damage field is shown at three different stages of imposed displacements $\bar{u}_y = \{0.065, 0.085, 1\}\bar{U}$ (with increasing values from left to right). It is remarkable that although the inclusion inclination is such that stress singularities are not activated during the elastic response and therefore the mechanical fields are homogeneous (Fig. 3.11a), as soon as the yield stress is reached (due to the elastic neutrality, this occurs simultaneously at every point of the domain), the inelastic (and incrementally anisotropic) response induces a stress concentration at each inclusion tip (Fig. 3.11b) giving rise to the non-symmetric formation of shear bands (Fig. 3.11c).

3.4.2. A PAIR OF STIFF INCLUSIONS

Shear bands that originate from the interaction of two stiff inclusions of equal half-length $a \approx 0.077L$ and at different angles with respect to the horizontal axis are studied next. As shown in Fig. 3.12, each inclusion is centered within the two vertical halves of the square domain and their inclinations are considered through different combinations of the angles $\bar{\theta} = 90^\circ$ (i.e., parallel to the y axis), $\bar{\theta} = 0^\circ$ (i.e., parallel to the x axis), $\bar{\theta} = \bar{\theta}_{\rm n} \approx 24.09^\circ$ (i.e., inclined at the neutral inclination), and $\bar{\theta} = 50^\circ$. At variance with the rest of the analyses in this section, we have assumed $\bar{\sigma}_0/E_{\rm b} = 0.0003$.

The case with only one inclusion (not centered in specimen) is reported in panels d and f and taken as reference to discuss the interaction of the two-inclusion cases.

Panels g and i show the responses for the symmetric cases of two inclusions both parallel to the y and to the x axes, respectively. In both cases the shear bands in each vertical half domain closely resemble the corresponding shear bands in the vertical half domain of the reference panels d and f.

Panel e shows that when the two inclusions are arranged as the superposition of the fields related to the two single-inclusion cases reported in panels d and f, the resulting shear bands are very close to those obtained by combining the reference shear bands in the corresponding halves of panels d and f.

The case of an inclusion with inclination $\bar{\theta} = 50^\circ$ interacting with another parallel to the y axis or the x axis is reported in panels b and h, respectively. In both cases, a strong localized deformation arises at the inclined inclusion tips with an inclination $\theta_{\rm sb}^{(+)}$. The width of the bands is comparable to that of the bands arising from the inclusion parallel to y axis (panel b), but considerably wider than that of the inclusion parallel to the x axis (panel h).

Finally, panels a and c show that adding an inclusion inclined at the neutral inclination $\bar{\theta} = \bar{\theta}_{\rm n} \approx 24.09^\circ$ to the two single-inclusions reference configurations (panels d and f) does not qualitatively affect shear bands emergence, where however a perturbation is generated in the left-hand side of panel c. A visual comparison with the corresponding half in panel a (i.e., the right-hand side half domain) suggests that the inclusions at the neutral inclination have a reduced influence region compared to inclusions at a generic angle. This can be appreciated from panel a, where the shear bands nucleated from the vertical inclusion tips are not perturbed by the other inclusion unlike those nucleated from the tips of the horizontal inclusions that are closer to the inclusion at the neutral inclination (panel c).

A comparison of the reference shear bands (panels d and f) with the shear bands in

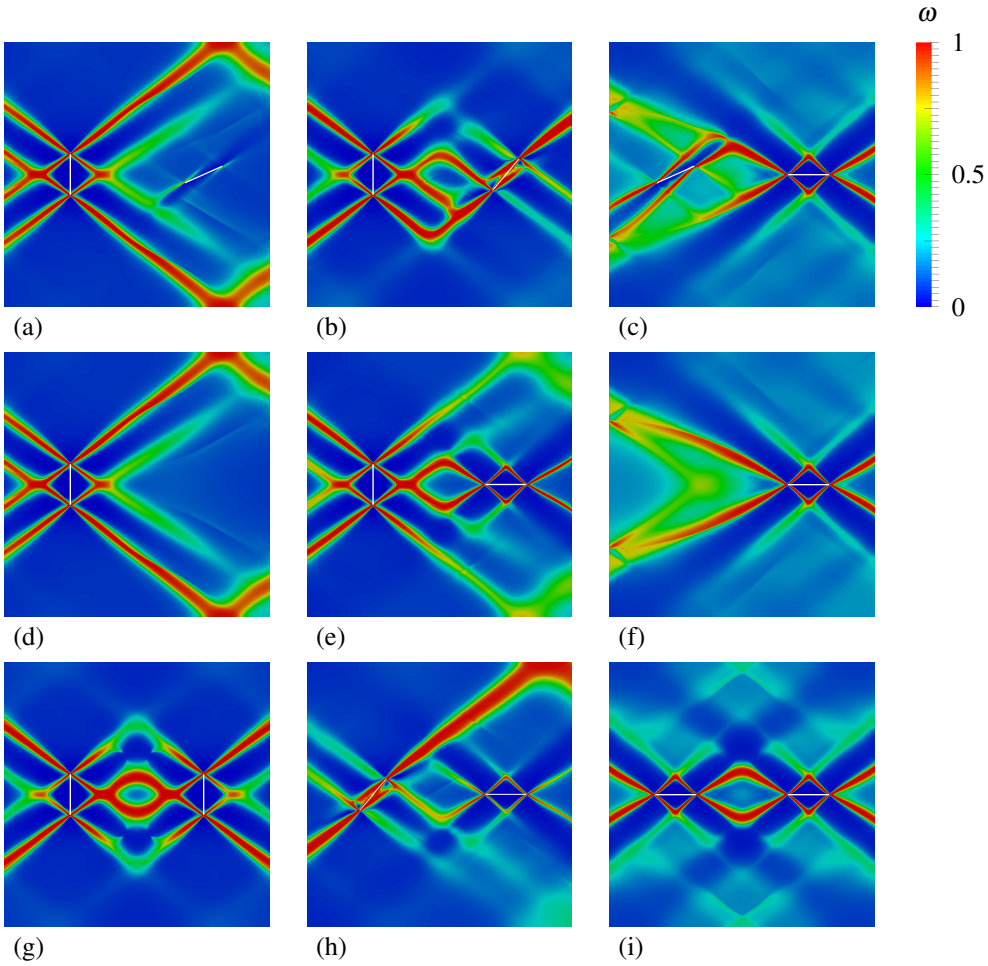

Figure 3.12: Shear bands originating from the interaction of two stiff inclusions at various inclinations: (a) vertical and neutral inclination ($\bar{\theta} = \bar{\theta}_{\mathrm{n}} \approx 24.09^{\circ}$), (b) vertical and oriented ($\bar{\theta} = 50^{\circ}$), (c) neutral ($\bar{\theta} = \bar{\theta}_{\mathrm{n}} \approx 24.09^{\circ}$) and horizontal, (e) vertical and horizontal, (g) both vertical, (h) oriented ($\bar{\theta} = 50^{\circ}$) and horizontal, (i) both horizontal. The shear bands originating from a single vertical (d) or horizontal (f) inclusion are taken as the reference fields.

panels b, e, g, h, and i seems to indicate that the influence area of each inclusion is roughly comparable in all these cases since the main characteristics of the shear bands around each inclusion is locally preserved, within the corresponding half domain, when another inclusion is added.

3.4.3. PERIODIC DISTRIBUTIONS OF STIFF INCLUSIONS

The shear band patterns that originate from periodic arrangements of stiff inclusions in a homogeneous matrix material are now investigated. To this end, the mixed boundary conditions employed in the previous analyses are replaced by their periodic counterpart described by [55], i.e., uniaxial tensile strain conditions in the vertical direction are prescribed by means of a constant macroscopic strain rate. Up to two families of inclusions can be present simultaneously in the square unit cell of size L: a single macro-inclusion of half-length $a_{\mathrm{M}} = 0.25L$ and a 10×10 array of micro-inclusions of half-length $a_{\mathrm{m}} = 0.025L$. Four inclusion inclinations are examined ($\bar{\theta} = \{0, 24.09, 50, 90\}^{\circ}$) and the corresponding shear bands are reported in Fig. 3.13, first row, for the macro-inclusion and in Fig. 3.13, second row, for the array of micro-inclusions (the latter is reported for an immediate visual comparison with the cases in the last two rows that are described later). Due to periodicity, the arrays of micro-inclusions generate damage patterns corresponding to the repetition of the shear bands around the macro-inclusion (scaled by a factor 0.1). As in the cases discussed earlier, the inclination of the stiff inclusion dramatically influences the shear band pattern, with symmetric networks involving both shear band inclinations $\theta_{\mathrm{sb}}^{(\pm)}$ in panels a ($\bar{\theta} = 0^{\circ}$) and d ($\bar{\theta} = 90^{\circ}$), while the other two inclinations in panels b and c generate non-symmetric networks, with localization mainly along inclination $\theta_{\mathrm{sb}}^{(+)}$ and a third further shear band inclination in panel c, close to that of the stiff inclusion.

The interaction between these two families of inclusions is illustrated by considering a macro-inclusion with $\bar{\theta}_{\mathrm{M}} = 0^{\circ}$ ($\bar{\theta}_{\mathrm{M}} = 90^{\circ}$) and an array of micro-inclusions with various inclinations, $\bar{\theta}_{\mathrm{m}} = \{0, 24.09, 50, 90\}^{\circ}$, and through the analysis of the corresponding damage fields reported in the third row (fourth row) of Fig. 3.13. These damage fields clearly show the strong mutual influence between the micro and macro inclusions. In particular, the array of micro-inclusions generates a fragmentation of the macro-pattern damage fields in a manner specific to each micro-inclusion inclination. This consideration does not hold for the micro-inclusions at the neutral inclination $\bar{\theta} = 24.09^{\circ}$, where the damage fields closely resemble those related to the macro-inclusion (cases $\bar{\theta} = 0^{\circ}$ and 90° in the first row). It also interesting to note that in all the considered cases the macro-inclusion shields the micro-inclusions inside the rhomboidal domain defined by the intersection of the shear bands nucleated from the macro-inclusion tips. In this domain damage is practically zero, with very low damage levels observed around the micro-inclusions close to the delimiting shear bands. Outside the shielded rhomboidal domain, the damage fields display micro-shear banding around the micro-inclusions (except for the neutral inclination case).

3.4.4. SHEAR BANDS NUCLEATED FROM AN IMPERFECTION AND THEIR INTERACTION WITH STIFF INCLUSIONS

Finally, we study how the shear bands nucleated from an imperfection interact with stiff inclusions. Within a square domain of size L, shear bands nucleate from an imperfection

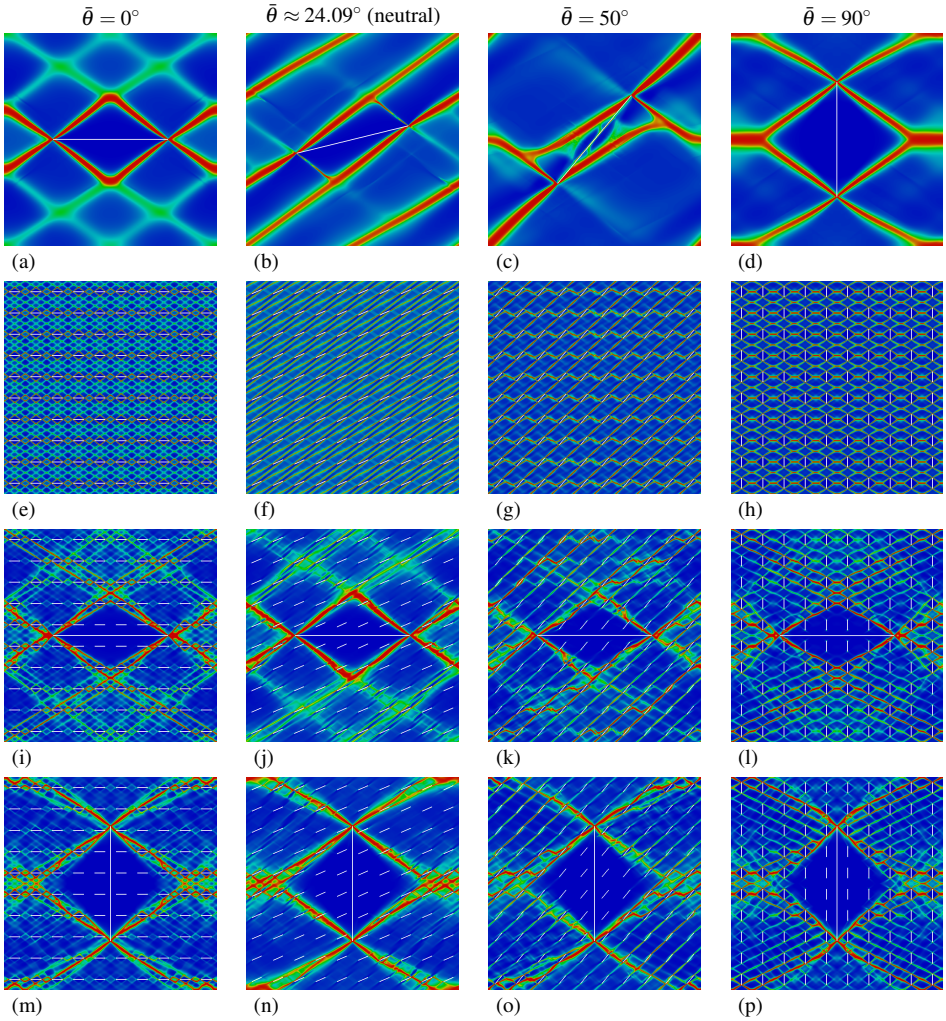

Figure 3.13: Shear bands nucleated at the tips of stiff inclusions periodically distributed in a square unit cell under periodic elongation along the vertical direction: one macro inclusion (first row), a 10×10 array of micro-inclusions (second row), a horizontal macro-inclusion and a 10×10 array of micro-inclusions (third row), and a vertical macro-inclusion and a 10×10 array of micro-inclusions (forth row). Four inclusion inclinations are considered: $\bar{\theta} = \{0, 24.09, 50, 90\}°$ in the first, second, third, and forth column, respectively. The color scale in this figure is the same as that in Fig. 3.12.

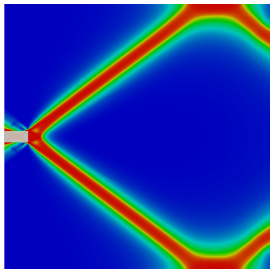

Figure 3.14: Shear bands nucleated from an imperfection symmetrically placed along the left-hand side boundary of the specimen. The color scale in this figure is the same as that in Fig. 3.12.

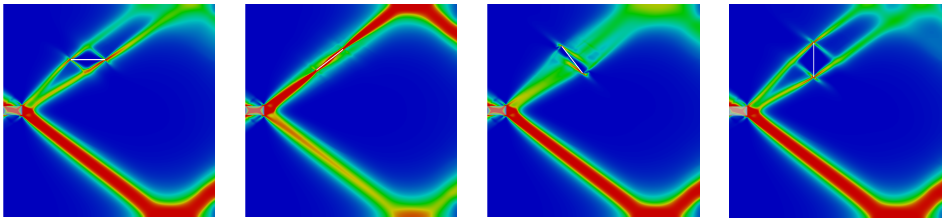

(a) (b) (c) (d)

Figure 3.15: Interaction of the shear bands nucleated from an imperfection with a stiff inclusion at varying inclinations. The color scale in this figure is the same as that in Fig. 3.12.

defined as a rectangular region ($0.0425L \times 0.0906L$) where the material is characterized by a reduction of 10% in the yield stress and of 90% in the Young's modulus with respect to bulk values. The rectangular imperfection is symmetrically placed along the left-hand side boundary of the specimen and, together with the boundary conditions and material properties described at the beginning of Section 3.4, generates a symmetric damage field that defines a set of reference shear bands (Fig. 3.14). The interaction of these shear bands with a small or a large number of stiff inclusions placed in the domain is analyzed in the following.

INTERACTION WITH ONE OR TWO STIFF INCLUSIONS

The change in the damage fields is investigated when one or two stiff inclusions, with varying inclination and length, are placed approximately in the middle of the reference shear bands.

Figure 3.15 shows the effect of a single inclusion of half-length $a = 0.08L$ at different inclinations ($\bar{\theta}^{[1]} = \{0, 37, -53, 90\}^\circ$ from panel a to d). The shear band fields in panels a, c, and d are characterized by a reduction of damage along the localization line crossing the inclusion and an increase of the damage along the other shear band direction, defining its thickening. Conversely, when the stiff inclusion is aligned with the localization line (panel b) the corresponding damage region remains almost unaltered, while the damage field in the other direction is almost completely deactivated.

The effect of two symmetric inclusions is shown in Fig. 3.16, where only the upper half of the specimen is shown because of symmetry. The two symmetrically-positioned

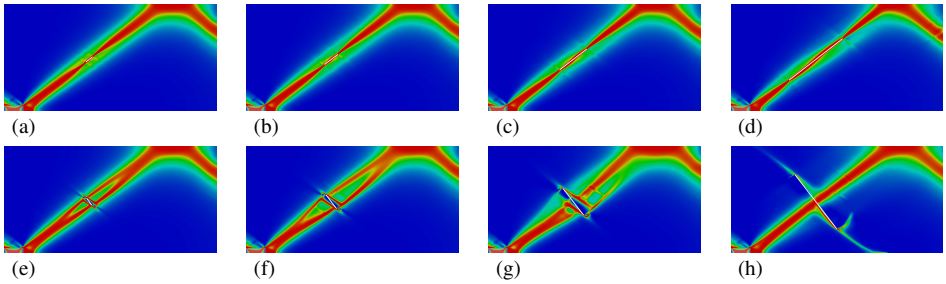

Figure 3.16: Interaction of the shear bands nucleated from an imperfection with two symmetric stiff inclusions of different lengths and at different inclinations. Due to symmetry, only the upper half of domain is reported. The color scale in this figure is the same as that in Fig. 3.12.

inclusions are inclined at $\bar{\theta}^{[1]} = -\bar{\theta}^{[2]} = 37°$ (panels a to d) and $\bar{\theta}^{[1]} = -\bar{\theta}^{[2]} = -53°$ (panels e to h), and have different half-lengths $a = \{0.02, 0.04, 0.08, 0.16\}L$ in panels a and e, b and f, c and g, d and h, respectively. As shown in the upper row of Fig. 3.16, an inclusion aligned to and embedded in a shear band causes only a modest reduction of the shear band thickness. Differently, stiff inclusions that are orthogonal to the unperturbed shear band direction (Fig. 3.14) and with size comparable to the unperturbed shear band thickness give rise to a splitting of the shear band in two smaller shear bands nucleating from the inclusion tips (panels e and f).

Non-symmetric cases for the imperfection interacting with a pair of stiff inclusions with varying lengths and inclinations are presented in Fig. 3.17. Two stiff inclusions with the same half-length, $a = \{0.02, 0.04, 0.08, 0.16\}L$, and inclination $\bar{\theta}^{[1]} = 37°$ and $\bar{\theta}^{[2]} = -53°$ are considered in panels a to-d. The inclusion aligned as the unperturbed shear band in the upper half slightly alter the damage field similarly to the corresponding symmetric case (panels a to d in Fig. 3.16). Conversely, the effect of the other inclusion in the lower half ranges from splitting the lower shear band into two smaller shear bands for $a = 0.02L$ in panel a, similar to the symmetric case in Fig. 3.14a, to the annihilation of the shear band for $a = 0.16L$ in panel d.

The lower half of Fig. 3.17 shows the case of two stiff inclusions of size $a = 0.08L$ for an inclination $\bar{\theta}^{[1]} = 37°$ for the inclusion in the upper half and with varying inclination ($\bar{\theta}^{[2]} = \{-37, 0, 37, 90\}°$ from panel e to h, respectively) for the inclusion in the lower half. As in the previous case, the shear band in the upper half of the specimen is basically unperturbed by the presence of the inclusion in the lower half (compare panels e to h in Fig. 3.17 with the mirror of the upper half in panel c of Fig. 3.16); the lower shear band is, however, almost annihilated by the presence of the lower inclusion, except for the inclusion at $\bar{\theta}^{[2]} = -37°$.

INTERACTION WITH A LARGE NUMBER OF STIFF INCLUSIONS

The failure mechanism of composites with a large number of stiff inclusions is investigated by considering five of the six distributions of 1500 stiff inclusions in Fig. 3.8 and a uniform distribution of 1500 stiff inclusion inclined at the neutral angle, all with the same half-length $a = 0.02L$. These distributions generate the reference (micro) shear bands fields in Fig. 3.18. The strong influence of the spatial arrangement of the inclusions is evident, with

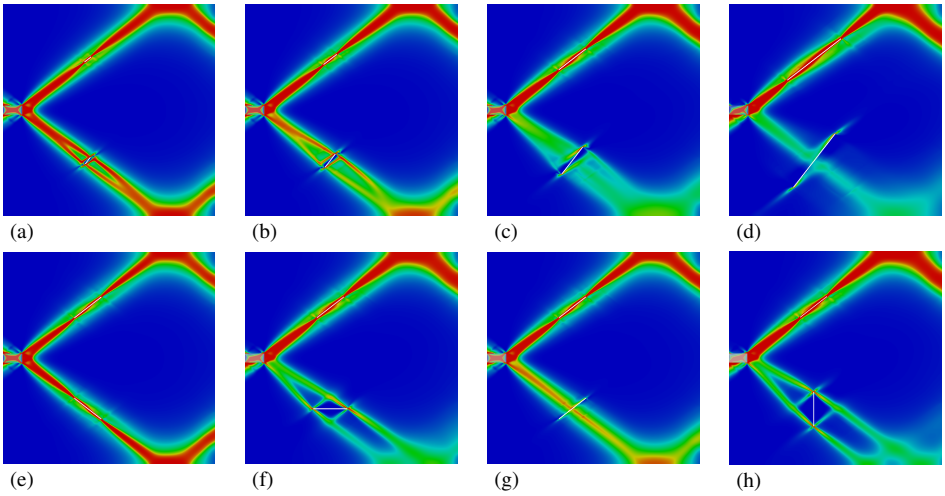

Figure 3.17: Interaction of the shear bands nucleated from an imperfection with two stiff inclusions with varying lengths and inclinations. The color scale in this figure is the same as that in Fig. 3.12.

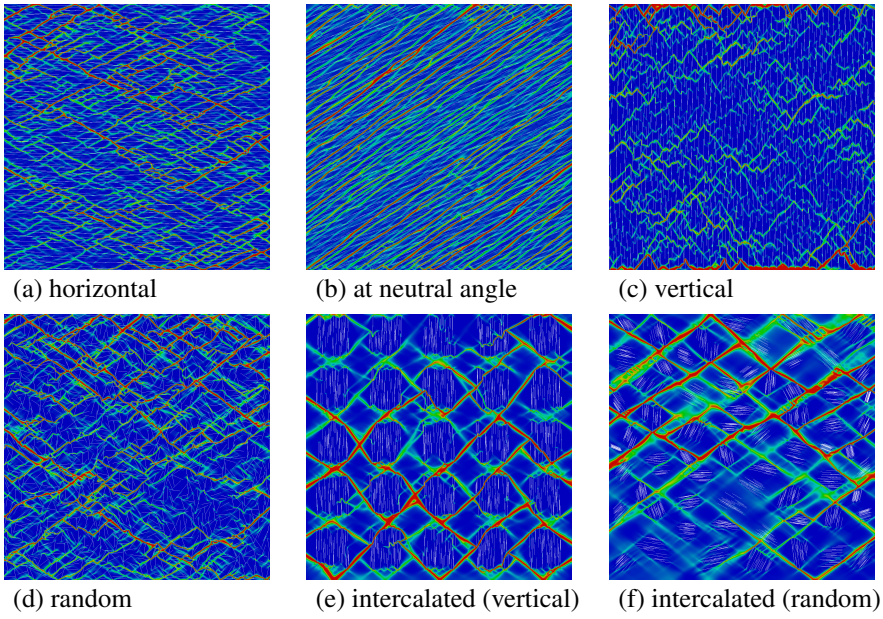

Figure 3.18: Shear bands nucleated from 1500 stiff inclusions at various inclinations and arrangements: uniformly distributed (a) horizontal (Fig. 3.8a), (b) inclined at neutral angle $\bar{\theta} \approx 24.09°$, (c) vertical (Fig. 3.8b), and (d) random (Fig. 3.8c) stiff inclusions; (e) vertically (Fig. 3.8d) and (f) randomly (Fig. 3.8f) intercalated stiff inclusions. The color scale in this figure is the same as that in Fig. 3.12.

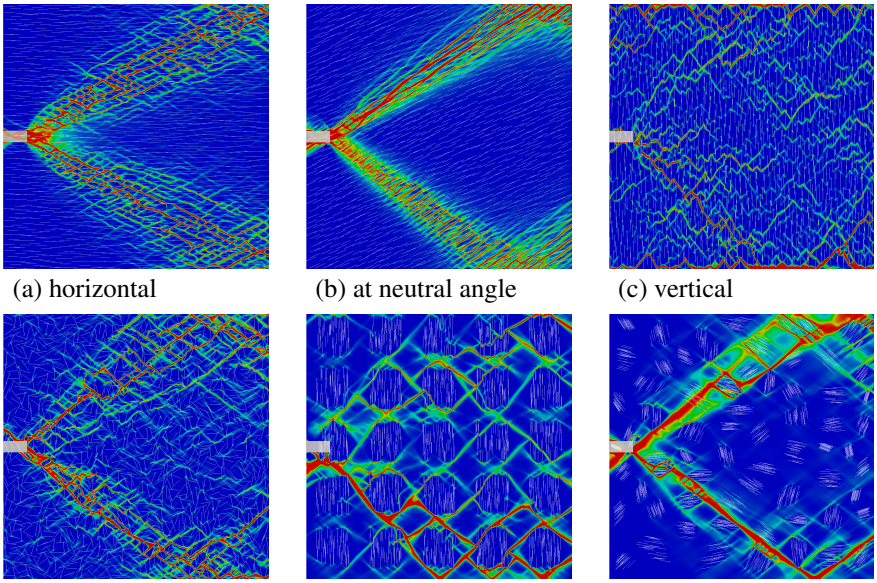

Figure 3.19: Interaction of the shear bands nucleated from 1500 stiff inclusions (Fig. 3.18) and an imperfection (Fig. 3.14). The color scale in this figure is the same as that in Fig. 3.12.

the generation of partially organized shear band patterns for all but the vertical distribution (panel c).

When the imperfection is also present in the specimen, the corresponding reference (macro) shear band pattern in Fig. 3.14 is fragmented to varying degree as shown in Fig. 3.19, from moderate (panels a, b) to severe (d, f), with cases of annihilation (panels c, e) recalling percolation patterns in highly anisotropic solids [56–58]). In all cases, inclusions and imperfections have a marked influence on the final shear band patterns. Even if the inclusions perturb the reference shear bands by fragmenting them, panels a, b, d, and f show that the influence regions of the reference shear bands are preserved. Fragmentation of the shear bands in the remaining two cases in panels c and e is very strong, with the final shear band fields that are very similar to the corresponding unperturbed fields in Fig. 3.18 in the central region defined by the macro shear bands. As a final remark, the neutral angle distribution in panel b appears to be the less disruptive for the development of the macro shear band, while the vertical distributions in panels c and e appear to be the most disruptive.

3.5. DISCUSSION

Embedded reinforcement methods are probably the most efficient approaches for the analysis of composites with planar or linear inclusions. The method adopted in this study, based on the formulation proposed by Balakrishnan and Murray [9], enables an accurate and computationally affordable analysis of composites with dense distributions of rigid line inclusions. Since the method describes each inclusion by means of an appropriate modi-

fication of the kinematic field description, interaction and orientation effects are properly accounted for in the prediction of the local stress fields. The description of each inclusion enables the analysis of multiple interacting rigid line inclusions embedded in a linear elastic or viscoplastic material irrespective of their multiplicity and relative position.

RLIs are almost always responsible for an effective elastic stiffening of the composite. The actual stiffening strongly depends on the inclusions' orientation and distribution patterns. As a limit case, the stiffening effect is null only in the particular case of parallel inclusions inclined at the neutral inclination with respect to uniform remote loading conditions. Nevertheless, even for this type of distribution, elastic stiffening is realized for loading along any other direction or because of the slight misalignment of even a single inclusion.

By endowing the matrix with a viscoplastic-damage behavior, the complex interplay between the shear bands generated by the presence of the inclusions is revealed. Indeed, through inelasticity, RLIs become sources of local instability by promoting the nucleation of localized shear bands emerging from the inclusion tips. However, RLIs can also be very effective means to hinder the formation of macro shear bands that would form from a macro-defect in the bulk material. Similarly to the stiffening of the elastic properties, this hindering property is strictly related to the inclusion orientation. Nevertheless, irrespective of the orientation, RLIs have always a disruptive effect, even when inclined at the neutral inclination, as shown in Fig. 3.11, because the concept of neutrality holds only for RLIs in elastic materials and loses its significance when inelasticity is considered.

REFERENCES

[1] W. J. Landis, *The strength of a calcified tissue depends in part on the molecular structure and organization of its constituent mineral crystals in their organic matrix,* Bone **16**, 533 (1995).

[2] Y. Kojima, A. Usuki, M. Kawasumi, A. Okada, Y. Fukushima, T. Kurauchi, and O. Kamigaito, *Mechanical properties of nylon 6-clay hybrid,* Journal of Materials Research **8**, 1185 (1993).

[3] S. Stankovich, D. A. Dikin, G. H. B. Dommett, K. M. Kohlhaas, E. J. Zimney, E. A. Stach, R. D. Piner, S. T. Nguyen, and R. S. Ruoff, *Graphene-based composite materials,* Nature **442**, 282 (2006).

[4] K. Hu, D. D. Kulkarni, I. Choi, and V. V. Tsukruk, *Graphene-polymer nanocomposites for structural and functional applications,* Progress in Polymer Science **39**, 1934 (2014).

[5] H. R. Lusti and A. A. Gusev, *Finite element predictions for the thermoelastic properties of nanotube reinforced polymers,* Modelling and Simulation in Materials Science and Engineering **12**, S107 (2004).

[6] N. Sheng, M. C. Boyce, D. M. Parks, G. C. Rutledge, J. I. Abes, and R. E. Cohen, *Multiscale micromechanical modeling of polymer/clay nanocomposites and the effective clay particle,* Polymer **45**, 487 (2004).

[7] S. E. Sanborn and J. H. Prévost, *Discrete modeling of crack bridging by a discontinuous platelet with a controlled interface,* International Journal of Solids and Structures **45**, 5059 (2008).

[8] O. C. Zienkiewicz, D. R. J. Owen, D. V. Phillips, and G. C. Nayak, *Finite element methods in the analysis of reactor vessels,* Nuclear Engineering and Design **20**, 507 (1972).

[9] S. Balakrishnan and D. W. Murray, *Finite element prediction of reinforced concrete behavior*, Structural Engineering Report No. 138 (Department of Civil Engineering, University of Alberta, Edmonton, Alberta, Canada, 1986).

[10] A. E. Elwi and T. M. Hrudey, *Finite element model for curved embedded reinforcement,* Journal of Engineering Mechanics **115**, 740 (1989).

[11] F. Barzegar and S. Maddipudi, *Three-dimensional modeling of concrete structures. II: Reinforced concrete,* Journal of Structural Engineering **123**, 1347 (1997).

[12] H. Hartl, *Development of a continuum-mechanics-based tool for 3D finite element analysis of reinforced concrete structures and application to problems of soil-structure interaction*, Ph.D. thesis, Graz University of Technology (2002).

[13] V. M. C. F. Cunha, J. A. O. Barros, and J. M. Sena-Cruz, *A finite element model with discrete embedded elements for fibre reinforced composites,* Computers & Structures **94–95**, 22 (2012).

[14] J. Zhang, J. Eisenträger, S. Duczek, and C. Song, *Discrete modeling of fiber reinforced composites using the scaled boundary finite element method,* Composite Structures **235**, 111744 (2020).

[15] J. E. Bolander and S. Saito, *Discrete modeling of short-fiber reinforcement in cementitious composites,* Advanced Cement Based Materials **6**, 76 (1997).

[16] J. Kozicki and J. Tejchman, *Effect of steel fibres on concrete behavior in 2D and 3D simulations using lattice model,* Archives of Mechanics **62**, 1 (2010).

[17] G. Cusatis, D. Pelessone, and A. Mencarelli, *Lattice Discrete Particle Model (LDPM) for failure behavior of concrete. I: Theory,* Cement and Concrete Composites **33**, 881 (2011).

[18] N. Nishimura and Y. J. Liu, *Thermal analysis of carbon-nanotube composites using a rigid-line inclusion model by the boundary integral equation method,* Computational Mechanics **35**, 1 (2004).

[19] J. Chatterjee, F. Ma, D. P. Henry, and P. K. Banerjee, *Advanced boundary element analysis of three-dimensional elastic solids with fiber reinforcements,* Journal of Engineering Mechanics **134**, 739 (2008).

[20] M. G. Pike, M. A. Hickman, and C. Oskay, *Interactions between multiple enrichments in extended finite element analysis of short fiber reinforced composites,* International Journal for Multiscale Computational Engineering **13** (2015).

[21] M. G. Pike and C. Oskay, *XFEM modeling of short microfiber reinforced composites with cohesive interfaces,* Finite Elements in Analysis and Design **106**, 16 (2015).

[22] F. K. F. Radtke, A. Simone, and L. J. Sluys, *A partition of unity finite element method for obtaining elastic properties of continua with embedded thin fibres,* International Journal for Numerical Methods in Engineering **84**, 708 (2010).

[23] F. Auricchio, G. Scalet, and P. Wriggers, *Fiber-reinforced materials: finite elements for the treatment of the inextensibility constraint,* Computational Mechanics **60**, 905 (2017).

[24] G. Alzetta and L. Heltai, *Multiscale modeling of fiber reinforced materials via non-matching immersed methods,* arXiv preprint arXiv:1906.03881 (2019).

[25] E. Barbieri and N. M. Pugno, *A computational model for large deformations of composites with a 2D soft matrix and 1D anticracks,* International Journal of Solids and Structures **77**, 1 (2015).

[26] A. Yaghoobi and M. G. Chorzepa, *Meshless modeling framework for fiber reinforced concrete structures,* Computers & Structures **161**, 43 (2015).

[27] Z. Y. Wang, H. T. Zhang, and Y. T. Chou, *Characteristics of the elastic field of a rigid line inhomogeneity,* Journal of Applied Mechanics **52**, 818 (1985).

[28] C. Atkinson, *Some ribbon-like inclusion problems,* International Journal of Engineering Science **11**, 243 (1973).

[29] Y. Z. Chen, *Singular behaviour at fixed rigid line tip in plane elasticity,* Engineering Fracture Mechanics **25**, 11 (1986).

[30] Y. Z. Chen, *Investigation of stress singularity coefficient for a finite plate containing rigid line,* Engineering Fracture Mechanics **40**, 17 (1991).

[31] F. Dal Corso, D. Bigoni, and M. Gei, *The stress concentration near a rigid line inclusion in a prestressed, elastic material. Part I: Full-field solution and asymptotics,* Journal of the Mechanics and Physics of Solids **56**, 815 (2008).

[32] G. Noselli, F. Dal Corso, and D. Bigoni, *The stress intensity near a stiffener disclosed by photoelasticity,* International Journal of Fracture **166**, 91 (2010).

[33] D. Bigoni, F. D. Corso, and M. Gei, *The stress concentration near a rigid line inclusion in a prestressed, elastic material. Part II: Implications on shear band nucleation, growth and energy release rate,* Journal of the Mechanics and Physics of Solids **56**, 839 (2008).

[34] D. Misseroni, F. Dal Corso, S. Shahzad, and D. Bigoni, *Stress concentration near stiff inclusions: Validation of rigid inclusion model and boundary layers by means of photoelasticity,* Engineering Fracture Mechanics **121**, 87 (2014).

[35] F. Dal Corso, S. Shahzad, and D. Bigoni, *Isotoxal star-shaped polygonal voids and rigid inclusions in nonuniform antiplane shear fields. Part I: Formulation and full-field solution,* International Journal of Solids and Structures **85**, 67 (2016).

[36] F. Dal Corso, S. Shahzad, and D. Bigoni, *Isotoxal star-shaped polygonal voids and rigid inclusions in nonuniform antiplane shear fields. Part II: Singularities, annihilation and invisibility,* International Journal of Solids and Structures **85**, 76 (2016).

[37] S. Misra and N. Mandal, *Localization of plastic zones in rocks around rigid inclusions: Insights from experimental and theoretical models,* Journal of Geophysical Research: Solid Earth **112** (2007).

[38] T. Özturk, W. J. Poole, and J. D. Embury, *The deformation of Cu-W laminates,* Materials Science and Engineering: A **148**, 175 (1991).

[39] F. Dal Corso and D. Bigoni, *The interactions between shear bands and rigid lamellar inclusions in a ductile metal matrix,* Proceedings of the Royal Society A: Mathematical, Physical and Engineering Sciences **465**, 143 (2009).

[40] M. Goudarzi and A. Simone, *Discrete inclusion models for reinforced composites: Comparative performance analysis and modeling challenges,* Computer Methods in Applied Mechanics and Engineering **355**, 535 (2019).

[41] A. Simone and L. J. Sluys, *The use of displacement discontinuities in a rate-dependent medium,* Computer Methods in Applied Mechanics and Engineering **193**, 3015 (2004).

[42] J. W. Ju, *On energy-based coupled elastoplastic damage theories: Constitutive modeling and computational aspects,* International Journal of Solids and Structures **25**, 803 (1989).

[43] C. Atkinson and R. V. Craster, *Theoretical aspects of fracture mechanics,* Progress in Aerospace Sciences **31**, 1 (1995).

[44] G. P. Cherepanov, *The propagation of cracks in a continuous medium,* Journal of Applied Mathematics and Mechanics **31**, 503 (1967).

[45] J. R. Rice, *A path independent integral and the approximate analysis of strain concentration by notches and cracks,* Journal of Applied Mechanics **35**, 379 (1968).

[46] J. C. Halpin, *Effects of Environmental Factors on Composite Materials.*, Tech. Rep. (AFML-TR 67-423, 1969).

[47] P. Pingle, J. Sherwood, and L. Gorbatikh, *Properties of rigid-line inclusions as building blocks of naturally occurring composites,* Composites Science and Technology **68**, 2267 (2008).

[48] L. Ni and S. Nemat-Nasser, *A general duality principle in elasticity,* Mechanics of Materials **24**, 87 (1996).

[49] P. S. Pingle, L. Gorbatikh, and J. A. Sherwood, *Analysis of multiple rigid-line inclusions for application to bio-materials,* in *Proceedings of IMECE2007, ASME International Mechanical Engineering Congress and Exposition, Seattle, Washington, USA* (2007) pp. 801–807.

[50] L. J. Hall, V. R. Coluci, D. S. Galvão, M. E. Kozlov, M. Zhang, S. O. Dantas, and R. H. Baughman, *Sign change of Poisson's ratio for carbon nanotube sheets,* Science **320**, 504 (2008).

[51] P. M. Suquet, *Elements of homogenization for inelastic solid mechanics,* in *Homogenization Techniques for Composite Media*, Vol. 272, edited by E. Sanchez-Palencia and A. Zaoui (Springer-Verlag, 1985) pp. 193–278.

[52] B. Liu, L. Zhang, and H. Gao, *Poisson ratio can play a crucial role in mechanical properties of biocomposites,* Mechanics of Materials **38**, 1128 (2006).

[53] J. Liu, W.-J. Boo, A. Clearfield, and H.-J. Sue, *Intercalation and exfoliation: A review on morphology of polymer nanocomposites reinforced by inorganic layer structures,* Materials and Manufacturing Processes **21**, 143 (2006).

[54] O. Pierard, C. Friebel, and I. Doghri, *Mean-field homogenization of multi-phase thermo-elastic composites: A general framework and its validation,* Composites Science and Technology **64**, 1587 (2004).

[55] O. Van der Sluis, P. J. G. Schreurs, W. A. M. Brekelmans, and H. E. H. Meijer, *Overall behaviour of heterogeneous elastoviscoplastic materials: effect of microstructural modelling,* Mechanics of Materials **32**, 449 (2000).

[56] D. Bigoni and G. Noselli, *Localized stress percolation through dry masonry walls. Part I–Experiments,* European Journal of Mechanics-A/Solids **29**, 291 (2010).

[57] D. Bigoni and G. Noselli, *Localized stress percolation through dry masonry walls. Part II–Modelling,* European Journal of Mechanics-A/Solids **29**, 299 (2010).

[58] P. A. Gourgiotis and D. Bigoni, *Stress channelling in extreme couple-stress materials Part II: Localized folding vs faulting of a continuum in single and cross geometries,* Journal of the Mechanics and Physics of Solids **88**, 169 (2016).

4

FIBER NEUTRALITY IN FIBER-REINFORCED COMPOSITES

We report numerical evidence for neutrality of thin fibers to a prescribed uniform stress field in a fiber-reinforced composite. Elastic finite element analyses of fiber-reinforced composites are carried out with a conventional fully-resolved model and a novel dimensionally-reduced fiber model. The two modeling approaches are compared in the analysis of mechanical properties and matrix-fiber slip profiles. An analysis of the effectiveness of various fiber orientations with respect to the loading direction shows that the notion of inclusion neutrality, originally formulated for rigid line inclusions by Wang et al. [*Journal of Applied Mechanics*, 52(4), 814–822, 1985], holds also for linear elastic thin fibers with imperfect interface.

4.1. INTRODUCTION

Apart from fiber shape, surface treatment, and volume fraction, fiber spatial orientation is an important characteristic controlling load-transmission mechanisms in fiber-reinforced composites [1]. Although the effect of fiber orientation can be accurately assessed by means of computational homogenization techniques [2–6], the generation of a conformal finite element mesh for composites with thin fibers is a tedious and time-consuming task. Embedded reinforcement techniques, in which fiber discretization is independent from the discretization of the composite domain, can be effectively used for this class of problems. Here we assess the validity of a novel embedded formulation and employ it to show inherent characteristics of composites reinforced with thin fibers.

Generally speaking, two classes of methods are available for the micro-mechanical study of fiber-reinforced composites: mean-field and direct numerical methods. Although

Reprinted from: M. Goudarzi and A. Simone, Fiber neutrality in fiber-reinforced composites: Evidence from a computational study, *International Journal of Solids and Structures*, 156:14–28, 2019.

mean-field methods such as Eshelby-based two-step homogenization schemes [7, 8] are fast and cost-effective, finite element (FE) averaging methods have gained popularity for their accurate geometrical representation of the composite micro-structure. A serious drawback of classical FE-based homogenization is the conformal mesh generation process for composites with many fibers. When the number of fibers is relatively low, the composite can still be discretized using classical conformal approaches as shown by Lusti and Gusev [6] and Tian *et al.* [8]: in Lusti and Gusev [6, Figure 1] the discretization for a composite with 350 nanotubes of aspect ratio 200 at a volume fraction of 0.5% consists of 3.5×10^6 nodes tessellated into 21×10^6 tetrahedral elements; in [8], the authors show that they can generate a discretization for a composite fiber volume fractions up to 20% considering 600 fibers (using therefore fibers with a relatively large diameter). Obviously, the study of composites with thousands or tens of thousands of fibers with volume fractions around 20% (typical of nanocomposites [9]) would be unfeasible with conformal approaches. Advanced discretization approaches such as embedded reinforcement methods [10–15] facilitate the discretization of high aspect ratio fibers by allowing their mesh-independent representation. In the literature, these methods have been applied to curved inclusions [11], sliding fibers [12, 13, 15], and to describe the interaction between pile foundations and the surrounding soil [14]. In the simulation in Section 4.5 we have used up to around 22000 fibers with relatively coarse discretizations.

To lift the conformal meshing requirements of standard FE methods, two key assumptions are made in embedded formulations: i) high aspect ratio fibers are described as one-dimensional bar or beam elements; and ii) the fiber kinematics is introduced by means of a displacement gap between matrix and fiber while preserving the continuity of the underlying matrix displacement field across the fiber. Relaxing the second assumption in an embedded formulation requires the use of special enriched approximations [16] that would significantly reduce the cost-effectiveness of the method and increase its complexity. For the analysis of composites with many fibers we prefer to adopt the most convenient approach from the computational point of view. In Section 4.2 we therefore propose a novel embedded reinforced technique, which is compared to a fully-resolved three-dimensional fiber-reinforced model in Section 4.3. The numerical formulation proposed in this chapter is superior to existing embedded reinforcement models in that it uses totally independent finite element meshes for fiber and matrix. This will eliminate the need for calculating intersections between fiber and matrix elements, which may require complex algorithms especially for curved fibers [17]. Even if the computational setup is very simple, the one-to-one comparison between a fully-resolved and a dimensionally-reduced fiber model allows us to assess the accuracy of the dimensionally-reduced model in terms of global (homogenized effective stiffness) and local (matrix-fiber slip profiles) quantities. To the author's knowledge, this type of comparison has not been reported in previous studies and validates the use of dimensionally-reduced models for fibers with sufficiently small diameters.

Numerical homogenization studies of fiber orientation effects [1, 8, 18] show that the composite stiffness is very sensitive to fiber misalignments. In a numerical study, Tian *et al.* [8, Figure 7b] showed that the effective Young's modulus along the loading direction in a carbon fiber composite decreases rather quickly when the fibers are misaligned with respect to the loading direction and reaches its minimum value, with a decrease of $\approx 25\%$ from its maximum, when the fibers are inclined at 60° to the loading direction. Although the authors

did not establish a correlation between elastic properties and geometrical properties such as fiber orientation and diameter, their results can be related, mutatis mutandis, to those obtained for zero-thickness rigid inclusions (or rigid line inclusions, RLIs) problems [19]. In RLI problems, the solution fields show a strong dependence on the inclusion orientation and matrix Poisson's contraction effects, with the limit case of the inclusion being neutral (this, e.g., means that the stress field is not perturbed for certain inclusion orientations). In the literature, inclusion neutrality has been demonstrated only for perfectly bonded RLIs and for in-plane states in experiments [20], theoretical studies [19, 21], and simulations [22]. In this contribution we demonstrate for the first time the validity of the concept of inclusion neutrality for high aspect ratio fibers in a three-dimensional volume. In Section 4.4, we show various forms of inclusion neutrality in a fiber-reinforced composite with linear elastic thin fibers with perfect and imperfect matrix-fiber interface using fully-resolved and dimensionally-reduced fiber models. Results are reported in terms of Young's moduli, shear moduli and Poisson's ratios. To demonstrate the applicability of the dimensionally-reduced model to composites with many fibers, Section 4.5 reports a detailed micro-mechanical study. Results, including some observations on fiber neutrality with respect to the effective Poisson's ratio of the composite, are compared with rule-of-mixtures predictions, while the limitations of the latter are pointed out.

4.2. METHOD

4.2.1. WEAK FORM OF THE GOVERNING EQUATIONS

With reference to the principle of virtual work for a small displacement elastostatics problem, the weak form of the governing equations for a fiber-reinforced composite without body forces is

$$\int_{\Omega_\mathrm{m}} \boldsymbol{\sigma}_\mathrm{m} : \nabla^\mathrm{s} \delta \boldsymbol{u}_\mathrm{m} \, \mathrm{d}\Omega_\mathrm{m} + \int_{\Omega_\mathrm{f}} \boldsymbol{\sigma}_\mathrm{f} : \nabla^\mathrm{s} \delta \boldsymbol{u}_\mathrm{f} \, \mathrm{d}\Omega_\mathrm{f} + \int_{\Gamma_\mathrm{int}} \boldsymbol{t}_\mathrm{c} \cdot \delta \boldsymbol{w} \, \mathrm{d}\Gamma_\mathrm{int} - \int_{\Gamma_\mathrm{t}} \bar{\boldsymbol{t}} \cdot \delta \boldsymbol{u}_\mathrm{m} \, \mathrm{d}\Gamma_\mathrm{t} = 0, \tag{4.1}$$

where ∇^s is the symmetric-gradient operator, and the integral over the total volume $\Omega = \Omega_\mathrm{m} \cup \Omega_\mathrm{f}$ is subdivided into matrix and fiber contributions. The virtual displacement vectors $\delta \boldsymbol{u}_\mathrm{m}$ and $\delta \boldsymbol{u}_\mathrm{f}$ and the corresponding stress tensors $\boldsymbol{\sigma}_\mathrm{m}$ and $\boldsymbol{\sigma}_\mathrm{f}$ are defined over matrix (m) and fiber (f) regions. The contribution along the matrix-fiber interface Γ_int represents the virtual mechanical work done by the interface tractions $\boldsymbol{t}_\mathrm{c}$ for the local virtual opening (sliding) vector $\delta \boldsymbol{w}$ across (between) the two sides of the interface. The interface integral is evaluated over the interface surface Γ_int of the embedded fibers and, for convenience, is expressed in a coordinate system local to each fiber. The last term in (4.1) is the work done by the external tractions $\bar{\boldsymbol{t}}$ over the external surface Γ_t.

4.2.2. DISCRETIZED WEAK FORM

In the context of the finite element method, the domain Ω is discretized into matrix and fiber finite elements, each with its own set of degrees of freedom. To introduce fiber and matrix-fiber interface contributions (second and third terms in (4.1)), reference is made to two fiber discretizations: a conformal approach and a mesh-independent approach. While the approximation of the fiber displacement vector $\boldsymbol{u}_\mathrm{f}$ and the opening/sliding vector $\boldsymbol{w}$, later referred to as the interface gap vector, is specific to each scheme, the final discretized

form of the governing equations is very similar for both techniques. Next, the discretization of matrix, fiber, and matrix-fiber interface is discussed in detail.

MATRIX

The matrix displacement field $\boldsymbol{u}_\mathrm{m}$ is approximated at the element level as

$$\boldsymbol{u}_\mathrm{m}(\boldsymbol{x}) \approx \boldsymbol{u}_\mathrm{m}^h(\boldsymbol{x}) = \sum_{i=1}^{n} N_i(\boldsymbol{x})\,\boldsymbol{u}_i = \boldsymbol{N}_\mathrm{u}\boldsymbol{d}, \tag{4.2}$$

where $N_i(\boldsymbol{x})$ and $\boldsymbol{u}_i$ are the standard Lagrange shape function and displacement vectors defined at node i, respectively, the number of nodes in an element is n, the matrix $\boldsymbol{N}_\mathrm{u}$ contains elemental shape functions, and $\boldsymbol{d}$ is the nodal displacement vector. Stiffness matrix

$$\boldsymbol{K}_\mathrm{m}^e = \int_{\Omega_\mathrm{m}^e} \boldsymbol{B}_\mathrm{u}^\mathrm{T}\boldsymbol{D}_\mathrm{m}\boldsymbol{B}_\mathrm{u}\,\mathrm{d}\Omega_\mathrm{m} \tag{4.3}$$

and external force vector

$$\boldsymbol{f}_\mathrm{ext}^e = \int_{\Gamma_\mathrm{t}^e} \boldsymbol{N}_u^\mathrm{T}\bar{\boldsymbol{t}}\,\mathrm{d}\Gamma, \tag{4.4}$$

with $\boldsymbol{D}_\mathrm{m}$ the matrix of elastic constants and $\boldsymbol{B}_\mathrm{u}$ the matrix of shape function derivatives, are obtained following standard procedures applied to the first and last terms in (4.1).

SOLID FIBER MODEL

A reference computational model is developed by meshing the exact geometry of the fiber in Ω_f with solid-type elements and by using a conformal discretization at the matrix-fiber interface. Although highly accurate, this approach requires the construction of a conformal discretization, a tedious operation for many practical problems. Here, both matrix and fiber regions are discretized using conventional non-structured linear tetrahedral elements as shown in Figure 4.1a for an inclined cylindrical fiber.

Using the counterpart of (4.2) for the fiber displacement field, the stiffness contribution related to the second term in (4.1) is

$$\boldsymbol{K}_\mathrm{f}^e = \int_{\Omega_\mathrm{f}^e} \boldsymbol{B}_\mathrm{u}^\mathrm{T}\boldsymbol{D}_\mathrm{f}\boldsymbol{B}_\mathrm{u}\,\mathrm{d}\Omega_\mathrm{f}, \tag{4.5}$$

where $\boldsymbol{D}_\mathrm{f}$ is the matrix of elastic constants of the fiber material.

To discretize the interface gap vector $\boldsymbol{w}$, zero-thickness conformal interface elements are included between matrix and fiber. This requires finding all matrix elements sharing at least one node with fiber elements (shaded in red in Figure 4.1a); shared nodes are then duplicated and zero-thickness interface elements are embedded between matrix and fiber as depicted in Figure 4.1b. The discretized interface gap vector,

$$\boldsymbol{w}^h = \boldsymbol{R}\boldsymbol{N}_\mathrm{int}\,\boldsymbol{d}_\mathrm{int}, \tag{4.6}$$

is expressed in a coordinate system local to the interface. Without loss of generality and by making reference to the node numbering in Figure 4.1b, this is achieved by defining

the rotation matrix $\boldsymbol{R}$ from the global to the local coordinate system, the interface shape functions matrix

$$\boldsymbol{N}_{\text{int}} = \left[\boldsymbol{N}^{\text{f}}_{\text{int}} \;\middle|\; \boldsymbol{N}^{\text{m}}_{\text{int}}\right] = \left[\, N_1\boldsymbol{I} \quad N_2\boldsymbol{I} \quad N_3\boldsymbol{I} \;\middle|\; -N_4\boldsymbol{I} \quad -N_5\boldsymbol{I} \quad -N_6\boldsymbol{I}\right] \tag{4.7}$$

expressed in terms of isoparametric coordinates for the zero-thickness interface element, and the interface nodal displacement vector

$$\boldsymbol{d}_{\text{int}} = \left[\boldsymbol{u}_{\text{f1}} \quad \boldsymbol{u}_{\text{f2}} \quad \boldsymbol{u}_{\text{f3}} \;\middle|\; \boldsymbol{u}_{\text{m4}} \quad \boldsymbol{u}_{\text{m5}} \quad \boldsymbol{u}_{\text{m6}}\right]^{\text{T}}, \tag{4.8}$$

where $\boldsymbol{I}$ is the identity matrix of size three, and $\boldsymbol{u}_{\text{f}i\,(i=1,2,3)}$ and $\boldsymbol{u}_{\text{m}i\,(i=4,5,6)}$ indicate the displacement vectors for fiber and matrix, respectively, in the global coordinate system.

Following standard procedures, the interface stiffness contribution

$$\boldsymbol{K}^{e}_{\text{int}} = \int_{\Gamma_{\text{int}}} \boldsymbol{N}^{\text{T}}_{\text{int}} \boldsymbol{R}^{\text{T}} \boldsymbol{D}_{\text{b}} \boldsymbol{R} \boldsymbol{N}_{\text{int}} \, \text{d}\Gamma_{\text{int}} \tag{4.9}$$

is obtained on substituting (4.6) into the third term in (4.1) and with the interface constitutive matrix $\boldsymbol{D}_{\text{b}} = \frac{\partial \boldsymbol{t}_{\text{c}}}{\partial \boldsymbol{w}} = \text{diag}\left(K_{\text{bt}}, K_{\text{bn1}}, K_{\text{bn2}}\right)$ for a linear elastic interface. The constants K_{bn1} and K_{bn2} represent the stiffnesses of the interface in the direction normal to the interface surface and perpendicular to it and to the fiber axis, respectively, and K_{bt} represents the stiffness of the interface in the direction tangential to the fiber axis. In this work, we only allow fiber slip in the direction tangential to the fiber axis by constraining the normal displacement gaps by means of penalty augmentation of the interface stiffnesses K_{bn1} and K_{bn2}. Additionally, interface elements are not introduced at the fiber endpoints where we assume no adhesion between fiber and matrix.

Expansion of the interface stiffness contribution (4.9), considering that the interface gap vector (4.6) is a function of both matrix and fiber displacements, results in

$$\boldsymbol{K}^{e}_{\text{int}} = \begin{bmatrix} \boldsymbol{K}^{\text{mm}}_{\text{int}} & \boldsymbol{K}^{\text{mf}}_{\text{int}} \\ \boldsymbol{K}^{\text{fm}}_{\text{int}} & \boldsymbol{K}^{\text{ff}}_{\text{int}} \end{bmatrix} = \begin{bmatrix} \int_{\Gamma_{\text{int}}} \boldsymbol{N}^{\text{m}\,\text{T}}_{\text{int}} \boldsymbol{R}^{\text{T}} \boldsymbol{D}_{\text{b}} \boldsymbol{R} \boldsymbol{N}^{\text{m}}_{\text{int}} \, \text{d}\Gamma_{\text{int}} & \int_{\Gamma_{\text{int}}} \boldsymbol{N}^{\text{m}\,\text{T}}_{\text{int}} \boldsymbol{R}^{\text{T}} \boldsymbol{D}_{\text{b}} \boldsymbol{R} \boldsymbol{N}^{\text{f}}_{\text{int}} \, \text{d}\Gamma_{\text{int}} \\ \int_{\Gamma_{\text{int}}} \boldsymbol{N}^{\text{f}\,\text{T}}_{\text{int}} \boldsymbol{R}^{\text{T}} \boldsymbol{D}_{\text{b}} \boldsymbol{R} \boldsymbol{N}^{\text{m}}_{\text{int}} \, \text{d}\Gamma_{\text{int}} & \int_{\Gamma_{\text{int}}} \boldsymbol{N}^{\text{f}\,\text{T}}_{\text{int}} \boldsymbol{R}^{\text{T}} \boldsymbol{D}_{\text{b}} \boldsymbol{R} \boldsymbol{N}^{\text{f}}_{\text{int}} \, \text{d}\Gamma_{\text{int}} \end{bmatrix}. \tag{4.10}$$

DIMENSIONALLY-REDUCED FIBER MODEL

When modeling high aspect ratio fibers, the conforming finite element model described in the previous section can be replaced by a mesh-independent dimensionally-reduced model with a drastic reduction of the computational cost.

In the proposed model, inspired by embedded reinforcement techniques [10, 11, 13], fibers are idealized as one-dimensional objects that respond to axial deformation only. This is a reasonable assumption when dealing with high aspect ratio fibers. A fiber discretization independent from the matrix discretization and consisting of linear one-dimensional Lagrange elements is used to represent embedded fibers. Figure 4.2 shows the case of a single embedded fiber although there are no limitations on the number of fibers that can cross a matrix element. Worth noticing is the independence of the two discretizations: fiber nodes do not coincide with intersection points between fiber axis and element faces. While any structured or unstructured fiber discretization can be used, in the numerical simulations in this chapter fiber nodes are uniformly distributed for convenience.

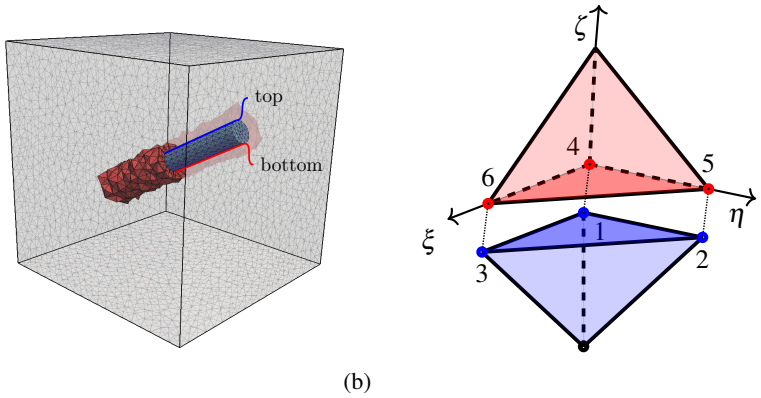

(a) (b)

Figure 4.1: (a) Reference conformal finite element model with a cylindrical fiber that is discretized using tetrahedral finite elements. (b) Zero-thickness conformal interface elements are placed between fiber (blue region) and surrounding matrix (red region) to allow fiber slip. It is assumed that no adhesion exists between the endpoints of the fiber and the matrix.

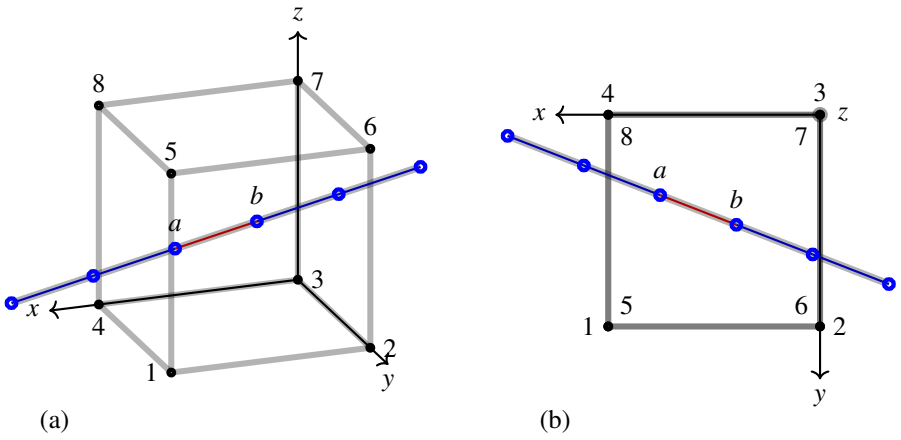

(a) (b)

Figure 4.2: A dimensionally-reduced fiber intersects a solid matrix element: (a) three-dimensional view, (b) top view. The fiber can be placed within the solid element region and can be discretized independently from it. Discretized fiber elements are shown in blue, separated by nodes. The figure shows also a fiber element, in red, between nodes *a* and *b*.

To simplify the generation of the stiffness matrix for elements that are intersected by one-dimensional fibers, stiffness matrix (4.3), with the integration performed over the total volume Ω^{e} of the element, is used for the matrix contribution. This however requires the use of an effective Young's modulus for the fibers to cancel out the already considered matrix contribution in the fiber region. The contribution of the kth fiber element (with endpoints a and b for the red fiber element in Figure 4.2) is identical to the stiffness matrix of a one-dimensional standard truss element in three-dimensional space and is written as

$$\boldsymbol{K}_{\mathrm{f}}^{k} = \frac{(E_{\mathrm{f}}^{k} - E_{\mathrm{m}})\, A^{k}}{L^{k}} \begin{bmatrix} \boldsymbol{T}^{k} & -\boldsymbol{T}^{k} \\ -\boldsymbol{T}^{k} & \boldsymbol{T}^{k} \end{bmatrix}, \tag{4.11}$$

where E_{m} and E_{f}^{k} are the matrix and fiber Young's moduli, respectively, A^{k} is the cross sectional area ($A^{k} = \pi d_{\mathrm{f}}^{2}/4$ with d_{f} the fiber diameter), and L^{k} is the fiber element length. The fiber orientation matrix

$$\boldsymbol{T}^{k} = \begin{bmatrix} e_x^k e_x^k & e_x^k e_y^k & e_x^k e_z^k \\ e_x^k e_y^k & e_y^k e_y^k & e_y^k e_z^k \\ e_x^k e_z^k & e_y^k e_z^k & e_z^k e_z^k \end{bmatrix} \tag{4.12}$$

with

$$e_x^k = \frac{x_b^k - x_a^k}{L^k} \;\;,\;\; e_y^k = \frac{y_b^k - y_a^k}{L^k} \;\;,\;\; e_z^k = \frac{z_b^k - z_a^k}{L^k}, \tag{4.13}$$

where (x_a, y_a, z_a) and (x_b, y_b, z_b) indicate the coordinates of the fiber element ends (e.g., nodes a and b for the red fiber element in Figure 4.2).

Consequently, the matrix-fiber interface is reduced to an equivalent line object, with interface gap vector (4.6) and stiffness matrix contribution (4.9) evaluated along it. The interface gap vector (4.6) is defined with

$$\boldsymbol{N}_{\mathrm{int}} = \left[\boldsymbol{N}_{\mathrm{int}}^{\mathrm{f}} \;\middle|\; \boldsymbol{N}_{\mathrm{int}}^{\mathrm{m}} \right] = \left[\begin{array}{cc|ccc} N_a^{\mathrm{f}} \boldsymbol{I} & N_b^{\mathrm{f}} \boldsymbol{I} & -N_1^{\mathrm{m}} \boldsymbol{I} & \cdots & -N_n^{\mathrm{m}} \boldsymbol{I} \end{array} \right] \tag{4.14}$$

and

$$\boldsymbol{d}_{\mathrm{int}} = \left[\begin{array}{cc|ccc} \boldsymbol{u}_a^{\mathrm{f}} & \boldsymbol{u}_b^{\mathrm{f}} & \boldsymbol{u}_1^{\mathrm{m}} & \cdots & \boldsymbol{u}_n^{\mathrm{m}} \end{array} \right]^{\mathrm{T}}, \tag{4.15}$$

where N_a^{f} and N_b^{f} are the one-dimensional Lagrange shape functions at nodes a and b defined in an isoparametric coordinate system local to the fiber, and the shape function N_i^{m} at node i of the parent matrix element is also defined in an isoparametric coordinate system.

In a small deformation setting, the interface gap vector is evaluated in the undeformed configuration at integration points within fiber elements (e.g., at a and b for the red fiber element in Figure 4.2 since we consider a two-point Gauss-Lobatto quadrature scheme). This implies that once the local coordinates of an integration point along a fiber element are defined, they are expressed into the global coordinate system and used to identify its parent matrix element by means of an octree structure [23, Section 9.1] that is constructed prior to the analysis.

The fiber shape function in (4.14) are directly evaluated at the integration point in an isoparametric coordinate system local to the fiber. The shape function of the matrix element

are also evaluated at the same point now expressed in the isoparametric coordinate system related to the matrix element and obtained through an inverse mapping procedure starting from its position in the global coordinate system. Matrix and fiber elements are connected through so-called bond elements that are defined with reference to the two fiber element nodes and the nodes of the matrix element in which the fiber element nodes are located (the discretization is therefore conforming on the side of the fiber and not conforming on the side of the matrix, and a fiber element can have nodes in two distinct matrix elements).

The interface contribution (4.9) related to the kth fiber element becomes

$$\boldsymbol{K}_{\text{int}}^{k} = C_{\text{f}}^{k} \int_{L^k} \boldsymbol{N}_{\text{int}}^{\text{T}} \boldsymbol{R}^{\text{T}} \boldsymbol{D}_{\text{b}} \boldsymbol{R} \boldsymbol{N}_{\text{int}} \, \text{d}s, \tag{4.16}$$

with $C_{\text{f}}^{k} = \pi d_{\text{f}}$ the circumference of the fiber, L^k the length of fiber-matrix bond element, and s the local coordinate along the bond element. Thus, for a system with n_{f} fibers each subdivided into n_{s} line elements, as shown in Figure 4.2, the total number of fiber and interface element contributions is equal to $2 \times n_{\text{f}} \times n_{\text{s}}$. Similar to (4.10), the interface contribution is shared between matrix and fiber degrees of freedom in the assembly of the corresponding stiffness matrix.

GLOBAL SYSTEM OF EQUATIONS

The $n_{\text{f}} \times n_{\text{s}}$ fiber element contributions and $n_{\text{f}} \times n_{\text{s}}$ matrix-fiber interface element contributions to the global stiffness matrix are assembled separately from those of the matrix elements. Irrespective of the fiber discretization scheme, the general form of global system of equations is

$$\begin{bmatrix} \boldsymbol{K}_{\text{mm}} & \boldsymbol{K}_{\text{mf}_1} & \boldsymbol{K}_{\text{mf}_2} & \dots & \boldsymbol{K}_{\text{mf}_{n_{\text{f}}}} \\ \boldsymbol{K}_{\text{f}_1\text{m}} & \boldsymbol{K}_{\text{f}_1\text{f}_1} & \boldsymbol{0} & \dots & \boldsymbol{0} \\ \boldsymbol{K}_{\text{f}_2\text{m}} & \boldsymbol{0} & \boldsymbol{K}_{\text{f}_2\text{f}_2} & \dots & \boldsymbol{0} \\ \vdots & \vdots & \vdots & \ddots & \vdots \\ \boldsymbol{K}_{\text{f}_{n_{\text{f}}}\text{m}} & \boldsymbol{0} & \boldsymbol{0} & \dots & \boldsymbol{K}_{\text{f}_{n_{\text{f}}}\text{f}_{n_{\text{f}}}} \end{bmatrix} \begin{bmatrix} \boldsymbol{m} \\ \boldsymbol{f}_1 \\ \boldsymbol{f}_2 \\ \vdots \\ \boldsymbol{f}_{n_{\text{f}}} \end{bmatrix} = \begin{bmatrix} \boldsymbol{F}_{\text{m}} \\ \boldsymbol{0} \\ \boldsymbol{0} \\ \vdots \\ \boldsymbol{0} \end{bmatrix}, \tag{4.17}$$

where $\boldsymbol{m}$ and $\boldsymbol{f}_i$ $(i = 1, ..., n_{\text{f}})$ are vectors containing matrix and individual fiber displacements, respectively. The submatrices in the global stiffness matrix in (4.17) are assembled by applying standard procedures to elemental stiffness contributions of matrix, fiber and matrix-fiber interface. In this framework, matrix and fiber stiffnesses lead to block diagonal terms while, as shown in (4.10), interface contributions ensuring the coupling between matrix and fibers lead to both block diagonal and block off-diagonal terms.

Throughout this study, linear elastic behavior is assumed for the constitutive models of matrix, fiber, and matrix-fiber interface.

4.3. VALIDITY OF THE DIMENSIONALLY-REDUCED APPROACH

The influence of the one-dimensional reduction of the fiber geometry on the mechanical response of a fiber-reinforced composite is studied. The geometrical reduction is performed

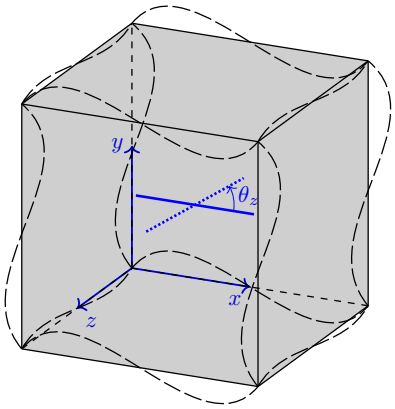

Figure 4.3: An $L \times L \times L$ ($L = 1$ mm) periodic simulation box with a fiber of length l_f in the middle aligned along the x axis. In the fiber orientation study (Section 4.4.1), the fiber can rotate around the z axis by an angle θ_z in the xy plane.

over the fiber diameter d_f, with fixed fiber length l_f. The validation of the dimensionally-reduced fiber model is performed against the solid fiber model described in Section 4.2.2 assuming the ratio between fiber diameter and domain size L as the characterizing parameter. To reduce the complexity of the discretization procedures due to the generation of a conforming mesh, only one fiber is considered in the configuration shown in Figure 4.1a for the reference model. Unless stated otherwise, in all the simulations in this chapter we have assumed that matrix Young's modulus E_m and Poisson's ratio ν_m are equal to 100 MPa and 0.4, respectively, and that in the solid fiber model, matrix and fiber have the same Poisson's ratio. Further, the effective mechanical properties of the composite are estimated through the procedure described in 4.6.

4.3.1. PERFECT BOND: EFFECTIVE MECHANICAL PROPERTIES

We now determine the range of fiber diameters over which the predictions of the dimensionally-reduced fiber model are valid. To this end, we compute the values of the effective longitudinal Young's modulus E_x^c of a composite with one fiber aligned with the x-axis ($\theta_z = 0^\circ$ in Figure 4.3) and compare them to the corresponding values obtained with the solid fiber model. It should be mentioned that this orientation is chosen among all orientations in the xy plane because it yields the largest increase in E_x^c. Computations are done with two different fiber lengths ($l_f = 0.4L$ and $l_f = 0.8L$). A large value of the interface tangential stiffness K_{bt} is used to mimic a perfectly bonded interface (hereafter referred to as perfect interface). Figure 4.4 shows the effective composite Young's modulus E_x^c for various values of the fiber Young's modulus E_f, both normalized by the matrix Young's modulus E_m. By reducing the ratio d_f/L, the responses of the numerical models converge to the same value. For $d_f/L < 0.01$ a very good agreement between them holds, and a one-dimensional

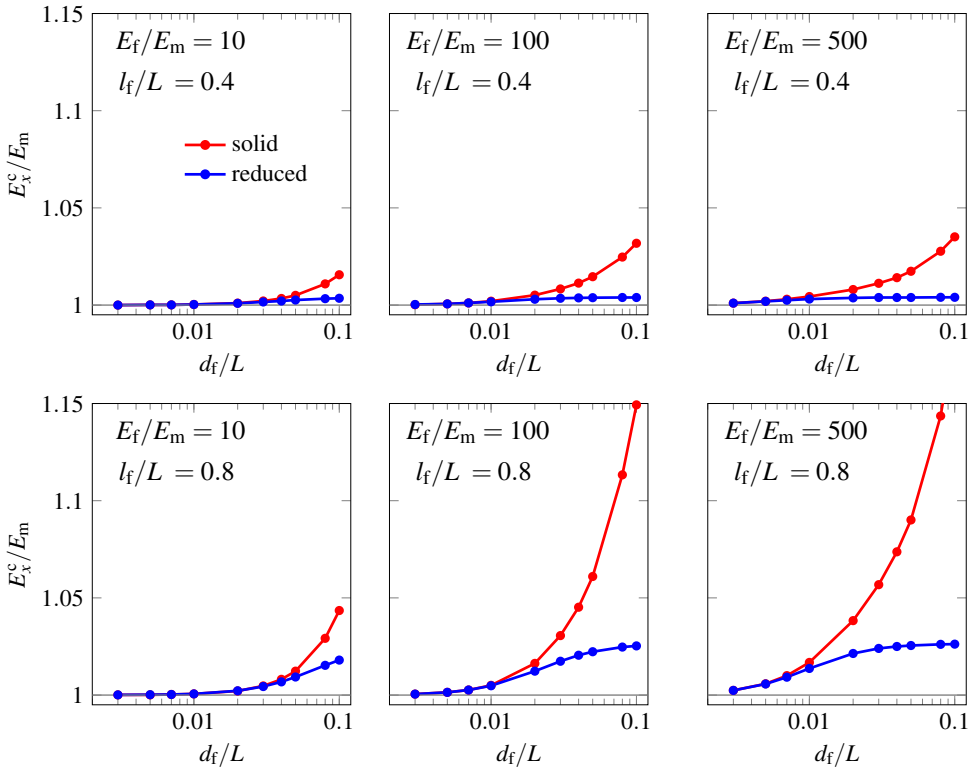

Figure 4.4: Normalized effective composite Young's modulus as a function of fiber diameter for a fiber with aspect ratio between 4 and 266. Predictions of both models agree for small fiber diameters relative to the domain size.

representation of the fiber can be justified.

4.3.2. IMPERFECT BOND: MATRIX-FIBER SLIP

Next, we study how the slip profiles between matrix and fiber compare for the reduced model and the solid fiber model when a linear elastic traction separation law is employed. While the dimensionally-reduced fiber model obviously generates one slip profile, an infinite number of slip profiles can be sampled with the solid-fiber model. To obtain a visually meaningful representation of the results, we have considered a very weak interface ($K_{bt} = 500$ N/mm^3), hereafter referred to as imperfect interface. The simulation box is deformed in the horizontal direction through the imposition of a periodic strain ($\varepsilon_{xx} = 0.1$) as discussed in 4.6. This computational setup eliminates the influence of the domain size L from the results. Figure 4.5a (4.5b) shows the resulting normalized fiber slip profiles for a fiber aligned with the loading direction ($\theta_z = 0^\circ$) and fiber diameter $d_f = 0.03L$ ($0.005L$). With reference to the solid fiber model, in this special case the points surrounding the fiber at the same horizontal coordinate experience the same displacement with respect to the corresponding fiber points. A unique slip profile is therefore generated which is found to be in a remarkably good agreement with the slip profile generated by the dimensionally-reduced

fiber model. In contrast, as shown in Figures 4.5c and 4.5d, an inclined fiber ($\theta_z \approx 28.6^\circ$ ($= 0.5$ rad)) does not slide uniformly with respect to the surrounding material. The gray shaded region represents all the fiber slip profiles sampled over the lateral surface in directions parallel to the fiber axis. These displacement slip profiles cannot be predicted by the reduced model where, instead, a single slip profile is predicted (dashed lines), which is however in good agreement with the average slip profile of the solid fiber model.

As shown in Figures 4.5c and 4.5d, the width of the shaded region decreases by reducing the fiber diameter indicating that the difference between the upper and lower interface displacement gap vectors becomes smaller. This means that the results obtained with the solid fiber model converge to those of the dimensionally-reduced fiber model as the fiber diameter decreases. To generalize the relation between fiber diameter and interfacial displacement gaps for inclined fibers, the normalized area A_e of the shaded region, referred to as normalized gap area, is plotted against the normalized fiber diameter in Figure 4.6. Results are shown in Figure 4.6a for different values of the fiber Young's modulus E_f and fiber length l_f. Irrespective of fiber length and material properties, the normalized gap area decreases with decreasing fiber diameter, and its value is obviously a function of fiber orientation, decreasing with decreasing fiber orientation angle as illustrated in Figure 4.6b.

4.4. FIBER NEUTRALITY

According to previous studies on planar reinforcements, perfectly bonded rigid inclusions become mechanically neutral under specific circumstances—mechanically neutral inclusions do not influence the mechanical response of the composite. Wang *et al.* [19] have derived the analytical solution for a zero-thickness RLI subjected to an inclined loading at infinity; for a given in-plane problem (plane stress/plane strain), the angle between the loading direction and the RLI at which the inclusion does not influence the stress field depends only on the Poisson's ratio of the matrix material. A similar property has not yet been reported in fiber-reinforced composites despite various studies on the role of fiber orientation in their homogenized mechanical properties [1, 8, 18]. Motivated by these observations, we perform a study on orientation effects and stress neutrality properties for linear elastic thin (high aspect ratio) fibers with imperfect matrix-fiber interface.

4.4.1. NEUTRALITY IN THE DIMENSIONALLY-REDUCED MODEL

Neutral orientations are determined for effective Young's and shear moduli and Poisson's ratios. For the sake of illustration, specimens with fiber volume fraction $v_f = 1.0\%$ (1300 aligned fibers) are considered. Length and diameter of the fibers, discretized with the dimensionally-reduced model, are set to $0.2L$ and $0.007L$, respectively. The results have been obtained with the numerical homogenization procedure described in 4.6. Numerical effective properties of the homogenized composite are reported in Figure 4.7a for fiber orientations θ_z ranging from 0° to 90°. In the simulations, the ratio E_f/E_m is set to 100 and an imperfect interface between fiber and matrix is assumed. Although we present results for this specific set of material properties, their validity for other parameter sets, also including the case of a rigid interface, was confirmed with simulations whose results are not reported here. A comparison with analytical micromechanical estimates is provided in Section 4.5.

As expected, the highest effective Young's modulus is obtained when fibers are aligned

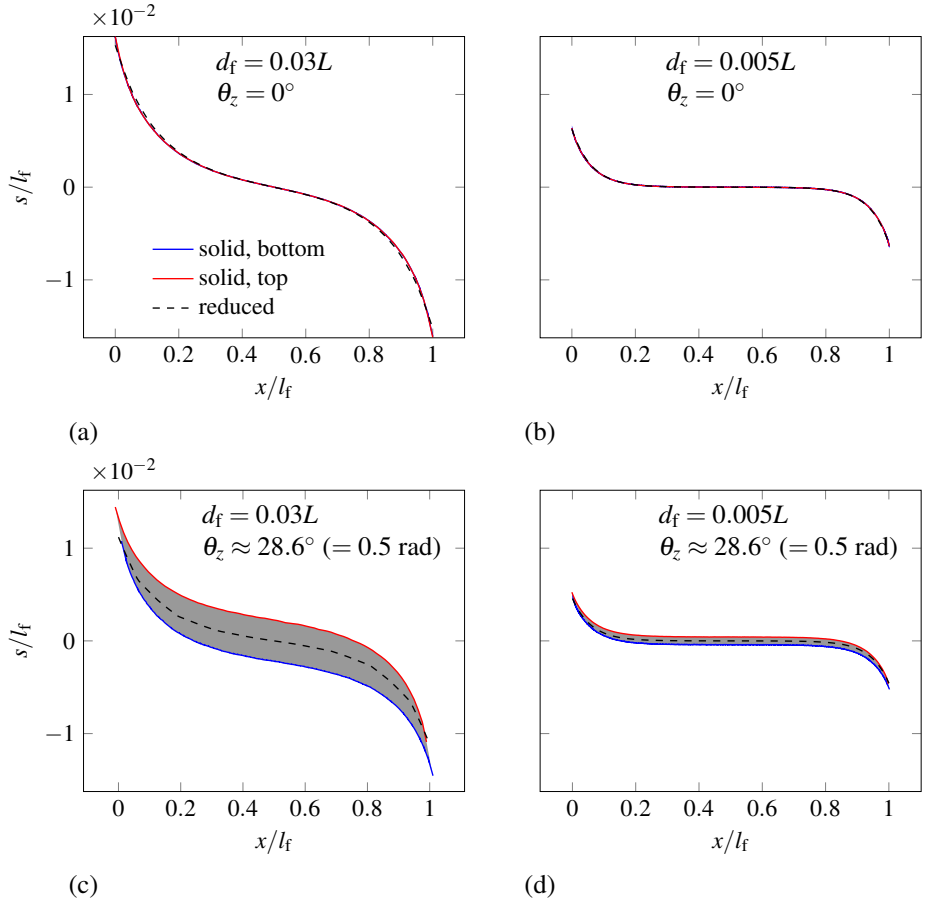

Figure 4.5: Normalized fiber slip s for a single embedded fiber with imperfect interface with $E_f/E_m = 10$ and $l_f = 0.8L$. (a,b) A unique slip profile can be identified for a fiber aligned with the loading direction. (c,d) The slip profile is not unique for an inclined fiber. The dimensionally-reduced model produces a unique slip profile that agrees with the average slip of the solid fiber model (dashed line). Refer to Figure 4.1a for the nomenclature used for the solid fiber model.

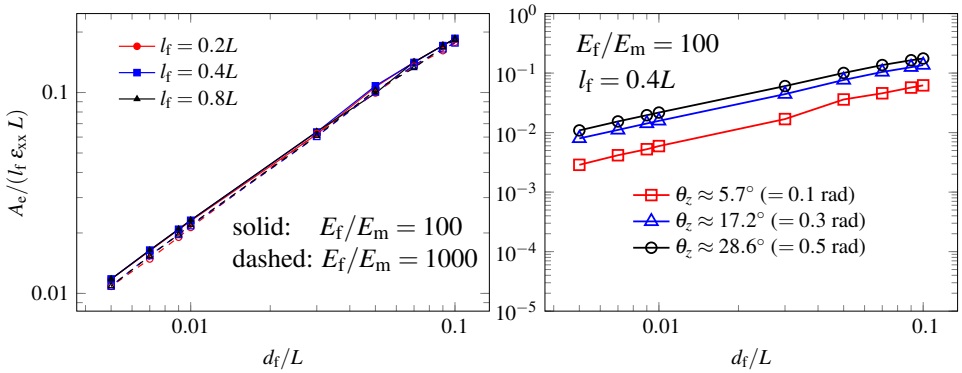

Figure 4.6: Effect of fiber diameter on the normalized gap area for a fiber with aspect ratio between 2 and 160. (a) Normalized gap area for fibers with different properties and $\theta_z \approx 28.6°$ (= 0.5 rad). (b) Normalized gap area for different fiber rotations θ_z.

with the loading direction. Contrary to the general understanding that fibers always increase the stiffness of a fiber-reinforced composite, corroborated also by results obtained with two-step mean-field homogenization procedures (see, e.g., Pierard *et al.* [7, Figure 3] and Tian *et al.* [8, Figures 7 to 10]), the minimum composite stiffness corresponds to a state of fiber neutrality. It is additionally implied from Figure 4.7a that fibers perpendicular to the loading direction ($\theta_z = 90°$) can, in general, increase the effective Young's modulus of the composite.

Fiber orientations corresponding to a neutral situation (i.e., neutral orientations θ_n at which fibers have no influence on the Young's modulus of the composite) are function of the Poisson's ratio ν_m of the matrix material only and are reported in Figure 4.7b (blue-filled circles). In the same figure we report values for plane states corresponding to the cases of unperturbed stress fields around a zero-thickness perfectly-bonded rigid planar inclusion according to the analytical solution by Wang *et al.* [19]. It is interesting to notice that dimensionally-reduced fibers are mechanically neutral at the neutral orientations valid for RLIs in a plane stress state.

As shown in Figure 4.8, neutrality is observed in terms of the effective shear modulus G^c_{xy} of the composite as well. In this case, neutral orientations are 0° and 90°. A similar stress neutrality has been reported in RLIs under uniform shear loading by Noselli *et al.* [20] using photoelasticity in a two-dimensional experimental study. Finally, various cases of neutrality in terms of the effective anisotropic Poisson's ratios can be identified in Figure 4.9.

These results confirm that linear elastic thin fibers share the neutrality feature of zero-thickness RLIs (i.e., the neutrality angle depends only on the matrix Poisson's ratio). As already mentioned, neutrality holds irrespective of fiber-matrix interface parameter. This is at variance with previously known cases of neutrality of arbitrary shaped inhomogeneities [24, 25] in which neutrality is achieved by designing non-ideal or imperfect interfaces between inclusion and matrix.

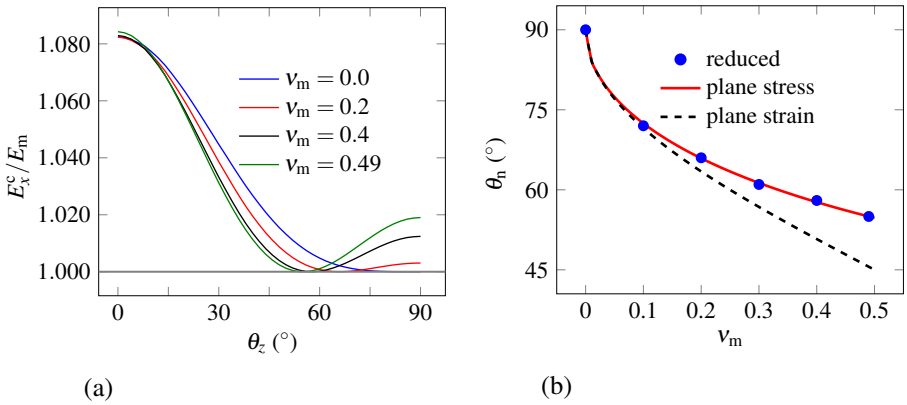

Figure 4.7: (a) Normalized effective Young's modulus E_x^c calculated at various fiber orientations θ_z and matrix Poisson's ratios ν_m. (b) The neutral orientation θ_n is the orientation corresponding to fibers experiencing no deformation under the applied load. Results obtained with $E_f/E_m = 100$, $K_{bt} = 500$ N/mm^3, and $\upsilon_f = 1\%$ (1300 aligned fibers with $d_f = 0.007L$ and $l_f = 0.2L$). Plane stress and plane strain results are from Wang *et al.* [19].

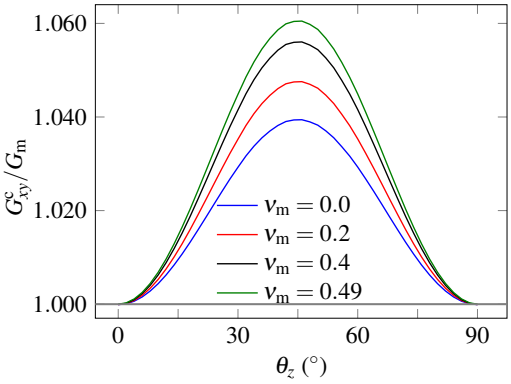

Figure 4.8: Normalized effective shear modulus G_{xy} calculated at various fiber orientations θ_z and matrix Poisson's ratios ν_m. Results obtained with $E_f/E_m = 100$, $K_{bt} = 500$ N/mm^3, and $\upsilon_f = 1\%$ (1300 aligned fibers with $d_f = 0.007L$ and $l_f = 0.2L$).

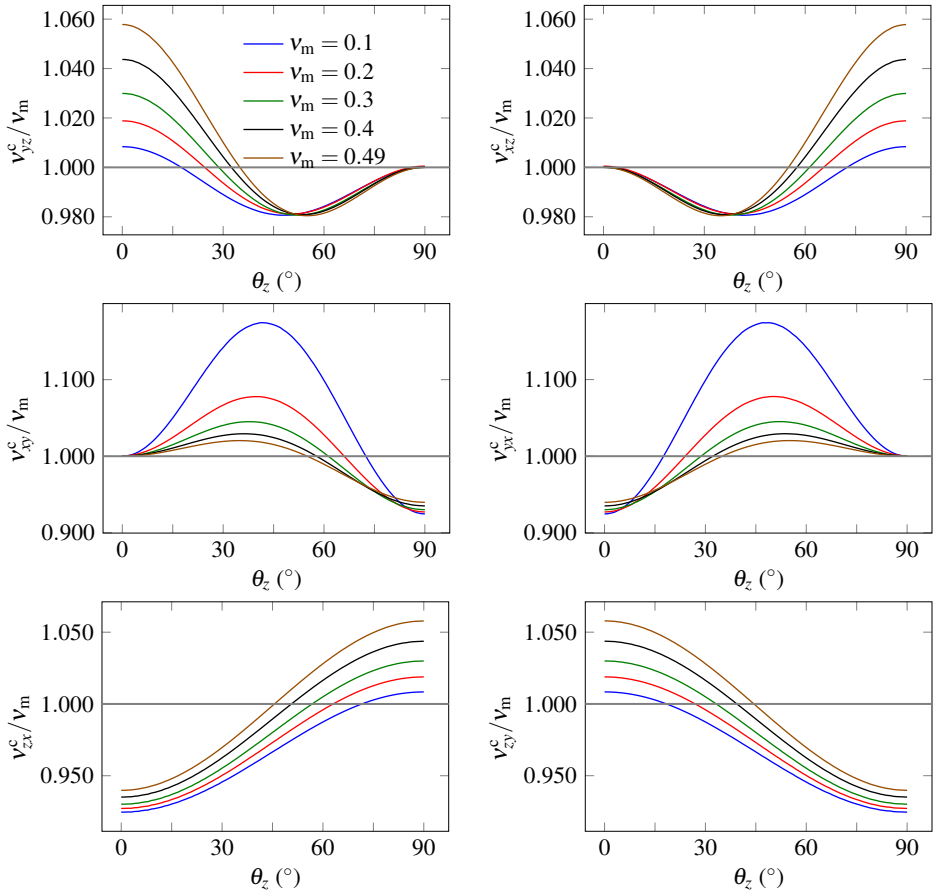

Figure 4.9: Normalized effective Poisson's ratio calculated at various fiber orientations θ_z and matrix Poisson's ratios ν_m. Results obtained with $E_f/E_m = 100$, $K_{bt} = 500$ N/mm^3, and $\upsilon_f = 3\%$ (1300 aligned fibers with $d_f = 0.007L$ and $l_f = 0.2L$).

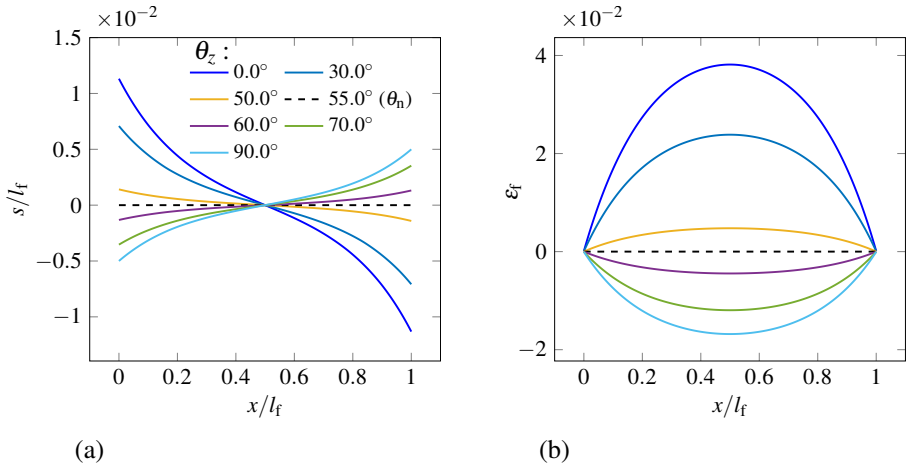

Figure 4.10: A one-fiber composite with a nearly incompressible matrix material ($\nu_m = 0.49$) under the action of a horizontal external load. Fiber slip s (a) and fiber axial strains ε_f (b) are strongly influenced by the fiber orientation θ_z. Results obtained with $E_f/E_m = 100$, $K_{bt} = 500$ N/mm^3, $d_f = 0.007L$ and $l_f = 0.8L$.

FIBER COMPRESSION UNDER TENSILE LOADING

At neutral orientations θ_n shown in Figure 4.7b, a fiber does not experience deformation. This implies a sign shift in the fiber strain and slip. Figure 4.10 shows the slip and strain profiles in the fiber of the one-fiber composite depicted in Figure 4.3 under tensile loading along the x-axis at various orientations (neutral angle $\theta_n \approx 55°$). Results are shown for the case of a nearly incompressible matrix with $\nu_m = 0.49$; the values of all other properties are taken from the example in the previous section. A similar set of results can be obtained for other matrix Poisson's ratios.

A shift in sign when θ_z exceeds the neutrality angle θ_n can be detected in both fiber slips and strain profiles. Tensile strains occur in fibers with orientations below θ_n while for orientations exceeding θ_n the sign reverses and compressive strains along the fiber axis are generated. This behavior could trigger composite failure in the form of fiber micro-buckling [26], even with externally applied tensile forces.

4.4.2. NEUTRALITY AND FIBER DIAMETER IN THE SOLID FIBER MODEL WITH PERFECT INTERFACE

In the previous section we have shown, using the dimensionally-reduced fiber model, that linear elastic thin fibers with imperfect matrix-fiber interface are neutral under specific circumstances. We now investigate how the fiber diameter influences this property considering a perfectly bonded solid fiber. The case of an imperfect matrix-fiber interface is discussed in the next section. The results are obtained using the simulation box in Figure 4.3 with one perfectly bonded fiber (length $l_f = 0.8L$) that is discretized using the solid and the dimensionally-reduced fiber models.

To investigate the relation between fiber diameter and the occurrence of fiber neutrality, the fiber is oriented along the neutral orientation that was determined for the dimensionally-

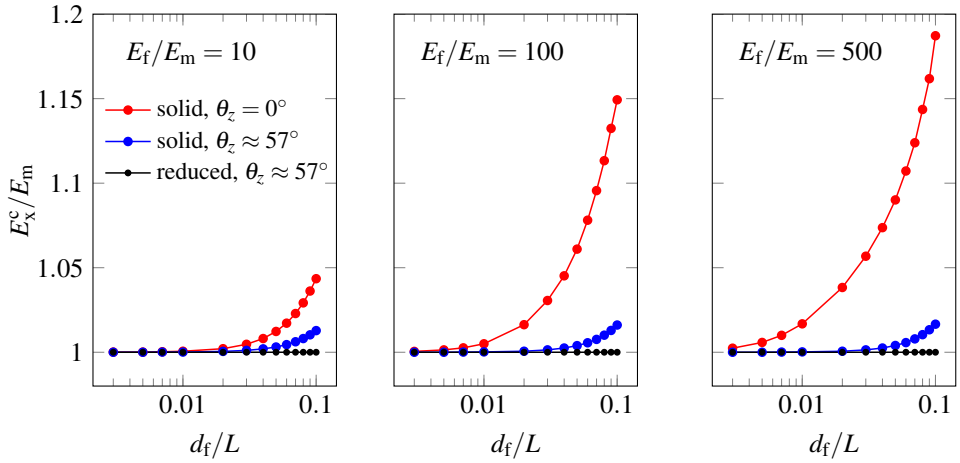

Figure 4.11: Normalized effective Young's modulus of the one-fiber composite (with $l_f = 0.8L$) as a function of fiber diameter for solid and dimensionally-reduced models at neutral orientation (Figure 4.7b: $\theta_z \approx 57°$ for $\nu_m = 0.4$) of the dimensionally-reduced model for a fiber with aspect ratio between 8 and 266. The longitudinal Young's modulus of a composite with a horizontal fiber ($\theta_z = 0°$) obtained with the solid fiber model (previously reported in Figure 4.4, second row) is also included.

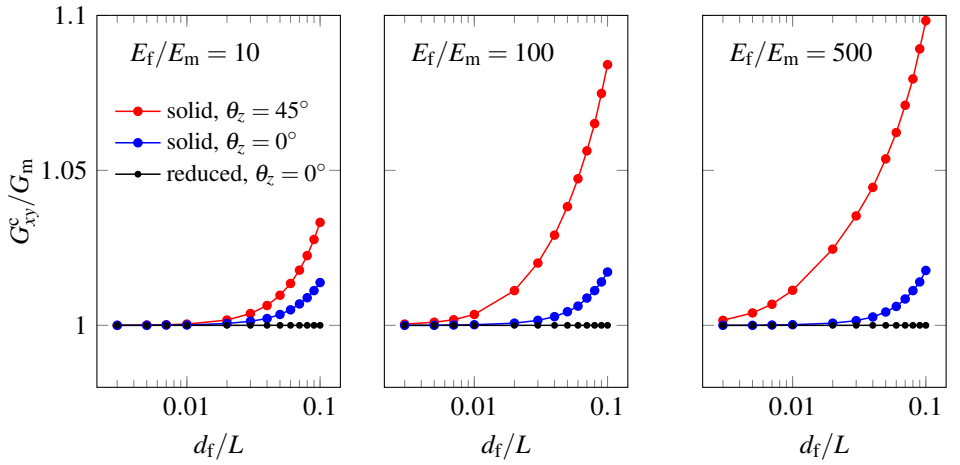

Figure 4.12: Normalized effective shear modulus of the one-fiber composite (with $l_f = 0.8L$) as a function of fiber diameter for solid and dimensionally-reduced models at neutral orientation ($\theta_z = 0°$ from Figure 4.8, irrespective of ν_m) of the dimensionally-reduced model for a fiber with aspect ratio between 8 and 266. The maximum shear modulus obtained with the solid fiber model for a fiber inclined at $\theta_z = 45°$ is also included.

reduced fiber model ($\theta_z = \theta_n \approx 57^\circ$ from Figure 4.7b, for a matrix with Poisson's ratio $\nu_m = 0.4$). The normalized effective Young's modulus E_x^c is reported in Figure 4.11 at different fiber diameters and stiffnesses. For the sake of comparison with the longitudinal Young's modulus, which gives the maximum achievable effective stiffness, solid fiber model results for the case with $\theta_z = 0^\circ$ are also included in the plots.

As shown in Figure 4.11, the dimensionally-reduced model predicts neutrality at all fiber diameters when $\theta_z \approx 57^\circ$ (black curves in Figure 4.11). Since the fiber is described as a line object, this is attributed to the fact that the diameter is not geometrically incorporated in an explicit manner but is considered as a parameter in the fiber and interface contributions to the stiffness matrix. However, when the exact geometry of the fiber is taken into account using the solid fiber model (blue curves in Figure 4.11), neutrality holds only for relatively small fiber diameters ($d_f/L < 0.01$). For $d_f/L > 0.01$ the increase of the effective Young's modulus is modest and is not significantly influenced by the fiber stiffness unlike the effective longitudinal Young's modulus (red curves).

Analogous observations hold for the effective shear modulus G_{xy}^c. Figure 4.12 shows a comparison of the two fiber models at $\theta_z = 0^\circ$ (according to Figure 4.8, neutrality in terms of G_{xy}^c occurs at $\theta_z = 0^\circ$). Results are now accompanied by the solid fiber model predictions for a fiber orientation ($\theta_z = 45^\circ$) that yields the maximum effective shear stiffness.

These observations are somehow in agreement with previous numerical studies of fiber orientation in short fiber-reinforced metal matrix composites [1, 8]. In these studies a modest increase of the effective Young's and shear moduli was found for fibers inclined at $\theta_z = 60^\circ$ and $\theta_z = 0^\circ$ in short carbon fiber composites (fiber with aspect ratio 15, $d_f \approx 0.03L$). In contrast, in the results shown in Figures 4.11 and 4.12, neutrality of fibers is expected at smaller diameters, and the effective stiffness of the composite will not change compared to the matrix stiffness computed at the orientations shown in Figure 4.7b.

4.4.3. NEUTRALITY AND IMPERFECT INTERFACE

Neutrality was already discussed in Section 4.4.1 under imperfect interface conditions with the analysis restricted to the single-interface assumption of the dimensionally-reduced fiber model. In this section, we discuss how neutrality can change considering the actual interface in a three-dimensional composite with a solid fiber and a two-dimensional planar composite with a thin inclusion.

SOLID FIBERS IN A THREE-DIMENSIONAL COMPOSITE

An imperfect interface leads to partial load transfer, with displacement jumps occurring between fiber and matrix. According to the non-uniqueness of the slip profile for an inclined fiber as discussed in Section 4.3.2, displacement differences between fiber edges (e.g., the top and bottom edges shown in Figure 4.5c,d) can occur. For relatively small fiber diameters, however, displacement differences between edges become small and the slip profiles can be approximated by a unique curve. Here we further assess this approximation and the significance of the different slip profiles by emphasizing their effect on the development of stress neutrality.

Similar to Section 4.4.2, a composite with one fiber oriented at the neutral orientation ($\theta_z = \theta_n \approx 57^\circ$ from Figure 4.7b, $\nu_m = 0.4$) is discretized using the solid fiber model. Values of Young's modulus E_x^c are plotted as a function of fiber diameter in Figure 4.13 for both

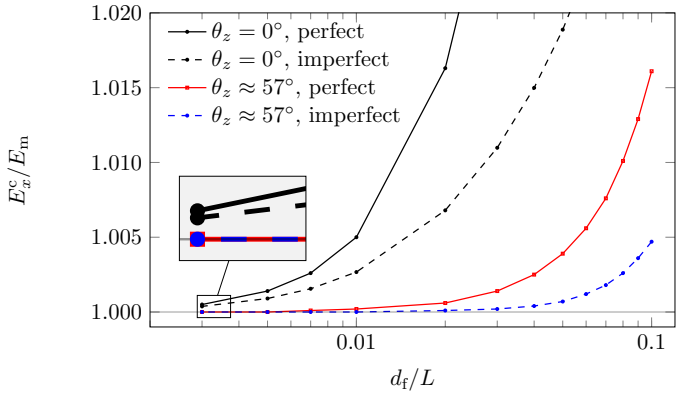

Figure 4.13: Normalized Effective Young's modulus of a composite with one fiber oriented at the neutral orientation obtained with the dimensionally-reduced fiber model ($\theta_z \approx 57°$ from Figure 4.7b, $\nu_m = 0.4$) and discretized using the solid fiber model under perfect and imperfect interface conditions for a fiber with aspect ratio between 8 and 266. The longitudinal Young's moduli obtained with the solid fiber model (previously reported in Figure 4.4, second row and second column) are also included. Both perfect and imperfect interface conditions are under a neutral state at small fiber diameters with $\theta_z = \theta_n \approx 57°$. Results obtained with $E_f/E_m = 100$, $K_{bt} = 500$ N/mm^3 and $l_f = 0.8L$.

perfect and imperfect interfaces. For the sake of comparison, the Young's moduli obtained with the solid fiber model with $\theta_z = 0°$ (black lines) are also included in the plot for both interface conditions.

Compared to the perfect interface case (solid lines), an imperfect interface (dashed lines) leads in general to lower values of the effective longitudinal Young's modulus E_x^c. More specifically, when the angle $\theta_z \approx 57°$, the reduction is only pronounced at relatively large fiber diameters; at small fiber diameters ($d_f/L < 0.01$) the longitudinal Young's modulus of the composite converges to the value of the Young's modulus of the matrix and, with a perfect or imperfect interface, a neutral state is predicted. When $\theta_z = 0°$ a reduced stiffness is detectable even at small fiber diameters (see inset in Figure 4.13).

To summarize, irrespective of the interface type, a fiber with a small diameter compared to the characteristic dimension of the domain is not strained when inclined at $\theta_z = \theta_n \approx 57°$ (neutral orientation for $\nu_m = 0.4$) and has therefore a null effect on the stiffness of the composite.

DIMENSIONALLY-REDUCED INCLUSION IN A TWO-DIMENSIONAL COMPOSITE

The two-dimensional conformal model in Figure 4.14, obtained as a limit case of the previously discussed solid fiber model, can adequately model certain types of two-dimensional composites [5, 27]. The model is employed to investigate the occurrence of neutral states (reported in Wang *et al.* [19] for perfectly-bonded two-dimensional planar inclusions) under imperfect interface conditions. In this computational setting, two interface surfaces can be identified when the inclusion is not perfectly bonded to the matrix: one at each side of the inclusion and physically disconnected from each other. Depending on the out of plane shape of the inclusion, different assumptions can be made regarding the continuity of the displacement field across it. For a situation with platelet inclusions, as in clay nanocomposites [5],

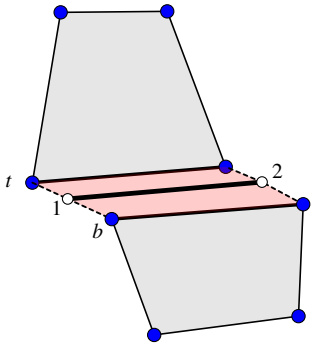

Figure 4.14: Single conforming inclusion with elastic imperfect interface. Interface elements are placed at each side of the inclusion. For illustrative purposes, both normal and tangential displacement jumps are depicted.

displacement jumps across the platelet adequately represent the expected kinematics even for platelets of small thickness. As soon as the inclusion out-of-plane dimension decreases and the inclusion represents a fiber, as in fiber networks in ordinary paper sheets or buckypaper [27], the double-interface model is not representative anymore, and a traditional single-interface model of the type described in Section 4.2.2 is to be preferred.

In the double-interface model shown in Figure 4.14, conceptually similar to the model by Pike *et al.* [28], zero-thickness interface elements are placed at each side of the inclusion to allow the occurrence of relative displacements between inclusion and matrix on both sides of the inclusion. In this situation, upper and lower interfaces move relative to each other. To describe this kinematics, the interface shape function matrix (4.7) is rewritten as

$$\boldsymbol{N}_{\text{int}}^{\text{t/b}} = \begin{bmatrix} N_1^{\text{i}} & 0 & N_2^{\text{i}} & 0 & -N_1^{\text{t/b}} & 0 & -N_2^{\text{t/b}} & 0 \\ 0 & N_1^{\text{i}} & 0 & N_2^{\text{i}} & 0 & -N_1^{\text{t/b}} & 0 & -N_2^{\text{t/b}} \end{bmatrix}, \tag{4.18}$$

where N_1^{i} and N_2^{i} are one-dimensional Lagrange shape functions evaluated at the inclusion end points 1 and 2, respectively. Similarly, $N_1^{\text{t/b}}$ and $N_2^{\text{t/b}}$ are the matrix nodal shape functions evaluated at points 1 and 2, and superscripts t and b denote top and bottom interfaces, respectively. The simpler single-interface model, which does not account for a discontinuous matrix displacement field, can be recovered by constraining the top and bottom nodes to experience the same displacement ($\boldsymbol{u}^t = \boldsymbol{u}^b$).

Figures 4.15a-c show the effective mechanical properties of the 1 mm $\times$ 1 mm periodic plate with a centered 0.5 mm long inclined inclusion as a function of the inclusion orientation θ_z. Mechanical properties are extracted using the procedure described in 4.6. In the analyses we used two values of the interfacial tangential stiffness K_{bt} (500 N/mm^2 and 1000 N/mm^2), and we assumed a unit thickness for the plate in the out-of-plane dimension. The relatively low values shown in Figure 4.15 are a consequence of the choice of the parameters and the modest mechanical effect of a single fiber.

Figure 4.15a shows that in the double-interface model the angle θ_z that corresponds to the minimum effective Young's modulus of the composite (marked in the figure) is a function of the interfacial tangential stiffness K_{bt}: the value of the angle increases with

increasing values of K_{bt} and tends to $\approx 50.7^{\circ}$. For the single-interface model, the value of K_{bt} has no effect on the angle at which E_x^{c} is at a minimum: this angle is equal to $\approx 50.7^{\circ}$ and corresponds to the neutral orientation previously discussed (in this specific case, $\theta_{\mathrm{n}} \approx 50.7^{\circ}$ for $\nu_{\mathrm{m}} = 0.4$ under plane strain as shown in Figure 4.7b). This means that in the range of validity of the dimensionally-reduced model, E_x^{c} will assume its minumum value, corresponding to a situation of fiber neutrality, at the same inclusion angle shown in Figure 4.7b, irrespective of the value of the interfacial tangential stiffness K_{bt}.

In the single-interface model the angle corresponding to the minimum value of E_x^{c} indicates a situation of inclusion neutrality. In the double-interface model however we observe that i) the composite Young's modulus can be lower than that of the matrix for a wide range of inclusion angles (stiffness degradation), and ii) the amplitude of the range decreases with increasing K_{bt} values. Similar considerations can be drawn for the shear modulus in Figure 4.15b although neutrality is only observed for the single-interface model at θ equal to 0° or 90°.

Under shear loading, relative movements between edges of the inclusion occur and, as shown in Figure 4.15b, a similar reduction in the value of the effective shear modulus to a value lower than the matrix shear modulus is obtained with the double-interface model. Additionally, maximum shear modulus is achieved for $\theta_z = 45^{\circ}$, where predictions of single- and double-interface models are the same.

As for the Poisson's ratio in Figure 4.15c, the double-interface model yields an increase of the composite effective Poisson's ratios ν_{xy} for all orientations compared to the single-interface model. For θ equal to 0° (90°), interfacial jumps (Figure 4.15d) are absent and the effective Young's modulus and Poisson's ratio values are equal in both models.

Degradation is attributed to the crack-like features of the interface and is not expected when a single-interface model is used or under a perfect interface condition. In these situations, inclusion neutrality is expected at the previously defined neutral orientations. Moreover, the minimum angles for the double-interface model, indicated by red marks in Figure 4.15a, and the degradation range are not only a function of the interface stiffness values, but are also affected by geometrical properties (e.g., fiber length, number of fibers, and their spatial arrangements).

4.5. MICROMECHANICAL ANALYSIS

Mesh-independent fiber models are a necessary tool for the modeling and simulation of composites with many fibers (Figure 4.16). To this end, a detailed analysis, taking into account the fiber volume fraction as a variable, is presented in this concluding section. Estimates obtained from commonly used micro-mechanical models summarized in 4.6 are contrasted to results obtained with the dimensionally-reduced model. The occurrence of fiber neutrality is also investigated.

We consider equally-shaped fibers with length $l_{\mathrm{f}} = 0.2L$ and diameter $d_{\mathrm{f}} = 0.007L$ that are n times stiffer than the matrix material ($n = 10,\ 100,\ 500$). To compare the numerical results with those obtained with analytical micromechanical models, fibers and matrix are perfectly bonded. The simulation box is discretized using a uniform grid of $31 \times 31 \times 31$ trilinear hexahedral elements, and each fiber is subdivided into 20 equally-spaced segments. The mesh-convergence study in Figure 4.17 confirms that the employed discretization is sufficiently accurate. As mentioned in the introduction, discontinuities in the stress field

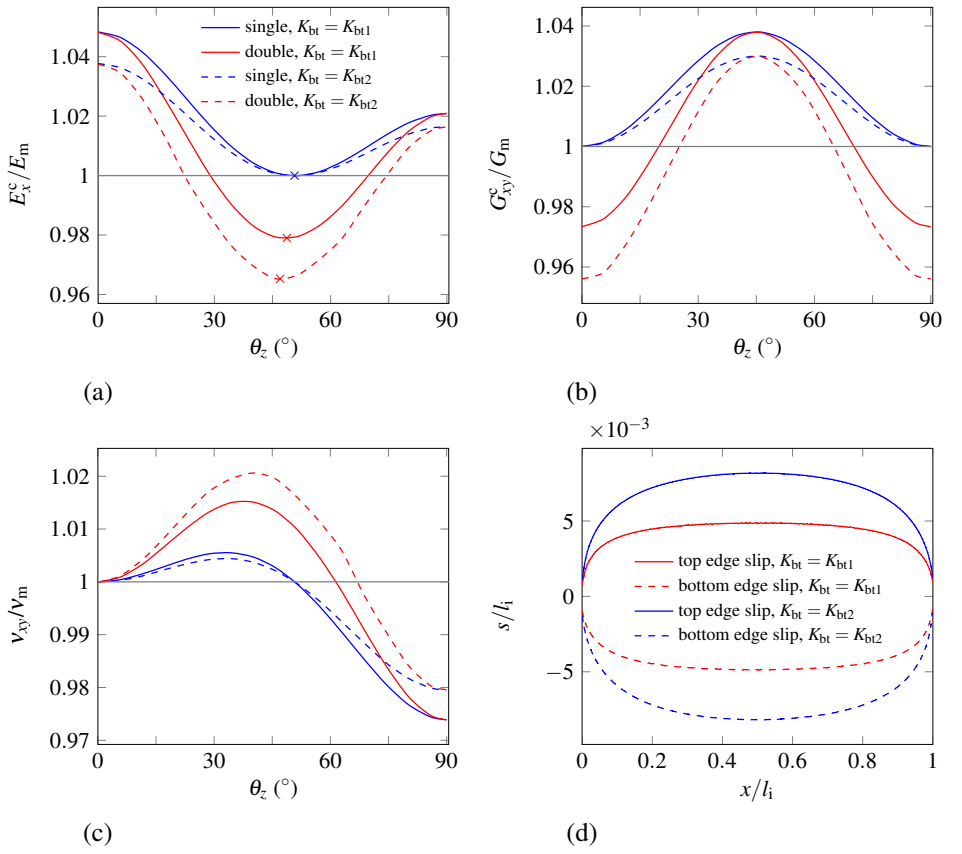

Figure 4.15: Effective (a) Young's modulus, (b) shear modulus and (c) Poisson's ratios of a two-dimensional composite with imperfect interface ($K_{bt1} = 1000\,\mathrm{N/mm^2}$, $K_{bt2} = 500\,\mathrm{N/mm^2}$, $E_f/E_m = 10$ and $\nu_m = 0.4$ in plane strain). The single-interface model shows neutrality for $\theta = \theta_n$ ($\theta_n \approx 50.7°$ from Figure 4.7b), while the double-interface model predicts degraded effective mechanical properties compared with intact matrix properties. (d) Fiber interfacial slips for $\theta = \theta_n$ using the double-interface model.

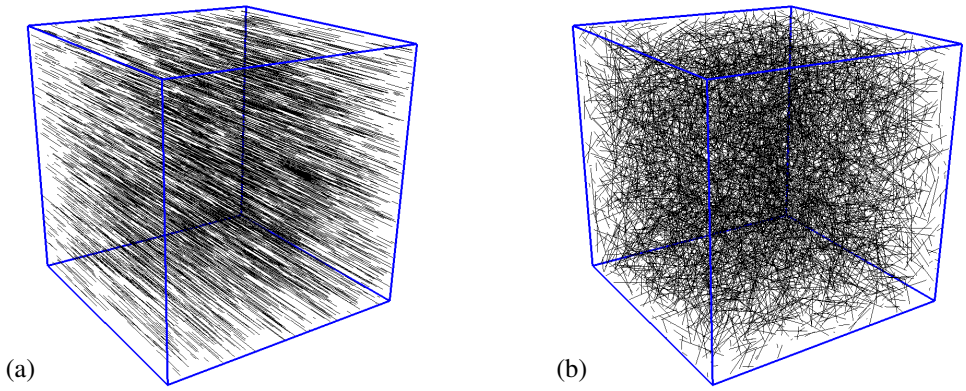

Figure 4.16: Two realizations of a composite with approximately 4700 fiber (length $l_f = 0.2L$ and diameter $d_f = 0.007L$) in an $L \times L \times L$ ($L = 1$ mm) periodic simulation box resulting in a fiber volume fraction $\upsilon_f = 3\%$: (a) aligned and (b) randomly distributed fibers.

across a fiber are neglected in dimensionally-reduced models to favor numerical efficiency. The error introduced with this approximation is not negligible for high stiffness contrast values n and large fiber volume fractions υ_f. In such cases a slower convergence is observed (Figure 4.17c). Distributions of homogeneously dispersed periodic fibers are obtained with a random sequential adsorption algorithm described in 4.6. In the simulations, fiber volume fractions up to 15% (approximately 22000 fibers) are considered. Two sample distributions with approximately 4700 aligned and randomly distributed discrete fibers are shown in Figure 4.16 yielding composites with transversely isotropic and nearly isotropic mechanical responses.

Young's moduli Figure 4.18 shows the homogenized Young's modulus E_x^c as a function of the fiber volume fraction υ_f for different material properties and distributions of fibers; in the figure, numerical results are compared with rule-of-mixtures (RoM) and Halpin-Tsai estimates. As shown in Figures 4.18a-c for a transversely isotropic composite, due to the slenderness of the fibers (aspect ratio $l_f/d_f \approx 30$), numerical results are generally in better agreement with RoM predictions especially for fibers with relatively low Young's modulus. The longitudinal Young's modulus increases with the fiber volume fraction υ_f and is hardly influenced by the matrix Poisson's ratio ν_m. Although a similar pattern is observed in Figures 4.18d-f for randomly distributed fibers, the resulting Young's moduli are significantly lower due to fiber orientation with respect to the loading direction and are in good agreement with the simple modified Voigt estimate provided by Pan [29].

In a transversely isotropic composite similar to that in Figure 4.16a, Young's moduli E_y^c and E_z^c ($= E_y^c$) are also enhanced for a matrix material with non-zero Poisson's ratio. However, as shown in Figure 4.19, the value of the transverse Young's modulus does not generally agree with RoM estimates and this is attributed to the unrealistic uniform stress assumption and the absence of Poisson's contraction effects [30]. For a nearly incompress-

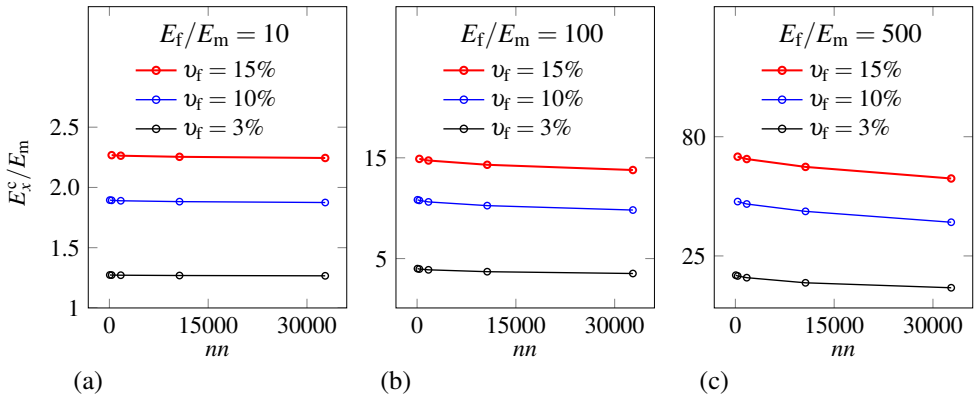

Figure 4.17: Effective Young's modulus along the x-axis for a transversely isotropic composite with aligned fibers for different mesh densities (*nn* indicates the number of mesh nodes) and fiber volume fractions υ_f. In the calculations reported in Section 4.5 ($d_f = 0.007L$ and $l_f = 0.2L$), the finest discretization with $31 \times 31 \times 31$ trilinear hexahedral elements and 32768 nodes has been used.

ible matrix, RoM predictions clearly underestimate the transverse Young's moduli of the transversely isotropic composite. It is also worth mentioning that our numerical results are in agreement with Hashin-Shtrikman-Willis lower bounds [31], although the good agreement is observed mainly at smaller fiber volume fractions.

Poisson's ratios Figure 4.20 shows the effective Poisson's ratios of the transversely isotropic composite for various fiber volume fractions. Similar to the transverse Young's moduli, Poisson's ratio $\nu^c_{zy} (= \nu^c_{yz})$ shows an increasing trend and a considerable dependence on the matrix Poisson's ratio. This dependence however is not predicted by RoM estimates, which clearly overestimates the numerical results. Conversely, $\nu^c_{yx} (= \nu^c_{zx})$ decreases, in good agreement with RoM, and the results are not influenced by the matrix Poisson's ratio. Finally, as shown in Figure 4.20c (and already reported in Figure 4.9c for a fixed volume fraction with $\theta_z = 0°$), ν^c_{xy} $(= \nu^c_{xz})$ remains equal to the matrix Poisson's ratio irrespective of fiber density, a property which is not predicted by RoM estimates (Equation 4.26).

Figures 4.21 and 4.22 show results for the homogenized effective Poisson's ratio of the nearly isotropic composite as a function of ν_m and υ_f. Values of the effective Poisson's ratio

$$\nu^c_{iso} = \frac{\lambda^c}{2(\mu^c + \lambda^c)}, \tag{4.19}$$

where λ^c and μ^c are the effective Lamé parameters averaged in the three directions, are computed assuming an isotropic behavior of the composite [32]. From Figure 4.21, it is interesting to notice that for a matrix with Poisson's ratio $\nu_m \approx 0.25$, the effective Poisson's ratio ν^c_{iso} of the homogenized composite is insensitive to the fiber volume fraction (the inclusions are neutral in terms of Poisson's ratio). For $\nu_m < 0.25$, an increased incompressibility of the composite is observed; for a matrix with $\nu_m > 0.25$, an increased compressibility, although less pronounced than the increase in incompressibility, is observed. In both cases,

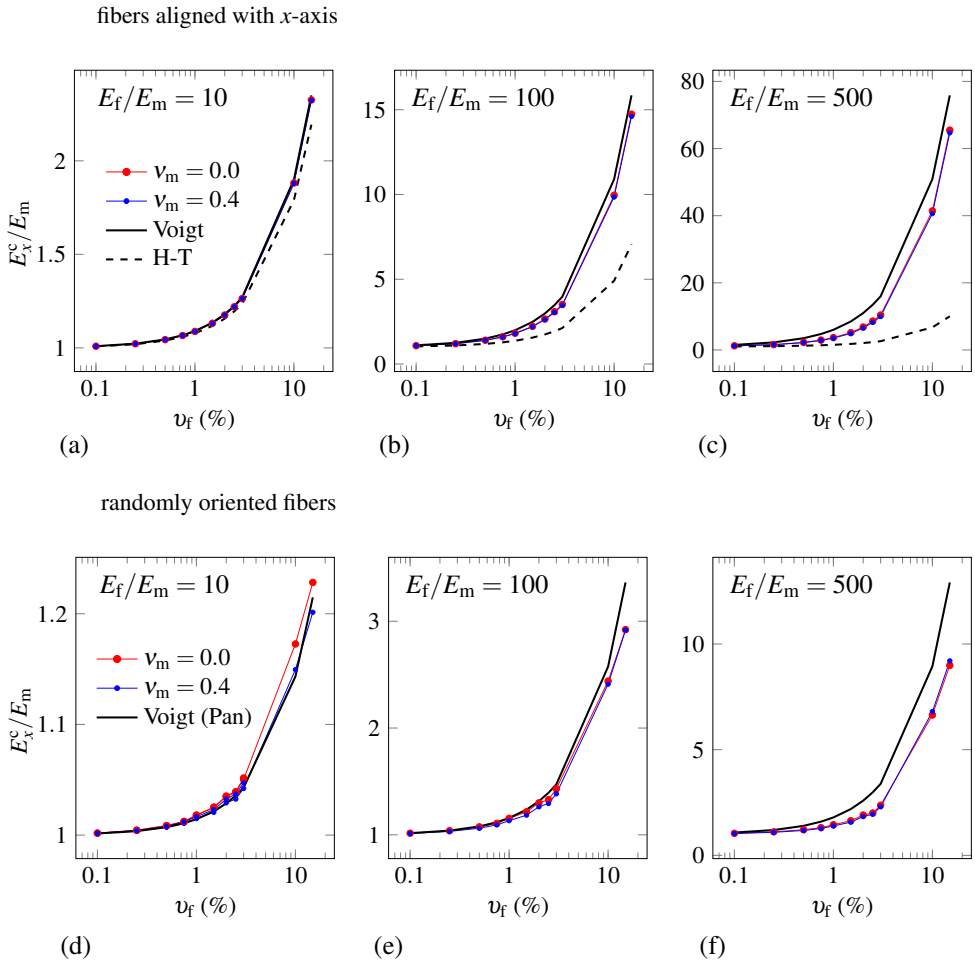

Figure 4.18: Effective Young's modulus along the x-axis for a transversely isotropic composite with aligned fibers (a-c) and a nearly isotropic composite with randomly distributed fibers (d-f) at different fiber volume fractions v_f ($d_f = 0.007L$ and $l_f = 0.2L$).

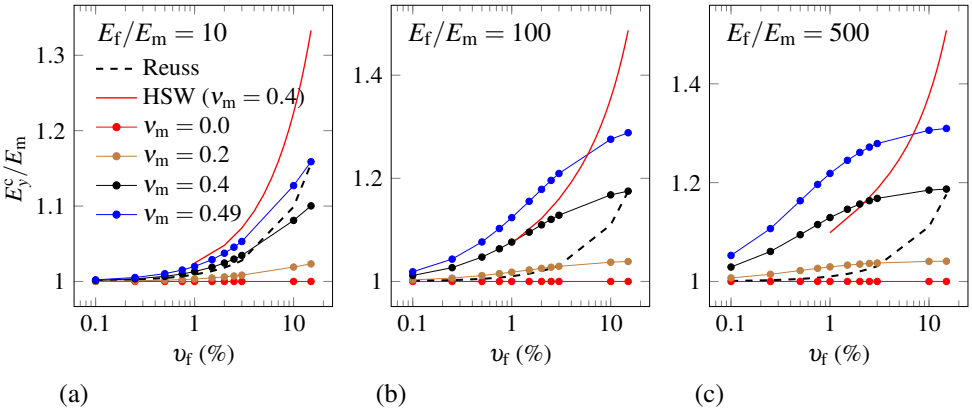

Figure 4.19: Effective transverse Young's moduli ($E_y^c = E_z^c$) for a transversely isotropic composite with aligned fibers at different volume fractions υ_f ($d_f = 0.007L$ and $l_f = 0.2L$).

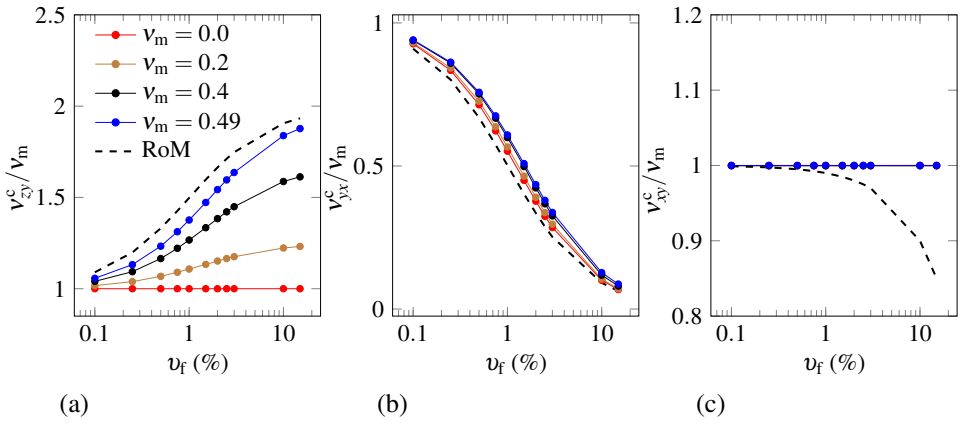

Figure 4.20: Effective Poisson's ratios of a transversely isotropic composite with aligned fibers for different volume fractions ($E_f/E_m = 100$, $d_f = 0.007L$ and $l_f = 0.2L$).

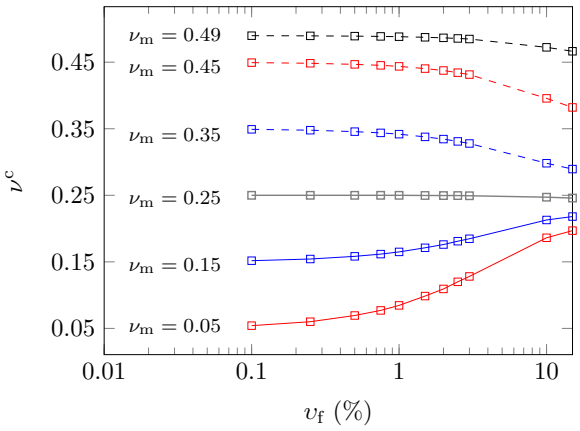

Figure 4.21: Effective Poisson's ratios ν^c_{iso} of a nearly isotropic composite with randomly distributed fibers for different volume fractions v_f (matrix Poisson's ratios ν_m, $E_f/E_m = 100$, $d_f = 0.007L$ and $l_f = 0.2L$).

values of the effective Poisson's ratio tends toward the value 0.25 by increasing the fiber volume fraction v_f. As shown in Figure 4.22 for different fiber stiffnesses, a similar observation can be made in terms of the mean anisotropic Poisson's ratios ν^c_a (averaged over anisotropic Poisson's ratios ν_{xy}, ν_{xz}, ν_{yx}, ν_{zx}, ν_{zy} and ν_{yz}, from Equation (4.21)). Due to the random distribution of the fibers, anisotropic Poisson's ratios only slightly deviate from the mean value. These observations are in agreement with previous findings by Das and MacKintosh [33] who used a mean-field approach for the theoretical investigation of the micromechanics of isotropic composites consisting of randomly distributed stiff fibers. By taking into account the reinforcing effect of individual fibers, the current numerical homogenization procedure validates averaging theories and neutrality in terms of Poisson's ratio for a composite with randomly distributed linear elastic fibers embedded in a matrix with Poisson's ratio $\nu_m = 0.25$ or a nearly incompressible matrix with $\nu_m \approx 0.5$.

Unlike mean-field homogenization, embedded reinforcement methods are not limited to composites with perfect matrix-fiber interfaces. Various distribution of fibers with arbitrary shapes and interface properties can be considered for the evaluation of the composite homogenized mechanical properties.

4.6. CONCLUDING REMARKS

It is well known that fiber orientation plays an important role in the mechanical response of composites. The common understanding is that fibers improve the mechanical properties of the matrix in which they are embedded, and that certain fiber orientations are better than others in some measure. This is not correct. The most unfavorable fiber orientation represents a state of fiber neutrality, a situation in which a fiber does not perturb the stress field and therefore has no influence on the mechanical properties of the composite. Fiber neutrality can be seen as the generalization of the concept of inclusion neutrality that was introduced for zero-thickness rigid inclusions by Wang *et al.* [19]. Here, we have demonstrated that inclusion neutrality holds also for thin linear elastic fibers with imperfect matrix-fiber

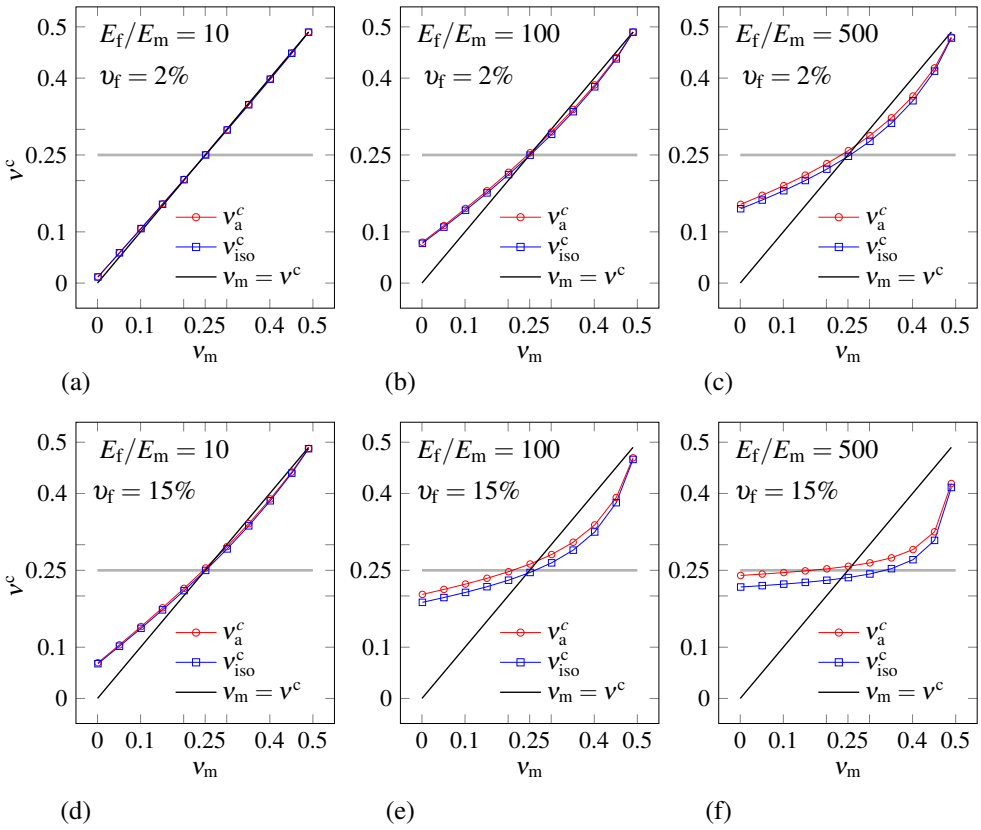

Figure 4.22: Effective Poisson's ratio of a nearly isotropic composite with randomly distributed fibers at two volume fractions υ_f and different matrix Poisson's ratios ν_m, with $d_f = 0.007L$ and $l_f = 0.2L$.

interfaces, with an immediate generalization to the perfect interface case.

Similar to rigid line inclusions, slenderness is a fundamental ingredient for the occurrence of neutrality. Neutral fibers are in fact not reported in existing studies where composites with relatively large fiber diameters were studied. In these cases the effective stiffness of the composite increases even though fibers are oriented at the most unfavorable angle—this angle would result in fiber neutrality if the fiber were thin.

4.A. COMPUTATION OF EFFECTIVE PROPERTIES

To extract the effective elastic coefficients of the fiber-reinforced composite, we employ the computational homogenization scheme described by Berger *et al.* [2]. As suggested by Xia *et al.* [3], homogeneous boundary conditions lead to over-constrained predictions of the effective properties. Instead, the periodic boundary conditions

$$u_i^k - u_i^l = \bar{\varepsilon}_{ij} L_j, \tag{4.20}$$

prescribed at the boundary of the simulation box with $\bar{\varepsilon}_{ij}$ $(i,j = x,y,z)$ the components of the applied strain tensor, yield more accurate estimations. Edge indexes k and l correspond to two opposite edges of the simulation box where periodic strains are imposed, and L_j is the size of the domain in the jth direction. In all the numerical results presented in this chapter, a unit cube simulation box is adopted (Figure 4.3).

Although 21 independent constants are defined for the general anisotropic case [32], here only the specific engineering constants in each direction are of interest. Three Young's moduli (E_x^{c}, $E_{\mathrm{y}}^{\mathrm{c}}$, $E_{\mathrm{z}}^{\mathrm{c}}$) relating tensile stresses and strains, three shear moduli ($G_{\mathrm{xy}}^{\mathrm{c}}$, $G_{\mathrm{yz}}^{\mathrm{c}}$, $G_{\mathrm{xz}}^{\mathrm{c}}$) relating shearing stresses and strains, and six Poisson's ratios ν_{ij}^{c} ($\nu_{\mathrm{xy}}^{\mathrm{c}}$, $\nu_{\mathrm{xz}}^{\mathrm{c}}$, $\nu_{\mathrm{yx}}^{\mathrm{c}}$, $\nu_{\mathrm{yz}}^{\mathrm{c}}$, $\nu_{\mathrm{zx}}^{\mathrm{c}}$, $\nu_{\mathrm{zy}}^{\mathrm{c}}$) representing contraction in the j-direction after the application of a tensile load in the i-direction can be extracted. These quantities may be expressed in terms of the coefficients of the compliance constants matrix as

$$\begin{aligned}
&E_{\mathrm{x}}^{\mathrm{c}} = \frac{1}{C_{11}},\ E_{\mathrm{y}}^{\mathrm{c}} = \frac{1}{C_{22}},\ E_{\mathrm{z}}^{\mathrm{c}} = \frac{1}{C_{33}},\\
&G_{\mathrm{xy}}^{\mathrm{c}} = \frac{1}{C_{44}},\ G_{\mathrm{yz}}^{\mathrm{c}} = \frac{1}{C_{55}},\ G_{\mathrm{xz}}^{\mathrm{c}} = \frac{1}{C_{66}},\\
&\nu_{\mathrm{xy}}^{\mathrm{c}} = -\frac{C_{21}}{C_{11}},\ \nu_{\mathrm{xz}}^{\mathrm{c}} = -\frac{C_{31}}{C_{11}},\\
&\nu_{\mathrm{yx}}^{\mathrm{c}} = -\frac{C_{12}}{C_{22}},\ \nu_{\mathrm{yz}}^{\mathrm{c}} = -\frac{C_{32}}{C_{22}},\\
&\nu_{\mathrm{zx}}^{\mathrm{c}} = -\frac{C_{13}}{C_{33}},\ \nu_{\mathrm{zy}}^{\mathrm{c}} = -\frac{C_{23}}{C_{33}}.
\end{aligned} \tag{4.21}$$

The compliance constants matrix $\boldsymbol{C}$ is evaluated by inverting the elastic coefficient matrix $\boldsymbol{D}$ as described in Malagù *et al.* [34].

4.B. ANALYTICAL MICROMECHANICAL MODELS

For the special case of a transversely isotropic composite with aligned fibers of the type shown in Figure 4.16a, simple analytical micromechanical models are available.

The well known rule of mixtures is widely used to predict the mechanical properties of elastic composites. The composite stiffness is approximated as a weighted mean of the moduli of two components [30]. The rule of mixtures does not consider geometrical details such as the fiber aspect ratio. With reference to the case of a composite with fibers that are aligned with the global x-axis, the effective longitudinal Young's modulus

$$E_x^{\mathrm{c}} = (1-\upsilon_{\mathrm{f}})\,E_{\mathrm{m}} + \upsilon_{\mathrm{f}}\,E_{\mathrm{f}} \tag{4.22}$$

is expressed as a function of the fiber volume fraction υ_{f}, where it is assumed that strains in the direction of the fibers are equal in the matrix and the fiber (this assumption is valid for perfectly bonded fibers with high aspect ratio). Equation (4.22) is referred to as the upper bound modulus (Voigt model).

Using the inverse rule of mixtures and assuming that stresses in the direction normal to the fibers are equal in the matrix and the fiber, the transverse Young's moduli

$$E_y^{\mathrm{c}} = E_z^{\mathrm{c}} = \left[\frac{\upsilon_f}{E_{\mathrm{f}}} + \frac{1-\upsilon_{\mathrm{f}}}{E_m}\right]^{-1}. \tag{4.23}$$

This expression is known as the lower-bound modulus (Reuss model).

According to the semi-empirical estimate of the Young's modulus proposed by Halpin [35],

$$E_x^{\mathrm{c}} = E_{\mathrm{m}}\,\frac{1+\xi\,\eta\,\upsilon_{\mathrm{f}}}{1-\eta\,\upsilon_{\mathrm{f}}} \tag{4.24}$$

with

$$\eta = \frac{E_{\mathrm{f}}/E_{\mathrm{m}}-1}{E_{\mathrm{f}}/E_{\mathrm{m}}+\xi} \qquad \text{and} \qquad \xi = 2l_{\mathrm{f}}/d_{\mathrm{f}}. \tag{4.25}$$

This expression is suitable for short fibers and takes into account the non-uniform distribution of strains and stresses in the composite. Predictions of Equation (4.24) lie within the range of the lower and upper bound moduli.

Similar formulas can be derived for the Poisson's ratios [30]:

$$\begin{aligned}
\nu_{xy}^{\mathrm{c}} &= (1-\upsilon_{\mathrm{f}})\,\nu_{\mathrm{m}} + \upsilon_{\mathrm{f}}\,\nu_{\mathrm{f}},\\
\nu_{yx}^{\mathrm{c}} &= \left[(1-\upsilon_{\mathrm{f}})\,\nu_{\mathrm{m}} + \upsilon_{\mathrm{f}}\,\nu_{\mathrm{f}}\right]\frac{E_y}{E_x}, \text{ and}\\
\nu_{yz}^{\mathrm{c}} &= 1-\nu_{yx}-\frac{E_y}{3K} \quad \text{with} \quad K = \left[\frac{\upsilon_f}{K_{\mathrm{f}}} + \frac{1-\upsilon_{\mathrm{f}}}{K_m}\right]^{-1},
\end{aligned} \tag{4.26}$$

where K_{m} and K_{f} are the bulk moduli of the constituents.

For a composite with randomly distributed fibers with isotropic behavior, the simple rule of mixtures estimate yields

$$E_{x,y,z}^{\mathrm{c}} = \left(1-\frac{\upsilon_{\mathrm{f}}}{2\pi}\right)E_{\mathrm{m}} + \frac{\upsilon_{\mathrm{f}}}{2\pi}\,E_{\mathrm{f}}, \tag{4.27}$$

where a probability density function is used to specify the random fiber orientation as proposed by Pan [29].

4.C. GENERATION OF PERIODIC SIMULATION BOX

For the generation of periodic fiber distributions in the simulation box, the random sequential adsorption algorithm [36] was implemented. Starting with a box of certain dimensions and knowing the volume fraction, length and diameter of the fibers, for each fiber the coordinates of one end point is determined using the Matlab® `rand` function. Orientation of the fiber is fixed for aligned fibers, while for the randomly distributed fibers, the orientation is determined using the `rand` function. Having the fiber orientation and coordinates of one fiber end point, the coordinates of the second point are determined. If the new point lies outside the simulation box, the out of box segment of the fiber is cut and moved to the opposite boundary to preserve periodicity. This process is repeated for all fibers consecutively until the desired volume fraction is achieved.

REFERENCES

[1] G. Z. Kang and Q. Gao, *Tensile properties of randomly oriented short $\delta - Al_2O_3$ fiber reinforced aluminum alloy composites: II. Finite element analysis for stress transfer, elastic modulus and stress-strain curve,* Composites Part A: Applied Science and Manufacturing **33**, 657 (2002).

[2] H. Berger, S. Kari, U. Gabbert, R. Rodriguez-Ramos, R. Guinovart, J. A. Otero, and J. Bravo-Castillero, *An analytical and numerical approach for calculating effective material coefficients of piezoelectric fiber composites,* International Journal of Solids and Structures **42**, 5692 (2005).

[3] Z. Xia, Y. Zhang, and F. Ellyin, *A unified periodical boundary conditions for representative volume elements of composites and applications,* International Journal of Solids and Structures **40**, 1907 (2003).

[4] B. Mortazavi, M. Baniassadi, J. Bardon, and S. Ahzi, *Modeling of two-phase random composite materials by finite element, Mori-Tanaka and strong contrast methods,* Composites Part B: Engineering **45**, 1117 (2013).

[5] N. Sheng, M. C. Boyce, D. M. Parks, G. C. Rutledge, J. I. Abes, and R. E. Cohen, *Multiscale micromechanical modeling of polymer/clay nanocomposites and the effective clay particle,* Polymer **45**, 487 (2004).

[6] H. R. Lusti and A. A. Gusev, *Finite element predictions for the thermoelastic properties of nanotube reinforced polymers,* Modelling and Simulation in Materials Science and Engineering **12**, S107 (2004).

[7] O. Pierard, C. Friebel, and I. Doghri, *Mean-field homogenization of multi-phase thermo-elastic composites: A general framework and its validation,* Composites Science and Technology **64**, 1587 (2004).

[8] W. Tian, L. Qi, C. Su, J. Zhou, and Z. Jing, *Numerical simulation on elastic properties of short-fiber-reinforced metal matrix composites: Effect of fiber orientation,* Composite Structures **152**, 408 (2016).

[9] R. Andrews, D. Jacques, M. Minot, and T. Rantell, *Fabrication of carbon multiwall nanotube/polymer composites by shear mixing,* Macromolecular Materials and Engineering **287**, 395 (2002).

[10] S. Balakrishnan and D. W. Murray, *Finite element prediction of reinforced concrete behavior*, Structural Engineering Report No. 138 (Department of Civil Engineering, University of Alberta, Edmonton, Alberta, Canada, 1986).

[11] A. E. Elwi and T. M. Hrudey, *Finite element model for curved embedded reinforcement,* Journal of Engineering Mechanics **115**, 740 (1989).

[12] H. Hartl, *Development of a Continuum-Mechanics-Based Tool for 3D Finite Element Analysis of Reinforced Concrete Structures and Application to Problems of Soil-Structure Interaction*, Ph.D. thesis, Graz University of Technology, Austria (2002).

[13] F. Barzegar and S. Maddipudi, *Three-dimensional modeling of concrete structures. II: Reinforced concrete,* Journal of Structural Engineering **123**, 1347 (1997).

[14] J. Ninić, J. Stascheit, and G. Meschke, *Beam-solid contact formulation for finite element analysis of pile-soil interaction with arbitrary discretization,* International Journal for Numerical and Analytical Methods in Geomechanics **38**, 1453 (2014).

[15] F. K. F. Radtke, A. Simone, and L. J. Sluys, *A partition of unity finite element method for obtaining elastic properties of continua with embedded thin fibres,* International Journal for Numerical Methods in Engineering **84**, 708 (2010).

[16] M. G. Pike and C. Oskay, *Three-dimensional modeling of short fiber-reinforced composites with extended finite-element method,* Journal of Engineering Mechanics **142**, 04016087 (2016).

[17] R. Durand, M. M. Farias, and D. M. Pedroso, *Computing intersections between non-compatible curves and finite elements,* Computational Mechanics **56**, 463 (2015).

[18] W. Tian, L. Qi, J. Zhou, and J. Guan, *Effects of the fiber orientation and fiber aspect ratio on the tensile strength of C_{sf}/Mg composites,* Computational Materials Science **89**, 6 (2014).

[19] Z. Y. Wang, H. T. Zhang, and Y. T. Chou, *Characteristics of the elastic field of a rigid line inhomogeneity,* Journal of Applied Mechanics **52**, 818 (1985).

[20] G. Noselli, F. Dal Corso, and D. Bigoni, *The stress intensity near a stiffener disclosed by photoelasticity,* International Journal of Fracture **166**, 91 (2010).

[21] F. Dal Corso, S. Shahzad, and D. Bigoni, *Isotoxal star-shaped polygonal voids and rigid inclusions in nonuniform antiplane shear fields. Part II: Singularities, annihilation and invisibility,* International Journal of Solids and Structures **85**, 76 (2016).

[22] E. Barbieri and N. M. Pugno, *A computational model for large deformations of composites with a 2D soft matrix and 1D anticracks,* International Journal of Solids and Structures **77**, 1 (2015).

[23] M. Duflot, *A meshless method with enriched weight functions for three-dimensional crack propagation,* International Journal for Numerical Methods in Engineering **65**, 1970 (2006).

[24] C.-Q. Ru, *Interface design of neutral elastic inclusions,* International Journal of Solids and Structures **35**, 559 (1998).

[25] Y. Benveniste and T. Miloh, *Neutral inhomogeneities in conduction phenomena,* Journal of the Mechanics and Physics of Solids **47**, 1873 (1999).

[26] B. Budiansky and N. A. Fleck, *Compressive failure of fibre composites,* Journal of the Mechanics and Physics of Solids **41**, 183 (1993).

[27] L. J. Hall, V. R. Coluci, D. S. Galvão, M. E. Kozlov, M. Zhang, S. O. Dantas, and R. H. Baughman, *Sign change of Poisson's ratio for carbon nanotube sheets,* Science **320**, 504 (2008).

[28] M. G. Pike, M. A. Hickman, and C. Oskay, *Interactions between multiple enrichments in extended finite element analysis of short fiber reinforced composites,* International Journal for Multiscale Computational Engineering **13**, 507 (2015).

[29] N. Pan, *The elastic constants of randomly oriented fiber composites: A new approach to prediction,* Science and Engineering of Composite Materials **5**, 63 (1996).

[30] D. Hull and T. W. Clyne, *An Introduction to Composite Materials* (Cambridge University Press, 1996).

[31] J. Willis, *Bounds and self-consistent estimates for the overall properties of anisotropic composites,* Journal of the Mechanics and Physics of Solids **25**, 185 (1977).

[32] S. Nemat-Nasser and M. Hori, *Micromechanics: Overall Properties of Heterogeneous Materials* (Elsevier, 1998).

[33] M. Das and F. C. MacKintosh, *Poisson's ratio in composite elastic media with rigid rods,* Physical Review Letters **105**, 138102 (2010).

[34] M. Malagù, M. Goudarzi, A. Lyulin, E. Benvenuti, and A. Simone, *Diameter-dependent elastic properties of carbon nanotube-polymer composites: Emergence of size effects from atomistic-scale simulations,* Composites Part B: Engineering **131**, 260 (2017).

[35] J. C. Halpin, *Effects of Environmental Factors on Composite Materials.*, Tech. Rep. (AFML-TR 67-423, 1969).

[36] S. Kari, H. Berger, and U. Gabbert, *Numerical evaluation of effective material properties of randomly distributed short cylindrical fibre composites,* Computational Materials Science **39**, 198 (2007).

5

COMPUTATIONAL MODELING OF FIBER-BASED BATTERIES

A dimensionally-reduced embedded formulation is proposed for the numerical modeling of Li-ion batteries characterized by high aspect ratio fiber-based electrodes. Various local and global quantities are analyzed and results are compared to results obtained with the standard finite element method and the porous-electrode theory. The proposed formulation is verified to give reliable predictions at considerably lower computational costs compared to the standard finite element method, hence making it possible to model large number of high aspect ratio fibers. We additionally report physically unexpected numerical predictions of the interface current distributions. This behavior seems to be triggered by the interaction between active inclusions and is also observed when using the standard finite element method.

5.1. INTRODUCTION

Fiber-based active materials are viable replacements to conventional particle-based materials for the design of high performance or multi-functional batteries. The main advantage of nanofibers is their high aspect ratio geometry, which provides large surface area to volume ratio, leading to an enhanced lithium exchange with the surrounding electrolyte material [1]. In this paper, an electro-chemical formulation is developed for fiber-based battery electrodes. For an accurate and computationally efficient representation of the micro-structure, an embedded technique that does not require conformal meshing between active fibers and the electrolyte material is proposed.

There is a trend towards the use of fiber-based active materials, with some of them contributing to the design of high performance or multi-functional lithium ion batteries [1, 2]. The one-dimensional geometry of nanofibers reduces the lithium diffusion pathways in an effective way, with nanofibers being used as anode, cathode, and separators in high

Reprinted from: M. Goudarzi, D. Grazioli and A. Simone, Computational modeling of fiber-based batteries, *to be submitted*.

performance batteries [3]. The use of nanofibers is further facilitated due to advances in production processes such as electrospining [4, 5]. Short fibers or whiskers are also known for their ideal mechanical reinforcing capabilities and have great potentials for use in multi-functional structural batteries [6–8]. In this design, battery components are exposed to certain functional mechanical loadings.

A computational modeling framework that incorporates micro details at an appropriate resolution is crucial for the design of composite batteries. A large part of the existing literature, however, does not explicitly model the heterogeneous micro-structure of composite battery and instead simplifying multiscale numerical strategies are applied [9, 10]. In this framework, the global behavior is usually governed by one-dimensional discretized differential equations, where information regarding the micro-structure is introduced through refined analytical expressions [9]. The main drawback of this approach is that it is suitable for simple configurations of spherical particles, and more importantly, the mutual interactions between inclusions are ignored. Obviously, the microstructure details are of considerable importance as the global response depends on the micro-level response which is in turn influenced by local features such as fiber distribution, homogeneity of the fiber distribution, degree of alignement.

Numerical discretization techniques such as the standard finite element method enable the detailed representation of geometrical features and are proven to give reliable results for the composite batteries [11–16]. Although the application of the standard finite element method to electro-chemical systems is well established and dedicated commercial packages are available, modeling composite electrodes with a complex microstructure requires special attention due to the costly computational efforts associated to mesh generation. The recently published mortar-based approach by Fang *et al.* [16] is a step forward towards reducing mesh generation costs by allowing coarse electrolyte finite element meshes while employing an appropriate discretization for the active material. In their contribution, active material and electrolyte are discretized with non-matching interfaces and a conformal discretization at edges, and the coupling between them is enforced through constraint relations. Although this approach is considerably helpful in many applications, producing a conformal finite element mesh for fiber-based electrodes with high aspect ratio fibers is practically undoable as it could lead to millions of elements even at dilute distributions [17].

Embedded techniques are finite element-based methods that treat cylindrical high aspect ratio fibers as one-dimensional entities [18, 19] that are meshed independently from the surrounding continuum. By means of simple additional kinematic assumptions, discrete fibers can be arbitrarily distributed within the composite's discretized domain, while coupling between the two finite element meshes is assured by an ad-hoc relation that governs the interaction between them.

Embedded methods are mainly applied to mechanical systems in which an imperfect interface is dealt with by specifying a relation between displacement gaps and traction forces at the fiber-matrix interface. In this paper, an analogous computational framework is proposed for electro-chemical systems. The framework considers the coupling between electric potential and concentration in the electrolyte material through the dilute-solution theory described in Section 5.2. The weak formulation is described in Section 5.3 with the corresponding discretized version derived for the standard finite element method and the embedded model in Section 5.4. The coupling between fibers and electrolyte is formu-

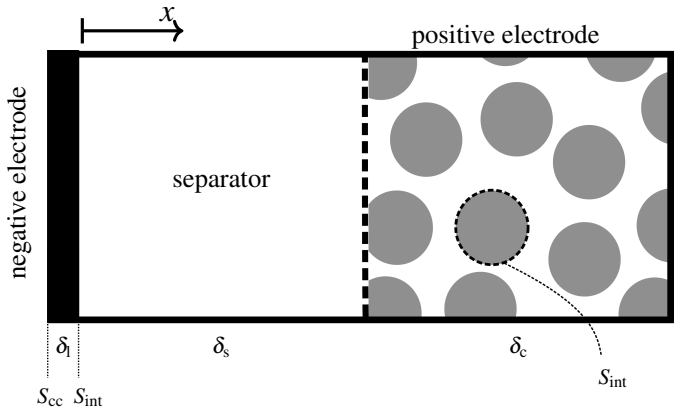

Figure 5.1: Schematic of a conventional half cell with composite particle based cathode [9].

lated by means of interface relations that employ the Butler-Volmer relation [11]. Coupling is achieved by means of additional degrees of freedom (DOFs) defined at the interface between a fiber and the electrolyte material. An important aspect of this work is the assessment of the validy of the assumptions involved in the embedded formulation approach. To this end, the dimensional reduction of fibers from cylindrical objects into one-dimensional lines is studied in detail. A one-to-one comparison between predictions of the embedded model and the standard finite element is conducted for a one-fiber problem in Section 5.5.3, a situation where a conformal finite element mesh can be easily generated. A comparison between the proposed embedded formulation and results obtained with a pseudo-2D model [9] is provided in Section 5.5.4 for a dense fiber composite cathode with more than 10000 high aspect ratio fibers, a situation where a conformal mesh cannot be generated. Special attention is paid to the roles of the interactions between active material fibers and inclusions (neglected in pseudo-2D models [9]) on the current distribution along the interface in Section 5.5.5.

5.2. GOVERNING EQUATIONS

The equations that govern the problem, including the interface conditions that define the interactions between electrode components, are summarized in this section. A schematic representation of the battery cell used in this work is reported in Figure 5.1. The following assumptions are considered:

- to reduce the simulation cost, only half-cells consisting of homogeneous negative electrode, separator, and composite positive electrode are considered in the simulations;
- the positive electrode consist of active material inclusions and the surrounding electrolyte (conductive additives and binder are not explicitly modeled);
- active material and electrolyte occupy two distinct domains; and

- the electrolyte is a binary ionic compound LiX that fully dissociates into Li^+ cations and X^- anions.

We describe processes taking place in the electrolyte by making use of the dilute-solution theory [20]. Models based on dilute-solution theory have been used for the investigation of battery cell geometries in one- [21, 22], two- [23, 24], and three- [25, 26] dimensional settings, either in combination with a porous-electrode theory [23] (electrolyte and active material treated as superimposed continua), or not [24–26] (electrolyte and active material treated as distinct domains). Models based on dilute- and concentrated-solution theories [20] entail the same basic ingredients, but the former present weaker non-linearities. It follows that the dilute-solution theory is suitable for manipulations that permit the derivation of analytical solutions useful for implementation verification (5.6). For these reasons, we consider the dilute-solution theory suitable for testing the novel numerical approach at the core of this study. The tools presented in this contribution are however general, and they can be used irrespective of the constitutive model selected for the electrolyte.

From now on, we identify the active material inclusions in the positive electrode as "active material". In what follows, governing equations are described for the active material and the electrolyte, denoted by subscripts am and el, respectively. The governing equations that refer to the negative electrode (denoted by subscript neg) are equal to those of the active material and are omitted for brevity. Likewise, the corresponding domain of validity of the constitutive equations are indicated with V_k, where k = am, el, or neg.

5.2.1. BULK MATERIAL FORMULATION

The problem is formulated in terms of molar concentration c (number of moles per unit volume) and electric potential ϕ in the active material of the positive electrode, electrolyte, and negative electrode. Material parameters are assumed to be constant unless otherwise indicated.

Active material The active material is responsible for lithium storage and release. Mass and charge balance are assumed to obey, respectively, the relations

$$\frac{\partial c_{\text{am}}}{\partial t} + \operatorname{div} \mathbf{h}_{\text{am}} = 0, \quad \mathbf{x} \in V_{\text{am}},\ t \in [0, t_{\text{end}}), \quad \text{and} \tag{5.1a}$$

$$\operatorname{div} \mathbf{i}_{\text{am}} = 0, \quad \mathbf{x} \in V_{\text{am}},\ t \in [0, t_{\text{end}}). \tag{5.1b}$$

Here, c_{am} and $\mathbf{h}_{\text{am}}$ denote the molar concentration and the mass flux (number of moles per unit time per unit area) of lithium in the active material, respectively, and $\mathbf{i}_{\text{am}}$ is the electric current density (electric charge per unit time per unit area). Fick's law

$$\mathbf{h}_{\text{am}} = -D_{\text{am}} \nabla c_{\text{am}}, \quad \mathbf{x} \in V_{\text{am}},\ t \in [0, t_{\text{end}}) \tag{5.2}$$

describes the mass flux, and Ohm's law

$$\mathbf{i}_{\text{am}} = -\kappa_{\text{am}} \nabla \phi_{\text{am}}, \quad \mathbf{x} \in V_{\text{am}},\ t \in [0, t_{\text{end}}) \tag{5.3}$$

describes the electric current density in the active material, where D_{am} is the lithium diffusivity ($\text{m}^2\ \text{s}^{-1}$) and κ_{am} the electronic conductivity (S m^{-1}). This formulation holds for the negative electrode and each active material inclusion of the composite positive electrode.

Electrolyte The ionic species are responsible for the charge transport through the electrolyte. As customary, we assume that the electroneutrality condition holds, so that the ionic concentrations c_{Li^+} and c_{X^-} reduce to a single molar concentration c_{el} according to

$$c_{\mathrm{Li}^+} = c_{\mathrm{X}^-} = c_{\mathrm{el}}, \quad \mathbf{x} \in V_{\mathrm{el}},\, t \in [0, t_{\mathrm{end}}). \tag{5.4}$$

Details about the implication of (5.4) and the derivation of the governing equations presented in this section can be found in Refs. [22, 24]. A summary is provided for completeness.

In view of (5.4) the set of balance equations in the electrolyte is restricted to

$$\frac{\partial c_{\mathrm{el}}}{\partial t} + \operatorname{div} \mathbf{h}_{\mathrm{el}} = 0, \quad \mathbf{x} \in V_{\mathrm{el}},\, t \in [0, t_{\mathrm{end}}), \quad \text{and} \tag{5.5a}$$

$$\operatorname{div} \mathbf{i}_{\mathrm{el}} = 0, \quad \mathbf{x} \in V_{\mathrm{el}},\, t \in [0, t_{\mathrm{end}}), \tag{5.5b}$$

describing the mass and charge balance, respectively. Here $\mathbf{h}_{\mathrm{el}}$ denotes the apparent mass flux and $\mathbf{i}_{\mathrm{el}}$ is the electric current density in the electrolyte. The Nernst-Plank's equation is used to model the fluxes of ionic species $\mathbf{h}_{\mathrm{Li}^+}$ and $\mathbf{h}_{\mathrm{X}^-}$, and (5.4) allows to perform algebraic manipulations that lead to the following expressions of apparent mass flux

$$\mathbf{h}_{\mathrm{el}} = -D_{\mathrm{el}} \nabla c_{\mathrm{el}}, \quad \mathbf{x} \in V_{\mathrm{el}},\, t \in [0, t_{\mathrm{end}}), \tag{5.6}$$

and electric current density

$$\mathbf{i}_{\mathrm{el}} = \gamma_c \nabla c_{\mathrm{el}} - \gamma_\phi\, c_{\mathrm{el}} \nabla \phi_{\mathrm{el}}, \quad \mathbf{x} \in V_{\mathrm{el}},\, t \in [0, t_{\mathrm{end}}). \tag{5.7}$$

Material parameters are collected into apparent diffusivity

$$D_{\mathrm{el}} = \frac{2 D_{\mathrm{Li}^+} D_{\mathrm{X}^-}}{D_{\mathrm{Li}^+} + D_{\mathrm{X}^-}}, \tag{5.8}$$

and coefficients

$$\gamma_c = F\,(D_{\mathrm{X}^-} - D_{\mathrm{Li}^+}) \quad \text{and} \quad \gamma_\phi = \frac{F^2}{RT}\,(D_{\mathrm{Li}^+} + D_{\mathrm{X}^-}), \tag{5.9}$$

where D_{Li^+} and D_{X^-} are the ionic diffusivities ($\mathrm{m^2\,s^{-1}}$) of the ionic species Li^+ and X^-, respectively, $F = 96485.3$ C mol^{-1} is the Faraday's constant, $R = 8.31447$ J K^{-1} mol^{-1} is the ideal gas constant, and T is the absolute temperature (K).

5.2.2. INTERFACE CONDITIONS

Continuity of the electric current density across the active material inclusion-electrolyte interface S_{int} is enforced through

$$\mathbf{i}_{\mathrm{am}} \cdot \mathbf{n}_{\mathrm{am}} = -\mathbf{i}_{\mathrm{el}} \cdot \mathbf{n}_{\mathrm{el}} = \lambda, \quad \mathbf{x} \in S_{\mathrm{int}},\, t \in [0, t_{\mathrm{end}}), \tag{5.10}$$

where $\mathbf{n}_{\mathrm{am}}$ and $\mathbf{n}_{\mathrm{el}}$ are the outward normals with respect to the electrode and electrolyte domains, respectively, and $\mathbf{n}_{\mathrm{el}} = -\mathbf{n}_{\mathrm{am}}$. The term λ quantifies the charge transfer across the

interface and, according to Faraday's law, it is related to the lithium transfer through

$$\mathbf{h}_{\text{am}} \cdot \mathbf{n}_{\text{am}} = \frac{1}{F}\lambda, \quad \mathbf{x} \in S_{\text{int}},\ t \in [0, t_{\text{end}}), \quad \text{and} \tag{5.11a}$$

$$\mathbf{h}_{\text{el}} \cdot \mathbf{n}_{\text{el}} = -\frac{1}{F}\frac{D_{\text{X}^-}}{D_{\text{Li}^+} + D_{\text{X}^-}}\lambda, \quad \mathbf{x} \in S_{\text{int}},\ t \in [0, t_{\text{end}}). \tag{5.11b}$$

Interface condition (5.11b) is obtained considering that while cations are transferred across the interface ($\mathbf{h}_{\text{Li}^+} \cdot \mathbf{n}_{\text{el}} = -\lambda/F$), anions are not ($\mathbf{h}_{\text{X}^-} \cdot \mathbf{n}_{\text{el}} = 0$) [22, 24].

The charge transfer λ is usually related to the values of the field variables at the two sides of the interface through equations that describe the electrochemical reaction. For the sake of generality, we express this relationship as

$$\lambda = g_{\text{int}}\left(\phi_{\text{am}}, \phi_{\text{el}}, c_{\text{am}}, c_{\text{el}}\right), \quad \mathbf{x} \in S_{\text{int}},\ t \in [0, t_{\text{end}}), \tag{5.12}$$

where g_{int} is a known function of field variables along the interface. Explicit expressions for g_{int} are provided in Section 5.5.2.

5

5.2.3. BOUNDARY CONDITIONS

We exclusively simulate galvanostatic discharge processes. To this end, we apply boundary conditions on the left hand side edge of the negative electrode (at $x = -\delta_{\text{l}}$ with reference to the choice of the coordinate system in Figure 5.1) as follows:

$$\mathbf{i} \cdot \mathbf{n}_{\text{neg}} = -I, \quad x = -\delta_{\text{l}}, \tag{5.13a}$$

$$\mathbf{h}_{\text{Li}} \cdot \mathbf{n}_{\text{neg}} = 0, \quad x = -\delta_{\text{l}}, \tag{5.13b}$$

where $\mathbf{n}_{neg}$ is the outward normal with respect to the negative electrode. According to (5.13a), a positive value of I represents a discharge process, i.e., lithium is extracted from the lithium foil and is inserted into the positive active material at the positive electrode. In the positive electrode, we assume there exists a fictitious electronic conductive network superimposed to the active material inclusions. We assume that the network is capable to keep all the active material inclusions at the same electric potential and that no lithium exchange occurs between the active material and the fictitious conductive network. We assume that the electric potential of all the active material inclusions is identically equal to zero:

$$\phi_{\text{am}} = 0, \quad \forall x \in [\delta_{\text{s}}, \delta_{\text{s}} + \delta_{\text{c}}]. \tag{5.14}$$

5.2.4. INITIAL CONDITIONS

To solve the governing equations, initial conditions must be considered. We assume initial concentration of lithium to be uniform at $t = 0$ inside each cell component, according to

$$c_{\text{el}} = c^0_{\text{el}}, \quad \mathbf{x} \in V_{\text{el}}, t = 0, \tag{5.15a}$$

$$c_{\text{am}} = c^0_{\text{am}}, \quad \mathbf{x} \in V_{\text{am}}, t = 0, \tag{5.15b}$$

$$c_{\text{neg}} = c^0_{\text{neg}}, \quad \mathbf{x} \in V_{\text{neg}}, t = 0, \tag{5.15c}$$

where c^0_{el}, c^0_{am}, and c^0_{neg} are assigned.

The initial values of the electric potentials are determined solving equations (5.1-5.3) and (5.5-5.7) under equilibrium condition (*i.e.*, setting time derivatives to zero), with boundary conditions (5.13), (5.14), and $I = 0$. Under these conditions, the charge transfer λ is identically equal to zero at each active material-electrolyte interface. The equilibrium potentials in the negative electrode, electrolyte, and active material in the positive electrode are determined inverting (5.12).

5.3. WEAK FORM

Following a general Galerkin approach, weak forms of the governing equations are obtained for sub-domains V_{am}, V_{el}, and V_{neg}. The formulation provided here for the active material inclusions equally applies to the negative electrode (not reported for sake of conciseness).

The weak forms of charge and mass balance (5.1) defined over the active material volume V_{am} read

$$\kappa_{\text{am}} \int_{V_{\text{am}}} \nabla \hat{\phi}_{\text{am}} \cdot \nabla \phi_{\text{am}} \; \mathrm{d}V + \int_{S_{\text{int}}} \hat{\phi}_{\text{am}} \; \lambda \; \mathrm{d}S = 0, \tag{5.16a}$$

$$\int_{V_{\text{am}}} \hat{c}_{\text{am}} \frac{\partial c_{\text{am}}}{\partial t} \; \mathrm{d}V + D_{\text{am}} \int_{V_{\text{am}}} \nabla \hat{c}_{\text{am}} \cdot \nabla c_{\text{am}} \; \mathrm{d}V + \int_{S_{\text{int}}} \hat{c}_{\text{am}} \; \frac{1}{F} \lambda \; \mathrm{d}S = 0, \tag{5.16b}$$

analogously, the weak forms of (5.5) defined over the electrolyte volume V_{el} read

$$\gamma_\phi \int_{V_{\text{el}}} \nabla \hat{\phi}_{\text{el}} \cdot c_{\text{el}} \nabla \phi_{\text{el}} \; \mathrm{d}V - \gamma_c \int_{V_{\text{el}}} \nabla \hat{\phi}_{\text{el}} \cdot \nabla c_{\text{el}} \; \mathrm{d}V - \int_{S_{\text{int}}} \hat{\phi}_{\text{el}} \; \lambda \; \mathrm{d}S = 0, \tag{5.17a}$$

$$\int_{V_{\text{el}}} \hat{c}_{\text{el}} \frac{\partial c_{\text{el}}}{\partial t} \; \mathrm{d}V + D_{\text{el}} \int_{V_{\text{el}}} \nabla \hat{c}_{\text{el}} \cdot \nabla c_{\text{el}} \; \mathrm{d}V - \int_{S_{\text{int}}} \hat{c}_{\text{el}} \; \frac{1}{F} \frac{D_{\text{X}^-}}{D_{\text{Li}^+} + D_{\text{X}^-}} \lambda \; \mathrm{d}S = 0, \tag{5.17b}$$

where $\hat{\phi}$ and $\hat{c}$ indicate admissible test functions. The last terms at left-hand side of each equation in (5.16) and (5.17) account for the charge (5.10) and lithium (5.11) transfer across the active material inclusions-electrolyte interface S_{int}. The definition of the charge transfer λ (5.12) completes the formulation, and it is applied along the interface in its weak form

$$\int_{S_{\text{int}}} \hat{\lambda} \Big(\lambda - g_{\text{int}} \left(\phi_{\text{am}}, \phi_{\text{el}}, c_{\text{am}}, c_{\text{el}} \right) \Big) \; \mathrm{d}S = 0, \tag{5.18}$$

where $\hat{\lambda}$ represents the admissible test function restricted to the interface S_{int}.

To avoid convergence issues from an ill-conditioned tangent matrix, the weak forms (5.16) and (5.17) are recast into their corresponding non-dimensional equivalent [27, 28]. This is achieved by dividing (5.16a) and (5.17a) by

$$\left(D_{\text{Li}^+} + D_{\text{X}^-} \right) \, RT \, c_{\text{ref}} \, l_{\text{ref}}, \tag{5.19}$$

and (5.16b) and (5.17b) by

$$\frac{c_{\text{ref}}^2 \, {l_{\text{ref}}}^3}{\Delta t}. \tag{5.20}$$

Terms c_{ref} and l_{ref} represent a reference concentration (here $c_{\text{ref}} = c_{\text{el}}^0$) and a characteristic length of the problem, respectively, and Δt (expressed in seconds) represents the time increment used in the numerical simulations. Furthermore, non-dimensional field variables

are defined as

$$\phi^* = \frac{F}{RT}\,\phi \qquad \text{and} \qquad c^* = \frac{1}{c_{\text{ref}}}\,c\,, \tag{5.21}$$

which upon using, the weak forms (5.16) change to the non-dimensional form

$$\begin{aligned} &\Upsilon_1^{\text{am}} \int_{V_{\text{am}}} \nabla\hat{\phi}^* \cdot \nabla\phi^* \;\mathrm{d}V + \Upsilon_2^{\text{am}} \int_{S_{\text{int}}} \hat{\phi}^* \;\lambda\; \mathrm{d}S = 0\,, \\ &\Upsilon_3^{\text{am}} \int_{V_{\text{am}}} \hat{c}^* \frac{\partial c^*}{\partial t} \;\mathrm{d}V + \Upsilon_4^{\text{am}} \int_{V_{\text{am}}} \nabla\hat{c}^* \cdot \nabla c^* \;\mathrm{d}V + \Upsilon_5^{\text{am}} \int_{S_{\text{int}}} \hat{c}^* \;\lambda\; \mathrm{d}S = 0\,, \end{aligned} \tag{5.22}$$

and the weak forms (5.17) become

$$\begin{aligned} &\Upsilon_1^{\text{el}} \int_{V_{\text{el}}} \nabla\hat{\phi}^* \cdot c^* \nabla\phi^* \;\mathrm{d}V - \Upsilon_2^{\text{el}} \int_{V_{\text{el}}} \nabla\hat{\phi}^* \cdot \nabla c^* \;\mathrm{d}V - \Upsilon_3^{\text{el}} \int_{S_{\text{int}}} \hat{\phi}^* \;\lambda\; \mathrm{d}S = 0\,, \\ &\Upsilon_4^{\text{el}} \int_{V_{\text{el}}} \hat{c}^* \frac{\partial c^*}{\partial t} \;\mathrm{d}V + \Upsilon_5^{\text{el}} \int_{V_{\text{el}}} \nabla\hat{c}^* \cdot \nabla c^* \;\mathrm{d}V - \Upsilon_6^{\text{el}} \int_{S_{\text{int}}} \hat{c}^* \;\lambda\; \mathrm{d}S = 0\,. \end{aligned} \tag{5.23}$$

The subscript am and el have been omitted to lighten the notation.

Coefficients

$$\Upsilon_1^{\text{am}} = \frac{\kappa_{\text{am}}\,RT}{(D_{\text{Li}^+} + D_{\text{X}^-})\,F^2\,c_{\text{ref}}\,l_{\text{ref}}}\,, \qquad \Upsilon_2^{\text{am}} = \frac{1}{(D_{\text{Li}^+} + D_{\text{X}^-})\,F\,c_{\text{ref}}\,l_{\text{ref}}}\,, \tag{5.24a}$$

$$\Upsilon_3^{\text{am}} = \frac{\Delta t}{{l_{\text{ref}}}^3}\,, \qquad \Upsilon_4^{\text{am}} = \frac{D\,\Delta t}{{l_{\text{ref}}}^3}\,, \qquad \Upsilon_5^{\text{am}} = \frac{1}{F}\,\frac{\Delta t}{c_{\text{ref}}\,{l_{\text{ref}}}^3}\,, \tag{5.24b}$$

are defined for the active material inclusions, and coefficients

$$\Upsilon_1^{\text{el}} = \frac{1}{l_{\text{ref}}}\,, \qquad \Upsilon_2^{\text{el}} = \frac{1}{l_{\text{ref}}}\,\frac{D_{\text{Li}^+} - D_{\text{X}^-}}{D_{\text{Li}^+} + D_{\text{X}^-}}\,, \qquad \Upsilon_3^{\text{el}} = \frac{1}{(D_{\text{Li}^+} + D_{\text{X}^-})\,F\,c_{\text{ref}}\,l_{\text{ref}}} \tag{5.25a}$$

$$\Upsilon_4^{\text{el}} = \Upsilon_3^{\text{am}}\,, \qquad \Upsilon_5^{\text{el}} = \Upsilon_4^{\text{am}}\,, \qquad \Upsilon_6^{\text{el}} = \frac{1}{F}\,\frac{D_{\text{X}^-}}{D_{\text{Li}^+} + D_{\text{X}^-}}\,\frac{\Delta t}{c_{\text{ref}}\,{l_{\text{ref}}}^3}\,. \tag{5.25b}$$

are defined for the electrolyte.

5.4. NUMERICAL ELABORATION

The weak formulation described in the previous section is discretized using the finite element method. Numerical features are first described for a standard model with conformal mesh between active materials and electrolyte. The mesh conformity restriction however makes the standard approach expensive when high aspect ratio fibers are considered. Therefore a modified version of the standard model which is tailored for high aspect ratio fibers and allows fibers to be distributed within the electrolyte mesh is described in Section 5.4.5.

5.4.1. SPATIAL DISCRETIZATION

Electrodes and electrolyte are discretized using conventional elements in the context of the finite element method: hexahedral (H8) or tetrahedral (T4) element types in three-dimensional settings and triangular (T3) element types in two-dimensional settings. The

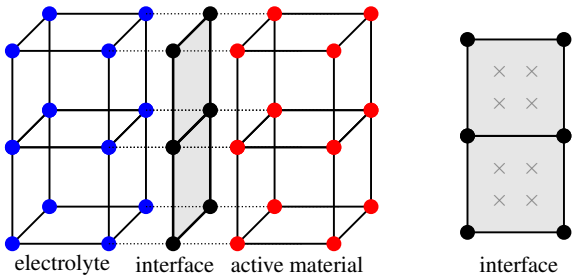

Figure 5.2: (a) Coupling between the electrolyte (blue nodes) and active material (red nodes) in the standard finite element model with Lagrange DOFs assigned at the interface (black nodes). (b) The interface elements and integration points.

approximated electric potential and concentration fields at any arbitrary domain point are

$$\phi^*(\boldsymbol{x}) = \sum_{i=1}^{n} N_i(\boldsymbol{x})\,\phi_i^* \quad \text{and} \quad c^*(\boldsymbol{x}) = \sum_{i=1}^{n} N_i(\boldsymbol{x})\,c_i^*, \tag{5.26}$$

where N_i are the standard element nodal shape functions and n is the number of element nodes. Here no distinction is made between active materials and electrolyte on the way field variables are interpolated.

Along the active material-electrolyte interface S_{int} (black nodes in Figure 5.2), we introduce an additional set of variables to evaluate the local charge transfer λ. These variables act as Lagrange multipliers that enforce the continuity equations (5.10) and (5.11). The exchanged current at an arbitrary point located along the active material-electrolyte interface is thus approximated as

$$\lambda(\boldsymbol{x}) = \sum_{i=1}^{m} M_i(\boldsymbol{x})\,\lambda_i, \tag{5.27}$$

where M_i are the interface element nodal shape functions, m is the number of nodes at each interface element.

In a 3-D context, Q4 and T3 elements are used for the interface discretization when H8 and T4 element types are used for the bulk domains, respectively. In a 2-D context, linear (L2) element type are used for the discretization of the interface. A sample 3-D discretization is shown in Figure 5.2, where H8 are used for both active material (red nodes) and electrolyte (blue nodes) bulk regions, and Q4 elements are used for the interface.

5.4.2. TIME DISCRETIZATION AND ITERATIVE SCHEME

A backward-Euler integration scheme is used to transform the time-continuum system of equations (5.22), (5.23) and (5.18) into its incremental form. The finite element approximation described in Sec. 5.4.1 is adopted for the spatial discretization. By gathering all the element contributions $\mathbf{a}_e$ (5.34) into vector $\mathbf{a}$, the problem reduces to finding $\mathbf{a}_{n+1}$ at time $t_{n+1} = t_n + \Delta t$ such that the incremental finite element equation

$$\mathbf{r}(\mathbf{a}_{n+1}) \equiv \mathbf{f}^{\,\text{int}}(\mathbf{a}_{n+1}) - \mathbf{f}^{\text{ext}}_{n+1} = \mathbf{0} \tag{5.28}$$

is satisfied. In computational mechanics approaches [29], $\mathbf{f}^{\text{int}}$ and $\mathbf{f}^{\text{ext}}$ are the so-called internal force vector (function of the solution vector $\mathbf{a}$ evaluated at time t_{n+1}) and the external force vector (gathering Neumann boundary conditions evaluated at t_{n+1}), respectively.

A Newton-Raphson iterative scheme is used to address the non-linearities of the governing equations. At each iteration k of the Newton-Raphson iterative scheme, the linear system of equations

$$\mathbf{K}\,\delta\mathbf{a}^k = -\mathbf{r}^{k-1} \tag{5.29}$$

is solved for $\delta\mathbf{a}^k$ where the residual vector

$$\mathbf{r}^{k-1} \equiv \mathbf{f}^{\text{int}}\left(\mathbf{a}_{n+1}^{k-1}\right) - \mathbf{f}_{n+1}^{\text{ext}} \tag{5.30}$$

and the global tangent matrix

$$\mathbf{K} = \left.\frac{\partial \mathbf{r}}{\partial \mathbf{a}_{n+1}}\right|_{\mathbf{a}_{n+1}^{k-1}}. \tag{5.31}$$

The solution $\delta\mathbf{a}^k$ of the linear system (5.29) is applied to correct the vector of nodal unknowns

$$\mathbf{a}_{n+1}^{k} = \mathbf{a}_{n+1}^{k-1} + \delta\mathbf{a}^k. \tag{5.32}$$

The subscript $n+1$ and superscript $k-1$ emphasize that the nodal values refer to time step t_{n+1} at the $k-1$-th iteration. Explicit expressions for the tangent matrices and residual vectors for the Newton-Raphson iteration scheme (5.29) computed at the element level are provided below.

5.4.3. ELEMENT LEVEL IMPLEMENTATION

Attention is restricted in this section to the formulation of quantities at the element level. Expressions of nodal vectors and operators employed in the numerical implementation are provided. The nodal variables defined at the element level for either active materials or electrolyte are

$$\boldsymbol{\phi}_e = \begin{bmatrix}\phi_1^* & \dots & \phi_n^*\end{bmatrix}^T, \tag{5.33a}$$

$$\mathbf{c}_e = \begin{bmatrix}c_1^* & \dots & c_n^*\end{bmatrix}^T, \tag{5.33b}$$

$$\boldsymbol{\lambda}_e = \begin{bmatrix}\lambda_1 & \dots & \lambda_m\end{bmatrix}^T, \tag{5.33c}$$

and are gathered through the vector of element nodal unknowns

$$\mathbf{a}_e = \{\boldsymbol{\phi}_e, \mathbf{c}_e, \boldsymbol{\lambda}_e\}. \tag{5.34}$$

Vectors

$$\mathbf{N} = \begin{bmatrix}N_1(\boldsymbol{x}) & \dots & N_n(\boldsymbol{x})\end{bmatrix} \tag{5.35}$$

and

$$\mathbf{M} = \begin{bmatrix}M_1(\boldsymbol{x}) & \dots & M_n(\boldsymbol{x})\end{bmatrix} \tag{5.36}$$

collect the nodal shape functions of bulk and interface elements, respectively, and the array

$$\mathbf{B}_{\text{grad}} = \begin{bmatrix} \dfrac{\partial N_1}{\partial x} & \cdots & \dfrac{\partial N_n}{\partial x} \\ \dfrac{\partial N_1}{\partial y} & \cdots & \dfrac{\partial N_n}{\partial y} \\ \dfrac{\partial N_1}{\partial z} & \cdots & \dfrac{\partial N_n}{\partial z} \end{bmatrix} \tag{5.37}$$

defines the discrete gradient operator.

Active material sub-matrices The contributions to the element residual vector and tangent matrix that follow from the space-time discretization of (5.22) read

$$\begin{aligned} \mathbf{r}^{\phi}_{\text{am}e} &= \Upsilon^{\text{am}}_1 \int_{V_{\text{am}e}} \mathbf{B}^T_{\text{grad}} \ \mathbf{B}_{\text{grad}} \boldsymbol{\phi}^{\text{am}}_e \ \mathrm{d}V \,, \\ \mathbf{r}^{c}_{\text{am}e} &= \frac{1}{\Delta t} \Upsilon^{\text{am}}_3 \int_{V_{\text{am}e}} \mathbf{N}^T \ \mathbf{N} \Delta \mathbf{c}^{\text{am}}_e \ \mathrm{d}V + \Upsilon^{\text{am}}_4 \int_{V_{\text{am}e}} \mathbf{B}^T_{\text{grad}} \ \mathbf{B}_{\text{grad}} \boldsymbol{c}^{\text{am}}_e \ \mathrm{d}V \,, \end{aligned} \tag{5.38}$$

and

$$\begin{aligned} \mathbf{K}^{\phi\,\phi}_{\text{am}e} &= \frac{\partial \mathbf{r}^{\phi}_e}{\partial \phi_{\text{am}}} = \Upsilon^{\text{am}}_1 \int_{V_{\text{am}e}} \mathbf{B}^T_{\text{grad}} \mathbf{B}_{\text{grad}} \ \mathrm{d}V \,, \\ \mathbf{K}^{c\,c}_{\text{am}e} &= \frac{\partial \mathbf{r}^{c}_e}{\partial \mathbf{c}_{\text{am}}} = \frac{1}{\Delta t} \Upsilon^{\text{am}}_3 \int_{V_{\text{am}e}} \mathbf{N}^T \mathbf{N} \ \mathrm{d}V + \Upsilon^{\text{am}}_4 \int_{V_{\text{am}e}} \mathbf{B}^T_{\text{grad}} \mathbf{B}_{\text{grad}} \ \mathrm{d}V \,, \end{aligned} \tag{5.39}$$

respectively. Vectors $\boldsymbol{\phi}^{\text{am}}_e$ and $\boldsymbol{c}^{\text{am}}_e$ refer to the electric potential and concentration of the active material at current time step t_{n+1} and previous iteration $k-1$. The concentration increment is defined as

$$\Delta \mathbf{c}^{\text{am}}_e = \mathbf{c}^{\text{am}}_{e,n+1} - \mathbf{c}^{\text{am}}_{e,n} \,, \tag{5.40}$$

being $\mathbf{c}^{\text{am}}_{e,n}$ the vector containing the converged solution for (5.33b) at the previous time increment t_n.

Electrolyte sub-matrices The contributions to the element residual vector and tangent matrix that follow from the space-time discretization (5.23) read

$$\begin{aligned} \mathbf{r}^{\phi}_{\text{el}e} &= \Upsilon^{\text{el}}_1 \int_{V_{\text{el}e}} \mathbf{B}^T_{\text{grad}} \ \mathbf{B}_{\text{grad}} \boldsymbol{\phi}^{\text{el}}_e \ \mathbf{N} \mathbf{c}^{\text{el}}_e \ \mathrm{d}V - \Upsilon^{\text{el}}_2 \int_{V_{\text{el}e}} \mathbf{B}^T_{\text{grad}} \ \mathbf{B}_{\text{grad}} \mathbf{c}^{\text{el}}_e \ \mathrm{d}V \,, \\ \mathbf{r}^{c}_{\text{el}e} &= \frac{1}{\Delta t} \Upsilon^{\text{el}}_4 \int_{V_{\text{el}e}} \mathbf{N}^T \ \mathbf{N} \Delta \mathbf{c}^{\text{el}}_e \ \mathrm{d}V + \Upsilon^{\text{el}}_5 \int_{V_{\text{el}e}} \mathbf{B}^T_{\text{grad}} \ \mathbf{B}_{\text{grad}} \mathbf{c}^{\text{el}}_e \ \mathrm{d}V \,. \end{aligned} \tag{5.41}$$

and

$$\begin{aligned} \mathbf{K}^{\phi\,\phi}_{\text{el}e} &= \frac{\partial \mathbf{r}^{\phi}_e}{\partial \phi_{\text{el}}} = \Upsilon^{\text{el}}_1 \int_{V_{\text{el}e}} \mathbf{B}^T_{\text{grad}} \mathbf{B}_{\text{grad}} \ \mathbf{N} \mathbf{c}^{\text{el}}_e \ \mathrm{d}V \,, \\ \mathbf{K}^{\phi\,c}_{\text{el}e} &= \frac{\partial \mathbf{r}^{\phi}_e}{\partial \mathbf{c}_{\text{el}}} = \Upsilon^{\text{el}}_1 \int_{V_{\text{el}e}} \mathbf{B}^T_{\text{grad}} \ \mathbf{B}_{\text{grad}} \boldsymbol{\phi}^{\text{el}}_e \ \mathbf{N} \ \mathrm{d}V - \Upsilon^{\text{el}}_2 \int_{V_{\text{el}e}} \mathbf{B}^T_{\text{grad}} \mathbf{B}_{\text{grad}} \ \mathrm{d}V \,, \\ \mathbf{K}^{c\,c}_{\text{el}e} &= \frac{\partial \mathbf{r}^{c}_e}{\partial \mathbf{c}_{\text{el}}} = \frac{1}{\Delta t} \Upsilon^{\text{el}}_4 \int_{V_{\text{el}e}} \mathbf{N}^T \mathbf{N} \ \mathrm{d}V + \Upsilon^{\text{el}}_5 \int_{V_{\text{el}e}} \mathbf{B}^T_{\text{grad}} \mathbf{B}_{\text{grad}} \ \mathrm{d}V \,, \end{aligned} \tag{5.42}$$

respectively. Vectors $\boldsymbol{\phi}_e^{\text{el}}$ and $\mathbf{c}_e^{\text{el}}$ refer to the electrolyte electric potential and concentration vectors at current time step t_{n+1} and iteration $k-1$.

Interface sub-matrices The spatial discretization of charge and lithium exchange terms is limited to active material inclusions-electrolyte (and negative electrode-electrolyte) interfaces, and it involves the usage of shape functions (5.36). The residual vectors corresponding to the last term in each of the equations in weak forms (5.22) and (5.23) read

$$\mathbf{r}_{\text{am}e}^{\phi\lambda} = \Upsilon_2^{\text{el}} \int_{S_{\text{int}e}} \mathbf{M}^{\text{T}}\mathbf{M}\boldsymbol{\lambda}_e \ \text{d}S, \qquad \mathbf{r}_{\text{am}e}^{c\lambda} = \Upsilon_5^{\text{am}} \int_{S_{\text{int}e}} \mathbf{M}^{\text{T}}\mathbf{M}\boldsymbol{\lambda}_e \ \text{d}S, \tag{5.43}$$

and

$$\mathbf{r}_{\text{el}e}^{\phi\lambda} = -\Upsilon_3^{\text{el}} \int_{S_{\text{int}e}} \mathbf{M}^{\text{T}}\mathbf{M}\boldsymbol{\lambda}_e \ \text{d}S, \qquad \mathbf{r}_{\text{el}e}^{c\lambda} = -\Upsilon_6^{\text{el}} \int_{S_{\text{int}e}} \mathbf{M}^{\text{T}}\mathbf{M}\boldsymbol{\lambda}_e \ \text{d}S, \tag{5.44}$$

respectively. The discretization of weak form (5.18) leads to

$$\mathbf{r}_{\text{int}e}^{\lambda} = \int_{S_{\text{int}}} \mathbf{M}^{\text{T}}\mathbf{M}\boldsymbol{\lambda}_e \ \text{d}S - \int_{S_{\text{int}}} \mathbf{M}^{\text{T}} \ g_{\text{int}}\left(\mathbf{M}\boldsymbol{\phi}_e^{\text{am}}, \mathbf{M}\boldsymbol{\phi}_e^{\text{el}}, \mathbf{M}\mathbf{c}_e^{\text{am}}, \mathbf{M}\mathbf{c}_e^{\text{el}}\right) \ \text{d}S. \tag{5.45}$$

The contribution of the interface terms to the tangent matrix are evaluated as follows

$$\begin{aligned}
\mathbf{C}_{\text{am}e}^{\phi\lambda} &= \frac{\mathbf{r}_{\text{am}e}^{\phi\lambda}}{\partial\boldsymbol{\lambda}_e} = \Upsilon_2^{\text{am}} \int_{S_{\text{int}e}} \mathbf{M}^{\text{T}}\mathbf{M} \ \text{d}S, & \mathbf{C}_{\text{el}e}^{\phi\lambda} &= \frac{\mathbf{r}_{\text{el}e}^{\phi\lambda}}{\partial\boldsymbol{\lambda}_e} = -\Upsilon_3^{\text{el}} \int_{S_{\text{int}e}} \mathbf{M}^{\text{T}}\mathbf{M} \ \text{d}S, \\
\mathbf{C}_{\text{am}e}^{c\lambda} &= \frac{\mathbf{r}_{\text{am}e}^{c\lambda}}{\partial\boldsymbol{\lambda}_e} = \Upsilon_5^{\text{am}} \int_{S_{\text{int}e}} \mathbf{M}^{\text{T}}\mathbf{M} \ \text{d}S, & \mathbf{C}_{\text{el}e}^{c\lambda} &= \frac{\mathbf{r}_{\text{el}e}^{c\lambda}}{\partial\boldsymbol{\lambda}_e} = -\Upsilon_6^{\text{el}} \int_{S_{\text{int}e}} \mathbf{M}^{\text{T}}\mathbf{M} \ \text{d}S, \\
\mathbf{C}_{\text{int}e}^{\lambda\phi_{\text{am}}} &= \frac{\partial\mathbf{r}_{\text{int}e}^{\lambda}}{\partial\boldsymbol{\phi}_e^{\text{am}}} = -\int_{S_{\text{int}e}} \mathbf{M}^{\text{T}} \frac{\partial g_{\text{int}}}{\partial\boldsymbol{\phi}_e^{\text{am}}} \ \text{d}S, \\
\mathbf{C}_{\text{int}e}^{\lambda c_{\text{am}}} &= \frac{\partial\mathbf{r}_{\text{int}e}^{\lambda}}{\partial\mathbf{c}_e^{\text{am}}} = -\int_{S_{\text{int}e}} \mathbf{M}^{\text{T}} \frac{\partial g_{\text{int}}}{\partial\mathbf{c}_e^{\text{am}}} \ \text{d}S, \\
\mathbf{C}_{\text{int}e}^{\lambda\phi_{\text{el}}} &= \frac{\partial\mathbf{r}_{\text{int}e}^{\lambda}}{\partial\boldsymbol{\phi}_e^{\text{el}}} = -\int_{S_{\text{int}e}} \mathbf{M}^{\text{T}} \frac{\partial g_{\text{int}}}{\partial\boldsymbol{\phi}_e^{\text{el}}} \ \text{d}S, \\
\mathbf{C}_{\text{int}e}^{\lambda c_{\text{el}}} &= \frac{\partial\mathbf{r}_{\text{int}e}^{\lambda}}{\partial\mathbf{c}_e^{\text{el}}} = -\int_{S_{\text{int}e}} \mathbf{M}^{\text{T}} \frac{\partial g_{\text{int}}}{\partial\mathbf{c}_e^{\text{el}}} \ \text{d}S, \\
\mathbf{C}_{\text{int}e}^{\lambda\lambda} &= \frac{\mathbf{r}_{\text{int}e}^{\lambda}}{\partial\boldsymbol{\lambda}_e} = \int_{S_{\text{int}e}} \mathbf{M}^{\text{T}}\mathbf{M} \ \text{d}S.
\end{aligned} \tag{5.46}$$

Vectors $\boldsymbol{\phi}_e^{\text{am}}$, $\boldsymbol{c}_e^{\text{am}}$, $\boldsymbol{\phi}_e^{\text{el}}$, and $\mathbf{c}_e^{\text{el}}$ used to compute g_{int} and its derivatives, as well as vector $\boldsymbol{\lambda}_e$ are evaluated at current time step t_{n+1} and iteration $k-1$.

5.4.4. GLOBAL SYSTEM OF EQUATIONS AND LAGRANGE MULTIPLIERS

When standard finite elements are employed, active material inclusions, electrolyte, and negative electrode occupies distinct domains. Conformal meshes are used for the discretization of different domains, but without sharing nodes. Couples of nodes with the

same coordinates are generated along the active material inclusions-electrolyte and negative electrode-electrolyte interfaces S_{int}. For each i-th couple of nodes a Lagrange multiplier λ_i is introduced among the unknowns $\mathbf{a}$.

The set of unknowns that pertains to the active material and electrolyte, together with global residual vector and tangent matrix can be expressed as follows:

$$\delta\mathbf{a} = \begin{bmatrix} \delta\boldsymbol{\phi}_{\text{am}} \\ \delta\mathbf{c}_{\text{am}} \\ \delta\boldsymbol{\phi}_{\text{el}} \\ \delta\mathbf{c}_{\text{el}} \\ \delta\boldsymbol{\lambda} \end{bmatrix}, \mathbf{r} = \begin{bmatrix} \mathbf{r}^{\phi}_{\text{am}} + \mathbf{r}^{\phi\lambda}_{\text{am}} \\ \mathbf{r}^{c}_{\text{am}} + \mathbf{r}^{c\lambda}_{\text{am}} \\ \mathbf{r}^{\phi}_{\text{el}} + \mathbf{r}^{\phi\lambda}_{\text{el}} \\ \mathbf{r}^{c}_{\text{el}} + \mathbf{r}^{c\lambda}_{\text{el}} \\ \mathbf{r}^{\lambda}_{\text{int}} \end{bmatrix}, \mathbf{K} = \begin{bmatrix} \mathbf{K}^{\phi\phi}_{\text{am}} & 0 & 0 & 0 & \mathbf{C}^{\phi\lambda}_{\text{am}} \\ 0 & \mathbf{K}^{cc}_{\text{am}} & 0 & 0 & \mathbf{C}^{c\lambda}_{\text{am}} \\ 0 & 0 & \mathbf{K}^{\phi\,\phi}_{\text{el}} & \mathbf{K}^{\phi\,c}_{\text{el}} & \mathbf{C}^{\phi\lambda}_{\text{el}} \\ 0 & 0 & 0 & \mathbf{K}^{c\,c}_{\text{el}} & \mathbf{C}^{c\lambda}_{\text{el}} \\ \mathbf{C}^{\lambda\phi_{\text{am}}}_{\text{int}} & \mathbf{C}^{\lambda c_{\text{am}}}_{\text{int}} & \mathbf{C}^{\lambda\phi_{\text{el}}}_{\text{int}} & \mathbf{C}^{\lambda c_{\text{el}}}_{\text{int}} & \mathbf{C}^{\lambda\lambda}_{\text{int}} \end{bmatrix}, \tag{5.47}$$

where each of the matrices $\mathbf{K}^{ij}_{\text{am}}$ and $\mathbf{K}^{kl}_{\text{el}}$ collects the contributions of the corresponding element tangent matrices $\mathbf{K}^{ij}_{\text{am}e}$ and $\mathbf{K}^{kl}_{\text{el}e}$ assembled over the active material and electrolyte domains, respectively. The representation in (5.47) is aimed at emphasizing the relationship established through the Lagrange multipliers between nodal quantities that belong to different domains. The same approach is applied at the negative electrode-electrolyte interface.

5.4.5. DIMENSIONALLY-REDUCED FIBER MODEL

We introduce a dimensionally-reduced fiber model referred to as "fiber model" in this paper for the simulation of electrochemical processes involving fiber-shaped active material inclusions and the electrolyte surrounding them. Inspired by the embedded reinforcement method, extensively used in computational mechanics for the simulation of fiber-reinforced composites [18, 19, 30, 31], we represent the active material fibers as one dimensional objects (lines). In formulating the reduced model, we account for the aspects discussed in the remainder of the section.

Dimensional reduction of active fibers The following assumption underlies the representation of a fiber as a one-dimensional object: the extent of field variable gradients on an arbitrary cross section perpendicular to the fiber axis (fiber cross section, from now on) are negligible compared to the extent of field variable gradients along the axis of the fiber. Therefore a single value of ϕ_{am} and c_{am} is associated with an assigned coordinate along the fiber axis. The limit of applicability of the approach (in terms of fiber geometrical features and discharge rates) is determined in Section 5.5.3.

We assume that fibers are right circular cylinders with diameter d_{f} and length l_{f}. The integrals in Equations (5.16), (5.17), and (5.18) over fiber volume V_{f} and fiber-electrolyte

interface S_{int} modify as follows (Figure 5.3)

$$\int_{V_{\text{f}}} \dots \, \mathrm{d}V = A_{\text{f}} \int_{l_{\text{f}}} \dots \, \mathrm{d}s, \tag{5.48a}$$

$$\int_{S_{\text{int}}} \dots \, \mathrm{d}S = C_{\text{f}} \int_{l_{\text{f}}} \dots \, \mathrm{d}s, \tag{5.48b}$$

where A_{f} and C_{f} are fiber cross section area and circumference, respectively. For the sake of simplicity, we neglect the contributions of the two circular edges of the fiber while evaluating the integral (5.48b), so that S_{int} reduces to $C_{\text{f}} \times l_{\text{f}}$. In Section 5.5.3 we show that the implications of this simplification are negligible for fibers with high aspect ratio. Linear Lagrange elements are used for the discretization of the fiber (the nodes of the elements are shown in red in Figure 5.4).

In the half-cell battery configuration (Figure 5.3), the electrolyte occupies the whole separator $V_{\text{el}}^{\text{sep}}$ and the volume surrounding the fibers in the positive electrode V_{el}^{c}. By denoting the volume of the positive electrode with V^c, the relationship $V^c = V_{\text{el}}^{c} \cup V_{\text{am}}$ holds, where V_{am} stands for the volume occupied by the totality of active material fibers. Applying this subdivision, the integrals over V_{el} in weak form (5.23) are decomposed as follows:

$$\int_{V_{\text{el}}} \dots \, \mathrm{d}V = \int_{V_{\text{el}}^{\text{sep}}} \dots \, \mathrm{d}V + \int_{V_{\text{el}}^{c}} \dots \, \mathrm{d}V \; = \int_{V_{\text{el}}^{\text{sep}}} \dots \, \mathrm{d}V + \varepsilon \int_{V^c} \dots \, \mathrm{d}V \; , \tag{5.49}$$

where the porosity $\varepsilon = 1 - V_{\text{am}}/V^c$ quantifies the volume fraction of the positive electrode occupied by the electrolyte. In this study, we assume that the porosity is uniform and constant. As written in (5.49), the numerical integration of the composite electrode is significantly simplified by using conventional finite elements to represent the electrolyte gross volume $V^c = V_{\text{el}}^{c} \cup V_{\text{am}}$ (instead of the volume truly filled by the electrolyte, i.e. V_{el}^{c}) and the electrolyte contribution at regions where active fibers are present inside V^{c} are corrected through porosity ε factorization. This approach shows similarities with the macroscopic treatment of a pore-filling electrolyte typical of porous electrode theory [10]. By re-writing the volume integrals in (5.17) accounting for the porosity as in (5.49), the weak forms of equations (1), (2), (20), (23), and (24) of Ref. [10] are basically recovered (for a binary electrolyte without convective motion). A crucial difference however exists: we explicitly account for the fiber-electrolyte interactions through the integrals over S_{int}, rather than considering a volume-averaged charge transfer ($a\, i_n$ in the reference). This makes the approach more general, and allows us to explicitly take into account the effect of fiber orientation and to investigate the effect of the non-uniform lithiation of fibers along their own axis, for example.

Embedded fiber representation Active fibers are distributed independently from the the electrolyte mesh, i.e., without requiring a conformal mesh between fibers and electrolyte. The coupling between active fibers and the electrolyte is established through the interface conditions (5.10) and (5.11) discussed earlier for the standard model. Modifications are however needed for the interpolation of the interface contributions. As mentioned, the electrochemical couplings between electrodes and the electrolyte is achieved by defining a set of Lagrange multiplier DOFs at the electrode-electrolyte interface. As shown in the

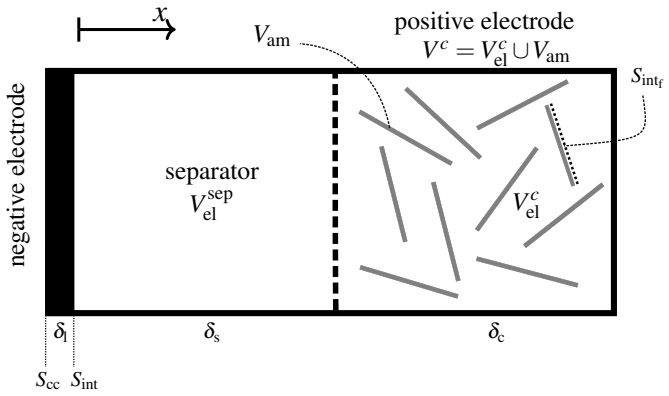

Figure 5.3: The design of a composite battery cell. In the reduced model, $V_{am} = l_{am} \times A_f$ and $S_{int_f} = l_{am} \times C_f$.

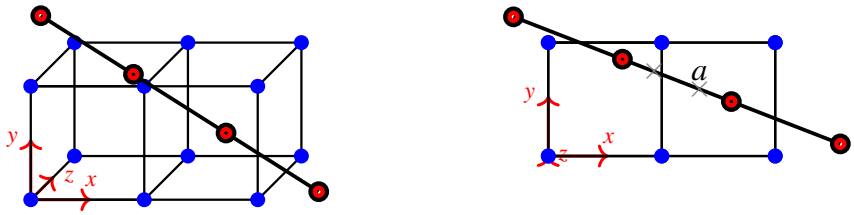

Figure 5.4: Discretization of an embedded fiber. Electrolyte nodes in blue, electrode nodes in red, and Lagrange multipliers nodes in black along the fiber. Integration points are shown by × marks.

sample discretization of the embedded fiber in Figure 5.4, fiber (red) and Lagrange multiplier (black) nodes are conformal, while electrolyte (blue) and fiber (interface) nodes are non-conformal.

For the numerical integration of the interface terms, potential ϕ^*_{el} and concentration c^*_{el} fields of the electrolyte and corresponding test functions are interpolated within the element by the same set of shape functions used for the electrolyte discretization. This can be written at any arbitrary point at the interface as

$$\phi^*_{el}(\boldsymbol{\xi}) = \sum_{i=1}^{n} N_i(\boldsymbol{\xi})\, \phi^*_i = \mathbf{N}_{el} \boldsymbol{\phi}_e, \tag{5.50a}$$

$$c^*_{el}(\boldsymbol{\xi}) = \sum_{i=1}^{n} N_i(\boldsymbol{\xi})\, c^*_i = \mathbf{N}_{el} \boldsymbol{c}_e, \tag{5.50b}$$

where $\boldsymbol{\xi}$ is the local isoparameteric coordinate of a sample intra-element integration point a shown in Figure 5.4 , and $\mathbf{N}_{el}$ collects all the nodal shape functions at this point:

$$\mathbf{N}_{el} = \begin{bmatrix} N^{(1)}(\boldsymbol{\xi}) & \dots & N^{(n)}(\boldsymbol{\xi}) \end{bmatrix}. \tag{5.51}$$

In the numerical evaluation of the interface integrals, all the nodes of an electrolyte

element in which a fiber integration point is located are involved (e.g., the right element in Figure 5.4b for the integration point a). In addition to what mentioned for the standard model in Section 5.4.1, the following steps should be taken in the finite element implementation of the fiber-based model:

1. Determine the parent electrolyte element corresponding to a fiber integration point a. We use structured H8 finite elements for the discretization of the electrolyte, for which this information can be efficiently obtained by means of octree data structures [32] at the preprocessing stage.

2. Evaluate the element local coordinate at point a ($\boldsymbol{\xi}_a$) by inverse mapping. For a structured H8 mesh, this is simply known as a function of element nodal coordinates.

3. Evaluate shape functions at the intra-element space (point a in Figure 5.4) and form the constraint coefficients shape function matrix (5.51). Constraint equations are evaluated as a function of electric potential and concentrations at the intra-element integration point a.

Apart from these modifications, the framework discussed in Section 5.4.1 remains unchanged for both standard and fiber-based models. If the fiber and electrolyte element nodes coincide, these expressions simply reduce to the standard model.

5.5. NUMERICAL EXAMPLES

We assess the capability of the reduced model to simulate electrochemical processes in fiber-based electrodes. We perform three numerical examples and contrast the results of the reduced model against the solution of standard finite element (FE) model or reference solutions from the literature. Local fields (c_{am}, c_{el}, and λ) distribution and battery cell response are part of the evaluation.

In Section 5.5.3 we identify the range of applicability of the dimensional reduction approximation of the fiber. A single fiber positive electrode is considered in a three-dimensional setting. The impact of fiber geometrical features and discharge rate on the reduced model response is evaluated using the FE results as reference solution. In Section 5.5.4 we analyze the results of the reduced model simulations performed on a fiber-based electrode in a three-dimensional setting. Roughly 10000 active material fibers occupy 70% of the electrode volume. A conformal FE mesh is not generated for such a geometry, we rather select the pseudo-2D model results of Doyle *et al.* [9] as reference solution. Finally, we investigate the dependence of the reduced model response on the relative position of fibers. In Section 5.5.5 we compare the results of reduced and FE models for a two-fibers positive electrode in a two-dimensional setting.

The numerical examples are preformed on a half-cell configuration and considering the same cell components and materials parameters as Doyle *et al.* [9]. The half-cell configuration allows to focus on a single fiber-based electrode at a time, thus limiting the computational cost. Figure 5.1 shows the domains making up the cell: i) homogeneous lithium foil negative electrode; ii) positive electrode made of titanium disulfide (TiS_2) active material inclusions embedded in polyethylene oxide-lithium trifluoromethane sulfonate (PEO-$LiCF_3SO_3$) polymer electrolyte; and, iii) PEO-$LiCF_3SO_3$ separator layer.

There are two main differences between this study and that of [9]. First, we replace TiS_2 spherical inclusions with fiber-shaped inclusions, an arbitrary choice that is not purely abstract, as TiS_2 nanotubes can be synthesized and employed in battery applications [33, 34]. Second, we describe the electrolyte replacing concentrated- with dilute-solution theory (Section 5.2). The adaptations required by the different modeling assumption are described in Section 5.5.1, while the particularization of functional (5.12) at the negative electrode-electrolyte and active material-electrolyte interfaces is described in Section 5.5.2. Despite the different modeling assumptions, the work of Doyle *et al.* [9] provides a suitable reference solutions for the verification of the proposed approach, as confirmed by the successful comparison in Section 5.5.4. A thorough discussion about the consequences that follow form the selection of different models and modeling assumption is provided in the same section.

In the coming sections we repeatedly refer to the quantities defined below while describing the results of the numerical simulations.

State of charge We express the state of charge (SOC) of the positive electrode as

$$\mathrm{SOC} = \frac{c_{\mathrm{am,avg}}}{c_{\mathrm{am}}^{\max}}, \tag{5.52}$$

where $c_{\mathrm{am,avg}}$ is the average concentration of lithium in the active material of the positive electrode. For galvanostatic processes, the relation

$$c_{\mathrm{am,avg}} = \frac{It}{F V_{\mathrm{am}}} + c_{\mathrm{am}}^0$$

holds, where V_{am} is the volume occupied by the active material in the positive electrode, and t is the time elapsed from the beginning of the process.

Cell potential We determine the cell potential as

$$\Delta\phi = \phi_{\mathrm{am}} - \phi_{\mathrm{neg}}(x = -\delta_{\mathrm{l}}),$$

that simplifies into

$$\Delta\phi = -\phi_{\mathrm{neg}}(x = -\delta_{\mathrm{l}}) \tag{5.53}$$

in view of (5.13b). Since we assume that the negative electrode is a perfect conductor, the electric potential ϕ_{neg} is uniform on the cross section (yz-plane) at $x = -\delta_{\mathrm{l}}$ (Figure 5.1).

5.5.1. MATERIAL PARAMETERS

We make use of the material parameters reported by Doyle et al. [9], exception made for the following adaptations. We determine D_{Li^+} and D_{X^-} inverting [20]

$$D_{\mathrm{ionic}} = \frac{2D_{\mathrm{Li}^+}D_{\mathrm{X}^-}}{D_{\mathrm{Li}^+} + D_{\mathrm{X}^-}}, \qquad t_+^0 = \frac{D_{\mathrm{Li}^+}}{D_{\mathrm{Li}^+} + D_{\mathrm{X}^-}}, \tag{5.54}$$

where $D_{\mathrm{ionic}} = 7.5 \times 10^{-12}\ \mathrm{m}^2\, s^{-1}$ and $t_+^0 = 0.160$ are the electrolyte diffusion coefficient and transference number provided in Ref. [9] for $c_{\mathrm{el}} = c_{\mathrm{el}}^0$, respectively. We assume D_{Li^+}

Table 5.1: Material parameters, geometrical features, initial and boundary conditions. All data from Doyle et al. [9] unless otherwise specified.

Material/region	Symbol	Quantity	Value
negative electrode (lithium foil)	D_{neg}	Li diffusivity[a]	$1.0 \times 10^{-11}\ \text{m}^2\,\text{s}^{-1}$
	κ_{neg}	Electronic conductivity[b]	$1.0 \times 10^{6}\ \text{S}\,\text{m}^{-1}$
	c^0_{neg}	Initial concentration of Li	$150000\ \text{mol}\,\text{m}^{-3}$
electrolyte (PEO-$LiCF_3SO_3$)	D_{Li^+}	Li^+ diffusivity[c]	$4.46 \times 10^{-12}\ \text{m}^2\,\text{s}^{-1}$
	D_{X^-}	$CF_3SO_3^-$ diffusivity[c]	$23.4 \times 10^{-12}\ \text{m}^2\,\text{s}^{-1}$
	c^0_{el}	Initial concentration of $LiCF_3SO_3$	$1000\ \text{mol}\,\text{m}^{-3}$
	$c^{\max}_{\text{el}}$	Saturation limit of $LiCF_3SO_3$	$3920\ \text{mol}\,\text{m}^{-3}$
active material (TiS_2)	D_{am}	Li diffusivity	$5.0 \times 10^{-13}\ \text{m}^2\,\text{s}^{-1}$
	κ_{TiS_2}	Electronic conductivity	$1.0 \times 10^{4}\ \text{S}\,\text{m}^{-1}$
	c^0_{am}	Initial concentration of Li	$100\ \text{mol}\,\text{m}^{-3}$
	$c^{\max}_{\text{am}}$	Saturation limit of Li	$29000\ \text{mol}\,\text{m}^{-3}$
Li-PEO interface	k_{neg}	Reaction rate constant	$7.6422 \times 10^{-8}\ \text{m}\,\text{s}^{-1}$
	$U_{\text{OC,neg}}$	Open circuit potential	0
TiS_2-PEO interface	k_{am}	Reaction rate constant	$10^{-10}\ \text{m}^4\,\text{mol}^{-1}\,\text{s}^{-1}$
	U_{ref}	Reference open potential	2.17 V
	β	First coefficient	$-0.000558\ \text{m}^3\text{mol}^{-1}$
	ζ	Second coefficient	8.10
Entire cell	T	Temperature	373.15 K
	α_a, α_c	Transfer coefficients	0.5
	l_{ref}	Reference length[d]	10^{-6} m
	c_{ref}	Reference concentration[d]	$1000\ \text{mol}\,\text{m}^{-3}$

[a] Value arbitrarily selected to comply with the assumption of ideal reservoir of lithium.
[b] Value arbitrarily selected to comply with the assumption of perfect conductor.
[c] Adapted from Ref. [9] according to (5.54).
[d] Arbitrarily selected.

and D_{X^-} are constant and employ the same values in separator and positive electrode. We explicitly model the lithium metal foil through the active material formulation described in Section 5.2. Lithium diffusivity and electronic conductivity are chosen assuming that the positive electrode is an ideal reservoir of lithium and a perfect conductor. Table 5.1 summarizes the material parameters used in the numerical simulations.

5.5.2. ELECTROCHEMICAL REACTIONS AT THE NEGATIVE ELECTRODE- AND ACTIVE MATERIAL-ELECTROLYTE INTERFACES

We provide definitions for the functional (5.12) at negative electrode-electrolyte and active material-electrolyte interfaces. It is customary to relate the charge transfer λ to concentra-

tions c_{am}, c_{el} and electric potentials ϕ_{am}, ϕ_{el} through the Butler-Volmer equation [20]

$$\lambda_k = i_{0,k}\left(\exp\left(\frac{\alpha_a F\,\eta_k}{RT}\right) - \exp\left(-\frac{\alpha_c F\,\eta_k}{RT}\right)\right), \quad \mathbf{x}\in S_{\text{int},k}, \quad k=\text{am, neg}, \tag{5.55}$$

where, $i_{0,k}$ represents the exchange current density ($\text{A}\,\text{m}^{-2}$) at interface k, and α_a and α_c are the so-called apparent transfer coefficients (such that $\alpha_a+\alpha_c=1$). The surface overpotential η_k is related to the electric potential at the two sides of the interface through

$$\eta_k = \phi_k - \phi_{\text{el}} - U_{\text{OC},k}, \quad \mathbf{x}\in S_{\text{int},k}, \quad k=\text{am, neg}, \tag{5.56}$$

where $U_{\text{OC},k}$ represents the open circuit potential (V). Explicit expressions of $i_{0,k}$ and $U_{\text{OC},k}$ are provided next.

The linearized form of the Butler-Volmer equation

$$\lambda_k = i_{0,k}\frac{F\eta_k}{RT}, \quad \mathbf{x}\in S_{\text{int},k}, \quad k=\text{am, neg}, \tag{5.57}$$

is equivalent to (5.55) as long as condition $|F\eta_k/R/T| \ll 1$ holds. We performed tests on the cell geometry described in 5.6 at the discharge rates considered in the numerical simulations of Section 5.5. Since the results showed no appreciable changes when (5.57) was used in place of (5.55), we make use of the linear form (5.57) as the definition of functional (5.12). The same approach was followed, *e.g.*, by Garcia et al. [11].

The numerical implementation of (5.57) differs for FE and reduced models. The former makes use of the values of ϕ_{am}, ϕ_{el}, c_{am} and c_{el} evaluated at the interface nodes, while the latter makes use of the nodal values of the one-dimensional representation of the fiber (no distinction between surface and bulk values applies to the reduced model, Section 5.4.5). Due to the different treatment, the evolution of $i_{0,k}$, η_k, and λ_k during the discharge process is, in general, different for reduced and FE model. The quantification of the discrepancies between FE and reduced model responses, as well as the identification of the causes of the discrepancies, are addressed in Section 5.5.3.

Active material inclusions-electrolyte interface At the interface between TiS_2 and PEO, the exchange current density takes the form [9, Eq. (30)]

$$i_{0,\text{am}} = F\,k_{\text{am}}\,(c_{\text{el}}^{\max}-c_{\text{el}})^{\alpha_{\text{c}}}\,c_{\text{el}}^{\alpha_{\text{a}}}\,(c_{\text{am}}^{\max}-c_{\text{am}})^{\alpha_{\text{a}}}\,c_{\text{am}}^{\alpha_{\text{c}}}, \quad \mathbf{x}\in S_{\text{int},am}, \tag{5.58}$$

where k_{am} is the reaction rate constant at the active material-electrolyte interface in the positive electrode, and $c_{\text{el}}^{\max}$ and $c_{\text{am}}^{\max}$ identify the saturation limits of salt in the electrolyte and of lithium in the active material, respectively. We account for the dependence of the open circuit potential on the lithium concentration in the active material through [9]

$$U_{\text{OC,am}} = U_{\text{ref}} + \frac{RT}{F}\left(\ln\left(\frac{c_{\text{am}}^{\max}-c_{\text{am}}}{c_{\text{am}}}\right)+\beta c_{\text{am}}+\zeta\right), \quad \mathbf{x}\in S_{\text{int},am}. \tag{5.59}$$

Parameters U_{ref}, β and ζ can be identified by fitting experimental data: we make use of the values reported in Ref. [9] and listed in Table 5.1.

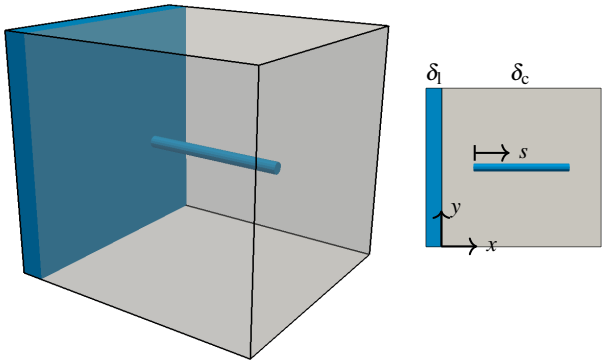

Figure 5.5: Geometry of the one-fiber problem.

Negative electrode-electrolyte interface At the interface between the lithium and the PEO, the exchange current density takes the form [9]

$$i_{0,\text{neg}} = F\, k_{\text{neg}}\, (c_{\text{el}}^{\max} - c_{\text{el}})^{\alpha_c}\, c_{\text{el}}^{\alpha_a}, \quad \mathbf{x} \in S_{\text{int,neg}}, \tag{5.60}$$

where k_{neg} is the reaction rate constant at the negative electrode-electrolyte interface. We set $U_{\text{OC,neg}} = 0$ according to Ref. [9].

5.5.3. REDUCED VS FE MODEL: SINGLE FIBER INVESTIGATION

We evaluate the capability of the reduced model to approximate the response of standard FE through a numerical example that allows a direct comparison between the two methods. The same governing equations (Sections 5.2 and 5.5.2) and material parameters (Table 5.1) are used for the two models. The FE model implementation was first verified against the semi-analytical solutions obtained for a three-layer battery cell. Details are provided in 5.6. In the reminder of this section, we refer to the relative difference in terms of the generic quantity a as

$$\Delta a_{\text{rel}} = \frac{a_{\text{R}} - a_{\text{FE}}}{a_{\text{FE}}} \times 100, \tag{5.61}$$

where subscript R and FE refers to the result of the reduced and finite element model, respectively.

Figure 5.5 shows the geometry of the battery cell considered in the numerical simulations. The cell consists of a lithium plate (negative electrode) and a fiber-based (positive) electrode of thickness $\delta_l = 10\mu$m and $\delta_c = 100\ \mu$m, respectively. The latter is made up by a single active material fiber of length $l_f = 60\ \mu$m and the surrounding electrolyte. The axis of the fiber is perpendicular to the lithium plate, and the midpoint of the axis is located at a distance $\delta_c/2$ from the plate. The battery cell has a uniform cross section $A_s = \delta_c^2$ (yz-plane). Simulations are performed with fiber diameters d_f such that $d_f/\delta_c = 0.01, 0.05, 0.1,$

0.2, and 0.4, the aspect ratio of the fiber (l_f/d_f) ranges from 60 to 1.5 accordingly. The positive electrode porosity needed for the reduced model simulations (refer to Section 5.4.5) is calculated as $\varepsilon = 1 - V_{am}/\delta_c^3$, where V_{am} equals the volume of the fiber V_f.

In the FE simulations we use non-structured T4 elements. The number of nodes of the discretization increases from 2504 to 10859 as d_f/δ_c reduces from 0.4 to 0.01 (since fiber and electrolyte meshes comply, the element size in the fiber and surrounding electrolyte are equally reduced). In the reduced model simulations, lithium plate and electrolyte are discretized using $4 \times 15 \times 15$ and $15 \times 15 \times 15$ structured H8 elements, respectively, while the fiber is discretized using 50 equally-sized line elements. The number of discretization nodes amounts to 5426 irrespective of the fiber diameter.

We apply boundary and initial conditions described in Sections 5.2.3 and 5.2.4, respectively. In addition, we impose the mass flux and electric current density to be null across i) the external surfaces of the simulation domain parallel to the axis of the fiber and ii) the external surface at $x = \delta_c$. We perform simulations at 1 C rate discharge by applying the current density

$$I = \frac{c_{am}^{max}\, F\, V_{am}}{A_s\, t_d}, \tag{5.62}$$

where $c_{am}^{max}\, F\, V_{am}$ represents the capacity of the positive electrode, and t_d is the discharge time set equal to 1 hour. Both FE and reduced model simulations have been performed with a constant time step $\Delta t = 5$s.

During discharge processes, the lithium insertion process stops either when the lithium concentration reaches the saturation limit on the surface of the fiber or when the surrounding electrolyte is depleted of lithium, as dictated by the exchange current density definition (5.58). The lithium concentration profile on a fiber cross section is, in general, non-uniform. Due to the symmetry of the problem, the concentration on an arbitrary fiber cross section far from the two circular edges is maximum at the fiber-electrolyte interface (where lithium insertion takes place) and is minimum at the center. Since the reduced model evaluates (5.58) assuming the concentration is uniform over the fiber cross section, the responses of reduced and FE models differ when a strong concentration gradient develops along the fiber radius. We thus aim to assess the capability of the reduced model to describe: i) the local evolution of the field variables, ii) the conditions that cause the interruption of the charge transfer across the fiber-electrolyte interface, and iii) the impact of these factors on the cell potential curve. We focus on the role of fiber geometry (d_f/δ_c) and discharge rate (I). For the sake of simplicity, the numerical simulations described in this section are performed neglecting the dependence of the open circuit potential on the lithium content of the active material (5.59): we identically set $U_{OC,am} = U_{ref}$.

The model presented in Section 5.5.2 (definitions (5.57), (5.58), and (5.60)) shows that the charge transfer λ_k at each interface $k = \text{am}, \text{neg}$ is proportional to the surface overpotential η_k through the reaction rate constant k_k. An analogous treatment can be found in fiber-reinforced composites modeling, where tractions at the interface between fiber and hosting matrix are related to the fiber-matrix sliding through a set of constants [35]. This set of constants describes the stiffness of the fiber-matrix interface and represents the solid mechanics counterpart of k_k.

Since the value of the reaction rate constant typically varies depending on the electrode-electrolyte interface, we assess the impact of this parameter on the accuracy of the reduced

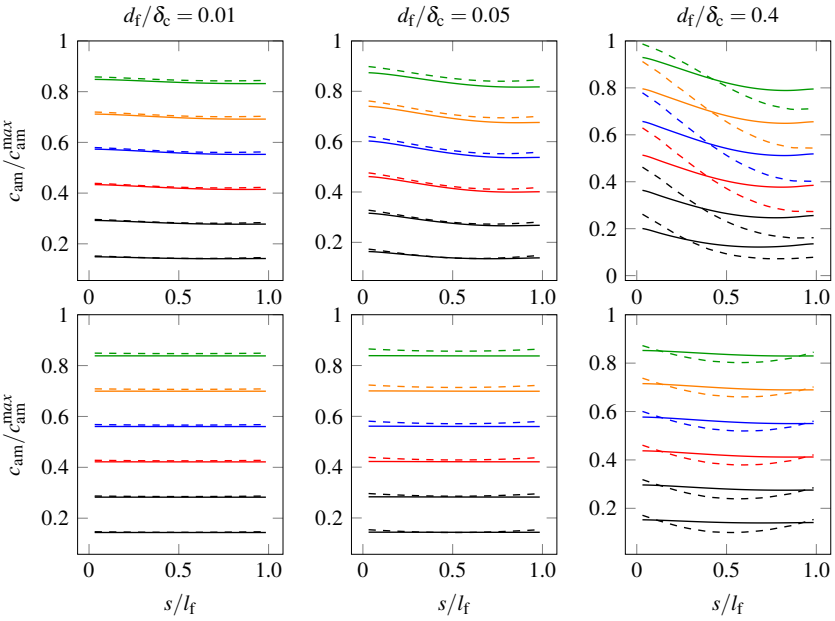

Figure 5.6: Concentration distribution along the length of the fiber at SOC = 0.14, 0.28, 0.42, 0.56, 0.69, and 0.83. Results are shown for different fiber diameters, and for $k_{s2} = 10^{-10}$ m^4 mol^{-1} s^{-1} (top) and $k_{s2} = 10^{-12}$ m^4 mol^{-1} s^{-1} (bottom). Solid and dashed lines refer to reduced and FE model, respectively.

model performing two sets of simulations: i) using the parameters reported in Table 5.1, and ii) using $k_{am} = 10^{-12}$ m^4 mol^{-1} s^{-1} in place of $k_{am} = 10^{-10}$ m^4 mol^{-1} s^{-1}.

We first assess the performance of the reduced model through the examination of local fields: concentration distribution within fiber and surrounding electrolyte, and fiber-electrolyte charge transfer across the interface. As a preliminary verification of the numerical implementation, we ascertain that equality

$$I\, A_s\, t = F \int_{V_{am}} c_{am} - c_{am}^0 \, dV \tag{5.63}$$

holds at any time t of the numerical simulations. Equality (5.63) ensures that the lithium content in the fiber is proportional to the charge transferred and that lithium is neither artificially generated nor consumed. The right-hand side of (5.63) is evaluated through numerical integration over the elements representing the fiber, *i.e.*, one- and three-dimensional elements for the reduced and FE model, respectively.

Figure 5.6 shows the evolution of the lithium concentration distribution along the fiber length for a selection of fiber diameters (d_f/δ_c = 0.01, 0.05, and 0.4) and for both values of k_{am}. For the FE model we report the values at the nodes located along the fiber axis. The concentration profiles obtained with reduced and FE models are consistent: the pointwise difference is 11% at the most (for $d_f/\delta_c = 0.4$ and $k_{am} = 10^{-10}$ m^4 mol^{-1} s^{-1}). The smaller the fiber diameter, the better the agreement between the results of the two models. Two are the main reasons. First, the entity of concentration variation on the fiber cross section is

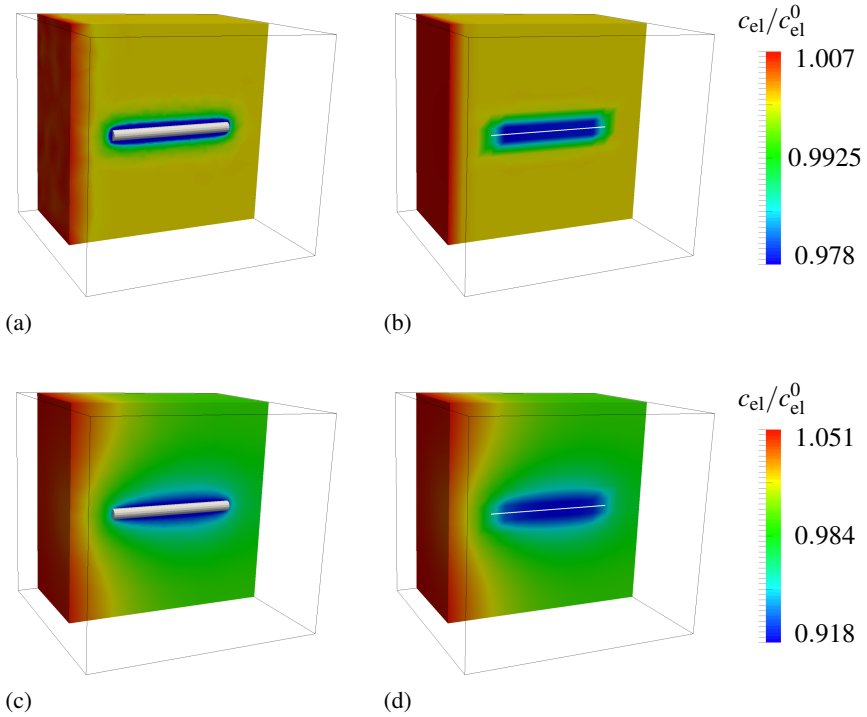

Figure 5.7: Concentration distribution around a fiber with $d_f/\delta_c = 0.05$ and $I = 1.4651\text{Am}^{-2}$ and $k_{s2} = 10^{-10}$ $\text{m}^4\,\text{mol}^{-1}\,s^{-1}$ for: (a,c) the full model and (b,d) the reduced model. Top and bottom refer to SOC = 5×10^{-3} and SOC=0.5, respectively.

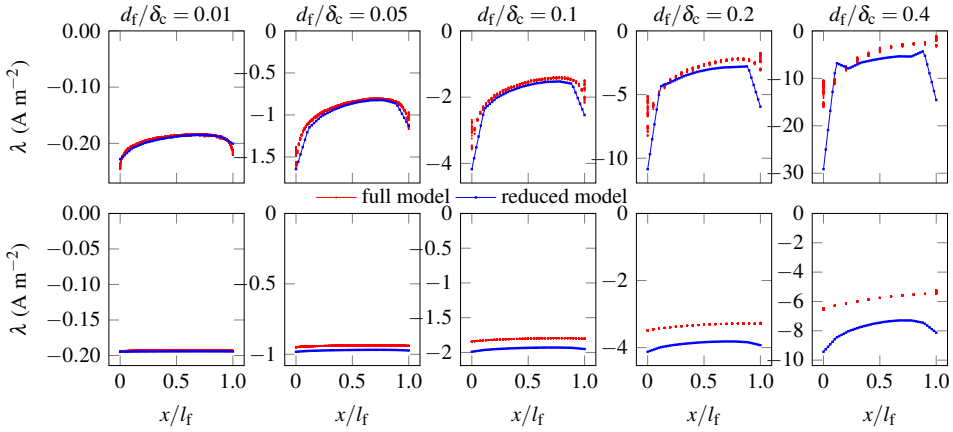

Figure 5.8: Values of interface current (λ) at different fiber diameters. Top: $k_{s2} = 10^{-10}$ m^4 mol^{-1} s^{-1}. Bottom: interface $k_{s2} = 10^{-12}$ m^4 mol^{-1} s^{-1}. Results are shown at time = 1800 seconds. The applied currents were calculated from (5.62), equal, from left to right, to: $I = \{0.0036, 0.0915, 0.3662, 1.4651, 5.8603\}$Am^{-2}.

5

directly proportional to the fiber radius. Second, the influx of lithium from the circular edges (especially the one close to the lithium plate) is directly proportional to the surface, and thus to the radius. Since the reduced model is insensitive to these aspects (Section 5.4.5), the reduced model better approximates the FE model as the fiber radius reduces.

Figure 5.6 shows that the concentration profiles obtained with the reduced model underlie those obtained with the FE model for $d_f/\delta_c = 0.01$ and 0.05. These discrepancies are caused by the approximate representation of a cylindrical volume by means of T4 finite elements. For example, the FE discretization used to obtain the results reported in Figure 5.6 with $d_f/\delta_c = 0.05$ (17609 elements in total, 7357 elements for the discretization of the fiber) leads to an underestimation of the fiber volume of about 3%, and thus causes the erroneous overestimation of the concentration observable in Figure 5.6 (it is easy algebra to check that the gaps in the plots between reduced and FE models are consistent with the extent of the volume underestimation). Two remarks further support this conclusion. First, equation (5.63) holds for both models if the integral on the right-hand side is performed on the discretized fiber domain. Second, the extent of the mismatch is directly proportional to the amount of lithium in the fiber. We stress that, since the evaluation of the fiber volume is intrinsically exact with the reduced model (Section 5.4.5), the approach is especially suitable for applications where condition $d_f/\delta_c \ll 1$ holds, *i.e.*, when the representation of a single fiber with standard FE requires an unreasonably fine mesh.

Figure 5.7 shows the concentration distribution in the electrolyte obtained with reduced (a,c) and FE (b,d) models for $d_f/\delta_c = 0.05$ and $k_{am} = 10^{-10}$ m^4 mol^{-1} s^{-1}. The contour plots refer to SOC $= 5 \times 10^{-3}$ ($t = \Delta t$) and SOC $= 0.5$. This visual inspection confirms that the concentration distribution evaluated with the reduced model perfectly agrees with the distribution obtained with the standard FE model.

The assessment of the reduced model performance would not be complete without the examination of the charge transfer across the fiber-electrolyte interface, which is coupled to

fiber and electrolyte concentrations through equations (5.11), (5.57) and (5.58). Figure 5.8 shows the charge transfer distribution along the fiber length at SOC = 0.5. The results of the FE model are reported for all the nodes that belong to the fiber-electrolyte interface. The profiles of the reduced model perfectly replicate those of the FE model for $d_f/\delta_c \leq 0.1$: for a fixed axial fiber coordinate, the relative difference between the nodal value of the reduced model and the average over the circular interface of the FE model is 10% at the most ($d_f/\delta_c = 0.1$). A weaker agreement is found when $d_f/\delta_c \geq 0.2$. Two are the main causes. First, concentration variations along the fiber radius are directly proportional to the fiber diameter. Second, the lithium influx across the two circular edges becomes substantial when the aspect ratio of the fiber approaches one (*e.g.*, the contribution of the two circular edges is about 30% of the whole fiber-electrolyte interface surface when $d_f/\delta_c \leq 0.4$). We stress that, even if fibers with larger diameters are subjected to larger current densities (5.62), the contribution of the increased value of I on the mismatch between reduced and FE model is secondary compared to the two aspects just mentioned, as demonstrated by the investigation described at the end of this section.

The different fiber-electrolyte interface surface available with reduced and FE models impacts on the average value of λ, as apparent in Figure 5.8 for $k_{am} = 10^{-12}$ m^4 mol^{-1} s^{-1}. To ensure that the charge transfer at the fiber-electrolyte interface $S_{int,am}$ is consistent with boundary condition (5.13), we check that equality

$$I\,A_s = \int_{S_{int,am}} \lambda_{am}\,\mathrm{d}S \tag{5.64}$$

holds at each time step of all numerical simulations performed (with both standard FEM and reduced models). The integral at the right-hand side of (5.64) is evaluated through numerical integration over i) the one-dimensional representation of the fiber when the reduced model is used, and ii) the elements representing the fiber-electrolyte interface when the FE model is used (refer to Section 5.4.1).

We evaluate the performance of the reduced model in predicting the overall cell response through the analysis of cell potential vs SOC curves. Figure 5.9 shows the cell potential (5.53) as a function of the SOC (5.52) for all values of fiber diameter considered in the study and for both values of k_{am}. The trend of the curves is dictated by the dependence of the exchange current density on the concentration within fiber (5.58), as Figure 5.7 shows that the concentration redistribution within the electrolyte is modest. The cell potential peak (apparent for $k_{am} = 10^{-12}$ m^4 mol^{-1} s^{-1}) is consistent with definitions (5.57) and (5.58): since the concentration on the fiber surface is approximately $c_{am}^{max}/2$ at SOC = 0.5, the exchange current density $i_{0,am}$ and the cell potential $\Delta\phi$ attain a minimum and a maximum, respectively. The cell potential drops when the fiber concentration c_{am} approaches the saturation limit c_{am}^{max} on a large portion of the fiber surface, because the exchange current density (5.58) approaches zero.

The results of reduced and FE models show the same trends and the maximum cell potential relative difference (5.61) is 3% at the most ($d_f/\delta_c = 0.4$). Since the fiber surface concentration determined with the FE model exceeds the average cross section concentration determined with the reduced model (for assigned instant of time and fiber cross section), the exchange current density (5.58) and the cell potential (5.53) evaluated with FE model drop to zero at lower SOC (this is apparent from Figure 5.10).

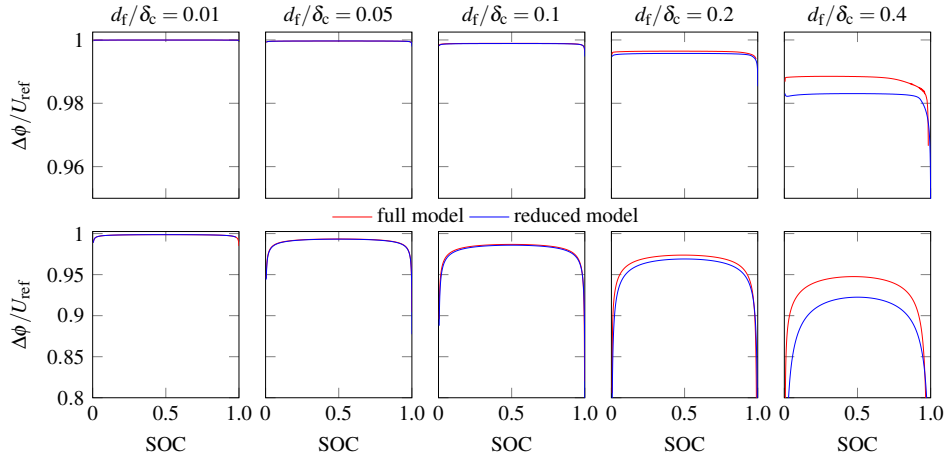

Figure 5.9: Cell potential at different fiber diameters. top: interface $k_{s2} = 10^{-10}$ m$^4\,mol^{-1}\,s^{-1}$, bot: interface $k_{s2} = 10^{-12}$ m$^4\,mol^{-1}\,s^{-1}$. The applied currents were calculated from (5.62), and from left to right are equal to: $I = \{0.0036, 0.0915, 0.3662, 1.4651, 5.8603\}$Am^{-2}.

5

The cell potential determined with the FE model exceeds that of the reduced model in all the numerical simulations. We attribute the reason to the contribution of the circular edges to the lithium insertion process: as the negative electrode-circular edge distance is shorter than negative electrode-fiber body distance the length of the lithium ion transport path reduces, and so does the resistivity of the system.

We analyze the impact of the current density on the reduced model response by applying different values of boundary condition (5.13a) on a fiber with $d_f/\delta_c = 0.05$. The values of the current density are $I = 3.6 \cdot 10^{-3}$, $9.2 \cdot 10^{-2}$, $3.7 \cdot 10^{-1}$, 1.5, and 5.9 Am^{-2}, they correspond to 1 C rate discharge for the five fiber diameters considered so far.

Figure 5.10 shows that the results of the reduced model replicate the trends of the results of the FE model irrespective of the value of the applied current. Differences between reduced and FE model results are detectable for $I = 5.9$ Am^{-2} (*i.e.*, 64 C rate discharge for a fiber with $d_f/\delta_c = 0.05$), which is a tremendously high absolute value for real situation. Indeed, the results reported in Section 5.5.4 show that the current density experienced by a single fiber is $1.5 \cdot 10^{-1}$ Am^{-2} at the most when the overall porous electrode undergoes a 10 C rate discharge process.

Figures 5.9 and 5.10 show that when $k_{am} = 10^{-10}$ m^4 mol^{-1} s^{-1} the cell potential approaches the open circuit potential $U_{OC,am}$, suggesting that the surface overpotential η_{am} is approximately zero. This situation corresponds to the so-called "perfect interface", and it is always associated with a smaller relative difference between reduced and FE model results compared to the case $k_{am} = 10^{-12}$ m^4 mol^{-1} s^{-1}.

5.5.4. POROUS ELECTRODE

The results in section 5.5.3 confirm the reliability of the reduced model predictions at a wide range of fiber diameters and under different applied currents in terms of both local and global quantities. In this section the reduced model is applied to a fiber-based electrode

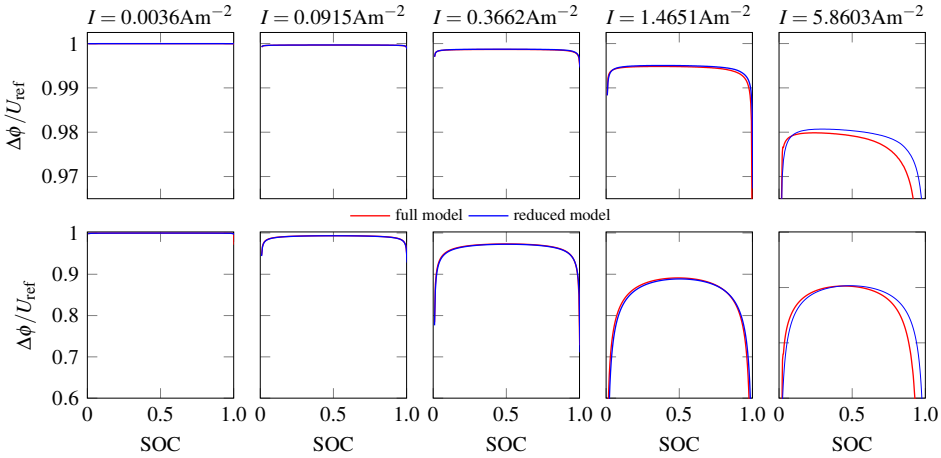

Figure 5.10: Cell potential for the case with $d_f/\delta_c = 0.05$ at different applied currents. top: $k_{s2} = 10^{-10}$ m^4 mol^{-1} s^{-1}, bot: $k_{s2} = 10^{-12}$ m^4 mol^{-1} s^{-1}. The applied currents were calculated from (5.62), and from left to right are equal to: $I = \{0.0036, 0.0915, 0.3662, 1.4651, 5.8603\}\text{Am}^{-2}$. These applied currents are corresponding to C rate $= I/I_{1C} = \{0.04, 1, 4, 16, 64\}$.

with high fiber volume fraction. In the numerical example, active material inclusions are high aspect ratio fibers (Figure 5.11). A conformal finite element mesh, needed for the standard model, can not be generated for the geometrical configuration here and instead we make reference to numerical results of Doyle et al. [9], in which a porous electrode with the same active material volume fraction (in form of particles) was investigated through the pseudo-2D model.

In the numerical example considered by Doyle *et al.* [9], a composite positive electrode is made of active spherical particles of certain radius ($r_p = 1\mu$m), and its porosity is set to $\varepsilon = 0.3$ (with volume fraction of active particles $v_p = 1 - \varepsilon = 0.7$). Accordingly we generate a fiber-based electrode with the same volume fraction of active material, *i.e.*, $v_f = 0.7$, to ensure that the fiber-based electrode has the same nominal capacity as that of the reference. Furthermore, in this specific case, the fiber distribution is such that it conforms with the assumption of uniform porosity. We choose the value of fiber radius r_f to be the same as that of the spherical particles modeled by Doyle et al. [9], so that $r_f = r_p = 1\,\mu$m, and we arbitrarily select the fiber length to be $l_f = 20\,\mu$m. These geometrical parameters correspond to a fiber diameter ratio $d_f/\delta_c = 0.02$, that lies within the range of values that ensures the best agreement versus standard model, according to the investigation performed in Section 5.5.3. These geometrical choice led to around 11000 active fibers, generated using the random sequential adsorption technique [36]. At variance with the work of Doyle *et al.* [9] in which isolated particles do no mutually interact, the proposed approach incorporates local interactions between fibers.

Material properties and the applied boundary conditions are identical to that of Doyle et al. [9] and were discussed earlier. The size of anode lithium layer, separator and composite cathode are chosen as $\delta_l = 20\mu$m, $\delta_s = 50\mu$m and $\delta_c = 100\mu$m, respectively, and the box dimensions along the y and z axes are set to $L = 100\mu$m. Uniform fine and coarse H8

discretizations of $n \times n \times n$ (with $n = 6,\ 21,\ 30$) were used for the electrolyte, and unless specified otherwise, each fiber was discretized into 10 equally sized segments.

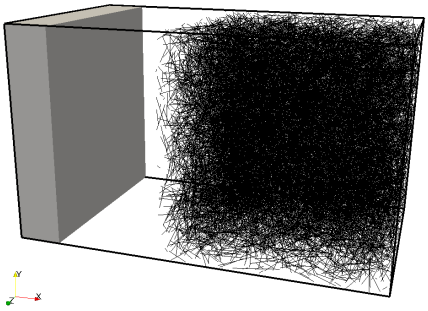

Figure 5.11: Problem configuration with 70% fiber volume fraction ($\varepsilon = 0.3$, with around 11000 fibers). The fiber distribution was generated using the random sequential adsorption technique.

Electrolyte concentration Lithium concentrations along the center line of the electrolyte are shown in Figure 5.12 for two different external currents $I = \{5,\ 10\}$ Am^{-2} at various time steps (for a fine electrolyte mesh with $n = 30$). The gradients of concentrations along the x axis are directly proportional to the external current value. For a smaller external current ($I = 5$ Am^{-2}) as shown in Figure 5.12a, the gradients are smaller and the electrolyte concentration does not reach a zero value even after around 10 hours of simulated time (SOC≈ 0.92). Therefore the required lithium supply is available in the electrolyte so that all active fibers reach their maximum capacity. The results are compared with reference results in Figure 5.12b for a larger external current ($I = 10$ Am^{-2}), where different from the previous case, the concentration gradients are steeper and shortage of lithium inside the electrolyte is clear at a region close to the right edge. Although a good agreement is observed with reference concentration predictions initially, the two results deviate as the simulations further continue. This is because the time dependency of diffusivity of the electrolyte is neglected in the present study, and gradients of the concentration along the x axis are intensified [37, 38]. Eventually, negative concentrations are reached at time $t = 4900$ seconds (UOC≈ 0.25), while reference concentrations do not reach zero until the end of simulations. To resume simulations after time $t = 4900$ s (UOC≈ 0.25) without reaching non-physical negative concentrations, a heuristic numerical treatment is employed: whenever the concentration of an electrolyte node is equal to zero or negative, the degree of freedom is constrained with c_{el} fixed to zero for the rest of the simulation. This implies that corresponding value of λ becomes equal to zero because of relation (5.58). Therefore, as shown in Figure 5.12b, the numerical simulations predict a region of zero lithium concentration inside the electrolyte. Despite the described numerical treatment, we check that the relationship

$$c_{\text{el}}^0\,(\delta_s + \varepsilon\,\delta_{\text{c}}) = \int_0^{\delta_{\text{s}}} c_{\text{el}}\,\mathrm{d}x \;+\; \varepsilon \int_{\delta_{\text{s}}}^{\delta_{\text{s}}+\delta_{\text{c}}} c_{\text{el}}\,\mathrm{d}x,$$

holds at every time step of the numerical simulation. This ensures that the mass conservation is satisfied within the electrolyte.

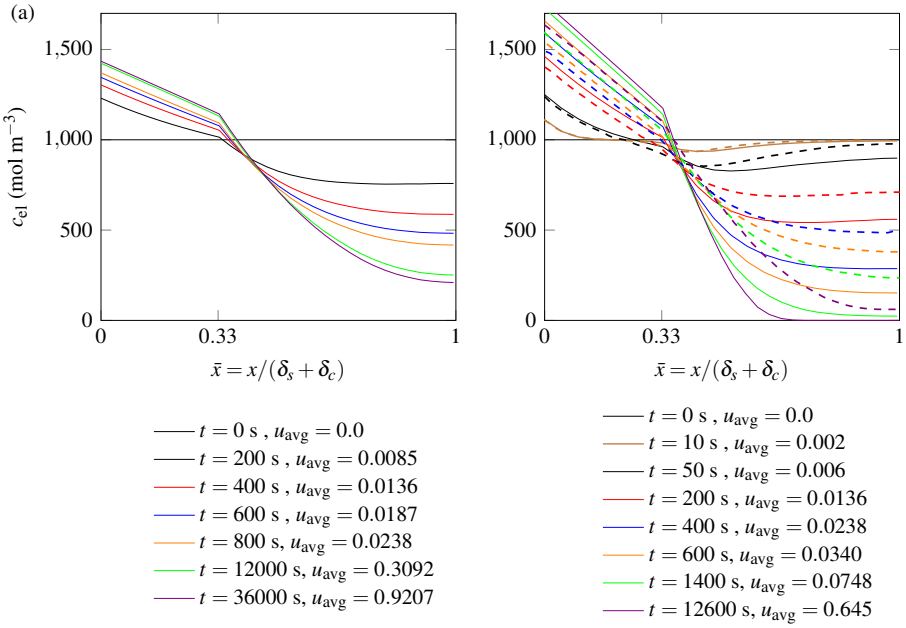

Figure 5.12: Concentration profiles in the electrolyte with (a) $I = 5$ A/m^2, and (b) $I = 10$ A/m^2, where the numerical predictions are compared to [9]. A good agreement especially at the initial steps is observed. Differences are mainly due to the fact that we replaced particles by fibers, and that a dilute solution theory is used instead of the concentrated solution theory used by Doyle *et al.* [9].

Fiber concentrations As shown in the previous part, small concentrations along the right edge follows from the combination of dilute-solution theory and discharge rate. This leads to partial utilization of active fibers, where small or very limited supply of lithium exist for active fibers at regions close to the right edge. This can be observed in terms of the fiber concentrations shown in Figure 5.13. For the case of smaller applied current ($I = 5$ Am^{-2}) shown in Figure 5.13a, fibers reach their maximum capacity and are fully utilized. For a larger current ($I = 10$ Am^{-2}) in Figure 5.12b however fibers close to the right edge do not effectively gain lithium and are not utilized due to the depleted electrolyte. Figure 5.13b further confirms that the proposed approach captures a trend similar to that of the reference work. The differences are attributed to the different (fiber-based) micro-structure studied in this work, and the fact that Doyle *et al.* [9] did not consider interactions between active material inclusions. Moreover, the non-smoothness of the curves after t = 4900s (SOC$\approx$ 0.25) is attributed to the numerical treatment that was applied to let the simulations continue. A visual inspection of fiber concentration fields at different time steps of the simulation are shown in Figure 5.14 for $I = 10$ Am^{-2}. For this case, shortage of lithium supply from the electrolyte due to large gradients does not allow full utilization of fibers close to the right

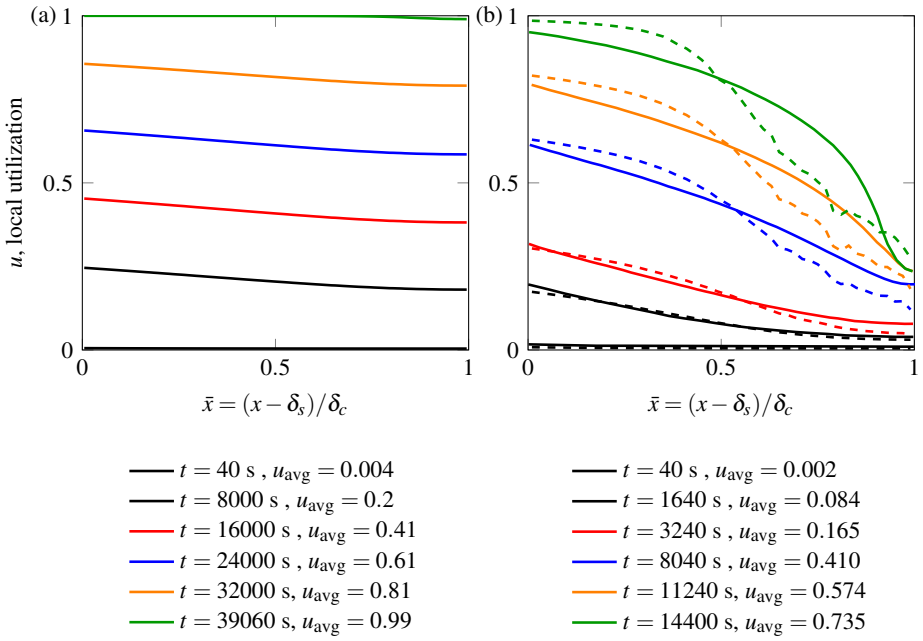

Figure 5.13: Concentration profiles in the active material of the cathode electrode with (a) $I = 5$ A/m^2, and (b) $I = 10$ A/m^2, where the numerical predictions are compared to results from Doyle *et al.* [9]

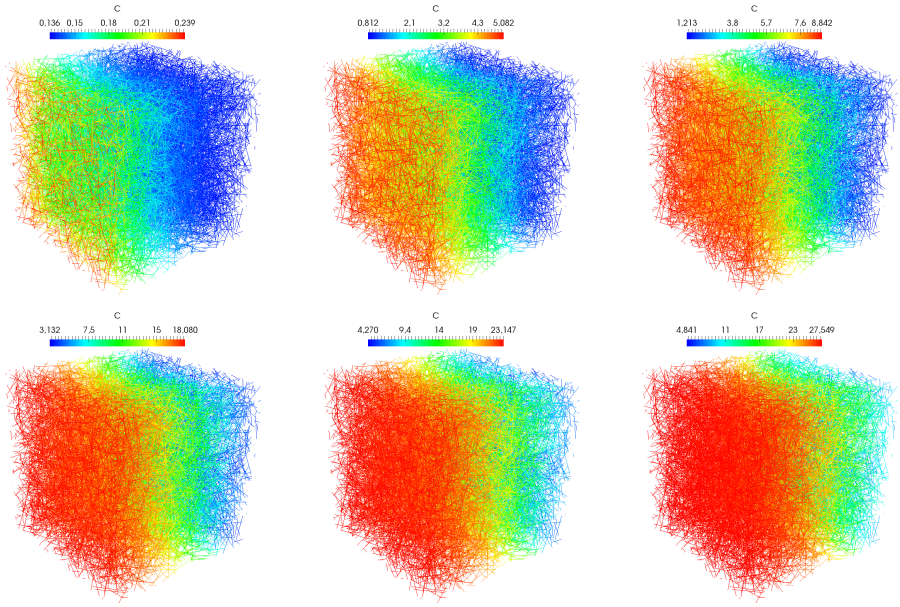

Figure 5.14: Lithium concentration at different times for $I = 10$ A/m^2. Values correspond to the curves in Figure 5.13b.

edge. In the results not reported here, we confirmed that the mass conservation is preserved at every time step of the numerical simulation by checking that the condition

$$I t = c_{\mathrm{s,avg}} F \varepsilon \delta_{\mathrm{c}},$$

is always satisfied.

Cell potential Next a comparison in terms of the global response of the cell is provided. Figure 5.15 reports the cell potential (potential differences between anode and cathode) as a function of SOC for the reduced and reference models at three different applied currents $I = \{5, 10, 20\}$ Am^{-2} in a discharge process. The numerical results reproduce a response similar to that of the reference work especially at smaller external current ($I = 5$ Am^{-2}), where a converged solution could be obtained even using a very coarse electrolyte mesh with $n = 6$. For higher external currents ($I = \{10, 20\}$ Am^{-2}) both models predict partial utilization of active fibers due to steep concentration gradient and low concentration supply in the electrolyte. Although the trends generally agree well, differences are observed between the two models at these applied currents. Again the differences are mainly attributed to the dilute-solution theory adopted in this work for the electrolyte material which leads to a region of zero concentration inside the electrolyte. It should also be mentioned that as shown in Figure 5.15 for cases with larger applied currents, finer electrolyte meshes were needed to get reliable cell potentials. This is attributed to steeper concentration gradients, and regions of zero concentration which required more refinements to be properly resolved.

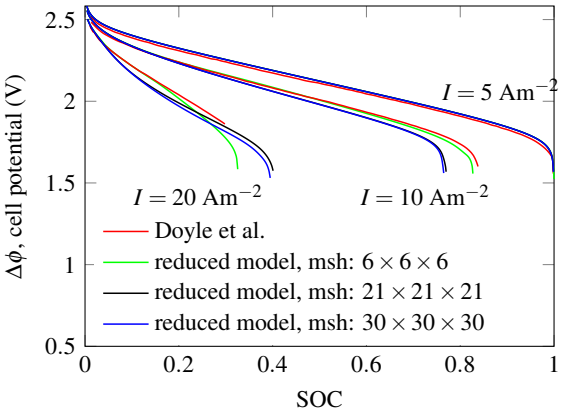

Figure 5.15: Cell potential at different current densities $I = \{5, 10, 20\}$ Am^{-2}. All curves refer to a discharge process.

Interface currents Next we investigate the exchanged currents at the interface between active fibers and electrolyte. Values are reported in figures 5.16 and 5.17 for two different applied currents ($I = \{5, 10\}$ Am^{-2}) at various time steps. The shaded region represents the average interface currents at the interface of all fibers as a function of global position along the x axis (the average current of each fiber interface is plotted at its center point) and the solid line is a polynomial fit to the shaded region. As shown for the early time steps in Figure 5.16, fibers close to the anode are mainly active. As the simulations continue, currents are redistributed and more fibers become active. A similar pattern was observed in [9].

A quantitative comparison is made between results obtained with the proposed numerical model and results reported by Doyle *et al.* [9] in Figure 5.17, where the distribution of currents are plotted after 50 and 200 seconds. Two different fiber diameters are considered. Figure 5.17a shows the current values for the fiber diameter considered so far, with $r_f = r_p$ and volume fraction of fibers equal to the particles as considered by [9]. Although the trend matches well with what observed for particle based cathode [9], the corresponding curves are not close due to the fact that the total lateral surface of cylindrical fibers are not equal to that of particles for the same volume fraction of active materials. Figure 5.17b instead considers a situation where $r_f = 2/3 r_p$, for which a unique lateral surface is obtained and the number of fibers is increased to 25000 to keep the volume fraction of active fibers equal to that of the particles. In this case, the agreement between interface currents is considerably better, where the deviations are primarily attributed to the different micro-structure of fiber-based cathode.

As mentioned, the values reported in Figure 5.16 are averaged over each fiber interface. Interactions between inclusions however leads to arbitrary distribution of currents along each fiber-electrolyte interface. The interface currents are shown in Figure 5.18b for 4 sample fibers marked in Figure 5.18a. For this problem, a finer mesh is used for the fibers and each fiber is discretized into 20 equally sized segments. The local distribution of currents

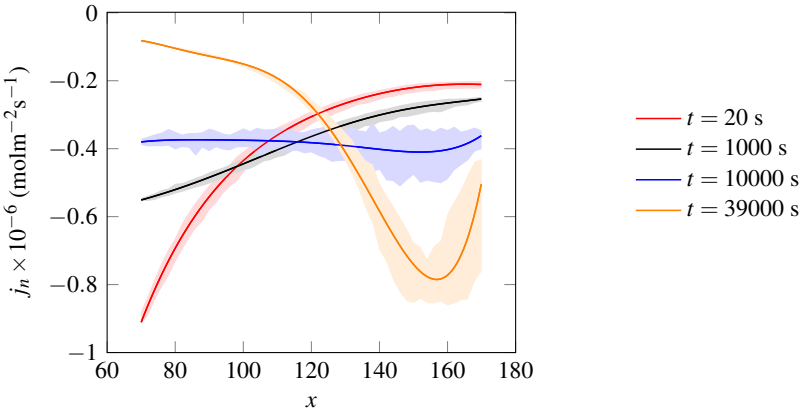

Figure 5.16: Interface current values for $I = 5$ Am^{-2} at different times. Results are averaged over fibers in three dimensions and fitted by a polynomial.

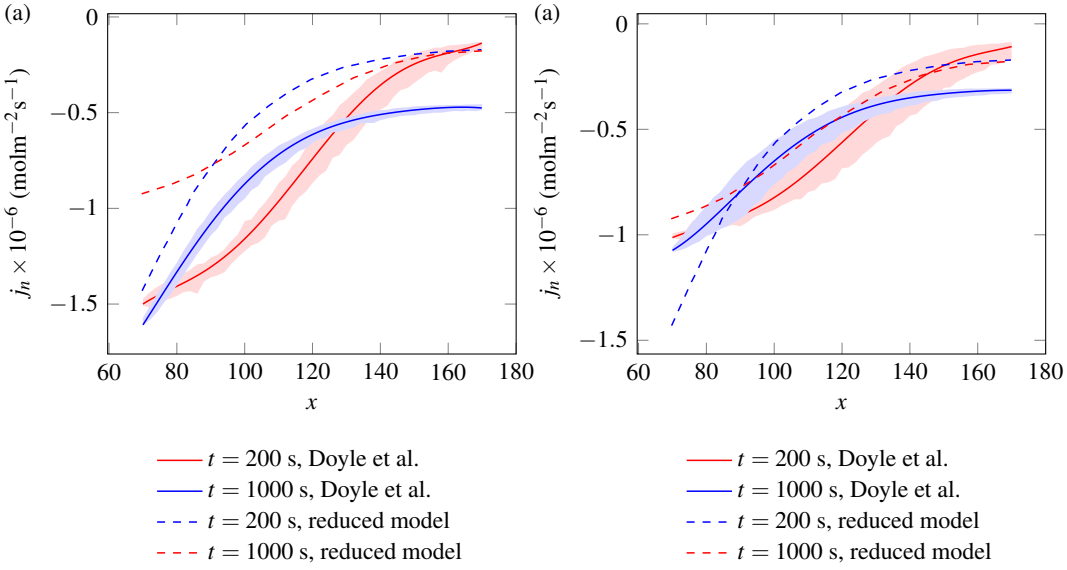

Figure 5.17: Interface current values for $I = 10$ Am^{-2}, compared to [9]. Results are averaged over fibers in three dimensions and fitted by a polynomial, (a) $r_f = r_p = 1\mu$m with 11000 fibers, (b) $r_f = 2/3r_p = 2/3\mu$m with 25000 fibers.

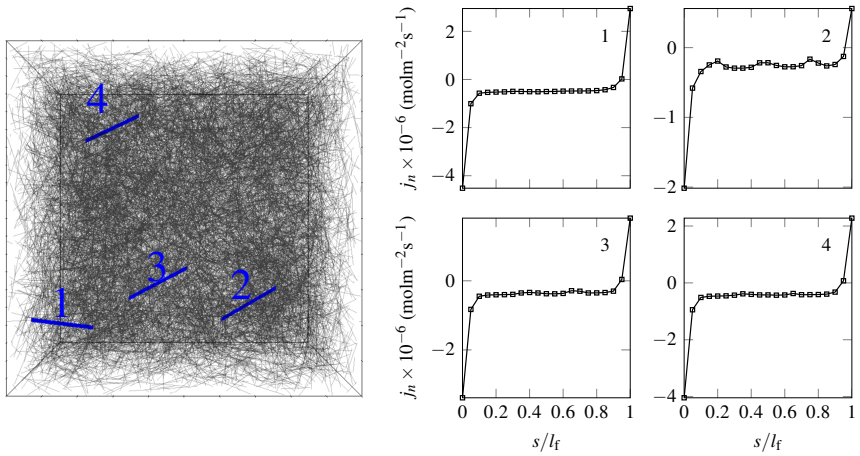

(a) (b)

Figure 5.18: Interface current values for $I = 5$ Am^{-2}. Due to fiber interactions, a uniform distribution is not observed for currents. $t = 1000$ s

is non-uniform along the fiber-electrolyte interface—a local decrease is observed near the tip closer to the anode and a local increase is observed near the far tip. Interestingly the numerical results predict that the current sign reverses locally near the far tip. The applied boundary conditions however always promote lithium insertion into the fiber and as shown in Figure 5.17, the average trends are in good agreement with predictions of reference results.

5.5.5. INTERACTIONS BETWEEN ACTIVE PARTICLES

The sign inversion behavior reported in Section 5.5.4 is attributed to interactions between active materials, and has not been reported elsewhere. To further verify that such behavior is not an artifact of the reduced model, results are reported for a simple 2-D configuration with two rectangular inclusions discretized using the standard model.

The half cell in Figure 5.19 is considered, where anode is a 20×20 μm^2 square, and the composite electrolyte is a rectangle with dimensions 150×20 μm^2. Maximum width of the active particles is equal to 20 μm and their thickness is set to 6μm. To minimize the sharp edges effect, particles corners are round-shaped.

Material properties and applied boundary conditions are the ones reported in Section 5.5.1, and a discharge process with $I = 15$ Am^{-2} is considered. To ensure that maximum interactions occur between the two particles, they are placed very close to each other (with their inner distance set equal to 1μm). To evaluate the effect of distance from anode, particles are positioned at two different locations along the long axis as shown in Figure 5.19.

Figure 5.20 reports the concentrations along the center line of the electrolyte and the values of particle-electrolyte interface currents. Results are shown for both standard model and a 2-D version of the reduced model discussed in Section 5.4.5. A larger electrolyte

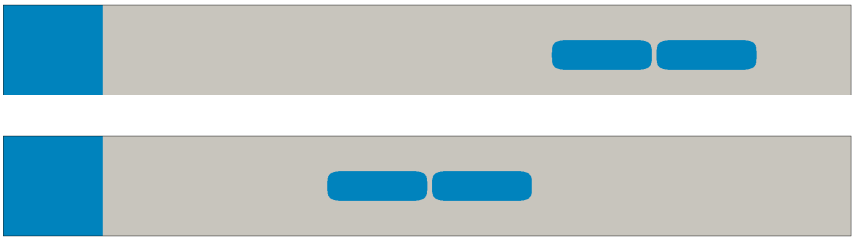

Figure 5.19: configurations used for inclusion interaction study. The inclusion has fixed size of 20 μm, and edge to edge distance between them is set to 1 μm.

diffusivity equal to ten times the one adopted by Doyle *et al.* [9] is also considered for the standard model.

Irrespective of the particles position, both models predict a non-uniform distribution of currents along the particle-electrolyte interface with a trend similar to the ones observed in Section 5.5.4. Among the considered configurations, the sign inversion only happens when particles are placed at a longer distance from the anode, and when the lower electrolyte diffusivity as used by Doyle *et al.* [9] is adopted. The sign inversion occurs for both numerical models at the inner edge around the particle which is closer to the anode. The sign inversion occurrence is triggered by lowered values of the electrolyte diffusivity and increased distance between the active particles and the anode, where as shown in Figure 5.20, both result to lower concentration of the lithium inside the electrolyte. As such, numerical simulations suggest that the governing equations discussed in Section 5.2 allows locally reversed current directions when electrolyte concentrations become very low, irrespective of the adopted numerical model.

5.6. CONCLUDING REMARKS

The proposed formulation is general, and can be applied for the modeling of high performance or multi-functional batteries with fiber-based electrodes. The numerical results show that results obtained with the standard finite element method can be accurately reproduced with a considerable reduction of the computational costs due to the embedded representation of fibers. The approach can also reproduce results obtained with the porous-electrode theory when an equivalent representation of the porous microstructure is considered. The method however comes with simplifications. The distributions of field variables, namely electric potential and concentrations are assumed to be uniform at each fiber cross section. This makes the method particularly suitable when dealing with relatively small fiber diameters, as in the case of structural batteries [39] and electrospun nanofibers electrodes [40]. Further, the porosity of the electrolyte material inside the composite electrodes was taken into account by averaging theorems through volume correction coefficients. The modified flow of lithium due to the micro structure tortuosity were also not explicitly defined.

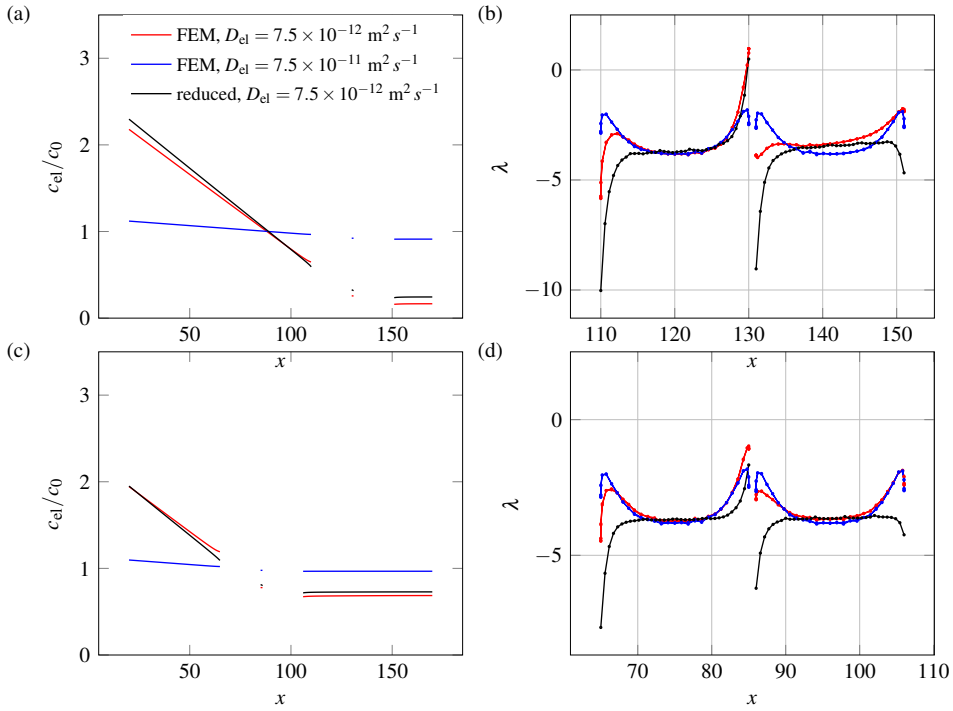

Figure 5.20: Electrolyte concentrations and interface currents for the two inclusion problem placed at two different positions along the electrolyte. Due to interactions between inclusions, current distribution around inclusions is not uniform, where in (a,b) particles are placed at a longer distance to anode, and in (c,d) particles are placed at a shorter distance to anode. The results predict a sign change close to the inclusion tips, when inclusion is placed in longer distance from left electrode or at regions where electrolyte concentration is low. Similarly, choosing a higher diffusivity for the electrolyte results in higher concentrations in electrolyte and therefore positive currents are not observed. Results are shown at cathode utilization of around 60%. Applied external current is equal to $I = 15\text{Am}^{-2}$.

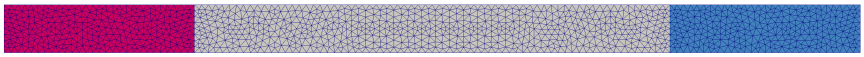

Figure 5.21: The three layer battery cell discretized using T3 mesh.

5.A. ANALYTICAL SOLUTION OF THE 3-LAYER BATTERY CELL

An analytical evaluation of the three layer battery cell (Figure 5.21) is presented. Unlike the composite battery cell discussed throughout this chapter, here we consider two homogeneous electrodes. For the sake of clarity, "pos" and "neg" identify positive and negative electrode, while "el" is used to identify the electrolyte between them. The governing equations are equivalent to what discussed in Section 5.2, while here they are recast into a one-dimensional format. The considered cell can be described by three domains such that:

$$l_{\text{neg}} = x \in [0, \delta_{\text{neg}}], \quad l_{\text{el}} = x \in [\delta_{\text{neg}}, \delta_{\text{neg}} + \delta_{\text{el}}], \quad l_{\text{pos}} = x \in [\delta_{\text{neg}} + \delta_{\text{el}}, \delta_{\text{tot}}]. \tag{5.65}$$

where $\delta_{\text{tot}} = \delta_{\text{neg}} + \delta_{\text{el}} + \delta_{\text{pos}}$. Mass and charge conservation equations in each layer read

$$\frac{\partial c_j}{\partial t} + \frac{\partial h_j}{\partial x} = 0, \quad x \in l_j, t \in [0, t_{\text{end}}) \tag{5.66a}$$

$$\frac{\partial i_j}{\partial x} = 0, \quad x \in l_j, t \in [0, t_{\text{end}}) \tag{5.66b}$$

where $j = \text{pos}, \text{neg}, \text{el}$, and the constitutive equations for the mass flux and charge density in positive and negative electrodes

$$h_j = -D_j \frac{\partial c_j}{\partial x}, \quad x \in l_j, t \in [0, t_{\text{end}}), \tag{5.67a}$$

$$i_j = -\kappa_j \frac{\partial \phi_j}{\partial x}, \quad x \in l_j, t \in [0, t_{\text{end}}), \tag{5.67b}$$

and the electrolyte

$$h_{el} = -D_{\text{el}} \frac{\partial c_{\text{el}}}{\partial x}, \tag{5.68a}$$

$$i_{el} = \gamma_c \frac{\partial c_{\text{el}}}{\partial x} - \gamma_\phi \, c_{\text{el}} \frac{\partial \phi_{\text{el}}}{\partial x}. \tag{5.68b}$$

are written. Charge transfer at the negative electrode-electrolyte interface is described through

$$\lambda_{\text{neg}} = i_0^{\text{neg}}(c_{\text{el}}) \left(\frac{F}{RT} \left(\phi_{\text{neg}} - \phi_{\text{el}} \right) \right), \tag{5.69a}$$

$$i_0{}^{\text{neg}}(c_{\text{el}}) = F \, k_{s1} \left(c_{\max}^{\text{el}} - c_{\text{el}} \right)^{\alpha_{c1}} c_{\text{el}}^{\alpha_{a1}}, \tag{5.69b}$$

where $x = \delta_{\text{neg}}, t \in [0, t_{\text{end}})$. Charge transfer at the positive electrode-electrolyte interface is described through

$$\lambda_{\text{pos}} = i_0^{\text{pos}}(c_{\text{pos}}, c_{\text{el}}) \left(\frac{F}{RT} \left(\phi_{\text{pos}} - \phi_{\text{el}} - U_{OC}^{\text{pos}} \right) \right), \tag{5.70a}$$

$$i_0{}^{\text{pos}}(c_{\text{pos}}, c_{\text{el}}) = F\, k_{s2} \left(c_{\max}^{\text{SPE}} - c_{\text{SPE}} \right)^{\alpha_{c2}} c_{\text{SPE}}^{\alpha_{a2}} \left(c_{\text{pos}}^{\max} - c_{\text{pos}} \right)^{\alpha_{a2}} c_{\text{neg}}^{\alpha_{c2}}, \tag{5.70b}$$

$$U_{OC}^{\text{neg}}(c_{\text{pos}}) = U_2^{\theta} - U_{\text{ref}}^{\theta} + \frac{RT}{F} \left[\ln \left(\frac{c_{\text{pos}}^{\max} - c_{\text{pos}}}{c_{\text{pos}}} \right) + \beta c_{\text{pos}} + \zeta \right], \tag{5.70c}$$

where $x = \delta_{\text{neg}} + \delta_{\text{el}}, t \in [0, t_{\text{end}})$.

The problem boundary conditions are

$$h_{\text{neg}} = 0, \quad x = 0, t \in [0, t_{\text{end}}), \tag{5.71a}$$

$$i_{\text{neg}} = I, \quad x = 0, t \in [0, t_{\text{end}}). \tag{5.71b}$$

$$h_{\text{pos}} = 0, \quad x = \delta_{\text{tot}}, t \in [0, t_{\text{end}}). \tag{5.71c}$$

$$\phi_{\text{pos}} = 0, \quad x = \delta_{\text{tot}}, t \in [0, t_{\text{end}}). \tag{5.71d}$$

with $I > 0$ ($I < 0$) corresponding to a discharge (charge) process. Initial conditions for concentration read

$$c_{\text{neg}} = c_{\text{neg}}^0, \quad x \in l_{\text{neg}}, t = 0, \tag{5.72a}$$

$$c_{\text{el}} = c_{\text{el}}^0, \quad x \in l_{\text{el}}, t = 0, \tag{5.72b}$$

$$c_{\text{pos}} = c_{\text{pos}}^0, \quad x \in l_{\text{pos}}, t = 0. \tag{5.72c}$$

and due to the layered geometry, conditions

$$i_{\text{neg}} = i_{\text{el}} = i_{\text{pos}} = I, \quad \text{and} \tag{5.73a}$$

$$\lambda_{\text{neg}} = -\lambda_{\text{pos}} = I, \tag{5.73b}$$

hold for $t \in [0, t_{\text{end}})$. The initial condition for the electric potential can be determined from (5.66b), (5.69), (5.70) and (5.72) by setting $I = 0$. This leads to

$$\phi_{\text{pos}} = 0, \tag{5.74a}$$

$$\phi_{\text{el}} = -U_{OC}^{\text{pos}}(c_{\text{pos}}^0), \tag{5.74b}$$

$$\phi_{\text{neg}} = -U_{OC}^{\text{pos}}(c_{\text{pos}}^0). \tag{5.74c}$$

Due to the simple layered geometry, mass conservation equations (5.66a) can be solved for each domain independently. For the negative electrode the mass conservation problem read

$$\frac{\partial c_{\text{neg}}}{\partial t} + \frac{\partial h_{\text{neg}}}{\partial x} = 0, \quad x \in l_{\text{neg}}, t \in [0, t_{\text{end}}), \tag{5.75a}$$

$$h_{\text{neg}} = 0, \quad x = 0, t \in [0, t_{\text{end}}), \tag{5.75b}$$

$$h_{\text{neg}} = \frac{I}{F}, \quad x = \delta_{\text{neg}}, t \in [0, t_{\text{end}}), \tag{5.75c}$$

$$c_{\text{neg}} = c_{\text{neg}}^0, \quad x \in l_{\text{neg}}, t = 0, \tag{5.75d}$$

for which the analytical solution is provided in [41, page 112, Eq. (3)]. The same holds for the negative electrode, where boundary conditions are simply flipped with respect to (5.75).

For the electrolyte, the mass conservation problem read

$$\frac{\partial c_{\text{el}}}{\partial t} + \frac{\partial h_{\text{el}}}{\partial x} = 0, \quad x \in l_{\text{el}}, t \in [0, t_{\text{end}}), \tag{5.76a}$$

$$h_{\text{el}} = \frac{D_{\text{X}^-}}{D_{\text{Li}^+} + D_{\text{X}^-}} \frac{I}{F}, \quad x = \delta_{\text{neg}}, t \in [0, t_{\text{end}}), \tag{5.76b}$$

$$h_{\text{el}} = \frac{D_{\text{X}^-}}{D_{\text{Li}^+} + D_{\text{X}^-}} \frac{I}{F}, \quad x = \delta_{\text{neg}} + \delta_{\text{el}}, t \in [0, t_{\text{end}}), \tag{5.76c}$$

$$c_{\text{el}} = c_{\text{el}}^0, \quad x \in l_{\text{el}}, t = 0. \tag{5.76d}$$

where by taking advantage of the symmetric boundary conditions (the total amount of concentration is constant in the electrolyte), it is possible to split domain l_{el} into two parts of equal length and rephrase the problem on each subdomain. The concentration is thus assigned and constant along one of the edges in each subdomain. For $x \in [\delta_{\text{neg}} + \delta_{\text{el}}/2, \delta_{\text{neg}} + \delta_{\text{el}}]$, the problem rephrases as

$$\frac{\partial c_{\text{el}}}{\partial t} + \frac{\partial h_{\text{el}}}{\partial x} = 0, \quad x \in [\delta_{\text{neg}} + \frac{\delta_{\text{el}}}{2}, \delta_{\text{neg}} + \delta_{\text{el}}], t \in [0, t_{\text{end}}), \tag{5.77a}$$

$$c_{\text{el}} = c_{\text{el}}^0, \quad x = \delta_{\text{neg}} + \frac{\delta_{\text{el}}}{2}, t \in [0, t_{\text{end}}), \tag{5.77b}$$

$$h_{\text{el}} = \frac{D_{\text{X}^-}}{D_{\text{Li}^+} + D_{\text{X}^-}} \frac{I}{F}, \quad x = \delta_{\text{neg}} + \delta_{\text{el}}, t \in [0, t_{\text{end}}), \tag{5.77c}$$

$$c_{\text{el}} = c_{\text{el}}^0, \quad x \in [\delta_{\text{neg}} + \frac{\delta_{\text{el}}}{2}, \delta_{\text{neg}} + \delta_{\text{el}}], t = 0. \tag{5.77d}$$

Solution to the above problem is found in [41, page 113, Eq. (5)]. A similar solution applies to subdomain $x \in [\delta_{\text{neg}}, \delta_{\text{neg}} + \delta_{\text{el}}/2]$.

Once the time-dependent concentration profile is know in the electrolyte, the electric potential in the electrolyte can be determined by integrating the non-linear ordinary differential equation (5.68b), refer, for example, to Danilov and Notten [21].

The electric potential profile in the entire cell is determined solving (5.66b), while taking into account that i) conditions (5.73) hold and ii) the electric potential discontinuities at the interfaces can de determined by inverting (5.69) and (5.70). Proceeding from right (the electric potential is known for $x = \delta_{\text{tot}}$) to left, the unknown electric potential at the side of the interface can be determined as

$$\phi_{\text{neg}} = \phi_{\text{el}} + \frac{RT}{F} \frac{I}{i_0^{\text{neg}}(c_{\text{el}})}, \quad x = \delta_{\text{pos}}, t \in [0, t_{\text{end}}), \tag{5.78a}$$

$$\phi_{\text{el}} = \phi_{\text{pos}} - U_{OC}^{\text{pos}}(c_{\text{pos}}) + \frac{RT}{F} \frac{I}{i_0^{\text{pos}}(c_{\text{pos}}, c_{\text{el}})}, \quad x = \delta_{\text{pos}} + \delta_{\text{el}}, t \in [0, t_{\text{end}}) \tag{5.78b}$$

In view of the boundary conditions (5.71d), the cell potential $\Delta\phi = \phi_{\text{pos}}(x = \delta_{\text{tot}}) - \phi_{\text{neg}}(x = 0)$ reduces to

$$\Delta\phi = -\phi_{\text{neg}}(x = 0), t \in [0, t_{\text{end}}). \tag{5.79}$$

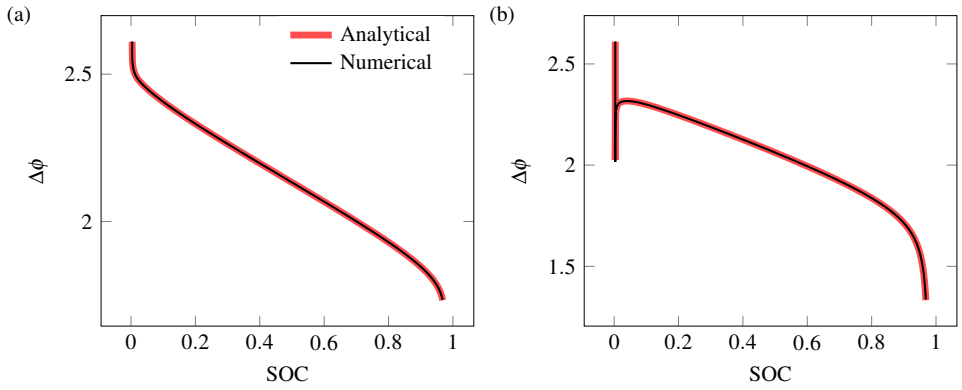

Figure 5.22: Cell potential curves for the three-layer cell under applied current I = 5Am^{-2} and for the interface parameter (a) $k_{s2} = 10^{-10}$ m^4 mol^{-1} s^{-1} and (b) $k_{s2} = 10^{-12}$ m^4 mol^{-1} s^{-1}.

5

The same problem was solved numerically using the standard model described in Section 5.4.1, where the cell potential curves and concentrations inside the electrolyte/cathode are compared against the analytical solutions in Figures 5.22 and 5.23, respectively. Non-structured T3 elements as shown in Figure 5.21 are used for the discretization of the problem and the material properties are similar to what reported in Section 5.5.1. The perfect agreement with analytical solutions in these figure verifies the numerical model predictions.

In the results not reported here, the described procedure was repeated using the general expression of the Butler-Volmer equation (5.55), where the non-linear counterparts of equations (5.69a) and (5.70a) have been numerically inverted. We did not observe appreciable differences in terms of SOC-cell potential curves (Figure 5.22) when the complete and linearized formulation were used for I equal to 5, 10 and 20 A m^{-2}. This suggests that the linearized form of the Butler-Volmer equation (5.57), adopted throughout this paper, is a suitable approximation for the explored range of electric current densities.

REFERENCES

[1] E. S. Pampal, E. Stojanovska, B. Simon, and A. Kilic, *A review of nanofibrous structures in lithium ion batteries,* Journal of Power Sources **300**, 199 (2015).

[2] P. Liu, E. Sherman, and A. Jacobsen, *Design and fabrication of multifunctional structural batteries,* Journal of Power Sources **189**, 646 (2009).

[3] V. Aravindan, J. Sundaramurthy, P. S. Kumar, Y.-S. Lee, S. Ramakrishna, and S. Madhavi, *Electrospun nanofibers: A prospective electro-active material for constructing high performance li-ion batteries,* Chemical Communications **51**, 2225 (2015).

[4] L. Persano, A. Camposeo, C. Tekmen, and D. Pisignano, *Industrial upscaling of electrospinning and applications of polymer nanofibers: a review,* Macromolecular Materials and Engineering **298**, 504 (2013).

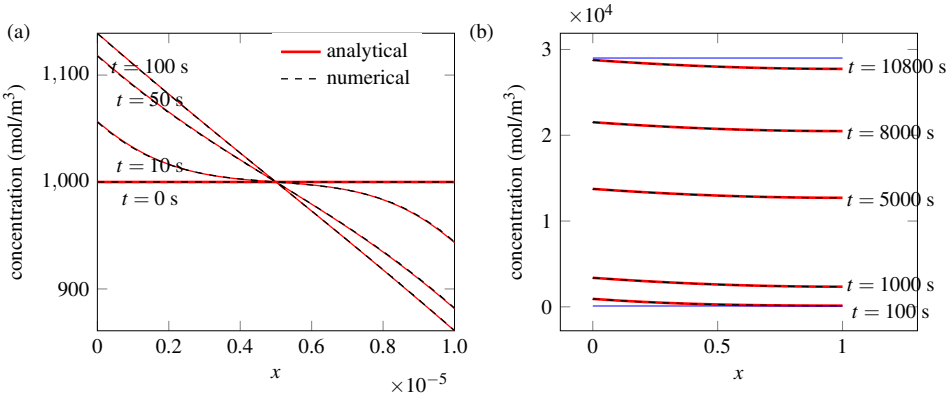

Figure 5.23: Concentration distribution in (a) electrolyte, (b) right electrode (cathode). Applied current I = 5Am^{-2} and interface parameter $k_{s2} = 10^{-10}$ m^4 mol^{-1} s^{-1} are considered.

[5] W. Li, L. Zeng, Y. Wu, and Y. Yu, *Nanostructured electrode materials for Lithium-ion and Sodium-ion batteries via electrospinning,* Science China Materials **59**, 287 (2016).

[6] L. E. Asp and E. S. Greenhalgh, *Structural power composites,* Composite Science and Technology **101**, 41 (2014).

[7] L. E. Asp, M. K. G. Johansson, G. Lindbergh, J. Xu, and D. Zenkert, *Structural battery composites: A review,* Functional Composites and Structures **1** (2019).

[8] L. E. Asp, *Multifunctional composite materials for energy storage in structural load paths,* Plastics, Rubber and Composites **42**, 144 (2013).

[9] M. Doyle, T. F. Fuller, and J. Newman, *Modeling of galvanostatic charge and discharge of the lithium/polymer/insertion cell,* Journal of the Electrochemical society **140**, 1526 (1993).

[10] J. Newman and W. Tiedemann, *Porous-electrode theory with battery applications,* AIChE Journal **21**, 25 (1975).

[11] R. E. Garcıa, Y.-M. Chiang, W. C. Carter, P. Limthongkul, and C. M. Bishop, *Microstructural modeling and design of rechargeable lithium-ion batteries,* Journal of The Electrochemical Society **152**, A255 (2005).

[12] R. T. Purkayastha and R. M. McMeeking, *An integrated 2-d model of a lithium ion battery: the effect of material parameters and morphology on storage particle stress,* Computational Mechanics **50**, 209 (2012).

[13] V. Zadin, D. Brandell, H. Kasemägi, J. Lellep, and A. Aabloo, *Designing the 3D-microbattery geometry using the level-set method,* Journal of Power Sources **244**, 417 (2013).

[14] V. Zadin, H. Kasemägi, A. Aabloo, and D. Brandell, *Modelling electrode material utilization in the trench model 3D-microbattery by finite element analysis,* Journal of Power Sources **195**, 6218 (2010).

[15] P. Priimägi, D. Brandell, S. Srivastav, A. Aabloo, H. Kasemägi, and V. Zadin, *Optimizing the design of 3D-pillar microbatteries using finite element modelling,* Electrochimica Acta **209**, 138 (2016).

[16] R. Fang, P. Farah, A. Popp, and W. A. Wall, *A monolithic, mortar-based interface coupling and solution scheme for finite element simulations of lithium-ion cells,* International Journal for Numerical Methods in Engineering **114**, 1411 (2018).

[17] H. R. Lusti and A. A. Gusev, *Finite element predictions for the thermoelastic properties of nanotube reinforced polymers,* Modelling and Simulation in Materials Science and Engineering **12**, S107 (2004).

[18] S. Balakrishnan and D. W. Murray, *Finite element prediction of reinforced concrete behavior*, Tech. Rep. Structural Engineering Report No. 138 (Department of Civil Engineering, The University of Alberta, 1986).

[19] A. E. Elwi and T. M. Hrudey, *Finite element model for curved embedded reinforcement,* Journal of Engineering Mechanics **115**, 740 (1989).

[20] J. Newman and K. Thomas-Alyea, *Electrochemical systems*, 3rd ed. (John Wiley and Sons, 2004).

[21] D. Danilov and P. H. L. Notten, *Mathematical modelling of ionic transport in the electrolyte of Li-ion batteries,* Electrochimica Acta **53**, 5569 (2008).

[22] D. Grazioli, O. Verners, V. Zadin, D. Brandell, and A. Simone, *Electrochemical-mechanical modeling of solid polymer electrolytes: Impact of mechanical stresses on Li-ion battery performance,* Electrochimica Acta **296**, 1122 (2019).

[23] V. Zadin, D. Brandell, H. Kasemägi, J. Lellep, and A. Aabloo, *Designing the 3D-microbattery geometry using the level-set method,* Journal of Power Sources **244**, 417 (2013).

[24] D. Grazioli, V. Zadin, D. Brandell, and A. Simone, *Electrochemical-mechanical modeling of solid polymer electrolytes: Stress development and non-uniform electric current density in trench geometry microbatteries,* Electrochimica Acta **296**, 1142 (2019).

[25] V. Zadin and D. Brandell, *Modelling polymer electrolytes for 3D-microbatteries using finite element analysis,* Electrochimica Acta **57**, 237 (2011).

[26] S. A. Roberts, V. E. Brunini, K. N. Long, and A. M. Grillet, *A framework for three-dimensional mesoscale modeling of anisotropic swelling and mechanical deformation in lithium-ion electrodes,* Journal of The Electrochemical Society **161**, F3052 (2014).

[27] A. Salvadori, D. Grazioli, M. Geers, D. Danilov, and P. Notten, *A multiscale-compatible approach in modeling ionic transport in the electrolyte of (lithium ion) batteries,* Journal of Power Sources **293**, 892 (2015).

[28] A. Salvadori, D. Grazioli, M. Magri, M. Geers, D. Danilov, and P. Notten, *On the role of saturation in modeling ionic transport in the electrolyte of (lithium ion) batteries,* Journal of Power Sources **294**, 696 (2015).

[29] E. de Souza Neto, D. Perić, and D. Owen, *Computational methods for plasticity*, 1st ed. (Wiley, 2014).

[30] H. Hartl, *Development of a Continuum-Mechanics-Based Tool for 3D Finite Element Analysis of Reinforced Concrete Structures and Application to Problems of Soil-Structure Interaction*, Ph.D. thesis, Graz University of Technology, Austria (2002).

[31] F. Barzegar and S. Maddipudi, *Three-dimensional modeling of concrete structures. II: Reinforced concrete,* Journal of Structural Engineering **123**, 1347 (1997).

[32] M. Duflot, *A meshless method with enriched weight functions for three-dimensional crack propagation,* International Journal for Numerical Methods in Engineering **65**, 1970 (2006).

[33] J. Chen, Z.-L. Tao, and S.-L. Li, *Lithium intercalation in Open-Ended TiS2 Nanotubes,* Angewandte Chemie International Edition **42**, 2147 (2003).

[34] S. Li, J. Liu, and B. Liu, *First principles study of nanostructured TiS_2 electrodes for Na and Mg ion storage,* Journal of Power Sources **320**, 322 (2016).

[35] M. Goudarzi and A. Simone, *Fiber neutrality in fiber-reinforced composites: Evidence from a computational study,* International Journal of Solids and Structures **156–157**, 14 (2019).

[36] B. Widom, *Random sequential addition of hard spheres to a volume,* The Journal of Chemical Physics **44**, 3888 (1966).

[37] S. Golmon, K. Maute, and M. L. Dunn, *Numerical modeling of electrochemical-mechanical interactions in lithium polymer batteries,* Computers & Structures **87**, 1567 (2009).

[38] L. O. Valøen and J. N. Reimers, *Transport properties of LiPF6-based Li-Ion battery electrolytes,* Journal of The Electrochemical Society **152**, A882 (2005).

[39] P. Liu, E. Sherman, and A. Jacobsen, *Design and fabrication of multifunctional structural batteries,* Journal of Power Sources **189**, 646 (2009).

[40] S. Jayaraman, V. Aravindan, P. Kumar, W. Ling, S. Ramakrishna, and S. Madhavi, *Exceptional performance of $TiNb_2o_7$ anode in all one-dimensional architecture by electrospinning,* ACS Applied Material Interfaces **6**, 8660 (2014).

[41] H. S. Carslaw and J. C. Jaeger, *Conduction of heat in solids,* Oxford: Clarendon Press, 1959, 2nd ed. (1959).

6

CONCLUDING REMARKS AND FUTURE WORK

The numerical tools discussed in this thesis facilitate the analysis of high aspect ratio (thin) inclusion composites with accuracy comparable to a fully-resolved finite element analysis. The proposed general three-dimensional modeling framework was verified for both mechanical and electro-chemical systems consisting of dense inclusion distributions. An important outcome of this thesis is the confirmation that the two major assumptions in embedded techniques, namely (i) geometrical reduction of fibers/platelets into mathematically equivalent one-dimensional objects, and (ii) continuous gradient fields across an inclusion, do not significantly impair their applicability. A one-to-one comparison with fully-resolved finite element method results confirmed the suitability of these tools for a wide range of applications using either mechanical or electrochemical formulations. These assumptions facilitate the study of dense inclusion composites (up to around 20000 discrete fibers were considered). We however identified certain conditions under which the validity of embedded models is not guaranteed.

Inaccuracies could arise either in form of oscillatory response (in the slip profile), or wrong estimation of the composite effective mechanical properties. Attempts were made to identify a set of dimensionless parameters for which the embedded method gives an accurate response. This however is usually challenging due to the existence of various coupled parameters. It is therefore recommended to perform a parameter sensitivity analysis before applying the embedded technique to practical problems. In general, inaccuracies in the predictions of embedded models are more severe when using large inclusion diameter/thickness (relative to the domain size), large contrast of material properties (ratio of Young's moduli or diffusion constant of inclusion to matrix material), and large interface constant (interface resistance parameter).

The main conclusions of this study can be summarized as follows:

- The major shortcomings of embedded methods with non-conformal meshing are demonstrated. These limitations manifest themselves in lowered convergence rate

and oscillatory slip response and are mainly attributed to continuous field derivatives (e.g. the matrix displacement gradients) across an inclusion (Chapter 2).

- One expensive treatment to minimize inaccuracies would be the use of the proposed strain discontinuity enriched embedded reinforcement model with slip (sdERS). This model however requires the generation of a background integration mesh, an expensive task that is not advised in situations with dense inclusion distributions. Besides, a three-dimensional implementation of this method does not seem straightforward (Chapter 2).

- Elastic fields and stress singularity due to rigid inclusions are accurately captured using the embedded reinforcement method. Interactions between inclusions, orientation effects, and local damage fronts are properly accounted for. Although the addition of inclusions is almost always increasing the elastic moduli of the composite, the level of improvement and post-elastic response are highly dependent on the orientation and distribution patterns (Chapter 3).

- A one-to-one comparison between the embedded model and a fully-resolved finite element method is performed. Results of the embedded model are valid only beyond certain ratios of fiber diameter with respect to the domain size (Chapter 4). This is attributed to the fact that variations of displacements across the fiber diameter are not taken into account in the embedded model.

- The notion of neutrality has been demonstrated for high aspect ratio fibers through the numerical analysis of a dimensionally-reduced fiber model and a fully-resolved finite element model. The common understanding that fibers improve the mechanical properties of the matrix in which they are embedded is not correct. The most unfavorable fiber orientation represents a state of fiber neutrality, a situation in which a fiber does not perturb the stress field and therefore has no influence on the mechanical properties of the composite (Chapter 4).

- A fiber-diameter study similar to that performed in Chapter 4 was also performed for the coupled electrochemical problem with the fiber-based battery model in Chapter 5. As a general remark, it was found that a better agreement with the standard finite element method solution is observed for the electrochemical problem compared to a mechanical problem at larger fiber diameters.

The attempts made in this thesis are an initial step towards a general computational tool for micro-mechanical analysis of high aspect ratio inclusion composites. The following improvements can be considered:

- Extension of the discontinuous gradient method discussed in Chapter 2 to three-dimensional fibers to improve the convergence properties of the method and to significantly lower the non-physical slip oscillations. Discontinuous gradient methods can be proposed on the basis of more powerful numerical candidates like virtual element method, domain fitting algorithms, and interface generalized finite element method.

- Existing techniques are only applicable to relatively small fiber diameters. An extension of current numerical models that can handle arbitrary fiber geometries with large diameters is considered as highly desirable for many applications. The numerical methods mentioned in the previous item are ideal candidates for such improvements.
- A detailed study considering large deformations is important. Investigations can be done for the limit case of rigid inclusions which show singular stress fields in the elastic range. A detailed evaluation of inclusion reorientation effect is of importance especially for rubber like materials and naturally occurring composites which are characterized by very soft matrices.
- A combination of the model for the mechanical problem (Chapters 2-4) and the electro-chemical problem (Chapter 5) leads to a general modeling framework that can be readily applied to multi-functional structural batteries.
- Further improvements of the fiber-based battery model discussed in Chapter 5 can be proposed by incorporating local concentration variations across the fiber diameter by means of local closed-form solutions. Effect of fiber concentrations gradients can be significant when external currents are very high and large diameters are considered, and can lead to surface saturation of fibers even if the maximum fiber capacity is not reached.

ACKNOWLEDGEMENTS

The research presented in this thesis has received funding from the European Research Council under the European Union's Seventh Framework Programme (FP7/2007-2013) / ERC Grant agreement n° 617972. The work presented in Chapter 3 has been done in collaboration with Francesco Dal Corso and Davide Bigoni who gratefully acknowledge financial support from the Italian Ministry of Education, Universities and Research (MIUR) through the grant PROSCAN (MIUR-ARS01_01384.

I would like to express my gratitude to my promotors, A. Simone and L. J. Sluys who made it possible for me to pursue my research at TU Delft, and especially to A. Simone who trusted me in taking part as a member of this project. Special thanks go to the staff members at TU Delft who helped me with the administrative works, and my former colleagues with whom I had amazing moments and who supported me in this journey towards Ph.D. I would like to extend my especial thanks to Ali, Jafar, Behrouz, Davide, Mehdi, Fariborz, Arman, Mingzhao, Prashanth, Yaolu, Dragan, Liting, Zheng, Tiziano, Luiz, Richard, Lu, Dongyu, Amin, Mohammad, Sanaz, Marcello, Frans, Frank, Rafid, Anneke, Jaap and Osvalds for all the fruitful discussions and moments. I am particularly indebted to Davide Grazioli for his support on the works in Chapter 5, and to Francesco Dal Corso for his contribution to Chapter 3.

Finally, I would like to dedicate this work to my family, and especially appreciate the support of my parents who have been a strong foundation of good advice and empathy. Also, my deepest sense of appreciation goes to the ancient country that I come from and which continuously motivates me, and the amazing country that I currently live in.

Mohsen Goudarzi
Delft, March 2020

CURRICULUM VITÆ

Mohsen GOUDARZI

16-06-1989 Born in Tehran, Iran.

September 2007 – June 2011	B.Sc. in Civil Engineering Karaj Islamic Azad University Karaj, Iran
August 2011 – June 2014	M.Sc. in Civil Engineering University of Tehran Tehran, Iran
September 2014 – July 2019	Ph.D. candidate Delft University of Technology Delft, the Netherlands
July 2019 – November 2019	Researcher University of Twente Enschede, the Netherlands
November 2019 – present	Researcher Utrecht University Utrecht, the Netherlands

LIST OF PUBLICATIONS

JOURNAL PUBLICATIONS

1. Malagu' M., **Goudarzi M.**, Lyulin A, Benvenuti E, Simone A., "Diameter dependent elastic properties of carbon nanotube-polymer composites: Emergence of size effects from atomistic to continuum scale." *Composites Part B*, 2017.

2. **Goudarzi M.**, Simone A., "Fiber neutrality in fiber-reinforced composites: Evidence from a computational study." *International Journal of Solids and Structures*, 2018.

3. **Goudarzi M.**, Simone A., "Discrete inclusion models for reinforced composites: Comparative performance analysis and modeling challenges." *Computer Methods in Applied Mechanics and Engineering*, 2019.

4. **Goudarzi M.**, Dal Corso F., Bigoni D, Simone A., "Rigid line inclusions as elastic stiffeners and shear band instability triggers." *submitted*.

5. **Goudarzi M.**, Grazioli D., Simone A., "Computational modeling of fiber-based batteries." *in preparation*.

CONFERENCE PRESENTATIONS

1. **Goudarzi M.**, Simone A., "A Generalized Finite Element Method Approach to Rigid Line Inclusions", ESMC 9, Madrid, Spain, July 2015.

2. **Goudarzi M.**, Simone A., "Adaptive enriched embedded reinforcement approaches for discrete fiber modeling: Performance and challenges", WCCM XII, Seoul, South Korea, July 2016.

3. **Goudarzi M.**, Simone A., "Discrete fiber modelling: Validity of dimensionally reduced models", ICCS 20, Paris, France, September 2017.

4. **Goudarzi M.**, Grazioli D., Simone A., "An efficient computational tool for fiber-based lithium-ion batteries", ECCM 6, Glasgow, UK, June 2018.